



ISSN 2959-0663 (Print)
ISSN 2959-0671 (Online)
ISSN-L 2959-0663

EURASIAN JOURNAL OF CHEMISTRY

2024. Vol. 29 No. 4(116)



ISSN 2959-0663 (Print)
ISSN 2959-0671 (Online)
ISSN-L 2959-0663

EURASIAN JOURNAL OF CHEMISTRY

2024

Volume 29, No. 4 (116)

Founded in 1996

Published 4 times a year

Karaganda
2024

Publisher: Karagandy University of the name of academician E.A. Buketov

Postal address: 28, Universitetskaya Str., Karaganda, 100024, Kazakhstan

E-mail: chemistry.vestnik@ksu.kz;
irina.pustolaikina@ksu.kz;
ipustolaikina@gmail.com

Tel./fax: +7(7212) 34-19-40.

Web-site: <https://ejc.buketov.edu.kz>

Editor-in-Chief

Ye.M. Tazhbayev, Doctor of Chemical sciences

Executive Editor

I.A. Pustolaikina, Candidate of Chemical sciences

Editorial board

- Z.M. Muldakhmetov**, Academician of NAS RK, Doctor of chem. sciences, Institute of Organic Synthesis and Coal Chemistry of the Republic of Kazakhstan, Karaganda (Kazakhstan);
- S.M. Adekenov**, Academician of NAS RK, Doctor of chem. sciences, International Research and Production Holding "Phytochemistry", Karaganda (Kazakhstan);
- S.E. Kudaibergenov**, Doctor of chem. sciences, Institute of Polymer Materials and Technologies, Almaty (Kazakhstan);
- V. Khutoryanskiy**, Professor, University of Reading, Reading (United Kingdom);
- Fengyun Ma**, Professor, Xinjiang University, Urumqi (PRC);
- Xintai Su**, Professor, South China University of Technology, Guangzhou (PRC);
- R.R. Rakhimov**, Doctor of chem. sciences, Norfolk State University, Norfolk (USA);
- N. Nuraje**, Associate Professor, Nazarbayev University, Astana (Kazakhstan);
- S.A. Beznosyuk**, Doctor of phys.-math. sciences, Altai State University, Barnaul (Russia);
- B.F. Minaev**, Doctor of chem. sciences, Bohdan Khmelnytsky National University of Cherkasy, Cherkasy (Ukraine);
- I.V. Kulakov**, Doctor of chem. sciences, University of Tyumen (Russia);
- R.P. Bhole**, PhD, Associate Professor, Dr. D.Y. Patil Institute of Pharmaceutical Sciences and Research, Sant Tukaram Nagar, Pimpri, Pune (India);
- S.S. Gurav**, PhD, Professor, Goa College of Pharmacy, Panaji (India);
- A.A. Atakhanov**, Doctor of techn. sciences, Institute of Polymer Chemistry and Physics, Tashkent (Uzbekistan);
- I.V. Korolkov**, PhD, Associated Professor, Astana branch, Institute of Nuclear Physics of the Republic of Kazakhstan, Astana (Kazakhstan);
- A.M. Makasheva**, Doctor of techn. sciences, Zh. Abishev Chemical-Metallurgical Institute, Karaganda (Kazakhstan);
- M.I. Baikenov**, Doctor of chem. sciences, Karagandy University of the name of acad. E.A. Buketov (Kazakhstan);
- L.K. Salkeeva**, Doctor of chem. sciences, Karagandy University of the name of acad. E.A. Buketov (Kazakhstan);
- G.I. Dzhardimalieva**, Doctor of chem. sciences, Federal Research Center of Problems of Chemical Physics and Medicinal Chemistry, Russian Academy of Sciences, Chernogolovka, Moscow Region (Russia);
- S.K. Filippov**, PhD, Project Leader, DWI-Leibniz Institute for Interactive Materials, Aachen, North Rhine-Westphalia, (Germany);
- S.A. Ivashenko**, Doctor of pharm. sciences, Karaganda Medical University (Kazakhstan).

Proofreader I.N. Murtazina

Computer layout V.V. Butyaikin

Eurasian Journal of Chemistry. — 2024. — Vol. 29, No. 4(116). — 108 p.

ISSN 2959-0663 (Print). ISSN 2959-0671 (Online). ISSN-L 2959-0663

Proprietary: NLC "Karagandy University of the name of academician E.A. Buketov".

Registered by the Ministry of Information and Social Development of the Republic of Kazakhstan. Re-registration certificate No. KZ95VPY00063697 dated 30.01.2023.

Signed in print 27.12.2024. Format 60×84 1/8. Offset paper. Volume 13,5 p.sh. Circulation 200 copies. Price upon request. Order № 135.

Printed in the Publishing house of NLC "Karagandy University of the name of academician E.A. Buketov". 28, University Str., Karaganda, 100024, Kazakhstan. Tel.: +7(7212) 35-63-16. E-mail: izd_kargu@mail.ru

© Karagandy University of the name of academician E.A. Buketov, 2024

CONTENTS

ORGANIC CHEMISTRY

- Gorokhov, V.Yu., Zabolotnykh, S.A., Chekanova, L.G., & Vaulina, V.N.* A New Method for the Synthesis of Ald(ket)azines and their Antioxidant Activity 4
- Kaldybekov, D.B., Shatabayeva, E.O., Polatkhan, A.A., Tuleyeva, R.N, Irmukhametova, G.S., & Khutoryanskiy, V.V.* Development and Investigation of Mucoadhesive Polymers Based on Chitosan for Intravesical Therapy 13

PHYSICAL AND ANALYTICAL CHEMISTRY

- Lahmar, N., Djehiche, M., & Bachiri, M.* Removal of E110 from Aqueous Solution Using Heat-Activated Persulfate..... 22
- Abdulsattar, M.A.* Effect of Acetylene Properties on its Gas Sensing by NiO Doped ZnO Clusters: A Transition State Theory Model..... 35
- Rakhimzhanova, A.S., Muzaparov, R.A., Pustolaikina, I.A., Kurmanova, A.F., Nikolskiy, S.N., Kapishnikova, D.D., Stalinskaya, A.L., & Kulakov, I.V.* A Series of Novel Integrastatins Analogues: *In Silico* Study of Physicochemical and Bioactivity Parameters 44

INORGANIC CHEMISTRY

- Turovets, M.A., Fomin, V.N., Kelesbek, N.K., Kaykenov, D.A., Sadyrbekov, D.T., Aynabayev, A.A., Aldabergenova, S.K.* Chemometric Approach for the Determination of Vanadium by the LIBS Method . 61
- Soualmi, S., Henni, M., Djahnit, L., & Hamdani, H.* Sol-gel Synthesized ZnO-SrMn₂O₄ Nanocomposite and Its Antibacterial Properties..... 71

CHEMICAL TECHNOLOGY

- Khoshimov, I.E., Turdialieva, Sh.I., Seytnazarov, A.R., Namazov, Sh.S., & Rifky, M.* Investigation of Vapor Pressure and Infrared Spectroscopic Analysis of Phosphoric Acid Extract Evaporation after Desulfation with SrCO₃ 82
- Surov, O.V., & Voronova, M.I.* Obtaining Cellulose Nanocrystals in a Medium of Primary Monohydric Alcohols 92
- Index of articles published in “Eurasian Journal of Chemistry” in 2024..... 106

ORGANIC CHEMISTRY

Article

Received: 7 June 2024 | Revised: 8 October 2024 |
Accepted: 15 October 2024 | Published online: 23 November 2024

UDC 547-304.2, 547-304.6

<https://doi.org/10.31489/2959-0663/4-24-7>

Valeriy Yu. Gorokhov ^{*}, Svetlana A. Zabolotnykh ,
Larisa G. Chekanova , Vera N. Vaulina 

*Institute of Technical Chemistry of the Ural Branch of the Russian Academy of Sciences;
Perm Federal Research Center of the Ural Branch of the Russian Academy of Sciences, Perm, Russia*

(*Corresponding author's e-mail: Gorokhov_V.Yu@mail.ru)

A New Method for the Synthesis of Ald(ket)azines and their Antioxidant Activity

The synthesis of biologically active compounds frequently requires the establishment of specific conditions (such as pressure, temperature, medium, solvent, and catalyst) or the use of expensive equipment. An important task is the search for simple synthesis methods for promising biologically active compounds. This paper presents data on a rapid method for the synthesis of ald(ket)azines (azines) with a variety of biological and physicochemical properties. Hydrazine hydrate reacts readily by condensation with aromatic (heterocyclic) aldehydes or ketones to form azines. The reaction occurs at room temperature in acetic acid. The synthesis is completed in a short period of time, between 5 and 15 seconds, with yields of 32 % to 98 % after recrystallization. The formation rate of ald(ket)azines depends on the reaction medium and the presence of hydrogen donors in the system, and increases with increasing acidity. The investigation did not yield any discernible pattern in the impact of electron-donor or electron-acceptor substituents in the *para*-, *meta*-, or *ortho*-positions at aromatic (heterocyclic) aldehydes or ketones on the azines yield. The synthesized compounds were studied using ¹H NMR spectroscopy, chromatography, and elemental analysis. The Ferric Reducing Antioxidant Power (FRAP) spectrophotometric method was used to study the antioxidant activity of the compounds obtained. Compounds with an N,N-dimethyl- or N,N-diethyl group in the *para*-position of the aldehyde fragment of azine showed a significant antioxidant effect. The results obtained exceed the antioxidant value of ascorbic acid — an industrially used oxidation inhibitor.

Keywords: condensation reaction, aldazines, ketazines, azines, synthesis, Schiff bases, hydrazinium monoacetate.

Introduction

Schiff bases (imines, azomethines, azines) containing the structural element (–CR=N–) represent a fairly common class of organic compounds with a wide range of practical applications. They possess antidiabetic [1], antitumour [2, 3], antimicrobial [4–7], antifungal [8, 9], cytotoxic [10, 11], luminescent properties [12, 13], and are used as plant growth regulators [14], chemosensors [15, 16], liquid crystals [17] or universal building blocks in organic synthesis [18, 19].

The known methods for azines synthesis are based on the interaction of hydrazine hydrate or its salts with aromatic aldehydes (ketones) in various solvents at different temperatures and stirring [9, 16, 17, 20–27], without solvent [28, 29] (with the addition of iodine/bromine [30], aluminium oxide [31, 32]) or using different catalysts (ruthenium complex [33], nickel [34] or its salts [35], bismuth [36]).

Many of the described methods for azines synthesis have a number of disadvantages, such as special reaction conditions, long reaction time, low yields and the use of expensive catalysts. The aim of our work is to develop a simple and rapid method for the ald(ket)azines synthesis.

Experimental

Materials

General Information: starting hydrazine hydrate (64 %, CAS 7803-57-8), phenylmethanal (≥ 99.5 %, CAS 100-52-7), 4-bromobenzaldehyde (99 %, CAS 1122-91-4), 4-chlorobenzaldehyde (97 %, CAS 104-88-1), 4-nitrobenzaldehyde (98 %, CAS 555-16-8), 4-methoxybenzaldehyde (≥ 98 %, CAS 123-11-5), 4-(dimethylamino)benzaldehyde (98 %, CAS 100-10-7), 4-(diethylamino)benzaldehyde (99 %, CAS 120-21-8), 4-hexyloxybenzaldehyde (99 %, CAS 5736-94-7), 4-decyloxybenzaldehyde (CAS 24083-16-7), 2-thiophenylaldehyde (98 %, CAS 98-03-3), 2-hydroxybenzaldehyde (≥ 98 %, CAS 90-02-8), 2-hydroxy-1-naphthaldehyde (CAS 708-06-5), 3-pyridinecarbaldehyde (98 %, CAS 500-22-1), 3-nitrobenzaldehyde (99 %, CAS 202-772-6), acetophenone (≥ 98 %, CAS 98-86-2), 4-nitroacetophenone (98 %, CAS 100-19-6), 2-hydroxyacetophenone (99 %, CAS 118-93-4), from Aldrich, Acros Organics, were used without purification.

The structure of the obtained compounds was confirmed by ^1H NMR spectroscopy, chromatography-mass spectrometry and elemental analysis. Mass spectra were recorded on an Agilent Technologies 6890N/5975B chromatography-mass spectrometer (USA); ^1H NMR spectra were recorded on a Bruker Advance III 400 (Bruker Corporation, USA) in DMSO-d_6 , CDCl_3 solvent; ^1H chemical shifts are given relative to SiMe_4 . Elemental analysis was performed on a VARIO EL CUBE elemental analyzer (Elementar, Germany). Melting points were determined on a Stuart SMP40 device (Stuart Scientific, UK).

General Procedure for the Synthesis of Ald(ket)azines **3a-r**

0.04 mol of aldehyde (ketone) **1a-r** and 0.17 mol of acetic acid were mixed until completely dissolved and 0.026 mol of hydrazine hydrate **2** was added dropwise to the resulting solution under stirring. After 5–15 seconds, the precipitate (compounds **3f, g** do not precipitate, they are precipitated by water) was neutralized with ammonia solution (except compound **3k, r**), washed with water, filtered and recrystallized from benzene, chloroform or dimethyl sulfoxide: ethanol mixture (ratio 1:1).

1,2-bis(benzylidene)hydrazine 3a. Yield is 3.03 g (73 %), yellow crystals, m.p. 92–93 °C (92–93 °C [37]). ^1H NMR spectrum (400.0 MHz, CDCl_3) δ , ppm: 7.39–7.44 m (6H, Ar-H), 7.80–7.85 m (4H, Ar-H), 8.64 s (2H, 2 CH=N). Mass spectrum, m/z ($I_{rel.}$, %): 208 (70.3), 131 (100), 104 (26.7), 90 (3.9), 77 (37.5). Found, %: C 80.70; H 5.79; N 13.42. $\text{C}_{14}\text{H}_{12}\text{N}_2$. Calculated, %: C 80.74; H 5.81; N 13.45.

1,2-bis(4-bromobenzylidene)hydrazine 3b. Yield is 6.92 g (95 %), yellow crystals, m.p. 230–231 °C (223–224 °C [28]). ^1H NMR spectrum (400.0 MHz, DMSO-d_6) δ : 7.71–7.74 m (4H, Ar-H, J 8.0 Hz), 7.83–7.85 m (4H, Ar-H, J 8.0 Hz), 8.65 s (2H, 2 CH=N). Mass spectrum, m/z ($I_{rel.}$, %): 366 (59.4) [M] $^+$, 209 (100), 183 (18.7), 156 (2.2). Found, %: C 45.90; H 2.71; N 7.62. $\text{C}_{14}\text{H}_{10}\text{N}_2\text{Br}_2$. Calculated, %: C 45.94; H 2.75; N 7.65.

1,2-bis(4-chlorobenzylidene)hydrazine 3c. Yield is 5.30 g (96 %), yellow crystals, m.p. 208–210 °C (208–210 °C [37]). ^1H NMR spectrum (400.0 MHz, CDCl_3) δ , ppm: 7.38–7.42 m (4H, Ar-H, J 8.0 Hz), 7.73–7.77 m (4H, Ar-H, J 8.0 Hz), 8.56 s (2H, 2 CH=N). Mass spectrum, m/z ($I_{rel.}$, %): 277 (51.6) [M] $^+$, 165 (100), 152 (2.3), 138 (28), 111 (29.7). Found, %: C 60.59; H 3.58; N 10.06. $\text{C}_{14}\text{H}_{10}\text{N}_2\text{Cl}_2$. Calculated, %: C 60.67; H 3.64; N 10.11.

1,2-bis(4-nitrobenzylidene)hydrazine 3d. Yield is 5.42 g (91 %), yellow crystals, m.p. 312–313 °C (312–313 °C [37]). ^1H NMR spectrum (400.0 MHz, DMSO-d_6) δ , ppm: 8.14–8.16 m (4H, Ar-H, J 8.0 Hz), 8.33–8.35 m (4H, Ar-H, J 8.0 Hz), 8.78 s (2H, 2 CH=N). Mass spectrum, m/z ($I_{rel.}$, %): 298 (46.7) [M] $^+$, 176 (100), 149 (6.5). Found, %: C 56.30; H 3.35; N 18.74. $\text{C}_{14}\text{H}_{10}\text{N}_4\text{O}_4$. Calculated, %: C 56.38; H 3.38; N 18.79.

1,2-bis(4-methoxybenzylidene)hydrazine 3e. Yield is 5.02 g (94 %), yellow crystals, m.p. 177–179 °C (178 °C [37]). ^1H NMR spectrum (400.0 MHz, DMSO-d_6) δ , ppm: 3.84 s (6H, 2 CH_3), 7.03–7.07 m (4H, Ar-H, J 8.0 Hz), 7.79–7.83 m (4H, Ar-H, J 8.0 Hz), 8.59 s (2H, 2 CH=N). Mass spectrum, m/z ($I_{rel.}$, %): 268 (100) [M] $^+$, 161 (65), 134 (21), 107 (3.1). Found, %: C 71.58; H 5.97; N 10.40. $\text{C}_{16}\text{H}_{16}\text{N}_2\text{O}_2$. Calculated, %: C 71.62; H 6.01; N 10.44.

1,2-bis(4-N,N-dimethylaminobenzylidene)hydrazine 3f. Yield is 5.73 g (97 %), yellow crystals, m.p. 263–264 °C (263–264 °C [38]). ^1H NMR spectrum (400.0 MHz, DMSO-d_6) δ , ppm: 3.02 s (12H, 4 CH_3), 6.78–6.81 d (4H, Ar-H, J 12.0 Hz), 7.65–7.68 d (4H, Ar-H, J 12.0 Hz), 8.48 s (2H, 2 CH=N). Mass spectrum, m/z ($I_{rel.}$, %): 294 (100) [M] $^+$, 174 (21.8), 147 (36), 133 (2.3), 120 (7.5). Found, %: C 73.40; H 7.51; N 19.00. $\text{C}_{18}\text{H}_{22}\text{N}_4$. Calculated, %: C 73.44; H 7.53; N 19.03.

1,2-bis(4-N,N-diethylaminobenzylidene)hydrazine 3g. Yield is 6.86 g (98 %), yellow crystals, m.p. 195–197 °C (193 °C [39]). ^1H NMR spectrum (400.0 MHz, CDCl_3) δ , ppm: 1.17–1.20 t (12H, 4 CH_3),

3.37–3.42 t (8H, 4CH₂), 6.64–6.66 d (4H, Ar-H, *J* 8.0 Hz), 7.63–7.76 d (4H, Ar-H, *J* 8.0 Hz), 8.52 s (2H, 2 CH=N). Mass spectrum, *m/z* (*I*_{rel.}, %): 350 (100) [*M*]⁺, 202 (9.4), 175 (15.6), 161 (20.3), 148 (1.6). Found, %: C 75.31; H 8.58; N 15.94. C₂₂H₃₀N₄. Calculated, %: C 75.39; H 8.63; N 15.98.

1,2-bis-(4-hexyloxybenzylidene)hydrazine 3h. Yield is 6.91 g (97 %), yellow crystals, m.p. 120–127 °C (turbid phase), at 128 °C full clearing. ¹H NMR spectrum (400.0 MHz, CDCl₃) δ, ppm: 0.88–0.92 t (6H, 2CH₃), 1.31–1.36 m (8H, 4CH₂), 1.42–1.50 m (4H, 2CH₂), 1.75–1.82 m (4H, 2CH₂) 3.98–4.01 t (4H, 2 OCH₂, *J* 8.0, 4.0 Hz), 6.92–6.94 d (4H, Ar-H, *J* 8.0 Hz), 7.75–7.77 d (4H, Ar-H, *J* 8.0 Hz), 8.60 s (2H, 2 CH=N). Mass spectrum, *m/z* (*I*_{rel.}, %): 408 (100) [*M*]⁺, 231 (89), 206 (2.2), 204 (4.3), 130 (2.1), 41 (45.5). Found, %: C 76.38; H 8.84; N 6.81. C₂₆H₃₆N₂O₂. Calculated, %: C 76.43; H 8.88; N 6.86.

1,2-bis(4-decyloxybenzylidene)hydrazine 3i. Yield is 9.15 g (88 %), yellow crystals, m.p. 121–128 °C (turbid phase), at 129 °C full clearing. ¹H NMR spectrum (400.0 MHz, CDCl₃) δ, ppm: 0.86–0.89 t (6H, 2CH₃), 1.26–1.30 m (16H, 8CH₂), 1.32–1.37 m (8H, 4CH₂), 1.42–1.49 m (4H, 2 CH₂), 1.75–1.82 m (4H, 2 CH₂), 3.98–4.01 t (4H, 2 OCH₂, *J* 4.0, 4.0 Hz), 6.92–6.94 d (4H, Ar-H, *J* 8.0 Hz), 7.75–7.77 d (4H, Ar-H, *J* 8.0 Hz), 8.60 c (2H, 2 CH=N). Mass spectrum, *m/z* (*I*_{rel.}, %): 520 (87.4) [*M*]⁺, 287 (100), 260 (10.5), 130 (7). Found, %: C 78.35; H 10.00; N 5.32. C₃₄H₅₂N₂O₂. Calculated, %: C 78.41; H 10.06; N 5.38.

1,2-bis(thiophen-2-ylmethylene)hydrazine 3j. Yield is 4.02 g (93 %), yellow crystals, m.p. 158–159 °C (161 °C [40]). ¹H NMR spectrum (400.0 MHz, CDCl₃) δ, ppm: 7.09–7.11 t (2H, Ar-H, *J* 4.0, 4.0 Hz), 7.39–7.41 d (2H, Ar-H, *J* 8.0 Hz), 7.45–7.46 d (2H, Ar-H, *J* 4.0 Hz), 8.75 s (2H, CH=N). Mass spectrum, *m/z* (*I*_{rel.}, %): 220 (100) [*M*]⁺, 137 (7.5), 110 (30.5), 96 (9.8), 83 (5.9). Found, %: C 54.47; H 3.60; N 12.66; S 29.07. C₁₀H₈N₂S₂. Calculated, %: C 54.52; H 3.66; N 12.72; S 29.10.

1,2-bis(2-hydroxybenzylidene)hydrazine 3k. Yield is 4.56 g (95 %), yellow crystals, m.p. 224 °C (224 °C [41]). ¹H NMR spectrum (400.0 MHz, DMSO-d₆) δ, ppm: 7.00–7.02 d (4H, Ar-H, *J* 8.0 Hz), 7.41–7.45 m (2H, Ar-H), 7.70–7.72 m (2H, Ar-H, *J* 8.0 Hz), 9.00 s (2H, 2 CH=N), 11.08 w.s. (2H, 2OH). Mass spectrum, *m/z* (*I*_{rel.}, %): 240 (100) [*M*]⁺, 147 (31.3), 120 (25), 106 (1.6), 93 (16.4). Found, %: C 69.90; H 4.98; N 11.60. C₁₄H₁₂N₂O₂. Calculated, %: C 69.99; H 5.03; N 11.66.

1,2-bis((2-hydroxynaphthalen-1-yl)methylene)hydrazine 3l. Yield is 6.56 g (96.5 %), yellow crystals, m.p. 233 °C (233 °C [28]). ¹H NMR spectrum (400.0 MHz, DMSO-d₆) δ, ppm: 7.23–7.31 d (2H, Ar-H, *J* 8.0 Hz), 7.45–7.49 t (2H, Ar-H, *J* 4.0, 16.0 Hz), 7.62–7.65 t (2H, Ar-H, *J* 8.0, 8.0 Hz), 7.92–7.94 d (2H, Ar-H, *J* 8.0 Hz), 8.03–8.05 d (2H, Ar-H, *J* 8.0 Hz), 8.61–8.64 d (2H, Ar-H, *J* 12.0 Hz), 9.91 s (2H, 2 CH=N). Mass spectrum, *m/z* (*I*_{rel.}, %): 340 (52.7) [*M*]⁺, 184 (0.9), 170 (100), 156 (1.6), 143 (5.3). Found, %: C 77.59; H 4.70; N 8.18. C₂₂H₁₆N₂O₂. Calculated, %: C 77.63; H 4.74; N 8.23.

1,2-bis(pyridin-3-ylmethylene)hydrazine 3m. Yield is 1.76 g (42 %), yellow crystals, m.p. 150–152 °C (144–145 °C [42]). ¹H NMR spectrum (400.0 MHz, CDCl₃) δ, ppm: 7.34–7.37 d.d (2H, Ar-H, *J* 4, 4 Hz), 8.16–8.19 d.t (2H, Ar-H, *J* 4, 2, 2, 2 Hz), 8.63 s (2H, Ar-H), 8.67–8.68 d.d (2H, 2CH=N, *J* 1.6, 1.6 Hz), 8.97 d (2H, 2CH=N, *J* 1.8 Hz). Mass spectrum, *m/z* (*I*_{rel.}, %): 210 (10.9) [*M*]⁺, 132 (100), 105 (10.9), 91 (1.6), 78 (11.7). Found, %: C 68.51; H 4.75; N 26.59. C₁₂H₁₀N₄. Calculated, %: C 68.56; H 4.79; N 26.65.

1,2-bis(3-nitrobenzylidene)hydrazine 3n. Yield is 4.70 g (79 %), yellow crystals, m.p. 188–190 °C (192–194 °C [28]). ¹H NMR spectrum (400.0 MHz, CDCl₃) δ, ppm: 7.82–7.84 t (2H, Ar-H, *J* 8, 8 Hz), 8.32–8.39 m (4H, Ar-H), 8.72–8.73 t (2H, Ar-H, *J* 1.8, 1.8 Hz) 8.87 s (2H, 2CH=N). Mass spectrum, *m/z* (*I*_{rel.}, %): 298 (67.8) [*M*]⁺, 252 (4.3), 176 (100), 149 (8.7), 130 (26.1), 122 (2.4), 117 (2.2), 103 (25), 89 (19.6), 76 (29.3). Found, %: C 56.36; H 3.35; N 18.77. C₁₄H₁₀N₄O₄. Calculated, %: C 56.38; H 3.38; N 18.79.

1,2-bis(1-phenylethylidene)hydrazine 3o. Yield is 4.32 g (91.5 %), yellow crystals, m.p. 129–131 °C (123–125 °C [43]). ¹H NMR spectrum (400.0 MHz, CDCl₃) δ, ppm: 2.32 s (6H, 2CH₃), 7.38–7.43 m (6H, Ar-H), 7.88–7.92 m (4H, Ar-H). Mass spectrum, *m/z* (*I*_{rel.}, %): 236 (44) [*M*]⁺, 221 (100), 159 (20.3), 132 (9.4), 118 (23.4), 104 (9.4), 77 (50). Found, %: C 81.28; H 6.79; N 11.81. C₁₆H₁₆N₂. Calculated, %: C 81.32; H 6.82; N 11.85.

1,2-bis(1-(4-nitrophenyl)ethylidene)hydrazine 3p. Yield is 5.93 g (91 %), orange crystals, m.p. 220–221 °C (204 °C [44]). ¹H NMR spectrum (400.0 MHz, CDCl₃) δ, ppm: 2.35 s (6H, 2CH₃), 8.05–8.07 d (4H, Ar-H, *J* 8.0 Hz), 8.25–8.27 d (4H, Ar-H, *J* 8.0 Hz). Mass spectrum, *m/z* (*I*_{rel.}, %): 326 (48.4) [*M*]⁺, 311 (100), 296 (4.7), 204 (14), 177 (4.7), 163 (7.81), 149 (5.5). Found, %: C 58.83; H 4.32; N 17.15. C₁₆H₁₄N₄O₄. Calculated, %: C 58.89; H 4.32; N 17.17.

1,2-bis(1-(2-hydroxyphenyl)ethylidene)hydrazine 3r. Yield is 1.77 g (32 %), yellow crystals, m.p. 201–202 °C (197–199 °C [45]). ¹H NMR spectrum (400.0 MHz, CDCl₃) δ, ppm: 6.87–6.91 t (2H, Ar-H, *J* 8.0, 4.0 Hz), 6.99–7.01 d (2H, Ar-H, *J* 8.0 Hz), 7.31–7.35 t (2H, Ar-H, *J* 8.0, 8.0 Hz), 7.58–7.61 d.d (2H, Ar-H, *J* 4.0, 4.0 Hz), 13.07 s (2H, 2OH). Mass spectrum, *m/z* (*I*_{rel.}, %): 268 (100) [*M*]⁺, 147 (9.8), 134 (34.7),

120 (15.1), 106 (3), 93 (5.9). Found, %: C 71.59; H 6.00; N 10.42. C₁₆H₁₆N₂O₂. Calculated, %: C 71.62; H 6.01; N 10.44.

Procedure for Antioxidant Activity Determination by the FRAP Method

The antioxidant activity (AOA) of ald(ket)azines **3a-r** was determined by the FRAP spectrophotometric method [46].

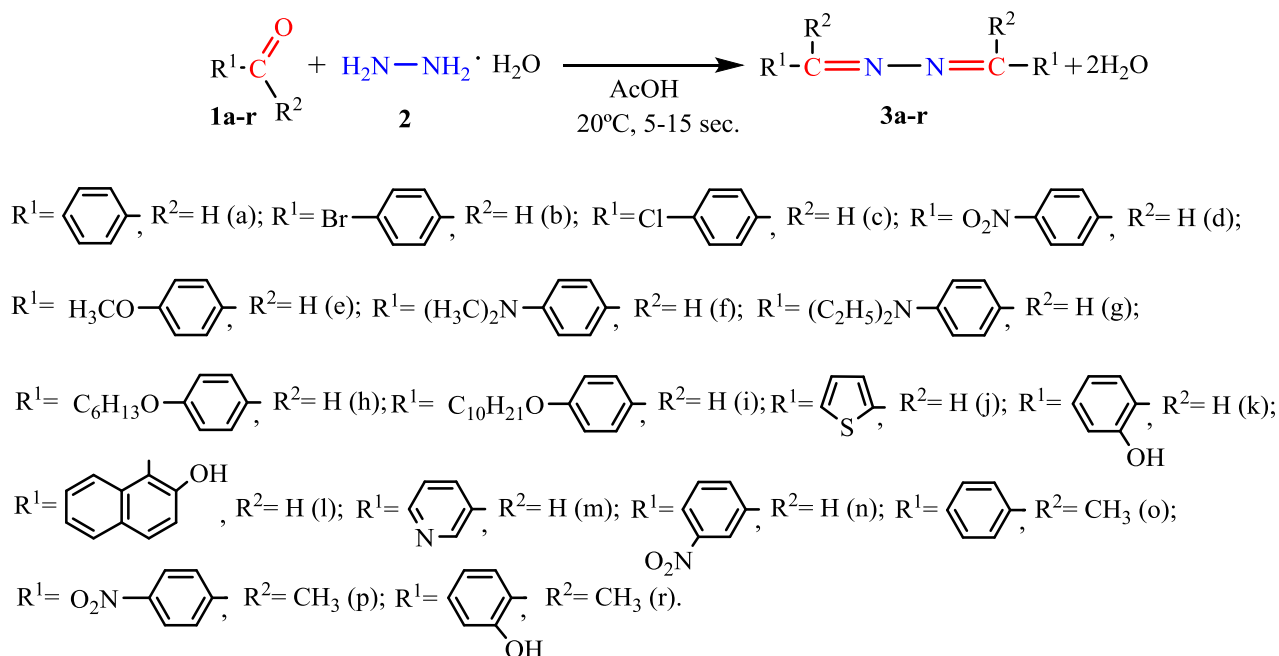
Ascorbic acid (AA), as one of the known antioxidants, was used as a reference [47]. Solutions with AA concentrations of 2.0–3.0·10⁻³ mol·L⁻¹ were prepared by dissolving an accurate suspension in water on the determination day, and 1.0 mL of organic solvent was added to AA aliquots for analysis. The samples investigated were dissolved in ethanol or DMSO, and the reagent content in the solutions was 4.0×10⁻⁴ or 1.0×10⁻³ mol·L⁻¹, respectively. The optical density of the solutions was measured on an SF-2000 spectrophotometer (Spektr, Russia) at λ = 510 nm in 10 mm cuvettes against a blank experiment [48]. Aliquots of 0.2–0.4 mL of the reagent solutions were taken for analysis, the corresponding organic solvent was added to the total volume of 1.0 ml, the AOA values were calculated from the calibration graph plotted from the AA content using the formula:

$$\text{AOA} = \frac{n_{\text{AA, CG}}}{n_r},$$

where $n_{\text{AA, CG}}$ is the amount of ascorbic acid found from the calibration graph, moles; n_r is the amount of reagent in the aliquot for analysis, moles.

Results and Discussion

The use of methanol [24], ethanol [21], toluene [25] or butanone-2 [17] is known to produce ald(ket)azines after 3, 5, 12 and 24 h, respectively. It has also been reported in the literature that the reaction rate of hydrazones or azines formation depends on the pH of the medium [49–53]. In contrast with the previously mentioned methods for the synthesis of ald(ket)azines, we carried out a reaction in an acetic acid medium (8.5 eq.) involving aromatic or heterocyclic aldehydes (ketones) **1a-r** (2 eq.) and hydrazine hydrate **2** (1.3 eq.) at room temperature (Scheme 1).

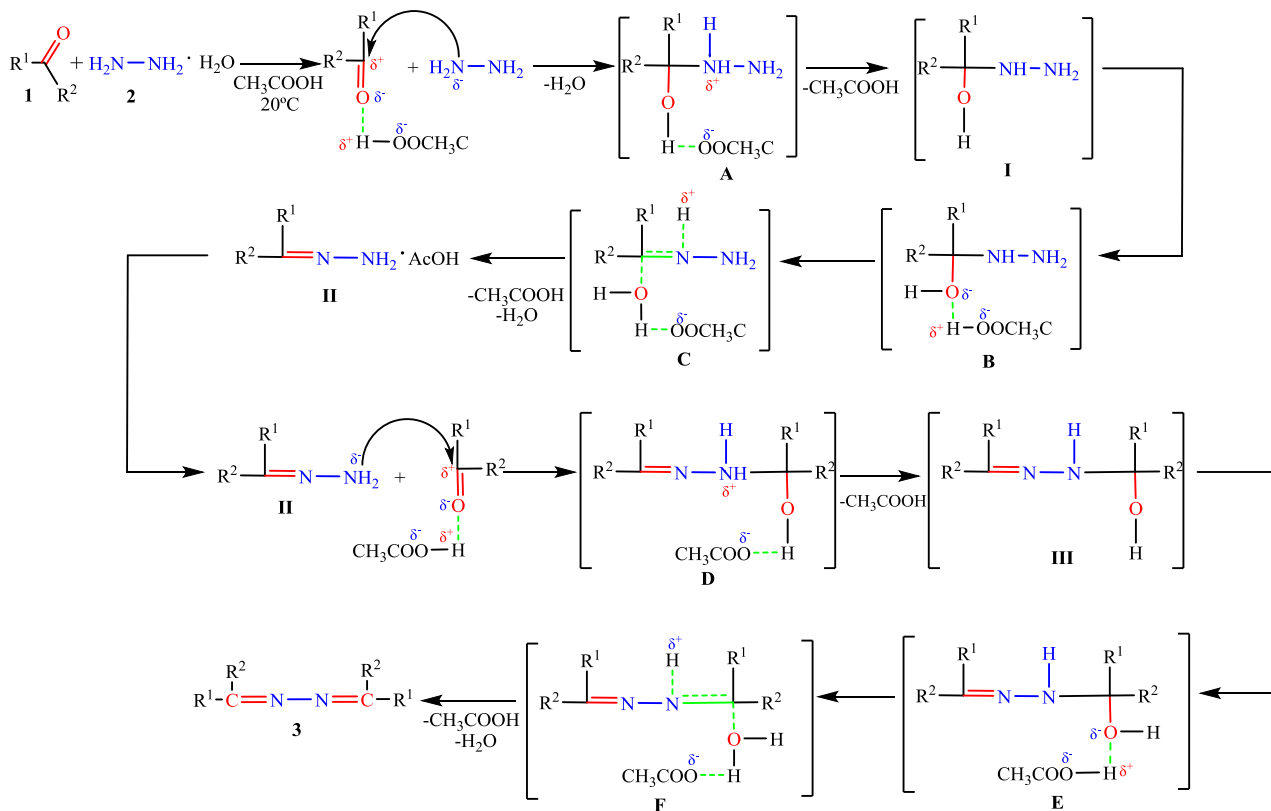


Scheme 1. Synthesis of ald(ket)azines

The azines **3a-e**, **h-p** formation was observed in 5–15 seconds after dropping hydrazine hydrate into the aldehyde (ketone) and acetic acid solution under stirring. Compounds **3f**, **g** did not precipitate and were precipitated with distilled water. Compound **3r** was formed as oil, which crystallized after 48 hours. The yield of azines **3a-r** after recrystallization was 32–98 %.

During the experiment, no clear trend of the effect of electron-donating or electron-accepting substituents in *para*-, *meta*- or *ortho*-positions in aldehydes or ketones on the azines **3a-l**, **o**, **p** yield was observed. The use of 3-pyridinecarbaldehyde **1m** or 2-hydroxyacetophenone **1r** resulted in lower yields.

The high formation rate of ald(ket)azines **3a-p** is achieved by acid catalysis. The authors [50–52] described the mechanism of hydrazones formation. A similar mechanism for the ald(ket)azines formation can be assumed (Scheme 2).



Scheme 2. Proposed mechanism for the ald(ket)azines formation

During the interaction between aldehydes/ketones **1** and hydrazine hydrate **2** in acidic medium, the protonation of the hydrazine hydrate molecule decreases its nucleophilicity. In contrast, acetic acid promotes an increase in the fractional positive charge on the carbon atom in the carbonyl group, which compensates for the decrease in hydrazine nucleophilicity [50–52]. In addition, at low pH values there is an increase in the rate of hydrazinocarbinols dehydration. This also compensates for the reduced nucleophilicity of hydrazine and allows the final ald(ket)azines to be obtained in a shorter time [50–52].

The mechanism described for the formation of ald(ket)azines is hypothetical, as the reaction may proceed through either one or two amino groups of hydrazine, which requires further study.

AOA values were determined for the obtained compounds **3a-g**, **j**, **k**, **m-r**. The results are presented in the table.

Table

Antioxidant activity of 3a-r compounds determined by the FRAP method

No.	Compound	EtOH, mol·L ⁻¹	AOA	DMSO, mol·L ⁻¹	AOA
1	2	3	4	5	6
1	3a	0.001	0.12±0.01	0.001	0
2	3b	< 0.0004	–	0.001	0.13±0.01
3	3c	0.0004	0.36±0.03	0.001	0.11±0.02
4	3d	< 0.0004	–	0.0004	0.12±0.01
5	3e	0.001	0.16±0.01	0.001	0
6	3f	0.0004	1.70±0.02	0.001	1.53±0.05

Continuation of the Table

1	2	3	4	5	6
7	3g	0.0004	1.18±0.01	0.001	1.35±0.04
8	3h	< 0.0004	–	< 0.0004	–
9	3i	< 0.0004	–	< 0.0004	–
10	3j	0.001	0.43±0.02	0.001	0.23±0.01
11	3k	0.001	0	0.001	0.14±0.02
12	3l	< 0.0004	–	0.001	–
13	3m	0.001	0	0.001	0
14	3n	< 0.0004	–	0.001	0
15	3o	0.001	0.14±0.01	0.001	0
16	3p	< 0.0004	–	0.001	0
17	3r	0.001	0.43±0.02	0.001	0.10±0.01

Note: “–” — compound is insoluble.

The compounds **3a-r** were dissolved in 95 % ethanol or dimethyl sulfoxide. For compounds **3h, i, l** no AOA study was carried out due to their low solubility in both solvents. The AOA for compounds **3b, d, n, p** was studied only in DMSO solution because of their poor solubility in EtOH.

It was found that compounds **3a, e, o** exhibited low AOA in ethanol solution (0.12/0.16/0.14) and in DMSO solution the AOA value was 0.

Moderate AOA values were found for compounds **3c, j, r** in ethanol (0.36/0.43/0.43), in DMSO the AOA values were reduced by more than half (0.11/0.23/0.10).

The significant AOA effect was exhibited by compounds **3f** (1.70±0.02/1.53±0.05) and **3g** (1.18±0.01/1.35±0.04) in ethanol/DMSO solution. The AOA values exceed those of ascorbic acid (reference) by 70/53 % (ethanol/DMSO) for compound **3f** and by 18/35 % (ethanol/DMSO) for compound **3g**.

During the study of the AOA, no specific dependence of its values on the use of different electron-donor or electron-acceptor substituents in ald(ket)azines **3a-r** was revealed, except for compounds containing N,N-dimethyl- or N,N-diethyl groups in the *para*-position of the aldehyde fragment of ald(ket)azine.

Conclusions

The interaction of hydrazine hydrate with aromatic or heterocyclic aldehydes (ketones) in an acetic acid medium results in the rapid formation of ald(ket)azines in quantitative yields. The high rate of the condensation reaction is due to the use of acetic acid, which provides optimal conditions for the reaction to proceed. Our findings indicate that compounds containing N,N-alkyl groups in the *para*-position of the ald(ket)azine aldehyde fragment exhibit antioxidant values that exceed those of ascorbic acid.

Funding

This work was financed under the State Contractual Order on the theme No. 124020500033-8.

Author Information*

*The authors' names are presented in the following order: First Name, Middle Name and Last Name

Valeriy Yurievich Gorokhov (*corresponding author*) — PhD in Chemistry, Researcher, Laboratory of Organic Complexing Reagents, “Institute of Technical Chemistry of the Ural Branch of the Russian Academy of Sciences” — a branch of the Perm Federal Research Center of the Ural Branch of the Russian Academy of Sciences, Korolev St. 3, 614013, Perm, Russia, *e-mail*: Gorokhov_V.Yu@mail.ru; <https://orcid.org/0000-0003-3829-5038>

Svetlana Aleksandrovna Zabolotnykh — PhD in Chemistry, Researcher, the Laboratory of Organic Complexing Reagent, “Institute of Technical Chemistry of the Ural Branch of the Russian Academy of Sciences” — a branch of the Perm Federal Research Center of the Ural Branch of the Russian Academy of Sciences, Korolev St. 3, 614013, Perm, Russia, *e-mail*: zabolotsveta@mail.ru; <https://orcid.org/0000-0001-8307-0386>

Larisa Gennadijevna Chekanova — PhD in Chemistry, Head of Laboratory of Organic Complexing Reagents, “Institute of Technical Chemistry of the Ural Branch of the Russian Academy of Sciences” — a

branch of the Perm Federal Research Center of the Ural Branch of the Russian Academy of Sciences, Korolev St. 3, 614013, Perm, Russia, *e-mail*: larchek.07@mail.ru; <https://orcid.org/0000-0003-1792-6945>

Vera Nikolaevna Vaulina — PhD in Chemistry, Researcher, Laboratory of Organic Complexing Reagent, “Institute of Technical Chemistry of the Ural Branch of the Russian Academy of Sciences” — a branch of the Perm Federal Research Center of the Ural Branch of the Russian Academy of Sciences, Korolev St. 3, 614013, Perm, Russia, *e-mail*: tveran79@mail.ru; <https://orcid.org/0000-0002-4993-3528>

Author Contributions

The manuscript was written through contributions of all authors. All authors have given approval to the final version of the manuscript. **CRedit**: **Valeriy Yurievich Gorokhov** conceptualization, data curation, formal analysis, validation, writing — original draft, writing — review & editing, supervision; **Svetlana Aleksandrovna Zabolotnykh** formal analysis, investigation, writing — original draft, writing — review & editing; **Larisa Gennadievna Chekanova** resources, supervision, validation, writing — original draft, writing — review & editing; **Vera Nikolaevna Vaulina** formal analysis, investigation, writing — original draft, writing — review & editing.

Acknowledgments

The work was carried out using the equipment of The Core Facilities Center “Research of materials and matter” at the PFRC UB RAS.

Conflicts of Interest

The authors declare no conflict of interest.

References

- 1 Diyali, N., Chettri M., De, A., & Biswas, B. (2022). Synthesis, crystal structure, and antidiabetic property of hydrazine functionalized Schiff base: 1,2-Di(benzylidene)hydrazine. *European Journal of Chemistry*, 13, 234–240. <https://doi.org/10.5155/eurjchem.13.2.234-240.2265>
- 2 Abu-Hashema, A.A., & Badriac, F.A. (2015). Design, Synthesis of Novel Thiourea and Pyrimidine Derivatives as Potential Antitumor Agents. *Journal of the Chinese Chemical Society*, 62, 506–512. <https://doi.org/10.1002/jccs.201400351>
- 3 Vajpayee, V., Lee, S., Kim, S.H, Kang, S.C., Cook, T.R., Kim, H., Kim, D.W., Verma, S., Lah, M.S., Kim, I.S., Wang, M., Stang, P.J., & Chi, K.W. (2013). Self-assembled metalla-rectangles bearing azodipyridyl ligands: synthesis, characterization and antitumor activity. *Dalton Trans.*, 42, 466–475. <https://doi.org/10.1039/c2dt31014g>
- 4 Gorokhov, V.Yu., Yunnikova, L.P., Makhova, T.V., & Alexandrova, G.A. (2012). Synthesis of *N*-aryl(heteryl)methylene-[4-(5*H*-chromeno[2,3-*b*]pyridin-5-yl)phenyl]amines and their antimycobacterial activity. *Butlerov communications*, 32, 27–29 [in Russian].
- 5 Gorokhov, V.Yu., & Makhova, T.V. (2016). Synthesis and Antibactericidal Activities of Amines and Imines Containing (Aza, Thio)Xanthene Rings. *Pharm. Chem. J.*, 50, 530–533. <https://doi.org/10.1007/s11094-016-1483-1>
- 6 Fathi, J., Masand, V., Jawarkar, R., Mouhoub, R., & Hadda, T.B. (2011). POMas efficient tools to predict and improve both antibacterial and antifungal activity of aryl aldazines. *Journal of Computer-Aided Molecular Design*, 1, 57–68.
- 7 Yousaf, M., Pervaiz, M., Sagir, M., Zaman, A.U., Mushtaq, M., & Naz, M.Y. (2013). Synthesis of Tetradentate Schiff Base Derivatives of Transition Bimetallic Complexes as Antimicrobial Agents. *Journal of the Chinese chemical society*, 60, 1150–1155. <https://doi.org/10.1002/jccs.201200628>
- 8 Backes, G.L., Neumann, D.M., & Jursic, B.S. (2014). Synthesis and antifungal activity of substituted salicylaldehyde hydrazones, hydrazides and sulfohydrazides. *Bioorganic & Medicinal Chemistry*, 22, 4629–4636. <https://doi.org/10.1016/j.bmc.2014.07.022>
- 9 Kurteva, V.B., Simeonov, S.P., & Stoilova-Disheva, M. (2011). Symmetrical Acyclic Aryl Aldazines with Antibacterial and Antifungal Activity. *Pharmacology & Pharmacy*, 2, 1–9. <https://doi.org/10.4236/pp.2011.21001>
- 10 Li, F.F., Chen, H.Y., Jin, Y., Zhao, Q.H., & Xie, M.J. (2018). Synthesis, x-ray structure and in vitro cytotoxic activity of a new dinuclear cobalt(III) complex with diazine ligands. *Pharm. Chem. J.*, 51, 889–892. <https://doi.org/10.1007/s11094-018-1711-y>
- 11 Nazneena, S., Alib, S., Shahzadib, S., & Shujahd, S. (2017). Synthesis, Characterization, and Biological Activity of Organotin(IV) Complexes with Schiff Bases. *Russ. J. Gen. Chem.*, 87, 2970–2978. <https://doi.org/10.1134/S1070363217120404>
- 12 Dhankhar, S.S., Nagaraja, C.M. (2020). Construction of highly water-stable fluorinated 2D metal-organic frameworks with various N,N'-donor spacers: syntheses, crystal structures and photoluminescence properties. *Journal of Solid State Chemistry*, 290, 121560. <https://doi.org/10.1016/j.jssc.2020.121560>
- 13 Nagaraja, C.M., & Ugale, B. (2018). Self-assembled coordination polymers of Zn(II): Syntheses, structural diversity, luminescence properties and base catalysis. *Polyhedron*, 155, 433–440. <https://doi.org/10.1016/j.poly.2018.09.002>

- 14 Gorokhov, V.Yu., Bykov, Ya.V., Batuev, S.A., Lystsova, E.A., Gorokhova, S.M., & Yaganova, N.N. (2019). Single-Pot Synthesis Method of 2-Hydroxybenzylidene-4-[(aza, thio)xanthenyl]anilines and Their Plant Growth Regulator Activity. *Russ. J. Gen. Chem.*, 89, 663–667. <https://doi.org/10.1134/S1070363219040042>
- 15 Singh, V.P., Tiwari, K., Mishra, M., Srivastava, N., & Saha, S. (2013). 5-[(2-Hydroxynaphthalen-1-yl)methylene]amino]-pyrimidine-2,4(1*H*,3*H*)-dione as Al³⁺ selective colorimetric and fluorescent chemosensor. *Sensors and Actuators B Chemical*, 182, 546–554. <https://doi.org/10.1016/j.snb.2013.03.083>
- 16 Sun, T., Niu, Q., Li, T., Guo, Z., & Liu, H. (2018). A simple, reversible, colorimetric and water-soluble fluorescent chemosensor for the naked-eye detection of Cu²⁺ in ~100 % aqueous media and application to real samples. *Spectrochimica Acta Part A: Molecular and Biomolecular Spectroscopy*, 188, 5411–417. <https://doi.org/10.1016/j.saa.2017.07.038>
- 17 Nandi, R., Singh, S.K., Singh, H.K., Singh, B., & Singh, R.K. (2014). Fabrication of liquid crystal based sensor for detection of hydrazine vapours. *Chemical Physics Letters*, 614, 62–66. <https://doi.org/10.1016/j.cplett.2014.09.020>
- 18 Halder, S., Mondal, J., Ortega-Castro, J., Frontera, A., & Roy, P. (2017). A Ni-based MOF for selective detection and removal of Hg²⁺ in aqueous medium: a facile strategy. *Dalton Trans.*, 46, 1943–1950. <https://doi.org/10.1039/C6DT04722J>
- 19 Wilkinson, S.M., Sheedy, T.M., & New, E.J. (2016). Synthesis and Characterization of Metal Complexes with Schiff Base Ligands. *Journal of Chemical Education*, 93, 351–354. <https://doi.org/10.1021/ACS.JCHEMED.5B00555>
- 20 Vilches-Herrera, M., Gallardo-Fuentes, S., Aravena-Opitz, M., Yáñez-Sánchez, M., Jiao, H., Holz, J., Boerner, A., & Lühr, S. (2020). Reduction over Condensation of Carbonyl Compounds Through a Transient Hemiaminal Intermediate Using Hydrazine. *J. Org. Chem.*, 85, 9213–9218. <https://doi.org/10.1021/acs.joc.0c01212>
- 21 Jin, X.Y., Wang, F., Cong, H., & Tao, Z. (2016). Host–guest interactions between hemicucurbiturils and a hydroxyl-substituted Schiff base. *Journal of Inclusion Phenomena and Macrocyclic Chemistry*, 86, 249–254. <https://doi.org/10.1007/s10847-016-0659-3>
- 22 Cui, M., Shen, L., Deng, X., & Zhou, K. (2020). Patent No WO 2020140924A1. [China]
- 23 Premkumar, P., Manikandan, R., Nirmala, M., Viswanathamurthi, P., & Maleck, J.G. (2017). Efficient and versatile catalysis for β -alkylation of secondary alcohols through hydrogen auto transfer process with newly designed ruthenium(II) complexes containing ON donor aldazine ligands. *Journal of Coordination Chemistry*, 70, 3065–3079. <https://doi.org/10.1080/00958972.2017.1381692>
- 24 Shen, S., Liu, X., Sun, J., Wang, M., Jiang, Z., Xia, G., & Wang, H. (2019). Excited state intramolecular single proton transfer mechanism of pigment yellow 101 in solid state: Experiment and DFT calculation. *Spectrochimica Acta Part A: Molecular and Biomolecular Spectroscopy*, 217, 93–100. <https://doi.org/10.1016/j.saa.2019.03.076>
- 25 Anbalagan, V., & Srivastava, T.S. (2004). Spectral and photophysical properties of mono and dinuclear Pt(II) and Pd(II) complexes: An unusual emission behavior. *Polyhedron*, 23, 3173–3183. <https://doi.org/10.1016/j.poly.2004.09.029>
- 26 Suenaga, Y., & Pierpont, C.G. (2005). Binuclear Complexes of Co(III) Containing Extended Conjugated Bis(Catecholate) Ligands. *Inorganic Chemistry*, 44, 6183–6191. <https://doi.org/10.1021/ic050250m>
- 27 Anitha, M.A., Rai, K.M.L., & Somashekar, R. (2017). Research Paper: Solvent-Free Green Synthesis of Pyridazine Derivatives by Hydrothermal Method and Characterization of their Mesogenic Properties. *Journal of Applicable Chemistry*, 6, 30–40.
- 28 Lee, B., Kang, S.H., Kang, D., Lee, K.H., Cho, J., Nam, W., & Hur, N.H. (2011). Isolation and structural characterization of the elusive 1:1 adduct of hydrazine and carbon dioxide. *Chem. Commun.*, 47, 11219–11221. <https://doi.org/10.1039/C1CC14542H>
- 29 Jiang, H., Reng, Z., Wan, W., & Shi, L. (2005). An Improved Synthesis of Azines under Solvent-Free Conditions. *Journal of Shanghai University*, 9, 369–371. <https://doi.org/10.1007/s11741-005-0055-5>
- 30 Pamar, M.G., Gannamani, R., Govender, P., Ramjugernath, D., & Nanjundaswamy, H.M. (2014). Rapid generation of N,N'-diacylhydrazines by I₂ or Br₂ / hydrazine hydrate: A facile route to 1,3,4-oxadiazoles. *Organic Chemistry An Indian Journal*, 10, 17–23 [in Indian].
- 31 Kaboudin, B., & Alipour, S. (2012). Microwave-Assisted Synthesis of 1-Hydrazinophosphonates via the Reaction of Aldazines with Dialkyl Phosphite. *Heteroatom Chemistry*, 23, 304–308. <https://doi.org/10.1002/hc.21019>
- 32 Loghmani-Khouzani, H., Sadeghi, M.M.M., Safari, J., & Sabzi-Fini, O. (2001). Synthesis of azines from carbonyl compounds in a solventfree condition. *Journal of Sciences, Islamic Republic of Iran*, 12, 233–235. [in Iran]
- 33 Bauer, J.O., Leitus, G., Ben-David, Y., & Milstein, D. (2016). Direct Synthesis of Symmetrical Azines from Alcohols and Hydrazine Catalyzed by a Ruthenium Pincer Complex: Effect of Hydrogen Bonding. *ACS Catalysis*, 6, 8415–8419. <https://doi.org/10.1021/acscatal.6b02946>
- 34 Shiekh, B.A., Kaur, D., & Godara, S.K. (2019). Unprecedented synthesis of symmetrical azines from alcohols and hydrazine hydrate using nickel based NNN-pincer catalyst: An experimental and computational study. *Catalysis Communications*, 124, 19–23. <https://doi.org/10.1016/j.catcom.2019.02.024>
- 35 Zhu, J. Duan, C., Ye, S., Zhang, Q., Li K., He G., Liu X., & Zhang Z. (2023). A general and selective Ni-catalysed reductive amination using hydrazine hydrate as facile hydrogen and nitrogen sources. *New Journal of Chemistry*, 47, 11318–11324. <https://doi.org/10.1039/D3NJ01643A>
- 36 Khan, K.M., Jamil, W., Ambreen, N., Taha, M., Perveen, S., & Morales, G.A. (2014). An expeditious synthetic approach towards the synthesis of Bis-Schiff bases (aldazines) using ultrasound. *Ultrasonics Sonochemistry*, 21, 1200–1205. <https://doi.org/10.1016/j.ultsonch.2013.12.011>
- 37 Nanjundaswamy, H.M., & Pasha, M.A. (2006). Selective Protection of Carbonyl Compounds as Azines and Their Facile Regeneration. *Synthetic Communications*, 36, 3161–3165. <https://doi.org/10.1080/00397910600908835>

- 38 Vatne, R.D., Budde, P.B., & Arrington, J.P. (1977). Patent No 4015014 [in USA]
- 39 Fu, Y., Li, H., & Hu, W. (2007). Small Molecular Chromogenic Sensors for Hg²⁺: A Strong “Push-Pull” System Exists after Binding. *Eur. J. Org. Chem.*, 15, 2459–2463. <https://doi.org/10.1002/ejoc.200601086>
- 40 Sek, D., Bijak, K., Grucela-Zajac, M., Filapek, M., Skorka, L., Siwy, M., Janeczek, H., & Schab-Balcerzak, E. (2012). Synthesis and study on the light absorbing, emitting, redox and electrochromic properties of azines and polyazines with thiophene units. *Synthetic Metals.*, 162, 1623–1635. <https://doi.org/10.1016/j.synthmet.2012.06.019>
- 41 Malutan, Th., Pui, A., Malutan, C., Tataru, L., & Humelnicu, D. (2008). A Fluorescence Emission, FT-IR and UV-VIS Absorption Study of the Some Uranium(VI) Schiff Bases Complexes. *Journal of Fluorescence*, 18, 707–713. <https://doi.org/10.1007/s10895-008-0339-9>
- 42 Allan, F., & Allan, G.J. (1985). Pyridinaldazines. *Org. Chem.*, 23, 639–640. <https://doi.org/10.1021/jo01098a625>
- 43 Miyatake, K. (1953). Studies on Azine Compounds. VI. Synthesis of Ketazines and Thiosemicarbazones. *Yakugaku Zasshi*, 73, 455–459. https://doi.org/10.1248/yakushi1947.73.5_455
- 44 Luo, Z.G., Liu, P., Fang, Y.Y., Xu, X.M., Feng, C.T., Li, Z., Zhang, X.M., & He, J. (2017). Cs₂CO₃-mediated decomposition of *N*-tosylhydrazones for the synthesis of azines under mild conditions. *Research on Chemical Intermediates*, 43, 1139–1148. <https://doi.org/10.1007/s11164-016-2688-3>
- 45 Lendl, A., Werner, I., Glasl, S., Kletter, C., Mucaji, P., Presser, A., Reznicek, G., Jurenitsch, J., & Taylor, D.W. (2005). Phenolic and terpenoid compounds from *Chione venosa* (SW.) URBAN var. *venosa* (Bois Bande'). *Phytochemistry (Elsevier)*, 66, 2381–2387. <https://doi.org/10.1016/j.phytochem.2005.07.002>
- 46 Berker, K.I., Güçlü, K., Tor, I., & Apak, R. (2007). Comparative evaluation of Fe(III) reducing power-based antioxidant capacity assays in the presence of phenanthroline, batho-phenanthroline, tripyridyltriazine (FRAP), and ferricyanide reagents. *Talanta*, 72, 1157–1165. <https://doi.org/10.1016/j.talanta.2007.01.019>
- 47 Tsyupko, T.G., Petrakova, I.S., Brilenok, N.S., Nikolaeva, N.A., Chuprygina, D.A., Temerdashev, Z.A., & Vershinin, V.I. (2011). Opredeleeniye obshchego sodержaniya antioksidantov metodom FRAP [Determination of total antioxidant content by FRAP method]. *Analitika i Kontrol — Analytics and Control*, 3, 287–298 [in Russian].
- 48 Trineeva, O.V. (2017). Metody opredeleniya antioksidantnoy aktivnosti ob"yektov rastitel'nogo i sinteticheskogo proiskhozhdeniya v farmatsii (obzor) [Methods for determining the antioxidant activity of objects of plant and synthetic origin in pharmacy (review)]. *Razrabotka i registraciya lekarstvennykh sredstv — Development and registration of medicinal products*, 4, 180–197 [in Russian].
- 49 Jencks, W.P. (1959). Studies on the mechanism of oxime and semicarbazone formation. *J. Am. Chem. Soc.*, 81, 475–481. <https://doi.org/10.1021/ja01511a053>
- 50 Kitaev, Yu.P., & Buzikin, B.I. (1974). *Gidrazoni [Gidrazony]*. M.: Nauka [in Russian].
- 51 Sayer, J.M., Peskin, M., Jencks, W.P. (1973). Imine-forming elimination reactions. I. General base acid catalysis and influence of the nitrogen substituent on rates and equilibria for carbinolamine dehydration. *J. Am. Chem. Soc.*, 95, 4277–4287. <https://doi.org/10.1021/ja00794a600>
- 52 Sayer, J.M., Pinsky, B., Schonbrunn, A., Washtien, W. (1974). Mechanism of carbinolamine formation. *J. Am. Chem. Soc.*, 96, 7998–8009. <https://doi.org/10.1021/ja00833a027>
- 53 Patai, S. (1975). *The Chemistry of the Hydrazo, Azo and Azoxy Groups*. New York.: Wiley & Sons, Ltd.

Daulet B. Kaldybekov^{1,2*} , Elvira O. Shatabayeva^{1,2} , Aziza A. Polatkhan^{1,2} ,
Rysgul N. Tuleyeva^{1,2} , Galiya S. Irmukhametova¹ , Vitaliy V. Khutoryanskiy³ 

¹*Al-Farabi Kazakh National University, Almaty, Kazakhstan;*

²*Institute of Polymer Materials and Technology, Almaty, Kazakhstan;*

³*University of Reading, Reading, United Kingdom*

(*Corresponding author's e-mail: daulechem@gmail.com)

Development and Investigation of Mucoadhesive Polymers Based on Chitosan for Intravesical Therapy

Intravesical drug delivery (IDD) refers to the administration of therapeutic agents directly into the urinary bladder through a catheter. Low permeability of the urinary bladder epithelium, poor retention of the therapeutic agents due to dilution and periodic urine voiding as well as frequent catheterizations (with potential risk of infections) are the major limitations of IDD used in the treatment of bladder-related disorders, such as bladder cancer. In this work, the mucoadhesive properties of polymeric materials based on chitosan, chitosan-gellan gum, and chitosan-Carbopol™ 940 containing sodium fluorescein (NaFI) were investigated for their potential application in intravesical drug delivery. The evaluation of mucoadhesive properties was carried out using an *in vitro* flow-through method with fluorescent detection that simulates the interaction conditions of polymers with the urinary bladder mucosa. Additionally, the release kinetics of NaFI from polymer compositions under conditions mimicking the physiological environment of the bladder was studied using a fluorescence spectrometry. The acquired data confirm the promise of using chitosan-based mucoadhesive polymers in developing systems for intravesical drug delivery, which could significantly enhance the efficacy of IDD therapy to treat urinary bladder-related disorders.

Keywords: chitosan, gellan gum, Carbopol™ 940, *in situ* gel, mucoadhesion, release, urinary bladder, intravesical drug delivery.

Introduction

Mucoadhesion is a critical property of materials that determines their capacity for prolonged interaction and adhesion to mucosal surfaces. This property holds a particular significance in the domain of transmucosal drug delivery, which is extensively utilized across various mucosal membranes, including ocular, nasal, rectal, and vaginal routes. Transmucosal delivery offers numerous advantages, including rapid absorption of active pharmaceutical ingredients into the systemic circulation and reduced degradation of drugs within the gastrointestinal tract, thereby presenting a promising strategy for a wide range of therapeutic applications [1–6]. In particular, mucoadhesive drug formulations can be especially beneficial for the local treatment of posterior segment eye diseases [7, 8] neurological disorders [9, 10] and urogenital diseases [11].

Intravesical drug delivery (IDD) involves the direct administration of active pharmaceutical ingredients into the bladder via a catheter through the urethra, proving to be highly effective for treating various conditions such as bladder cancer and interstitial cystitis. However, the effectiveness of this method is limited by several factors, including dilution and washout during periodic urination, which diminish the therapeutic efficacy and retention of the administered agents. Furthermore, the necessity for frequent catheterization poses potential risks of irritation, inflammatory reactions, and infections, making this procedure quite uncomfortable for patients [12–14].

To enhance the efficacy of IDD, mucoadhesive materials can be employed, which are capable of prolonging the retention time of the drug within the bladder cavity, thereby ensuring a more sustained therapeutic effect. These materials include hydrophilic polymers that are traditionally used as matrices in many formulations for transmucosal drug delivery, such as chitosan, carbopol (a weakly cross-linked polyacrylic acid), alginate, cellulose derivatives, etc. [15–17]. These macromolecules are able to interact with the glycosylaminoglycans/mucin present on the surface of mucus membranes through non-covalent interactions such as hydrogen bonding, electrostatic attractions, diffusion, and chain entanglement/interpenetration pro-

moting increased contact time with the mucosal lining [18]. The mucoadhesive properties of these polymers are mostly based on the mix of several mentioned mechanisms. Recent studies also indicate that thiolated polymers exhibit enhanced mucoadhesive properties due to the formation of disulfide bonds with mucin, further augmenting their ability to interact with mucosal surfaces [19–21]. Various strategies have also been introduced to improve the mucoadhesive properties of hydrophilic polymers by chemically modifying them with specific adhesive groups such as methacryloyl and maleimide moieties. These unsaturated functional groups are able to establish covalent bonds with cysteine residues within mucin glycoproteins through thiolene click Michael-type addition reactions to form strong mucoadhesive bonds [22–25].

The structure of the bladder wall, composed of transitional epithelium, plays a crucial role in the permeability and efficacy of drug delivery. The urothelium, consisting of multiple cellular layers, serves important protective functions and facilitates interactions with therapeutic agents, which can significantly influence treatment outcomes [26].

In this study, polymeric formulations based on chitosan with Carbopol™ 940 and gellan gum was developed. A comprehensive evaluation of their mucoadhesive properties was carried out, enabling an assessment of their potential application in intravesical drug delivery. The results of this research aim to contribute to the development of effective therapeutic strategies for the treatment of bladder diseases and to enhance the quality of life for patients.

Experimental

Materials

Chitosan (low molecular weight, Mw = 50–190 kDa), gellan gum (Phytigel™, Mw = 1000 kDa), sodium fluorescein (NaFl), urea, uric acid, and creatinine were obtained from Sigma-Aldrich (Germany); Carbopol™ 940 was sourced from Acros Organics (Belgium). All other chemicals were of analytical grade and used without further purification.

Development of Mucoadhesive Drug Formulations

The development of mucoadhesive drug formulations involved the systematic preparation of polymers, including chitosan, gellan gum, and Carbopol™ 940, mixed in 1:1 volume ratio containing sodium fluorescein (NaFl).

To prepare a 2 % chitosan solution, the polymer was dissolved in 100 mL of 0.1 M hydrochloric acid (HCl) to improve its solubility after which the solution pH was adjusted to pH 5.50 with 1 M NaOH. A 0.5 % Carbopol™ 940 solution was prepared by dispersing it in 50 mL of deionized water. A 0.5 % gellan gum solution was prepared by dissolving it in deionized water at 50–60 °C to ensure complete dissolution of the polymer, and a sodium fluorescein (NaFl) solution (concentration 0.1 mg/mL) was prepared in deionized water as a model drug compound.

Following the preparation of the polymer solutions, chitosan-based mixtures were formulated in a volumetric ratio of 50:50, combining chitosan with both gellan gum and Carbopol™ 940. This combination was found to balance optimal viscosity, mucoadhesion, and controlled release properties of the resulting formulations and to evaluate their potential applications in IDD.

Ex vivo Experimental Studies on Retention in Sheep Bladder Mucosa

Preparation of Artificial Urine Solution:

The artificial urine solution was prepared according to the methodology described in the literature [27]. Briefly, to achieve a final volume of 2000 mL, the following components were dissolved in deionized water at room temperature: urea (24.27 g), uric acid (0.34 g), creatinine (0.90 g), disodium citrate ($\text{Na}_3\text{C}_6\text{H}_5\text{O}_7 \times 2\text{H}_2\text{O}$, 2.97 g), sodium chloride (NaCl, 6.34 g), potassium chloride (KCl, 4.50 g), ammonium chloride (NH_4Cl , 1.61 g), calcium chloride dihydrate ($\text{CaCl}_2 \times 2\text{H}_2\text{O}$, 0.89 g), magnesium sulfate heptahydrate ($\text{MgSO}_4 \times 7\text{H}_2\text{O}$, 1.00 g), sodium bicarbonate (NaHCO_3 , 0.34 g), sodium oxalate ($\text{Na}_2\text{C}_2\text{O}_4$, 0.03 g), sodium sulfate (Na_2SO_4 , 2.58 g), disodium hydrogen phosphate ($\text{NaH}_2\text{PO}_4 \times \text{H}_2\text{O}$, 1.00 g), sodium phosphate dibasic (Na_2HPO_4 , 0.11 g).

The prepared artificial urine solution with pH 6.20 was maintained at 37 °C throughout the experiment. This solution served as a physiological mimic to evaluate the retention and performance of the mucoadhesive formulations under conditions that closely resemble those in the urinary bladder.

Preparation of Sheep Bladder Mucosa:

The *in vitro* retention of chitosan and its polymeric mixtures with gellan gum and Carbopol™ 940 on sheep bladder mucosa was assessed using a modified experimental method described in the literature [24, 28]. Freshly collected samples of sheep bladder mucosa were obtained from the Zhetysu Abattoirs (Almaty, Kazakhstan). The collected biological tissues were transported to the laboratory in a frozen plastic container to minimize structural changes. Upon arrival, the bladder was dissected, and the obtained mucosal tissue sections were prepared for further experimental investigations.

The bladder tissues were placed in a specialized glass vessel designed to mimic the anatomical structure of the bladder, oriented with the mucosal surface facing upward. Prior to the experimental procedures, the tissues were rinsed with 3 mL of artificial urine solution (pH 6.20). All experiments were carried out in an incubator maintained at 37 °C to ensure physiological conditions.

Aliquots of 5 mL from the mucoadhesive formulations containing either chitosan, chitosan-gellan gum, or chitosan-Carbopol™ 940, all formulated with sodium fluorescein (NaFl), were aspirated and uniformly applied to the mucosal surface of the bladder and subsequently irrigated at a constant flow rate of 2.0 mL/min using a syringe pump. This setup facilitated stable distribution of the tested materials over a period of 250 min, allowing for comprehensive evaluation of their retention and mucoadhesive properties.

Fluorescent images of the bladder tissues were captured using an iPhone 13 Pro under ultraviolet lighting provided by a Winzwon UV Torch. At each time interval following rinsing with artificial urine, the obtained microscopic images were analyzed using ImageJ® software for quantitative assessment of pixel intensity. The pixel intensity of control samples (bladder mucosa without fluorescent material) was subtracted from the measured values, allowing the data to be converted into objective quantitative metrics.

The experiment parameters, including the setup of the equipment and the conditions of the study, are illustrated in Figure 1. The experimental apparatus comprised a microscope, ultraviolet (UV) light source, and bladder simulator, all securely positioned using laboratory stands. The distance between the microscope objective and the mucosal surface was standardized at 10 cm, with the UV light source also maintained at 10 cm from the mucosa. Additionally, the needle tip was positioned 10 cm away from the mucosal surface. Artificial urine was administered to the mucosal surface from a distance of 20 cm at a constant flow rate of 2.0 mL/min. To ensure statistical significance and the reliability of the results, all experiments were carried out in triplicate.

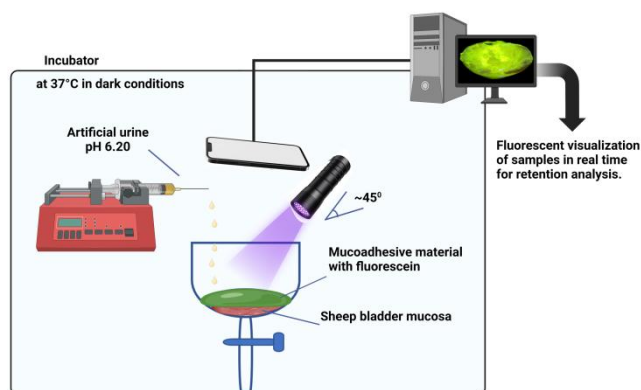


Figure 1. Experimental setup for investigating the retention of mucoadhesive formulations on the bladder mucosa

Release of the Model Drug Compound from Mucoadhesive Formulation

In vitro release of sodium fluorescein (NaFl) from polymeric materials was studied under controlled conditions using the dialysis method described in the literature [23]. Polymeric formulations containing NaFl, with a volume of 2 mL, were placed in a dialysis membrane and immersed in 30 mL of artificial urine solution (pH 6.20). The process was carried out at a temperature of 37 °C with continuous stirring at 80 rpm for 24 h.

At regular time intervals, aliquots of 5 mL were withdrawn from the dialysis solution and replaced with fresh artificial urine to maintain a constant volume within the system. The concentration of released sodium fluorescein (NaFl) was quantified using a fluorescence spectrometer (Varian Cary Eclipse fluorescence spec-

trophotometer, UK) by exciting the sodium fluorescein at $\lambda_{\text{excitation}} = 460$ nm and detecting the emitted light $\lambda_{\text{emission}} = 514$ nm, which corresponds to the peak emission of sodium fluorescein. The concentration of NaFl was determined based on the emitted signal at 514 nm, as it is directly related to the amount of fluorescein in the sample. Figure 2 presents the standard curve used for the quantitative analysis of the release. All release experiments were carried out with a minimum of three replicates to ensure statistical significance and the reliability of the results obtained.

Statistical Analysis

The obtained data were subjected to statistical analysis, including the calculation of means \pm standard deviations. One-way analysis of variance (ANOVA) was employed, followed by Student's *t*-test and *post hoc* Bonferroni correction for multiple comparisons. All statistical calculations were performed using GraphPad Prism software (version 7.0), with $p < 0.05$ set as the threshold for statistical significance.

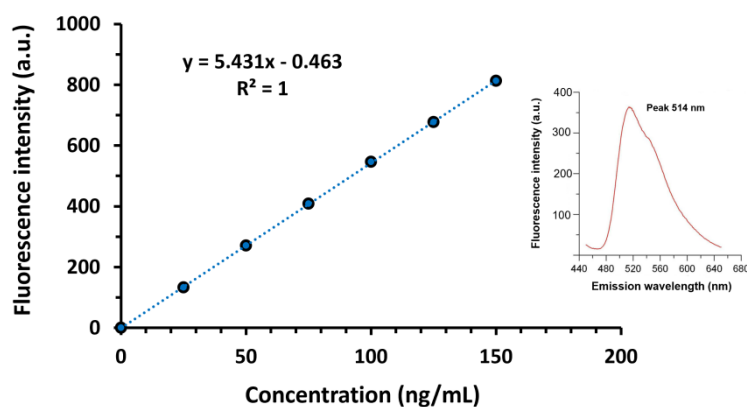


Figure 2. Standard curve used for the quantitative determination of sodium fluorescein (NaFl) released from polymeric material using a fluorescence spectrometer (Insert is an emission peak of NaFl)

Results and Discussion

Intravesical Delivery of Mucoadhesive Polymeric Materials

The mucoadhesive properties of polymeric materials based on chitosan, chitosan-gellan gum, and chitosan-Carbopol™ 940, containing sodium fluorescein (NaFl), were investigated using an updated version of in-house made *in vitro* flow-through method with fluorescent detection [28]. Sheep bladder mucosae were rinsed with 500 mL of artificial urine solution for 250 min period [24, 29]. The schematic of the experimental approach is presented in Figure 3.

In this study, gellan gum and Carbopol™ 940 were selected to enhance the mucoadhesive properties of chitosan. Chitosan is widely considered to be a “gold standard” mucoadhesive polymer due to its polyelectrolyte nature that usually exhibits superior mucoadhesive properties compared to non-ionic polymers [2, 15]. Gellan gum, a water-soluble anionic polysaccharide produced by the bacterium *Sphingomonas elodea*, undergoes a sol-to-gel transition in response to ion presence (ions present in urine), forming viscoelastic gels that enhance retention on mucosal surfaces. Carbopol™ 940, a weakly crosslinked synthetic polymer, provides a viscous gel environment, supporting drug retention on mucosal surfaces. Both polymers were chosen for their ability to further improve mucoadhesiveness of chitosan and extend drug release duration [30, 31]. This minimizes wash-out effects, thereby resulting in improved patient compliance and reduced administration frequency which is beneficial in IDD systems [2, 13].

Freshly excised samples of bladder mucosa were positioned in a specialized vessel designed to replicate the anatomical structure of the bladder and were rinsed with 3 mL of artificial urine solution. Subsequently, a fluorescent image of the mucosal surface was captured after the application of the polymeric material sample containing sodium fluorescein (NaFl), documenting the initial fluorescent image prior to rinsing. Throughout the experiment, microscopic images were analyzed at each rinsing time interval using ImageJ® software to quantitatively assess pixel intensity.

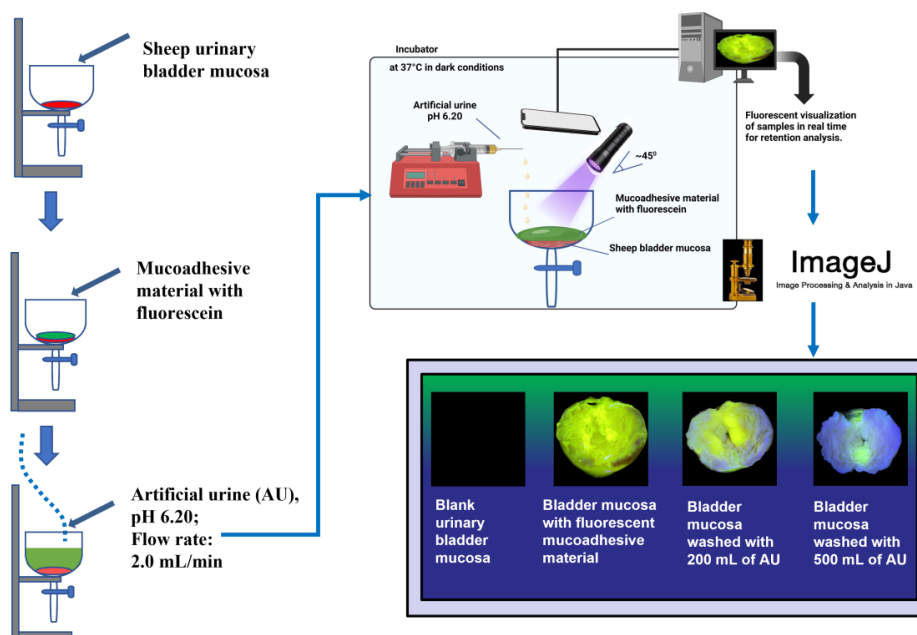


Figure 3. Stepwise process of the *in vitro* retention experiment on sheep bladder mucosa

The results of the fluorescent image analysis, illustrated in Figure 4, demonstrate the retention levels of chitosan and its mixtures with gellan gum and Carbopol™ 940 on the bladder mucosa following exposure to artificial urine. Analysis carried out using ImageJ® revealed that the retention of the chitosan-gellan gum and chitosan-Carbopol™ 940 mixtures on the bladder mucosa was statistically significantly higher compared to pure chitosan ($p < 0.05$). The enhanced mucoadhesive properties of the chitosan-gellan gum mixture can be attributed to the formation of an *in situ* gel within the saline solution. This phenomenon is further depicted in Figure 5, which presents the retention values for chitosan, chitosan-gellan gum, chitosan-Carbopol™ 940, and sodium fluorescein (NaFl) as the control.

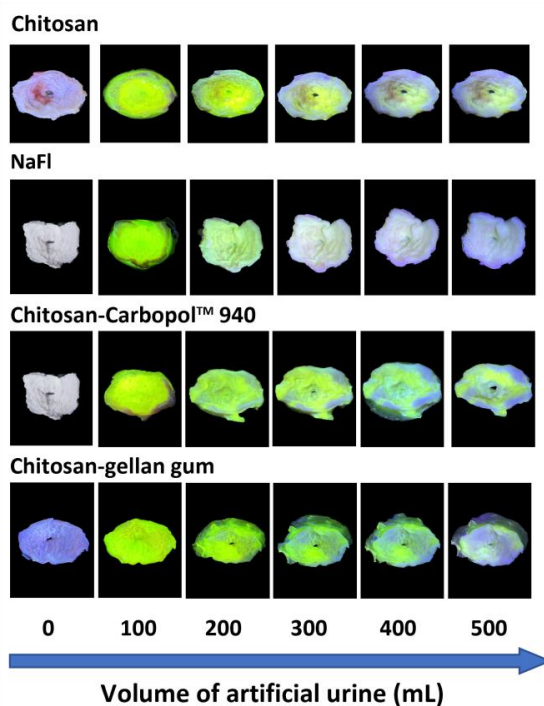


Figure 4. Fluorescent images illustrating the adhesion of polymeric materials to sheep bladder mucosa washed with artificial urine solutions of varying volumes

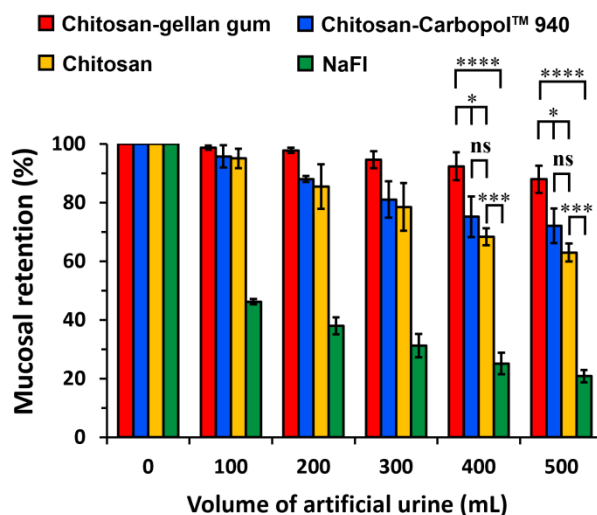


Figure 5. Retention of chitosan and its mixtures with gellan gum and Carbopol™ 940 on sheep bladder mucosa after washing with artificial urine solutions of varying volumes. Data are presented as mean \pm standard deviation ($n = 3$).

Statistically significant differences are indicated as follows: * — $p < 0.05$; *** — $p < 0.001$; *ns* — no significant differences

The adhesive properties of these polymers are primarily attributed to their ability to interact with glycosaminoglycans and mucins on mucosal surfaces through non-covalent interactions, including hydrogen bonding, electrostatic attraction, and conformational changes in the polymer chains. These interaction mechanisms are critical in determining the efficacy of mucoadhesive materials in the context of intravesical drug delivery.

Release of the Model Drug Compound

In vitro studies on the release of sodium fluorescein (NaFl) from polymeric formulations were carried out using a dialysis method in artificial urine solution at 37 °C. The cumulative release profiles are presented in Figure 6. Chitosan demonstrated rapid release of NaFl, reaching saturation levels within 4 h. In contrast, the chitosan-Carbopol™ 940 and chitosan-gellan gum mixtures provided prolonged release, achieving approximately 95 % release within 10–12 h, respectively. The extended release of NaFl from the chitosan-gellan gum polymeric mixture can be attributed to the formation of an *in situ* gel in artificial urine, which enhances the release efficiency and maintains therapeutically significant concentrations of the drug within the bladder following intravesical administration. Moreover, the sustained release of NaFl from the polymeric formulations may contribute to improved retention of the model drug compound within the bladder.

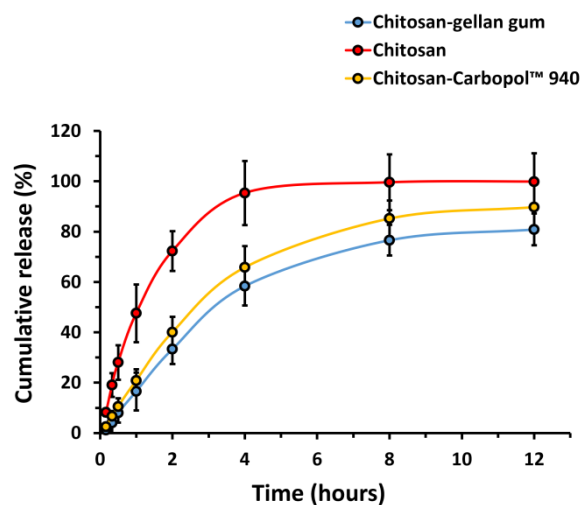


Figure 6. Cumulative release profile of sodium fluorescein from polymeric formulations. Data are presented as mean \pm standard deviation ($n = 3$)

Conclusions

In the present study, the mucoadhesive properties of chitosan-based polymeric materials, as well as its mixtures with gellan gum and Carbopol™ 940 containing sodium fluorescein (NaFl), were analyzed. Experiments carried out using an *in vitro* flow-through method demonstrated that these polymers effectively interact with sheep bladder mucosa.

Fluorescent images confirmed that the retention of the chitosan-gellan gum and chitosan-Carbopol™ 940 mixtures on the mucosal surface significantly exceeds that of pure chitosan ($p < 0.05$). This indicates that the incorporation of gellan gum and Carbopol™ 940 enhances the mucoadhesive characteristics of chitosan, which may be attributed to the formation of an *in situ* gel in the saline solution.

The key factor that makes the polymer complexes (chitosan-gellan gum and chitosan-Carbopol™ 940) more effective than chitosan alone is the synergistic enhancement of mucoadhesive properties. While chitosan contributes to the initial adhesion through electrostatic and hydrogen bonding interactions with mucins, the addition of gellan gum and Carbopol™ 940 enhances both the physical retention (through gel formation) and the sustained release of the drug, which collectively lead to prolonged therapeutic effects in IDD.

The release profiles for sodium fluorescein (NaFl) indicated that chitosan enables a rapid release of the active compound, attaining saturation levels within 4 h. In contrast, the chitosan-Carbopol™ 940 and chitosan-gellan gum formulations demonstrated a markedly prolonged release, with nearly 100 % of the drug released within 10 h. This extended release behavior is primarily attributed to the formation of a physically entrapped gel matrix, which significantly enhances the efficiency of drug delivery while simultaneously facilitating the maintenance of therapeutically relevant concentrations of NaFl in the bladder cavity over an extended period.

The formation of this gel structure not only creates a reservoir effect that supports sustained drug release but also mitigates the risk of concentration fluctuations, optimizing the therapeutic efficacy of the treatment. Such characteristics are particularly advantageous for intravesical drug delivery systems, where the maintenance of effective drug levels is crucial for the management of bladder-related pathologies. These findings highlight the potential of chitosan-based polymeric formulations, particularly in combination with gellan gum and Carbopol™ 940, to enhance therapeutic outcomes in clinical applications targeting bladder conditions.

Consequently, the findings of this investigation substantiate that the incorporation of chitosan mixtures with gellan gum and Carbopol™ 940 markedly improves mucoadhesive properties and facilitates the controlled release of therapeutic agents. This advancement presents novel opportunities for the development of effective mucoadhesive drug delivery systems within the field of urology.

Funding

This research was funded by the Science Committee of the Ministry of Science and Higher Education of the Republic of Kazakhstan (Grant No. AP14869167).

Author Information*

*The authors' names are presented in the following order: First Name, Middle Name and Last Name

Daulet Bolatovich Kaldybekov (*corresponding author*) — PhD, Senior Lecturer, Al-Farabi Kazakh National University, Al-Farabi Avenue, 71, 050040, Almaty, Kazakhstan; Principal Investigator, Institute of Polymer Materials and Technology, Microdistrict Atyrau 1, 3/1, 050019, Almaty, Kazakhstan; *e-mail*: daulechem@gmail.com; <https://orcid.org/0000-0002-7191-5465>

Elvira Orynbasarovna Shatabayeva — PhD Candidate, Senior Lecturer, Al-Farabi Kazakh National University, Al-Farabi Avenue, 71, 050040, Almaty, Kazakhstan; Research Scientist, Institute of Polymer Materials and Technology, Microdistrict Atyrau 1, 3/1, 050019, Almaty, Kazakhstan; *e-mail*: elvira.shatabayeva@gmail.com; <https://orcid.org/0000-0001-9153-5198>

Aziza Almaskhankyzy Polatkhan — PhD Candidate, Al-Farabi Kazakh National University, Al-Farabi Avenue, 71, 050040, Almaty, Kazakhstan; Research Scientist, Institute of Polymer Materials and Technology, Microdistrict Atyrau 1, 3/1, 050019, Almaty, Kazakhstan; *e-mail*: polathanaziza@mail.ru; <https://orcid.org/0000-0002-5594-0097>

Rysgul Nurlanovna Tuleyeva — PhD Candidate, Al-Farabi Kazakh National University, Al-Farabi Avenue, 71, 050040, Almaty, Kazakhstan; Research Scientist, Institute of Polymer Materials and Technology, Microdistrict Atyrau 1, 3/1, 050019, Almaty, Kazakhstan; *e-mail*: risgul_93@mail.ru; <https://orcid.org/0000-0002-9691-4274>

Galiya Serikbayevna Irmukhametova — Candidate of Chemical Sciences, Associate Professor, Al-Farabi Kazakh National University, Al-Farabi Avenue, 71, 050040, Almaty, Kazakhstan; *e-mail*: galiya.irm@gmail.com; <https://orcid.org/0000-0002-1264-7974>

Vitaliy Victorovich Khutoryanskiy — PhD, Professor of Formulation Sciences, University of Reading, Whiteknights House, RG6 6UR, Reading, United Kingdom; *e-mail*: v.khutoryanskiy@reading.ac.uk; <https://orcid.org/0000-0002-7221-2630>

Author Contributions

The manuscript was written through contributions of all authors. All authors have given approval to the final version of the manuscript. **CRedit**: **Daulet Bolatovich Kaldybekov** data curation, formal analysis, funding acquisition, resources, supervision, methodology, writing–review & editing; **Elvira Orynbasarovna Shatabayeva** data curation, formal analysis, visualization, writing–original draft; **Aziza Almaskhankyzy Polatkhan** data curation, formal analysis, investigation; **Rysgul Nurlanovna Tuleyeva** data curation, formal analysis, investigation; **Galiya Serikbayevna Irmukhametova** writing–review & editing; **Vitaliy Victorovich Khutoryanskiy** methodology, conceptualization, writing–review & editing.

Conflicts of Interest

The authors declare no conflict of interest.

References

- 1 Caramella, C. M., Rossi, S., Ferrari, F., Bonferoni, M. C., & Sandri, G. (2015). Mucoadhesive and thermogelling systems for vaginal drug delivery. *Advanced Drug Delivery Reviews*, 92, 39–52. <https://doi.org/10.1016/j.addr.2015.02.001>
- 2 Khutoryanskiy, V. V. (2011). Advances in mucoadhesion and mucoadhesive polymers. *Macromolecular Bioscience*, 11(6), 748–764. <https://doi.org/10.1002/mabi.201000388>
- 3 Neves, J., & Sarmiento, B. (2014). *Mucosal Delivery of Biopharmaceuticals: Biology, Challenges and Strategies*. <https://doi.org/10.1007/978-1-4614-9524-6>
- 4 Proserpi-Porta, G., Kedzior, S., Muirhead, B., & Sheardown, H. (2016). Phenylboronic-acid-based polymeric micelles for mucoadhesive anterior segment ocular drug delivery. *Biomacromolecules*, 17(4), 1449–1457. <https://doi.org/10.1021/acs.biomac.6b00054>
- 5 Rieger, C., Kunhardt, D., Kaufmann, A., Schendel, D., Huebner, D., Erdmann, K., Propping, S., Wirth, M. P., Schwenzer, B., Fuessel, S., & Hampel, S. (2015). Characterization of different carbon nanotubes for the development of a mucoadhesive drug delivery system for intravesical treatment of bladder cancer. *International Journal of Pharmaceutics*, 479(2), 357–363. <https://doi.org/10.1016/j.ijpharm.2015.01.017>
- 6 Seo, Y. G., Kim, D. W., Yeo, W. H., Ramasamy, T., Oh, Y. K., Park, Y. J., Kim, J. A., Oh, D. H., Ku, S. K., Kim, J. K., Yong, C. S., Kim, J. O., & Choi, H. G. (2013). Docetaxel-loaded thermosensitive and bioadhesive nanomicelles as a rectal drug delivery system for enhanced chemotherapeutic effect. *Pharmaceutical Research*, 30(7), 1860–1870. <https://doi.org/10.1007/s11095-013-1029-0>
- 7 Fangueiro, J. F., Veiga, F., Silva, A. M., & Souto, E. B. (2016). Ocular drug delivery — new strategies for targeting anterior and posterior segments of the eye. *Current Pharmaceutical Design*, 22(9), 1135–1146. <https://doi.org/10.2174/1381612822666151216145900>
- 8 Hornof, M., Weyenberg, W., Ludwig, A., & Bernkop-Schnürch, A. (2003). Mucoadhesive ocular insert based on thiolated poly(acrylic acid): Development and in vivo evaluation in humans. *Journal of Controlled Release*, 89(3), 419–428. [https://doi.org/10.1016/S0168-3659\(03\)00135-4](https://doi.org/10.1016/S0168-3659(03)00135-4)
- 9 Kapoor, M., Cloyd, J. C., & Siegel, R. A. (2016). A review of intranasal formulations for the treatment of seizure emergencies. *Journal of Controlled Release*, 237, 147–159. <https://doi.org/10.1016/j.jconrel.2016.07.001>
- 10 Kozlovskaya, L., Abou-Kaoud, M., & Stepsky, D. (2014). Quantitative analysis of drug delivery to the brain via nasal route. *Journal of Controlled Release*, 189, 133–140. <https://doi.org/10.1016/j.jconrel.2014.06.053>
- 11 Mugabe, C., Matsui, Y., So, A. I., Gleave, M. E., Baker, J. H. E., Minchinton, A. I., Manisali, I., Liggins, R., Brooks, D. E., & Burt, H. M. (2011). In vivo evaluation of mucoadhesive nanoparticulate docetaxel for intravesical treatment of non-muscle-invasive bladder cancer. *Clinical Cancer Research: An Official Journal of the American Association for Cancer Research*, 17(9), 2788–2798. <https://doi.org/10.1158/1078-0432.ccr-10-2981>

- 12 GuhaSarkar, S., & Banerjee, R. (2010). Intravesical drug delivery: Challenges, current status, opportunities and novel strategies. *Journal of Controlled Release*, 148(2), 147–159. <https://doi.org/10.1016/j.jconrel.2010.08.031>
- 13 Kolawole, O. M., Lau, W. M., Mostafid, H., & Khutoryanskiy, V. V. (2017). Advances in intravesical drug delivery systems to treat bladder cancer. *International Journal of Pharmaceutics*, 532(1), 105–117. <https://doi.org/10.1016/J.IJPHARM.2017.08.120>
- 14 Kolawole, O. M., & Khutoryanskiy, V. V. (2024). Potential bladder cancer therapeutic delivery systems: a recent update. *Expert Opinion on Drug Delivery*, 21(9), 1311–1329. <https://doi.org/10.1080/17425247.2024.2396958>
- 15 Sogias, I. A., Williams, A. C., & Khutoryanskiy, V. V. (2008). Why is chitosan mucoadhesive? *Biomacromolecules*, 9(7), 1837–1842. <https://doi.org/10.1021/bm800276d>
- 16 Hombach, J., & Bernkop-Schnürch, A. (2010). Mucoadhesive drug delivery systems. In M. Schäfer-Korting (Ed.), *Drug Delivery* (pp. 251–266). Springer. https://doi.org/10.1007/978-3-642-00477-3_9
- 17 Grassiri, B., Zambito, Y., & Bernkop-Schnürch, A. (2021). Strategies to prolong the residence time of drug delivery systems on ocular surface. *Advances in Colloid and Interface Science*, 288, 102342. <https://doi.org/10.1016/j.cis.2020.102342>
- 18 Bravo-Osuna, I., Noiray, M., Briand, E., Woodward, A. M., Argüeso, P., Martínez, I. T. M., Herrero-Vanrell, R., & Ponchel, G. (2012). Interfacial interaction between transmembrane ocular mucins and adhesive polymers and dendrimers analyzed by surface plasmon resonance. *Pharmaceutical Research*, 29(8), 2329–2340. <https://doi.org/10.1007/s11095-012-0761-1>
- 19 Bernkop-Schnürch, A., Guggi, D., & Pinter, Y. (2004). Thiolated chitosans: Development and in vitro evaluation of a mucoadhesive, permeation enhancing oral drug delivery system. *Journal of Controlled Release*, 94(1), 177–186. <https://doi.org/10.1016/j.jconrel.2003.10.005>
- 20 Bernkop-Schnürch, A. (2005). Thiomers: A new generation of mucoadhesive polymers. *Advanced Drug Delivery Reviews*, 57(11), 1569–1582. <https://doi.org/10.1016/j.addr.2005.07.002>
- 21 Barthelmes, J., Perera, G., Hombach, J., Dünhaupt, S., & Bernkop-Schnürch, A. (2011). Development of a mucoadhesive nanoparticulate drug delivery system for a targeted drug release in the bladder. *International Journal of Pharmaceutics*, 416(1), 339–345. <https://doi.org/10.1016/j.ijpharm.2011.06.033>
- 22 Kolawole, O. M., Lau, W. M., & Khutoryanskiy, V. V. (2018). Methacrylated chitosan as a polymer with enhanced mucoadhesive properties for transmucosal drug delivery. *International Journal of Pharmaceutics*, 550(1), 123–129. <https://doi.org/10.1016/j.ijpharm.2018.08.034>
- 23 Tonglairoum, P., Brannigan, R. P., Opanasopit, P., & Khutoryanskiy, V. V. (2016). Maleimide-bearing nanogels as novel mucoadhesive materials for drug delivery. *Journal of Materials Chemistry B*, 4(40), 6581–6587. <https://doi.org/10.1039/C6TB02124G>
- 24 Kaldybekov, D. B., Tonglairoum, P., Opanasopit, P., & Khutoryanskiy, V. V. (2018). Mucoadhesive maleimide-functionalised liposomes for drug delivery to urinary bladder. *European Journal of Pharmaceutical Sciences*, 111, 83–90. <https://doi.org/10.1016/j.ejps.2017.09.039>
- 25 Agibayeva, L. E., Kaldybekov, D. B., Porfiriyeva, N. N., Garipova, V. R., Mangazbayeva, R. A., Moustafine, R. I., Semina, I. I., Mun, G. A., Kudaibergenov, S. E., & Khutoryanskiy, V. V. (2020). Gellan gum and its methacrylated derivatives as in situ gelling mucoadhesive formulations of pilocarpine: In vitro and in vivo studies. *International Journal of Pharmaceutics*, 577, 119093. <https://doi.org/10.1016/j.ijpharm.2020.119093>
- 26 Grasso, M. (2008). Bladder Cancer: A Major Public Health Issue. *European Urology, Supplements*, 7(7), 510–515. <https://doi.org/10.1016/j.eursup.2008.04.001>
- 27 Chutipongtanate, S., & Thongboonkerd, V. (2010). Systematic comparisons of artificial urine formulas for in vitro cellular study. *Analytical Biochemistry*, 402(1), 110–112. <https://doi.org/10.1016/j.ab.2010.03.031>
- 28 Phuong Ta, L., Bujna, E., Kun, S., Charalampopoulos, D., & Khutoryanskiy, V. V. (2021). Electrospayed mucoadhesive alginate-chitosan microcapsules for gastrointestinal delivery of probiotics. *International Journal of Pharmaceutics*, 597, 120342. <https://doi.org/10.1016/j.ijpharm.2021.120342>
- 29 Kaldybekov, D. B., Filippov, S. K., Radulescu, A., & Khutoryanskiy, V. V. (2019). Maleimide-functionalised PLGA-PEG nanoparticles as mucoadhesive carriers for intravesical drug delivery. *European Journal of Pharmaceutics and Biopharmaceutics*, 143, 24–34. <https://doi.org/10.1016/j.ejpb.2019.08.007>
- 30 Vigani, B., Rossi, S., Sandri, G., Bonferoni, M. C., Caramella, C. M., & Ferrari, F. (2020). Recent Advances in the Development of In Situ Gelling Drug Delivery Systems for Non-Parenteral Administration Routes. *Pharmaceutics*, 12(9). <https://doi.org/10.3390/pharmaceutics12090859>
- 31 Kulkarni, R., Fansie, S., & Burgess, D. J. (2023). Mucoadhesive drug delivery systems: a promising noninvasive approach to bioavailability enhancement. Part II: formulation considerations. *Expert Opinion on Drug Delivery*, 20(3), 413–434. <https://doi.org/10.1080/17425247.2023.2181332>

PHYSICAL AND ANALYTICAL CHEMISTRY

Article

Received: 2 July 2024 | Revised: 21 October 2024 |
Accepted: 5 November 2024 | Published online: 23 November 2024

UDC 542.943+628.161

<https://doi.org/10.31489/2959-0663/4-24-6>

Nedjma Lahmar , Mokhtar Djehiche *, Marwa Bachiri 

Inorganic Materials Laboratory, University of M'sila, M'sila, Algeria
(*Corresponding author's e-mail: mokhtar.djehiche@univ-msila.dz)

Removal of E110 from Aqueous Solution Using Heat-Activated Persulfate

This paper presents an investigation into the efficiency of heat-activated persulfate (PS) in decolorizing E110 with a focus on the influence of several parameters. The decolorization efficiency was observed to increase with rising PS concentration (no linear correlation was identified), Cl^- , temperature, and time. However it was noted to decrease with rising initial dye concentration, pH, ion radius and NO_2^- . The rest of the water matrix components (CO_3^{2-} , HPO_4^{2-} , HCO_3^- , and NO_3^-) did not significantly impact on the degradation of E110 at 10^{-3} M. Among the metal ions used (Fe^{2+} , Ni^{2+} , Co^{2+} , Cu^{2+} , and Ag^+), iron and silver ions exhibited the greatest efficacy in activating PS through catalysis. A direct reaction between E110 and PS was not observed, as is the case with some anionic dyes, instead its degradation occurs via sulfate radicals (SRs) and other secondary mechanisms. The results of biological and chemical oxygen demand measurements indicate that E110 is not biodegradable. The kinetic activation parameters (E_a , ΔH^\ddagger , ΔS^\ddagger , ΔG^\ddagger) were calculated using Arrhenius and Eyring's equations. The results obtained were as follows: $155.4 \text{ kJ mol}^{-1}$, $152.7 \text{ kJ mol}^{-1}$, 0.14 kJ K^{-1} , $108.5 \text{ kJ mol}^{-1}$. Finally, a preliminary mechanism for the degradation of E110 by SR has been proposed, in which the destruction of aromatic ring structures accompanies the discoloration of E110.

Keywords: E110, persulfate, sulfate radical, dye decolorization, kinetic activation parameters, mechanism, heat-activated persulfate, aqueous solution, biodegradable.

Introduction

Many chemical industries use dyes, that produce toxic and carcinogenic wastewater, contaminating water and polluting the environment. The removal of color from waste is often more important than the removal of other colorless and organic substances because the presence of a small amount of dye (below 1 ppm) is easily visible and has a significant impact on the water environment [1]. A color additive is a substance that is added to food, drink, or other products to change their color. It can be a dye, pigment, or any other substance that reacts with another substance to produce color. Color additives are used for a variety of purposes, including compensating for color loss, enhancing natural colors to make them more appealing, adding color to initially colorless food products, and facilitating product identification, especially in the case of pharmaceuticals [2]. Synthetic colorants are preferred over natural colorants because they are less expensive, more stable, and more resistant to light, oxygen, and pH [3]. Recently, more attention has been paid to their toxicity, especially azo dyes [4]. Azo dyes represent the majority of dyes used in many industries because the azo bond ($-\text{N}=\text{N}-$) promotes the delocalization of π electrons, resulting in absorption at visible spectrum wavelengths [5]. Azo dyes are highly toxic due to the mutagenic nitro group, and they decompose to produce toxic products such as 1,4-phenylenediamine and o-tolidine [6]. Certain microorganisms can degrade azo dyes, yielding toxic, mutagenic, and carcinogenic intermediates [7]. E110, an azo dye, is a well-known synthetic food dye found in Kellogg's, hot fudge sundaes, tarts, soft drinks, and candies [8, 9]. This includes applications other than food, such as pharmaceutical, cosmetic, and textile products [10]. E110 is safe at a daily

dose of less than 2.5 mg/kg [2]. At high concentrations, it exhibits xenoestrogenic activity [11]. E110, among other dyes, is the type of food dye most commonly associated with human carcinogens [12].

PS (peroxydisulfate, $S_2O_8^{2-}$), a compound used in situ chemical oxidation (ISCO) technology, is a chemical oxidant for soil and groundwater decontamination [13]. This process treats a wide range of impurities using direct electron transfer or free radical processes, including halogenated olefins, BTEXs (benzene, toluene, ethylbenzene, and xylenes), perfluorinated chemicals, phenols, pharmaceuticals, inorganics, and pesticides [14]. The radical process generates SRs ($SO_4^{\cdot-}$) by activating PS (R1) with heat [15, 16], transition metals [17, 18], ultraviolet (UV) light [19] and other means [20–22]. Thermal treatment is expensive, which limits its use in pollutant removal. Despite the high cost of thermal treatment, which limits its use in pollutant removal, the use of solar thermal energy [23, 24] simplifies the use of heat to activate PSs. This approach uses solar energy as a heat source, which increases the efficiency of the PS activation process. PS ions decompose thermally (k_2 varies from $5.85 \times 10^{-8} \text{ s}^{-1}$ at 30 °C to $1 \times 10^{-4} \text{ s}^{-1}$ at 80 °C [13, 14, 25, 26]) to form two SRs (Eq. 2), which react with PS anions (Eq. 3), water (Eq. 4), self-reaction (Eq. 5) and organic compounds (Eq. 6):



According to Eq. 7, the SR can react with elements present in the water matrix (X^-) such as Cl^- , CO_3^{2-} , HPO_4^{2-} , HCO_3^- , NO_2^- and NO_3^- [27, 28]. This results in the formation of a radical (X^{\cdot}), which then reacts with organic compounds to decolorize them. However, the reaction between the produced radicals and non-target chemical species, whether natural or artificial, reduces reaction efficiency, resulting in a significant limitation [29].



PS can be activated by transition metals, including Fe^{2+} , Co^{2+} , Ni^{2+} , Cu^{2+} , and Ag^+ , resulting in the formation of SRs as shown in Eq. 23, where Mn^{n+} represents typical metal ions [17, 18, 30]:



The use of metal ions poses practical problems, particularly in terms of recycling and secondary pollution. However, iron ions and their oxides have been extensively studied, due to their environmentally-friendly, non-toxic and low-cost characteristics [31].

pH has a significant impact on dyes' chemical structure, stability, and ability to absorb light. Thus, pH is an important consideration when designing and maintaining in-situ chemical oxidation systems [32, 33]. Previous studies have investigated the decolorization of E110 through biological processes [34], adsorption [35], UV/ H_2O_2 , ultrasound [36], photocatalytic [1], and Fenton. However, the use of the activated PS process to degrade E110 has not been extensively researched. Although the activated PS process has been used to decolorize a variety of substances, including Acid blue 92, naphthalene, methylene blue, Ponceau 6R dye, sulfamethazine, trichloroethane, carbamazepine, propylparaben, polycyclic aromatic hydrocarbons, and metronidazole [37], its application to E110 is novel.

Thus, the study aims to assess the efficacy of heat-activated PS for E110 decolorization in aqueous solution. The study investigates the effects of activation temperature, PS concentration, time, water matrix, transition metals, and dye concentrations. It also investigates decolorization kinetics and thermodynamic properties such as Gibbs free energy, activation energy, and reaction entropies. Based on the results and the literature, we propose a mechanism for the degradation of E110 dye.

Experimental

This study utilized the following chemicals: E110 ($C_{16}H_{10}N_2Na_2O_7S_2$, 90 % Sigma–Aldrich), potassium persulfate ($K_2S_2O_8$, 99 % Merck), sulfuric acid (H_2SO_4 , 97 % Honeywell), hydrochloric acid (HCl, 37 % Honeywell), sodium hydroxide (NaOH, 99 % Biochem Chemopharma), sulfuric acid heptahydrate ($FeSO_4 \cdot 7H_2O$, 99 % Sigma–Aldrich), sulfuric acid ($CuSO_4$, 97 % Biochem Chemopharma), silver nitrate

(AgNO₃, 99 % Biochem Chemopharma), sodium chloride (NaCl, 99.5 % Honeywell), potassium chloride (KCl, 99 % Sigma–Aldrich), and sodium sulfate (Na₂SO₄, 99 % Sigma–Aldrich), sodium bicarbonate (NaHCO₃, 99.7 % Honeywell), sodium phosphate (Na₂HPO₄, 98 % Panreac), sodium nitrite (NaNO₂, 98 % Fluka), and sodium nitrate (NaNO₃, 99.5 % Biochem Chemopharma). Distilled water was used to prepare the study solutions. After dissolving the required amount of PS for the reaction medium in 5 ml of distilled water, the mixture was added to a beaker containing 200 ml of E110 solution and heated to the desired temperature with a thermostat. A Metrohm Model 781 pH/Ion meter was used to continuously monitor pH 3, which serves as the baseline for all tests. The decolorization process of the dye solutions was investigated using a 2401 PC UV spectrophotometer (Shimadzu, optical path = 1 cm), which measured dye absorbance at 480 nm. Chemical oxygen demand (COD) was measured using the ISO 6060 method, while biological oxygen demand (BOD5) is measured with the BOD 901 meter (made in Europe).

Results and Discussion

Effect of Initial PS and E110 Concentration

Figure 1 (top) depicts the effect of initial PS concentration on E110 elimination effectiveness. The decolorization process was completed in less than 90 minutes with PS concentrations of 7.4, 3.7, and 1.84 mM, but it took more than 200 minutes with concentrations of 0.92 and 0.18 mM. This indicates that elevated PS concentrations result in the formation of a greater number of SRs, thereby accelerating the oxidation of E110 [16, 37]. This relationship is not linear due to the nonlinear plot of E110 half-life values ($t_{1/2}$) as a function of initial PS concentration (Figure 1 bottom) is nonlinear, and its increase becomes meaningless at concentrations above 3.7 mM. This result is explained by an excess of PS in the solution, which slows the decolorization of E110. An excess of PS concentration can cause the following processes which slow down the decolorization mechanism [38]: (a) excess SO₄ radical recombination and annihilation (Eq. 5), (b) SR consumption with excess PS (Eq. 3), and (c) the occurrence of an unproductive PS decomposition reaction (with no generation of SR).

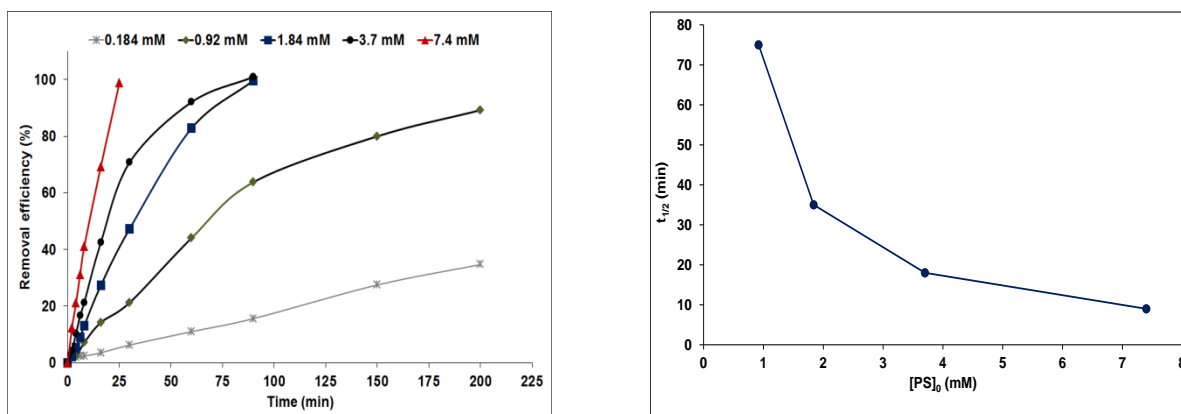


Figure 1. Evolution of E110 decolorization. Top: time dependence of E110 at different initial PS concentrations.

Bottom: Plot of E110 half-life time ($t_{1/2}$) values as a function of initial PS concentration. Initial conditions: $[E110]_0 = 0.66$ mM, pH = 3 and T = 60 °C. Removal efficiency (%) = $\frac{([E110]_0 - [E110]_t)}{[E110]_0} \times 100$, where $[E110]_0$ is the concentration at time 0 and $[E110]_t$ is the concentration at time t

On the other hand, different initial E110 concentrations of 0.22 mM, 0.66 mM, 1.33 mM, and 1.99 mM were investigated to determine the effect of the initial E110 concentration on elimination. The initial PS concentration was 3.7 mM, and the temperature remained constant at 60 °C. Figure 2 depicts a decrease in PS decolorization efficiency as the concentration of E110 increases. These results can be explained by the dye's high concentration, which consumes free radicals and thus reduces bleaching efficacy [27]. These results are consistent with previous research on the decolorization of other dyes by PS [39, 40]. In the remainder of this study, the PS concentration is limited to 3.7 mM for 0.66 mM of E110, as a higher concentration will not contribute to further improvement in E110 decolorization.

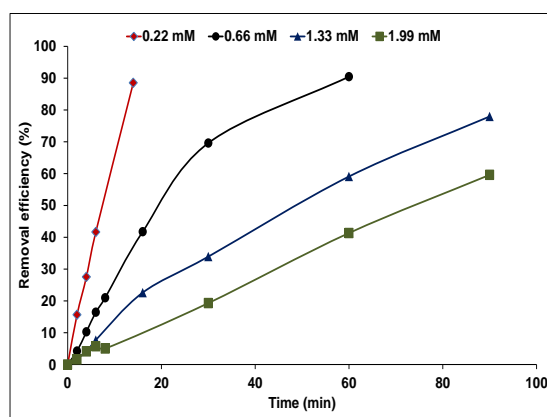


Figure 2. Time dependence of E110 removal efficiency at different initial E110 concentrations (initial conditions: $[PS]_0 = 3.7$ mM, pH = 3 and T = 60 °C)

Kinetic Study

The first- and second-order plots against time of the experimental points ($[PS]/[E110] = 0.27$ and 11.2), Figures 3a and 3b indicate that the reaction follows pseudo-first-order kinetics with an R^2 value (>0.99). This is in contrast to pseudo-second-order kinetics which exhibits an R^2 value (<0.99). It is well known that second-order reactions can exhibit first-order kinetics in a quasi-steady state [30, 41, 42], where one of the two reactants is in excess of the other. However, despite the low $[PS]/[E110]$ ratios (0.27 and 11.2), the experiments demonstrate first-order kinetics. This is due to the presence of SRs, which are, by definition, in quasi-stationary concentration [30, 41, 42], implying that the variation in SR concentration is zero ($\Delta[SO_4^{\cdot-}] = 0$). A number of studies on the decolorization of various dyes, conducted under conditions similar to ours, have reported SR concentrations of around 10^{-12} M [41, 43, 44], which are significantly lower than the concentration of E110. Thus, the decolorization of E110 can be thought to follow first-order kinetics, as described in Eq. 9.

$$-\frac{d[E110]}{dt} = k_6 [SO_4^{\cdot-}] [E110] = k_{obs} [E110], \quad (9)$$

where k_6 represents the second-order rate constant reaction of E110 with SR (Eq. 6), and k_{obs} represents the observed rate constant for E110 decolorization.

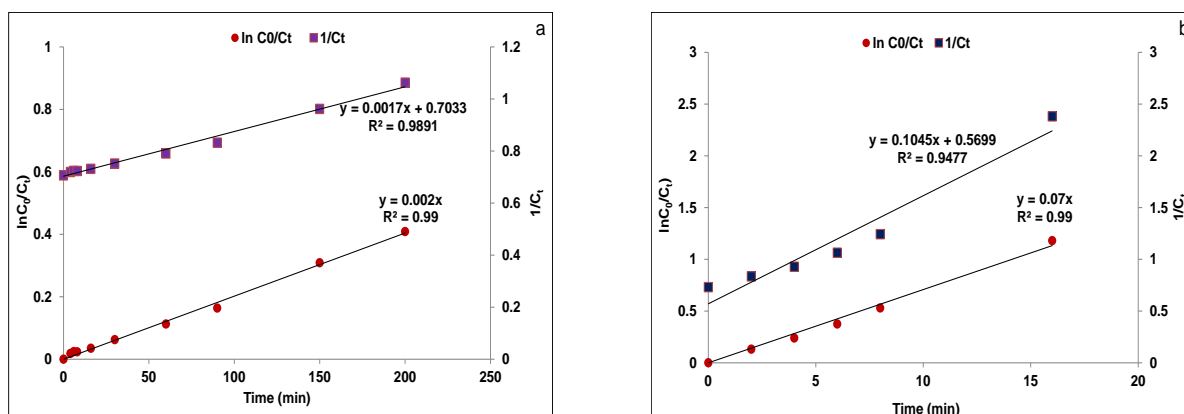


Figure 3. Plots of first and second-order E110 decolorization at $[PS]/[E110]$ ratios of a) 0.27 and b) 11.2. (Initial conditions: $[E110]_0 = 0.66$ mM, pH = 3 and T = 60 °C)

We used a numerical simulation model developed in our previous work [45, 46] to investigate the reaction between E110 and the dominant SRs (Eq. 6) at pH 3. With the exception of k_6 (Table 1), all rate constants were known; therefore, the latter was adjusted to ensure that the model matched experimental data (Fig. 4).

Rate constants for E110 degradation

Chemical reactions	Rate constants				Units	References
	25 °C	40 °C	50 °C	60 °C		
Equation (2)	0.25	3.36	19.4	59.4	$\times 10^{-7} [\text{s}^{-1}]$	[47]
Equation (3)	6.1	6.1	6.1	6.1	$\times 10^5 [\text{M}^{-1} \text{s}^{-1}]$	[48]
Equation (4)*	6.2	7.4	8.3	9.2	$\times 10^2 [\text{s}^{-1}]$	[43]
Equation (5)	4.8	4.8	4.8	4.8	$\times 10^8 [\text{M}^{-1} \text{s}^{-1}]$	[49]

Note: *The indicated rate constant is equal to $k_4 \times [\text{H}_2\text{O}]$.

The k_6 values used for the fit ($5 \times 10^{10} \text{ M}^{-1} \text{ s}^{-1}$) are significantly higher than those reported for other dyes in the literature ($< 1 \times 10^{10} \text{ M}^{-1} \text{ s}^{-1}$) [50]. This finding suggests that E110 is degraded not only by SRs but also through other mechanisms. One reason for this observation is the direct reaction between the E110 dye and the PS ion, which has also been observed at ambient temperature with many other anionic and cationic dyes, including Orange II and Rhodamine B [51, 52]. After 90 minutes of monitoring the absorbance of the E110 dye in the PS/E110 reaction mixture at 25 °C, it can be noted that there was no direct reaction between PS and E110 (Fig. 4).

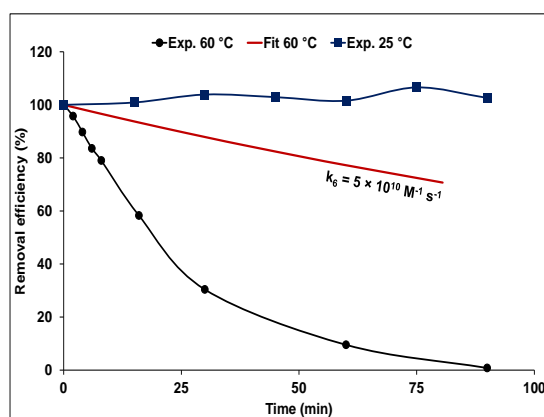


Figure 4. Time dependence of E110 removal efficiency (initial conditions: $[\text{E110}]_0 = 0.66 \text{ mM}$, $[\text{PS}]_0 = 3.7 \text{ mM}$, $\text{pH} = 3$)

Influence of Water Matrix on E110 Removal

Fixed quantities (10^{-3} M) of chloride, carbonate, nitrate, nitrite, and hydrogenphosphate ions were added to the E110/PS solution to determine the impact of these ions on the decolorization. Figure 5 depicts the evolution of removal efficiency over time. The chloride ion has the highest efficiency, while the nitrite ion has the lowest when compared to the control. According to previous studies [27, 28], chloride ions, through the chlorine radical (Cl^\bullet), are more effective than other elements found in water, such as HPO_4^{2-} , CO_3^{2-} and NO_3^- , for the decolorization of dyes. The low efficiency of nitrite has been attributed to its ability to scavenge SR, resulting in the generation of the nitrogen dioxide radical (NO_2^\bullet), which contributes to the formation of nitroaromatic by-products [53, 54]. The other salts have varying degrees of effectiveness compared to the control solution.

Figure 6 shows that the removal of E110 in the presence of monovalent cations with a common anion (Cl^-) proceeds in the following order: $\text{KCl} > \text{NaCl} > \text{HCl}$. Despite having the same ionic strength of 0.0005 M , the monocations have different effects on E110 decolorization.

This result is proportional to the ranking of the three cations according to their ionic radius ($\text{K}^+ > \text{Na}^+ > \text{H}^+$ [55]), whereby a larger radius is associated with a faster degradation kinetic. Despite the limited data on this phenomenon, it has been shown that each cation exerts a distinct influence on the degradation of the pollutant by affecting the activation energy of persulfate decomposition [56, 57].

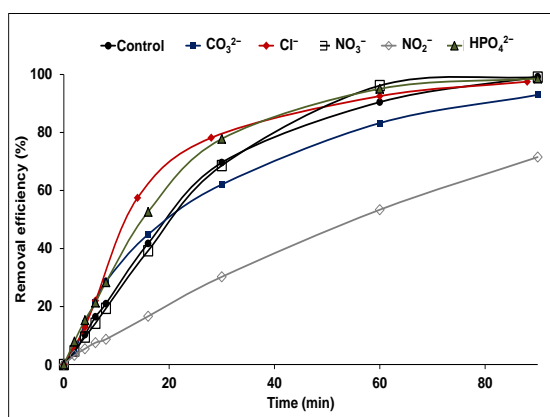


Figure 5. Time dependence of E110 removal efficiency at different initial salt concentrations (initial conditions: $[E110]_0 = 0.66$ mM, $[PS]_0 = 3.7$ mM, $[Salts]_0 = 1$ mM, pH = 3 and T = 60 °C)

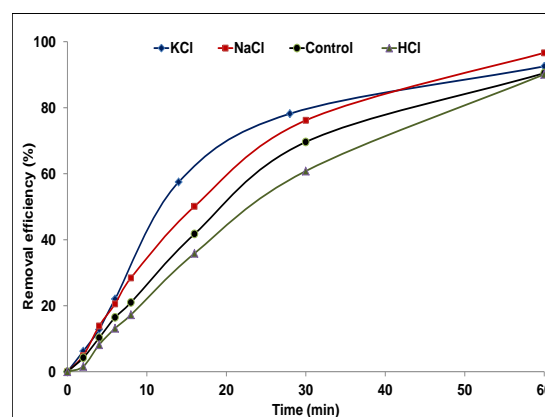


Figure 6. Effects of monovalent cations on the removal of E110 (initial conditions: $[E110]_0 = 0.66$ mM, $[PS]_0 = 3.7$ mM, $[Salts]_0 = 1$ mM, pH = 3 and T = 60 °C)

Effect of Transition Metals

To study the effect of specific transition metals on PS activation, we chose four types of ions (Fe^{2+} , Ni^{2+} , Cu^{2+} , Ag^+) and investigated their influence on E110 decolorization (Fig. 7). The initial concentrations of these four ions were held constant at 10^{-3} M, with 0.66 mM for the E110 and 3.7 mM for the PS. The decolorization of E110 occurred rapidly when iron was added, less rapidly when silver was added, and more slowly in the presence of copper, nickel, and cobalt. This observation is consistent with the results of several studies, in which silver and iron were found to be one of the most effective routes for generating sulfate radicals from persulfate [58, 59]. The difference in catalytic capacity cannot be attributed solely to the redox potential of each metal, but also to factors such as charge, ionic radius, and electronic structure [60].

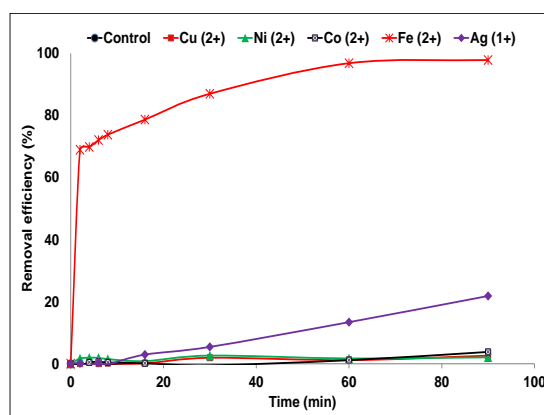


Figure 7. Time dependence of E110 removal efficiency at different initial transition metal concentrations (initial conditions: $[E110]_0 = 0.66$ mM, $[PS]_0 = 3.7$ mM, $[Mn^{n+}]_0 = 1$ mM, pH = 3 and T = 25 °C)

Effect of pH on E110 removal

Figure 8 shows the decolorization of E110 (0.66 mM) by PS (0.18 mM) at 60 °C and different pH values. In order to offset the decline in solution pH resulting from the generation of the H^+ proton (Eq. 4) and the addition of PS, the initial PS concentration was decreased in comparison to the previous experiments. The efficiency of dye elimination efficiency was observed to decline as the pH of the solution increased. This result has been reported in numerous studies and is explained by a decrease in the concentration of SRs, which react with hydroxide ions [61–64]. Similar elimination efficiencies were observed at pH levels 3 and 4, as well as 9 and 11 [65]. This result can be explained by the use of low PS concentrations, which resulted in similar elimination efficiencies across pH values. At pH 2, E110 has higher removal efficiency than at other pH values due to the greater production of SRs (Eq. 10) resulting from acid catalysts [66]:



On the other hand, at pH 12, E110 elimination efficiency improves when compared to alkaline pH values 9 and 11. This finding is explained by the formation of hydroxyl radicals (Eq. 11), which becomes more important as pH increases [67, 68], resulting in more hydroxyl radicals that contribute to dye decolorization.

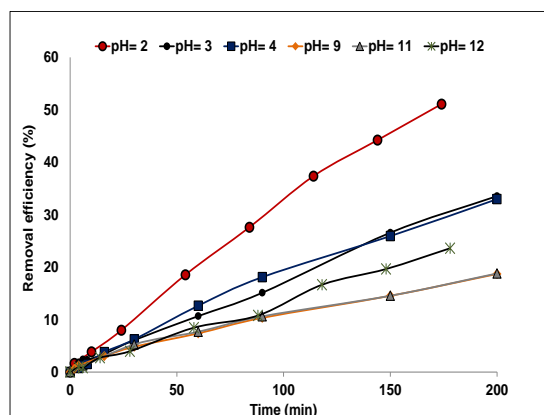


Figure 8. Time dependence of E110 removal efficiency at different pH values (initial conditions: $[\text{E110}]_0 = 0.66 \text{ mM}$, $[\text{PS}]_0 = 3.7 \text{ mM}$ and $T = 60 \text{ }^\circ\text{C}$)

Biochemical and Chemical Oxygen Demand

To determine the biodegradability of the dye, we need to measure both the Chemical Oxygen Demand (COD) and the Biochemical Oxygen Demand over five days (BOD). The BOD5/COD ratio indicates whether or not the dye is biodegradable. COD and BOD5 were measured in a 300 mg/L E110 solution at pH 3 and 20 °C. We measured 2 and 1800 mg/L of BOD5 and COD, respectively. As previously stated [69], the chemical oxygen demand for contaminants from the food and beverage industry pollutants can range from 700 to 3000 mg/L. Thus, the E110 solution has a five-day biochemical oxygen demand/chemical oxygen demand (BOD5/COD) ratio of 0.001, indicating that it is a non-biodegradable dye. Several studies on azo dyes consider them to be non-biodegradable colorants [70, 71].

Effect of Temperature

The effect of temperature on E110 decolorization was investigated at four different heating temperatures (40, 50, 60, and 70 °C). Throughout the experiments, we kept the initial concentration of E110 at 0.66 mM, PS at 3.7 mM, and pH at 3 (Fig. 9). The increased temperature had a positive effect on E110 decolorization. Indeed, elevated temperatures cause the O–O bond in PS to cleave, resulting in the formation of SR and thus accelerating the decomposition of E110 [72, 73].

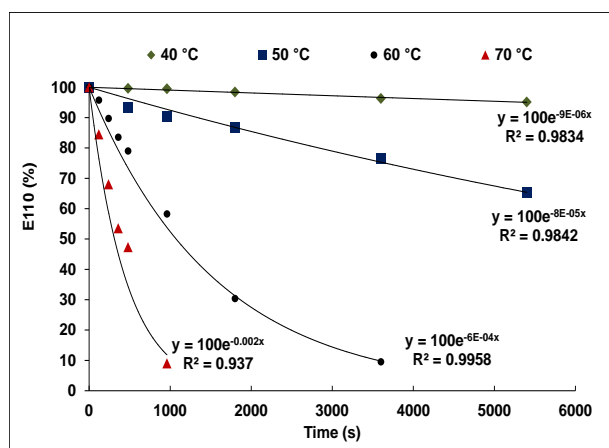


Figure 9. Time dependence of E110 removal efficiency at different temperatures (initial conditions: $[\text{E110}]_0 = 0.66 \text{ mM}$, $[\text{PS}]_0 = 3.7 \text{ mM}$, $\text{pH} = 3$ and $T = 60 \text{ }^\circ\text{C}$)

The activation parameters associated with decolorization are calculated using Arrhenius and Eyring's equations (Eqs. 12, 13, and 14) [39, 52] and by plotting $\ln(K_{obs})$ and $\ln(K_{obs}/T)$ vs. $1/T$, respectively (Fig. 10):



where A is the frequency factor, E_a is the activation energy ($\text{kJ}\cdot\text{mol}^{-1}$), R is the gas constant ($\text{J}\cdot\text{mol}^{-1}\cdot\text{K}^{-1}$), and T is the absolute temperature (K).

$$\ln\left(\frac{k_{obs}}{T}\right) = \left(\ln\left(\frac{k_B}{h}\right) + \frac{\Delta S^\ddagger}{R}\right) - \frac{\Delta H^\ddagger}{RT} \quad (13)$$

where, k_B is the Boltzmann constant ($1.38 \times 10^{-23} \text{ J K}^{-1}$), h is Planck's constant ($6.626 \times 10^{-34} \text{ J s}$), and ΔH^\ddagger and ΔS^\ddagger are the enthalpy and entropy of activation, respectively.

The free activation energy (ΔG_{298}^\ddagger) was determined using Eq. 14 at a T value equal to 298.15 K:

$$\Delta G_{298}^\ddagger = \Delta H^\ddagger - T\Delta S^\ddagger \quad (14)$$

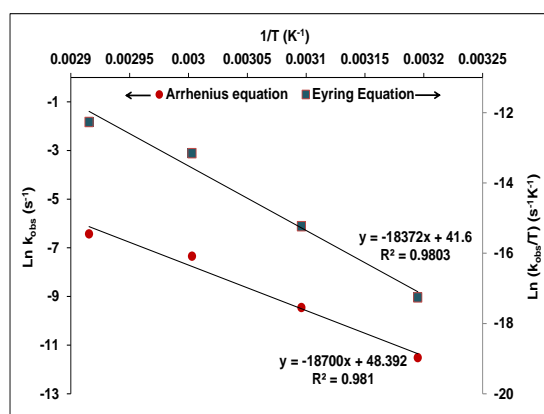


Figure 10. Arrhenius and Eyring Eq. plots for E110 decolorization ($[\text{E110}]_0 = 0.66 \text{ mM}$, $[\text{PS}]_0 = 3.7 \text{ mM}$, $\text{pH} = 3$ and $T = 40, 50, 60$ and $70 \text{ }^\circ\text{C}$)

The positive values for activation energy, enthalpy, entropy, and free energy (Table 2) indicate that the oxidation process requires a minimal amount of energy. Furthermore, it is described as endothermic, with little variation in the three-dimensional arrangement of the molecule's transition state [74].

Table 2

Activation thermodynamic parameters of the decolorization E110 by PS
($[\text{E110}]_0 = 0.66 \text{ mM}$, $[\text{PS}]_0 = 3.7 \text{ mM}$, $\text{pH} = 3$ and $T = 40, 50, 60$ and $70 \text{ }^\circ\text{C}$)

E_a (kJ mol^{-1})	ΔH^\ddagger (kJ mol^{-1})	ΔS^\ddagger (kJ K^{-1})	ΔG_{298}^\ddagger (kJ mol^{-1})
155.4	152.7	0.14	108.5

Orange G has an apparent activation energy of 92 kJ mol^{-1} [75], a structure similar to E110, and a concentration six times lower. It is important to note that the apparent activation parameters are determined by the dyes' initial concentrations and structures of the dyes [37, 74]. The oxidation of E110 by hydrogen peroxide in an alkaline medium required activation energy, enthalpy, entropy, and free energy of 51 kJ mol^{-1} , 54 kJ mol^{-1} , $+0.14 \text{ kJ K}^{-1}$, 10.3 kJ mol^{-1} , respectively [74].

UV-Visible Spectrum Analysis

The UV-visible spectra in Figure 11 show the decolorization of E110 using heated PS at $60 \text{ }^\circ\text{C}$ and $\text{pH} 3$. The characteristic absorption peak at 478 nm corresponds to E110's azo group $[\text{N}=\text{N}]$, which is responsible for its color. In contrast, the peaks at 269 and 310 nm in the ultraviolet region are attributed to the phenyl and naphthyl groups, respectively [64].

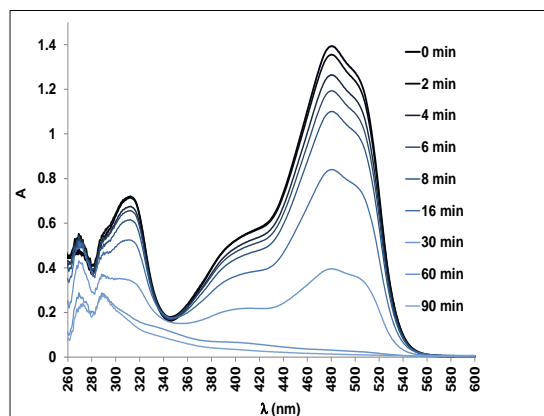


Figure 11. UV-VIS spectra of E110 solution during the decolorization by PS ($[E110]_0 = 0.66$ mM, $[PS]_0 = 3.7$ mM, pH = 3 and T = 60 °C)

During the reaction, the two distinct absorption peaks at 310 nm and 478 nm decreased significantly and nearly vanished after 90 minutes. This observation indicates the complete destruction of the chromophore and conjugated π system. In contrast, the peaks at 259 and 289 nm gradually decrease, indicating that the aromatic rings were still present and frequently were more difficult to oxidize than the azo structure [76, 77]. In general, the action of SRs on organic compounds causes hydroxylation. SRs react with water to form hydroxyl radicals (Eq. 4), which can then interact with aromatic rings to form hydroxyl adducts [48, 78]. SRs could also attack the aromatic ring directly, forming hydroxyl adducts [48, 79], or both processes may occur concurrently [80]. Based on the present results and the existing literature [48, 50, 74, 74, 78], E110 oxidation can occur via two mechanisms: symmetrical azo bond cleavage and asymmetrical azo bond cleavage (Fig. 12).

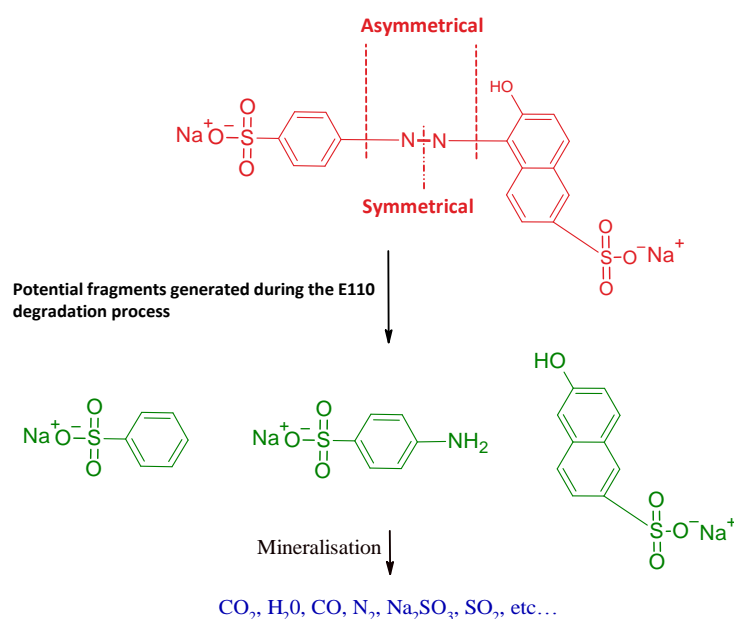


Figure 12. Possible route to the fragments of the E110 dye

Conclusion

This study focused on investigating the process of decolorizing E110 in an aqueous solution using thermally activated peroxydisulfate at a pH level of 3. The findings demonstrated that the effectiveness of E110 decolorization was enhanced by heating and by increasing the initial PS concentration. Conversely, an increase in the initial E110 concentration while the PS concentrations remain constant, will result in a reduction in E110 removal. The introduction of Cl^- , CO_3^{2-} , HPO_4^{2-} , HCO_3^- , NO_2^- or NO_3^- into the dye solutions

typically results in different impacts on the rates of decolorization. The extent of these effects varies depending on the specific salt utilized.

The chlorine ion exhibited the highest level of effectiveness among the tested ions, whereas the nitrite ion demonstrated the lowest level of effectiveness. Among the transition elements tested (Fe^{2+} , Ni^{2+} , Cu^{2+} , and Ag^+), only silver and iron caused E110 decolorization without the need for thermal activation. This finding may be explained by their ability to initiate the PS activation process. The decolorization's observed thermodynamic parameters (E_a , ΔH^\ddagger , ΔS^\ddagger and ΔG^\ddagger) were calculated using the observed rates obtained at various temperatures. Finally, the destruction of aromatic ring structures accompanies the discoloration of E110.

Author Information*

*The authors' names are presented in the following order: First Name, Middle Name and Last Name

Nedjma Lahmar — Student in Environmental Chemistry, Inorganic Materials Laboratory, University of M'sila, University Pole, Road Bourdj Bou Arreiridj, 28000, M'sila Algeria; e-mail: nedjma.lahmar@univ-msila.dz; <https://orcid.org/0009-0005-1849-0751>

Mokhtar Djehiche (corresponding author) — Doctor of Atmospheric Chemistry, Inorganic Materials Laboratory, University of M'sila, University Pole, Road Bourdj Bou Arreiridj, 28000, M'sila Algeria; e-mail: mokhtar.djehiche@univ-msila.dz; <https://orcid.org/0000-0002-3439-113X>

Marwa Bachiri — Student in Environmental Chemistry, Inorganic Materials Laboratory, University of M'sila, University Pole, Road Bourdj Bou Arreiridj, 28000, M'sila Algeria; e-mail: marwa.bachiri@univ-msila.dz; <https://orcid.org/0009-0006-1133-5801>

Author Contributions

The manuscript was written through contributions of all authors. All authors have given approval to the final version of the manuscript. **CRedit**: **Nedjma Lahmar** conceptualization, investigation, methodology, validation, visualization, writing — original draft; **Mokhtar Djehiche** Supervision, formal analysis, visualization, writing — review & editing; **Marwa Bachiri** investigation.

Acknowledgments

The authors thank the University of Mohamed Boudiaf for access to the library facilities.

Conflicts of Interest

The authors declare no conflict of interest.

References

- 1 Rajamanickam, D., Shanthi, M. (2014). Photocatalytic degradation of an azo dye Sunset Yellow under UV-A light using TiO_2/CAC composite catalysts. *Spectrochim Acta A Mol Biomol Spectrosc*, 128, 100–108. <https://doi.org/10.1016/j.saa.2014.02.126>
- 2 Amchova, P., Kotolova, H., Ruda-Kucerova, J. (2015). Health safety issues of synthetic food colorants. *Regul Toxicol Pharmacol*, 73, 914–922. <https://doi.org/10.1016/j.yrtph.2015.09.026>
- 3 Rovina, K., Prabakaran, P.P., Siddiquee, S., Shaarani, S.M. (2016). Methods for the analysis of Sunset Yellow FCF (E110) in food and beverage products- a review. *TrAC Trends Anal Chem*, 85, 47–56. <https://doi.org/10.1016/j.trac.2016.05.009>
- 4 Chen, H. (2012). Toxicological significance of azo dye metabolism by human intestinal microbiota. *Front Biosci*, E4, 568–586. <https://doi.org/10.2741/e400>
- 5 Levine, W.G. (1991). Metabolism of AZO Dyes: Implication for Detoxication and Activation. *Drug Metab Rev*, 23, 253–309. <https://doi.org/10.3109/03602539109029761>
- 6 Hashemi, S.H., Kaykhahi, M. (2022). Azo dyes: Sources, occurrence, toxicity, sampling, analysis, and their removal methods. In: *Emerging Freshwater Pollutants*, 267–287. Elsevier.
- 7 Fatimah, A. (2020). Role of microorganisms in biodegradation of food additive Azo dyes: A review. *Afr J Biotechnol*, 19, 799–805. <https://doi.org/10.5897/AJB2020.17250>
- 8 Minioti, K.S., Sakellariou, C.F., Thomaidis, N.S. (2007). Determination of 13 synthetic food colorants in water-soluble foods by reversed-phase high-performance liquid chromatography coupled with diode-array detector. *Anal Chim Acta*, 583, 103–110. <https://doi.org/10.1016/j.aca.2006.10.002>

- 9 Sha, O., Zhu, X., Feng, Y., Ma, W. (2015). Aqueous two-phase based on ionic liquid liquid–liquid microextraction for simultaneous determination of five synthetic food colourants in different food samples by high-performance liquid chromatography. *Food Chem*, *174*, 380–386. <https://doi.org/10.1016/j.foodchem.2014.11.068>
- 10 Newsome, A.G., Culver, C.A., Van Breemen, R.B. (2014). Nature's Palette: The Search for Natural Blue Colorants. *J Agric Food Chem*, *62*, 6498–6511. <https://doi.org/10.1021/jf501419q>
- 11 Axon, A., May, F.E.B., Gaughan, L.E., et al. (2012). Tartrazine and sunset yellow are xenoestrogens in a new screening assay to identify modulators of human oestrogen receptor transcriptional activity. *Toxicology*, *298*, 40–51. <https://doi.org/10.1016/j.tox.2012.04.014>
- 12 Sarıkaya, R., Selvi, M., Erkoç, F. (2012). Evaluation of potential genotoxicity of five food dyes using the somatic mutation and recombination test. *Chemosphere*, *88*, 974–979. <https://doi.org/10.1016/j.chemosphere.2012.03.032>
- 13 Ma, J., Li, H., Chi, L., et al. (2017). Changes in activation energy and kinetics of heat-activated persulfate oxidation of phenol in response to changes in pH and temperature. *Chemosphere*, *189*, 86–93. <https://doi.org/10.1016/j.chemosphere.2017.09.051>
- 14 Waclawek, S., Lutze, H.V., Gröbel, K., et al. (2017). Chemistry of persulfates in water and wastewater treatment: A review. *Chem Eng J*, *330*, 44–62. <https://doi.org/10.1016/j.cej.2017.07.132>
- 15 Ahmadi, S., Igwegbe, C.A., Rahdar, S. (2019). The application of thermally activated persulfate for degradation of Acid Blue 92 in aqueous solution. *Int J Ind Chem*, *10*, 249–260. <https://doi.org/10.1007/s40090-019-0188-1>
- 16 Bing, W., Wei, W. (2019). Degradation Phenol Wastewater by Heating Activated Persulfate. *Int J Environ Monit Anal*, *7*, 14. <https://doi.org/10.11648/j.ijema.20190701.12>
- 17 Wang, Z., Qiu, W., Pang, S., et al. (2020). Relative contribution of ferryl ion species (Fe(IV)) and sulfate radical formed in nanoscale zero valent iron activated peroxydisulfate and peroxymonosulfate processes. *Water Res*, *172*, 115504. <https://doi.org/10.1016/j.watres.2020.115504>
- 18 Dong, H., He, Q., Zeng, G., et al. (2017). Degradation of trichloroethene by nanoscale zero-valent iron (nZVI) and nZVI activated persulfate in the absence and presence of EDTA. *Chem Eng J*, *316*, 410–418. <https://doi.org/10.1016/j.cej.2017.01.118>
- 19 Hou, S., Ling, L., Shang, C., et al. (2017). Degradation kinetics and pathways of haloacetonitriles by the UV/persulfate process. *Chem Eng J*, *320*, 478–484. <https://doi.org/10.1016/j.cej.2017.03.042>
- 20 Miao, D., Zhao, S., Zhu, K., et al. (2020). Activation of persulfate and removal of ethyl-parathion from soil: Effect of microwave irradiation. *Chemosphere*, *253*, 126679. <https://doi.org/10.1016/j.chemosphere.2020.126679>
- 21 Gao, Y., Gao, N., Wang, W., et al. (2018). Ultrasound-assisted heterogeneous activation of persulfate by nano zero-valent iron (nZVI) for the propranolol degradation in water. *Ultrason Sonochem*, *49*, 33–40. <https://doi.org/10.1016/j.ultsonch.2018.07.001>
- 22 Matzek, L.W., Tipton, M.J., Farmer, A.T., et al. (2018). Understanding Electrochemically Activated Persulfate and Its Application to Ciprofloxacin Abatement. *Environ Sci Technol*, *52*, 5875–5883. <https://doi.org/10.1021/acs.est.8b00015>
- 23 Bhatia, S.C. (2014). Solar thermal energy. In: *Advanced Renewable Energy Systems*. Elsevier, 94–143.
- 24 Jakubauskaite, V., Dikun, J., Jankunas, V., et al. (2015). Use of solar water heating system for oil contaminated soil treatment. In: *2015 Tenth International Conference on Ecological Vehicles and Renewable Energies (EVER)*. IEEE, Monte Carlo, 1–10.
- 25 Liang, C., Su, H.-W. (2009). Identification of Sulfate and Hydroxyl Radicals in Thermally Activated Persulfate. *Ind Eng Chem Res*, *48*, 5558–5562. <https://doi.org/10.1021/ie9002848>
- 26 House, D.A. (1962). Kinetics and Mechanism of Oxidations by Peroxydisulfate. *Chem Rev*, *62*, 185–203. <https://doi.org/10.1021/cr60217a001>
- 27 Sun, S.-P., Li, C.-J., Sun, J.-H., et al. (2009). Decolorization of an azo dye Orange G in aqueous solution by Fenton oxidation process: Effect of system parameters and kinetic study. *J Hazard Mater*, *161*, 1052–1057. <https://doi.org/10.1016/j.jhazmat.2008.04.080>
- 28 Riga, A., Soutsas, K., Ntampegiotis, K., et al. (2007). Effect of system parameters and of inorganic salts on the decolorization and degradation of Procion H-ex1 dyes. Comparison of H₂O₂/UV, Fenton, UV/Fenton, TiO₂/UV and TiO₂/UV/H₂O₂ processes. *Desalination*, *211*, 72–86. <https://doi.org/10.1016/j.desal.2006.04.082>
- 29 Bennedsen, L.R., Muff, J., Søgaard, E.G. (2012). Influence of chloride and carbonates on the reactivity of activated persulfate. *Chemosphere*, *86*, 1092–1097. <https://doi.org/10.1016/j.chemosphere.2011.12.011>
- 30 Liang, C.-J., Huang, S.-C. (2012). Kinetic model for sulfate/hydroxyl radical oxidation of methylene blue in a thermally-activated persulfate system at various pH and temperatures. *Sustain Env Res*, 199–208.
- 31 Wei, L., Xia, X., Zhu, F., et al. (2020). Dewatering efficiency of sewage sludge during Fe²⁺-activated persulfate oxidation: Effect of hydrophobic/hydrophilic properties of sludge EPS. *Water Res*, *181*, 115903. <https://doi.org/10.1016/j.watres.2020.115903>
- 32 Baciocchi, R., D'Aprile, L., Innocenti, I., et al. (2014). Development of technical guidelines for the application of in-situ chemical oxidation to groundwater remediation. *J Clean Prod*, *77*, 47–55. <https://doi.org/10.1016/j.jclepro.2013.12.016>
- 33 Matzek, L.W., Carter, K.E. (2016). Activated persulfate for organic chemical degradation: A review. *Chemosphere*, *151*, 178–188. <https://doi.org/10.1016/j.chemosphere.2016.02.055>
- 34 Oranusi, N., Njoku, H. (2009). Biotransformation of Food Dyes by Human Intestinal Bacteria (*Streptococcus faecalis*, *Escherichia coli*). *J Appl Sci Environ Manag*, *10*. <https://doi.org/10.4314/jasem.v10i2.43698>
- 35 Abdel-Aziz, H.M., Abdel-Gawad, S.A. (2020). Removal of sunset YellowAzo dye using activated carbon entrapped in alginate from aqueous solutions. *Open Access J Sci*, *4*, 1–6. <https://doi.org/10.15406/oajs.2020.04.00142>

- 36 Feizi, R., Ahmad, M., Jorfi, S., Ghanbari, F. (2019). Sunset yellow degradation by ultrasound/peroxymonosulfate/CuFe₂O₄: Influential factors and degradation processes. *Korean J Chem Eng*, 36, 886–893. <https://doi.org/10.1007/s11814-019-0268-0>
- 37 Shuchi, S.B., Suhan, Md.B.K., Humayun, S.B., et al. (2021). Heat-activated potassium persulfate treatment of Sudan Black B dye: Degradation kinetic and thermodynamic studies. *J Water Process Eng*, 39, 101690. <https://doi.org/10.1016/j.jwpe.2020.101690>
- 38 Wang, S., Zhou, N. (2016). Removal of carbamazepine from aqueous solution using sono-activated persulfate process. *Ultrason Sonochem*, 29, 156–162. <https://doi.org/10.1016/j.ultsonch.2015.09.008>
- 39 Fayoumi, L.M.A., Ezzedine, M.A., Akel, H.H., Jamal, M.M. (2012). Kinetic Study of the Degradation of Crystal Violet by K₂S₂O₈. Comparison with Malachite Green: *Port Electrochimica Acta*, 30, 121–133. <https://doi.org/10.4152/pea.201202121>
- 40 Naser Elddine, H.A., Damaj, Z.K., Yazbeck, O.A., et al. (2015). Kinetic Study of the Discoloration of the Food Colorant E131 by K₂S₂O₈ and KIO₃: *Port Electrochimica Acta*, 33, 275–288. <https://doi.org/10.4152/pea.201505275>
- 41 Lian, L., Yao, B., Hou, S., et al. (2017). Kinetic Study of Hydroxyl and Sulfate Radical-Mediated Oxidation of Pharmaceuticals in Wastewater Effluents. *Environ Sci Technol*, 51, 2954–2962. <https://doi.org/10.1021/acs.est.6b05536>
- 42 Ahmadi, M., Behin, J., Mahnam, A.R. (2016). Kinetics and thermodynamics of peroxydisulfate oxidation of Reactive Yellow 84. *J Saudi Chem Soc*, 20, 644–650. <https://doi.org/10.1016/j.jscs.2013.07.004>
- 43 Mora, V.C., Rosso, J.A., Carrillo Le Roux, G., et al. (2009). Thermally activated peroxydisulfate in the presence of additives: A clean method for the degradation of pollutants. *Chemosphere*, 75, 1405–1409. <https://doi.org/10.1016/j.chemosphere.2009.02.038>
- 44 Chen, L., Xue, Y., Luo, T., et al. (2021). Electrolysis-assisted UV/sulfite oxidation for water treatment with automatic adjustments of solution pH and dissolved oxygen. *Chem Eng J*, 403, 126278. <https://doi.org/10.1016/j.cej.2020.126278>
- 45 Djehiche, M., Tomas, A., Fittschen, C., Coddeville, P. (2011). First Direct Detection of HONO in the Reaction of Methylnitrite (CH₃ONO) with OH Radicals. *Environ Sci Technol*, 45, 608–614. <https://doi.org/10.1021/es103076e>
- 46 Djehiche, M., Tomas, A., Fittschen, C., Coddeville, P. (2011). First Cavity Ring-Down Spectroscopy HO₂ Measurements in a Large Photoreactor. *Z Für Phys Chem*, 225, 938–992. <https://doi.org/10.1524/zpch.2011.0143>
- 47 Johnson, R.L., Tratnyek, P.G., Johnson, R.O. (2008). Persulfate Persistence under Thermal Activation Conditions. *Environ Sci Technol*, 42, 9350–9356. <https://doi.org/10.1021/es8019462>
- 48 Yu, X.-Y., Bao, Z.-C., Barker, J.R. (2004). Free Radical Reactions Involving Cl[•], Cl₂^{•-}, and SO₄^{•-} in the 248 nm Photolysis of Aqueous Solutions Containing S₂O₈²⁻ and Cl⁻. *J Phys Chem A*, 108, 295–308. <https://doi.org/10.1021/jp036211i>
- 49 Hayon, E., McGarvey, J.J. (1967). Flash photolysis in the vacuum ultraviolet region of sulfate, carbonate, and hydroxyl ions in aqueous solutions. *J Phys Chem*, 71, 1472–1477. <https://doi.org/10.1021/j100864a044>
- 50 Wojnárovits, L., Takács, E. (2019). Rate constants of sulfate radical anion reactions with organic molecules: A review. *Chemosphere*, 220, 1014–1032. <https://doi.org/10.1016/j.chemosphere.2018.12.156>
- 51 Yang, B., Luo, Q., Li, Q., et al. (2021). Selective oxidation and direct decolorization of cationic dyes by persulfate without activation. *Water Sci Technol*, 83, 2744–2752. <https://doi.org/10.2166/wst.2021.177>
- 52 Mcheik, A.H., Jamal, M.M.E. (2013). Kinetic Study of the Discoloration of Rhodamine B with Persulfate, Iron Activation. *J Chem Technol Metall*, 357–365.
- 53 Ji, Y., Wang, L., Jiang, M., et al. (2017). The role of nitrite in sulfate radical-based degradation of phenolic compounds: An unexpected nitration process relevant to groundwater remediation by in-situ chemical oxidation (ISCO). *Water Res*, 123, 249–257. <https://doi.org/10.1016/j.watres.2017.06.081>
- 54 Yang, P., Ji, Y., Lu, J., Huang, Q. (2019). Formation of Nitrophenolic Byproducts during Heat-Activated Peroxydisulfate Oxidation in the Presence of Natural Organic Matter and Nitrite. *Environ Sci Technol*, 53, 4255–4264. <https://doi.org/10.1021/acs.est.8b06967>
- 55 Shannon, R.D. (1976) Revised effective ionic radii and systematic studies of interatomic distances in halides and chalcogenides. *Acta Crystallogr Sect A*, 32, 751–767. <https://doi.org/10.1107/S0567739476001551>
- 56 Zhangm, H.-C., Han, J.-J., Zhang, X., et al. (2021). Undiscovered Multiple Roles of Multivalent Cations in the Pollutant Removal from Actual Water by Persulfate Activated by Carbon Materials. *ACS EST Eng*, 1, 1227–1235. <https://doi.org/10.1021/acsestengg.1c00121>
- 57 Zhang, R., Wang, X., Zhou L, Crump D (2019). Quantum chemical investigations of the decomposition of the peroxydisulfate ion to sulfate radicals. *Chem Eng J*, 361, 960–967. <https://doi.org/10.1016/j.cej.2018.12.145>
- 58 Xia, X., Zhu, F., Li, J., et al. (2020). A Review Study on Sulfate-Radical-Based Advanced Oxidation Processes for Domestic/Industrial Wastewater Treatment: Degradation, Efficiency, and Mechanism. *Front Chem*, 8, 592056. <https://doi.org/10.3389/fchem.2020.592056>
- 59 Park, S.-M., Lee, S.-W., Jeon, P.-Y., Baek, K. (2016). Iron Anode-Mediated Activation of Persulfate. *Water Air Soil Pollut*, 227, 462. <https://doi.org/10.1007/s11270-016-3169-4>
- 60 Anipsitakis, G.P., Dionysiou, D.D. (2004). Radical Generation by the Interaction of Transition Metals with Common Oxidants. *Environ Sci Technol*, 38, 3705–3712. <https://doi.org/10.1021/es035121o>
- 61 Bing, W., Wei, W. (2019). Degradation Phenol Wastewater by Heating Activated Persulfate. *Int J Environ Monit Anal*, 7, 14. <https://doi.org/10.11648/j.ijema.20190701.12>
- 62 Criquet, J., Leitner, N.K.V. (2009). Degradation of acetic acid with sulfate radical generated by persulfate ions photolysis. *Chemosphere*, 77, 194–200. <https://doi.org/10.1016/j.chemosphere.2009.07.040>

- 63 Thabet, M., El-Zomrawy, A.A. (2016). Degradation of acid red 17 dye with ammonium persulphate in acidic solution using photoelectrocatalytic methods. *Arab J Chem*, 9, S204–S208. <https://doi.org/10.1016/j.arabjc.2011.03.001>
- 64 Wang, C., Yang, Q., Li, Z., et al. (2019). A novel carbon-coated Fe-C/N composite as a highly active heterogeneous catalyst for the degradation of Acid Red 73 by persulfate. *Sep Purif Technol*, 213, 447–455. <https://doi.org/10.1016/j.seppur.2018.12.072>
- 65 Ghauch, A., Tuqan, A.M., Kibbi, N., Geryes, S. (2012). Methylene blue discoloration by heated persulfate in aqueous solution. *Chem Eng J*, 213, 259–271. <https://doi.org/10.1016/j.cej.2012.09.122>
- 66 Lee, Y.-C., Lo, S.-L., Kuo, J., Lin, Y.-L. (2012). Persulfate oxidation of perfluorooctanoic acid under the temperatures of 20–40 °C. *Chem Eng J*, 198–199, 27–32. <https://doi.org/10.1016/j.cej.2012.05.073>
- 67 Furman, O.S., Teel, A.L., Ahmad, M., et al. (2011). Effect of Basicity on Persulfate Reactivity. *J Environ Eng*, 137, 241–247. [https://doi.org/10.1061/\(ASCE\)EE.1943-7870.0000323](https://doi.org/10.1061/(ASCE)EE.1943-7870.0000323)
- 68 Liang, C., Wang, Z.-S., Bruell, C.J. (2007). Influence of pH on persulfate oxidation of TCE at ambient temperatures. *Chemosphere*, 66, 106–113. <https://doi.org/10.1016/j.chemosphere.2006.05.026>
- 69 Chmiel, H., Kaschek, M., Blöcher, C., et al. (2003). Concepts for the treatment of spent process water in the food and beverage industries. *Desalination*, 152, 307–314. [https://doi.org/10.1016/S0011-9164\(02\)01078-0](https://doi.org/10.1016/S0011-9164(02)01078-0)
- 70 Suzuki, M., Suzuki, Y., Uzuka, K., Kawase, Y. (2020). Biological treatment of non-biodegradable azo-dye enhanced by zero-valent iron (ZVI) pre-treatment. *Chemosphere*, 259, 127470. <https://doi.org/10.1016/j.chemosphere.2020.127470>
- 71 Feuzer-Matos, A.J., Testolin, R.C., Pimentel-Almeida, W., et al. (2022). Treatment of Wastewater Containing New and Non-biodegradable Textile Dyes: Efficacy of Combined Advanced Oxidation and Adsorption Processes. *Water Air Soil Pollut*, 233, 273. <https://doi.org/10.1007/s11270-022-05751-1>
- 72 Rahmani, A.R., Rezaeivahidian, H., Almasi, M., et al. (2016). A comparative study on the removal of phenol from aqueous solutions by electro-Fenton and electro-persulfate processes using iron electrodes. *Res Chem Intermed*, 42, 1441–1450. <https://doi.org/10.1007/s11164-015-2095-1>
- 73 Luo, Q. (2014). Oxidative treatment of aqueous monochlorobenzene with thermally-activated persulfate. *Front Environ Sci Eng*, 8, 188–194. <https://doi.org/10.1007/s11783-013-0544-x>
- 74 Fragoso, C.T., Battisti, R., Miranda, C., De Jesus, P.C. (2009). Kinetic of the degradation of C.I. Food Yellow 3 and C.I. Food Yellow 4 azo dyes by the oxidation with hydrogen peroxide. *J Mol Catal Chem*, 301, 93–97. <https://doi.org/10.1016/j.molcata.2008.11.014>
- 75 Xu, X.-R., Li, X.-Z. (2010). Degradation of azo dye Orange G in aqueous solutions by persulfate with ferrous ion. *Sep Purif Technol*, 72, 105–111. <https://doi.org/10.1016/j.seppur.2010.01.012>
- 76 Hu, E., Wu, X., Shang, S., et al. (2016). Catalytic ozonation of simulated textile dyeing wastewater using mesoporous carbon aerogel supported copper oxide catalyst. *J Clean Prod*, 112, 4710–4718. <https://doi.org/10.1016/j.jclepro.2015.06.127>
- 77 Wu, C.-H., Kuo, C.-Y., Chang, C.-L. (2008). Homogeneous catalytic ozonation of C.I. Reactive Red 2 by metallic ions in a bubble column reactor. *J Hazard Mater*, 154, 748–755. <https://doi.org/10.1016/j.jhazmat.2007.10.087>
- 78 Hori, H., Yamamoto, A., Hayakawa, E., et al. (2005). Efficient Decomposition of Environmentally Persistent Perfluorocarboxylic Acids by Use of Persulfate as a Photochemical Oxidant. *Environ Sci Technol*, 39, 2383–2388. <https://doi.org/10.1021/es0484754>
- 79 Anipsitakis, G.P., Dionysiou, D.D., Gonzalez, M.A. (2006). Cobalt-Mediated Activation of Peroxymonosulfate and Sulfate Radical Attack on Phenolic Compounds. Implications of Chloride Ions. *Environ Sci Technol*, 40, 1000–1007. <https://doi.org/10.1021/es050634b>
- 80 Gokulakrishnan, S., Parakh, P., Prakash, H. (2012). Degradation of Malachite green by Potassium persulphate, its enhancement by 1,8-dimethyl-1,3,6,8,10,13-hexaazacyclotetradecane nickel(II) perchlorate complex, and removal of antibacterial activity. *J Hazard Mater*, 213-214, 19–27. <https://doi.org/10.1016/j.jhazmat.2012.01.031>

Mudar A. Abdulsattar 

Ministry of Science and Technology, Baghdad, Iraq
(*Author's e-mail: mudarahmed3@yahoo.com)

Effect of Acetylene Properties on its Gas Sensing by NiO Doped ZnO Clusters: A Transition State Theory Model

The sensitivity of nickel oxide doped zinc oxide to industrial gas acetylene was calculated and compared to available experimental data. The adsorption of C_2H_2 on the NiO-doped ZnO surface and the activation transition states formed afterward were studied computationally. B3LYP version of density functional theory with 6-311G** basis set, including dispersion correction (GD3BJ) was performed for the calculations with the help of Gaussian 09 software. Thermodynamic quantities of the reaction of C_2H_2 with NiO-doped ZnO surfaces, such as Gibbs free energy, enthalpy, and entropy, were used to interpret the reaction at the temperature range 25–325 °C. Response and response time variation with different NiO doping percentages were calculated. The calculations took into account the combustion of acetylene as it approached its autoignition temperature, which was not considered in previous works. The results show that the optimum response operating temperature of the C_2H_2 gas sensor is below the autoignition temperature of acetylene at 300 °C. A good agreement of theoretical response and response time with variation of temperature and acetylene concentration was obtained with the experiment. This study was the first to take into account the autoignition of C_2H_2 in gas sensor calculations and noted that gases can be easily distinguished by their autoignition temperature.

Keywords: NiO-doping, ZnO cluster, acetylene gas sensor, Density Functional Theory, transition state.

Introduction

ZnO is in the hexagonal wurtzite structure [1], while NiO is in the NaCl cubic structure at ambient temperature [2]. When ZnO is doped with NiO, the hexagonal structure is transformed into a cubic NaCl structure as the NiO doping concentration increases [3]. ZnO in the NaCl structure occurs at high pressure [4]. On the other hand, the NiO in the hexagonal structure is also formed [5]. ZnO is an n-type semiconductor due to oxygen vacancies [6]. NiO is a p-type semiconductor since Ni can have higher oxides such as Ni_2O_3 (black nickel oxide) [7]. The doping of ZnO with NiO can form a *p-n* junction. ZnO is a very practical choice for gas sensors. ZnO is used to detect many gases, such as acetone [8], acetaldehyde [9], NO_2 [10], etc. NiO as an oxide is also utilized as a gas sensor for different gases such as H_2S [11], acetone [12], H_2 [13], etc. Small ZnO clusters that reflect the wurtzite structure are called wurtzoids [14, 15]. These clusters simplify gas sensor calculations within existing computing power while preserving the similarity of the electronic structure with particles of larger size. The gas-sensing process happens on the surface of the sensor. Since oxygen layers are inevitable during surface preparation under atmospheric conditions, Ni atoms on the surface are oxidized by the oxygen in the air or by oxygen already present in the ZnO.

Acetylene is an unsaturated hydrocarbon with the formula C_2H_2 , widely used in industry [16]. Acetylene has a number of properties that differ from many other gases. C_2H_2 is a sublimating gas at about –84 °C. It also has an autoignition temperature of 300 °C. Autoignition temperature is the temperature at which a material will spontaneously ignite in a normal atmosphere without the need for an external ignition source. This temperature puts limits on the highest temperature at which the gas can be detected, since it quickly burns out after reaching this temperature [17, 18]. The intrinsic properties of the detected gas are continuously ignored when calculating gas detection in a sensor. In the present work the properties of acetylene will play an important role in the detection of this gas, as we shall see later.

Transition state theory is one of the most used theories to simulate reactions that include gas sensors [19]. The parameters of this theory can be calculated using density functional theory (DFT). These parameters include thermodynamic quantities such as Gibbs free energy of activation, enthalpy, and entropy. These parameters usually depend on temperature.

The present work uses a NiO-doped ZnO cluster as a gas sensor to detect acetylene gas. The analysis is carried out theoretically using transition state theory and compared with available experimental data. Gibbs

free energy of transition or activation is calculated as a function of temperature. The calculated Gibbs energy of transition is transformed to the values of the experimental NiO-doped ZnO ratio using the modified Evans–Polanyi principle. The change in the density of acetylene gas as acetylene approaches its autoignition temperature is considered. Results show good agreement of theoretically calculated sensor response and response time with available experimental data. The novelty and motivation of the present work are derived from the fact that acetylene autoignition has never been considered in previous studies.

Computational Details

Gaussian 09 computational chemistry software was used in the present calculations [20]. B3LYP version of density functional theory with 6-311G** basis set, including dispersion correction (GD3BJ), showed satisfactory accuracy and execution time [21].

ZnO small clusters similar to the hexagonal wurtzite bulk structure are called wurtzoids [15, 22]. These clusters have been used frequently to replace the time-consuming periodic representation of bulk ZnO, including doping with different elements [14, 23]. Figure 1 shows the adsorption of C_2H_2 on pristine and NiO-doped ZnO clusters ($Zn_{13}O_{13}$ and $NiZn_{12}O_{13}$).

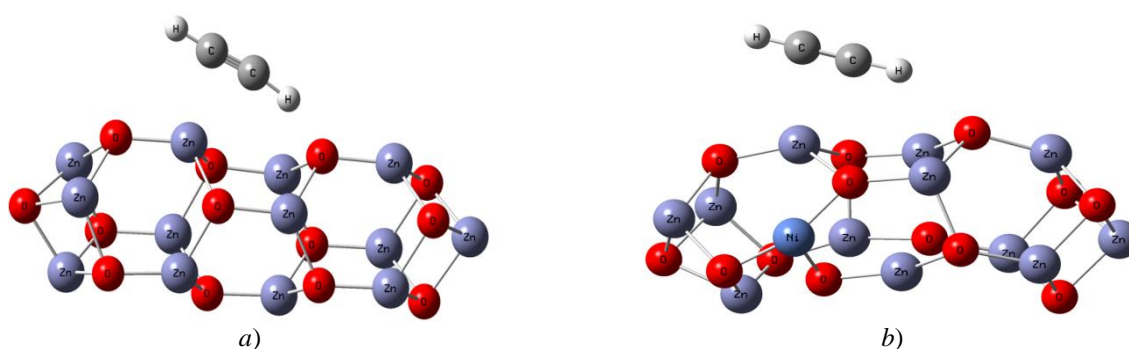


Figure 1. *a* — The adsorption of C_2H_2 on optimized pristine ZnO clusters ($Zn_{13}O_{13}$) designed as $[Zn_{13}O_{13} - C_2H_2]^a$; *b* — optimized $NiZn_{12}O_{13}$ with adsorbed C_2H_2 molecule designed as $[NiZn_{12}O_{13} - C_2H_2]^a$

The interaction between the cluster and acetylene diminishes as the number of neighbors increases. Typically, a fourth neighbor interaction cutoff is used so that results are highly correct with negligible remaining interactions [24]. Adsorption is characterized by the attraction of hydrogen atoms in C_2H_2 to oxygen atoms on pristine or doped ZnO. On the other hand, carbon atoms in C_2H_2 are attracted to Zn or Ni atoms. This van der Waals attraction is due to the positive charges on H, Zn, and Ni atoms and negative charges on C and O atoms. It can be noted that the Ni atom is connected to oxygen atoms (O–Ni–O angle), forming nearly 90- or 180-degree angles with them, which reflects the NaCl structure characterization of NiO.

After adsorption, a transition state is formed before the interaction of C_2H_2 with pristine and NiO-doped ZnO clusters. The transition state is defined as the state of the highest potential energy along the reaction path. The transition states developed from the adsorption states of Figure 1 are shown in Figure 2. The (TS) option of Gaussian 09 program using the Berny algorithm is adopted.

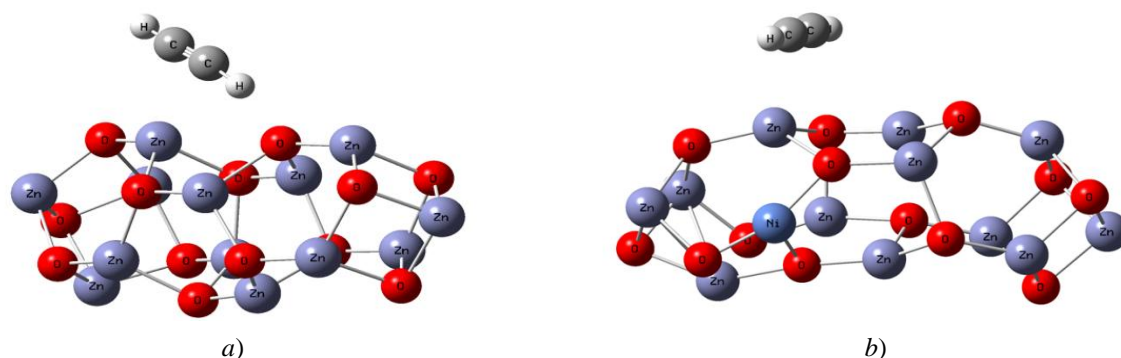


Figure 2. *a* — The optimized transition state of adsorbed C_2H_2 on pristine ZnO ($[Zn_{13}O_{13} - C_2H_2]^\ddagger$); *b* — The optimized transition state of $NiZn_{12}O_{13}$ with adsorbed C_2H_2 molecule $[NiZn_{12}O_{13} - C_2H_2]^\ddagger$

As can be seen from Fig. 2, the C_2H_2 molecule encounters a rotation from the adsorption state of Fig. 1. This rotation is more evident in the NiO-doped ZnO cluster in Fig. 2b.

The rate of a chemical reaction is influenced by several factors such as temperature, pressure, and concentration of the reacting materials. Many theories have been proposed to handle and calculate such rates, including the Arrhenius equation, collision theory, and transition state theory and their variations. At constant pressure, the general equation describing the reaction rate for the present reaction of ZnO with acetylene can be given as follows [25]:

$$\frac{d[ZnO]}{dt} = -[ZnO]^u [C_2H_2]_e^v k(T), \quad (1)$$

$$k(T) = AT^m \exp\left(\frac{-\Delta G^\ddagger}{k_B T}\right). \quad (2)$$

In the above two equations, $[ZnO]$ and $[C_2H_2]$ are the zinc oxide and acetylene concentrations, respectively. The exponents u and v in the concentrations are usually equal to 1 or $1/2$. The subscript e in the acetylene concentration represents the effective concentration of acetylene due to autoignition as acetylene approaches its autoignition temperature. $k(T)$ represents the effect of temperature on the reaction rate. The temperature dependence $k(T)$ reflects the type of gas and sensor, as well as the ability of the gas to diffuse into the sensor surface and reach the inner layers. The value of m for the temperature exponent in Eq. (2) is higher for gases that can diffuse deep in the sensor's layers. ΔG^\ddagger is the Gibbs energy of transition, while k_B is the Boltzmann constant. The effect of material properties such as morphology, surface area, crystallinity, and structure is inhibited in the pre-exponential parameter (A) in the $k(T)$ equation (Eq. (2)).

Evaluating the Gibbs transition energy for NiO-doped ZnO can sometimes be difficult since the exact doping percentage may involve many atoms, requiring a long computational time. However, a solution can be proposed using the modified Evans–Polanyi principle as follows [25]:

$$\Delta G^\ddagger = \Delta G_0^\ddagger + \beta \Delta G_1^\ddagger, \quad (3)$$

In the above equation, ΔG_0^\ddagger and ΔG_1^\ddagger are known Gibbs energy of transition of two structures that are near the required ΔG^\ddagger value using the interpolation parameter β . The values of ΔG_0^\ddagger and ΔG_1^\ddagger are that of pristine and NiO-doped ZnO in Fig. 2a and Fig. 2b respectively. Their values are 0.1487 and 0.1377 eV (at standard 25 °C and 1 bar conditions) respectively. The interpolation parameter β can be found using simple linear interpolation formulas. The original Evans–Polanyi principle concerns the interpolation of enthalpy ΔH^\ddagger . The addition of the activation entropy (S^\ddagger) transforms the relation to a Gibbs energy relation:

$$\Delta G^\ddagger = \Delta H^\ddagger - T\Delta S^\ddagger. \quad (4)$$

As mentioned in the description of Eq. (1), the effective concentration of acetylene is used due to the ignition of acetylene as its autoignition temperature of 300 °C approaches. A logistic function is used to describe the concentration of acetylene as it approaches the autoignition temperature [18]:

$$f(T) = \frac{1}{1 + e^{k_s(T-T_0)}}, \quad (5)$$

where k_s is the steepness of the decrease in acetylene concentration, T_0 is the temperature at which acetylene reaches half of its original concentration as it approaches autoignition temperature.

Eq. (5) is the critical equation that will shape the gas response curves that follow Eq. (1) for the reaction rate.

The detection of the acetylene gas is performed as a consequence of monitoring sensor resistance changes due to the reaction of acetylene with the sensing material. The sensor's resistance in the air is denoted R_a , while the resistance in the presence of a gas is denoted R_g . The ratio R_a/R_g is called the sensor's response. This ratio is proportional to the reaction rate of Eq. (1), as in the following equation:

$$\text{Response}(\text{theoretical}) = 1 + C \left| \frac{d[ZnO]}{dt} \right| \quad (6)$$

The value (1) is added in Eq. (6) because the response is 1 in the absence of gas ($R_a/R_g = 1$). C is the correlation factor linking the resistivity to the reaction rate.

An important quantity that measures the fast response of the gas sensor is the response time (t_{res}). This quantity can be obtained by integrating Eq. (1) concerning time (t) with the exponent ($u = 1$) in Eq. (1). The response time, which corresponds to the time needed for the resistivity to reach 90 % of its final resistance, is determined by the following formula [25]:

$$t_{res(90\%)} = \frac{\ln(10)}{[C_2H_2]_e^v AT^m \exp\left(\frac{-\Delta G^\ddagger}{k_B T}\right)} \quad (7)$$

Results and Discussion

Fig. 3 shows the variation of Gibbs free energy in the transition of pure and NiO-doped ZnO with temperature.

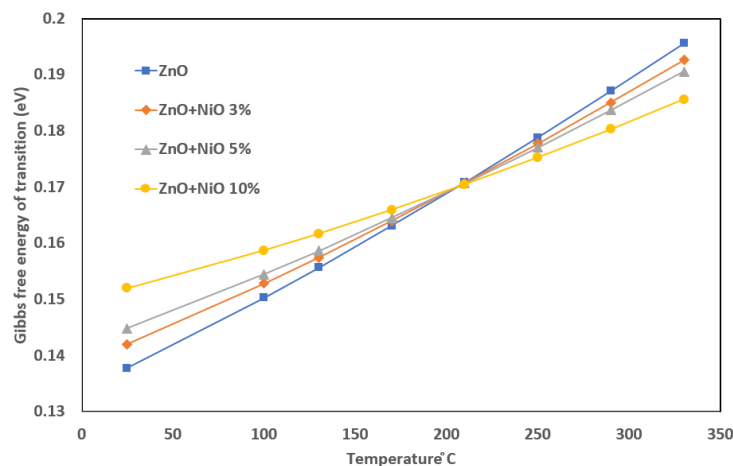
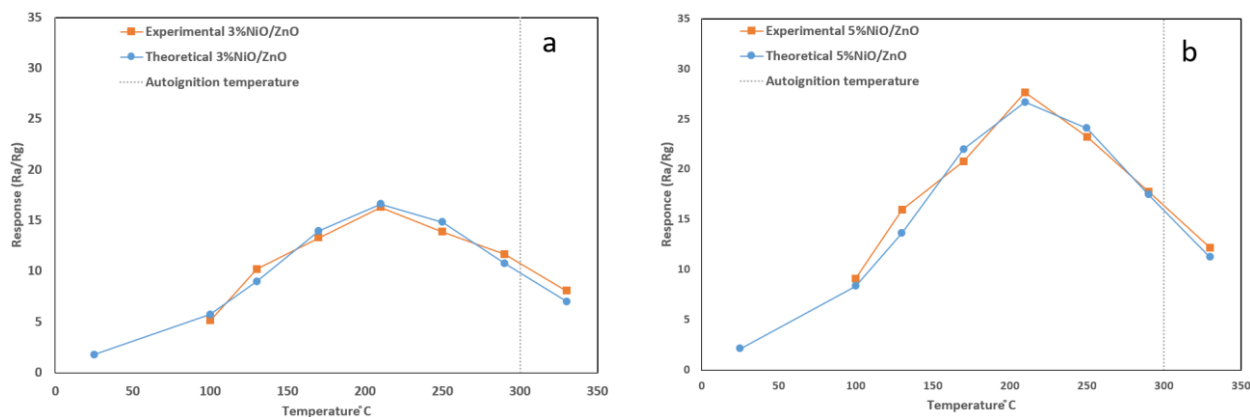


Figure 3. The Gibbs free energy of transition of the optimized transition state of adsorbed C_2H_2 on the four cases of pristine and 3, 5, 10 % NiO-doped ZnO as a function of temperature

As can be seen in Fig. 3, the Gibbs free energy of transition of pure and NiO doped ZnO are close and intersect at a temperature of 210 °C. This temperature has the same highest response and lowest response time, as seen in the corresponding figures.

Fig. 4 shows the change in theoretical response (R_a/R_g) for different NiO concentrations (3, 5, 10 % molar ratio) with temperature compared with experimental results [26] for 200 ppm C_2H_2 . The autoignition temperature of C_2H_2 is indicated.

As can be seen in Fig. 4, using the present theory, good agreement was obtained between the theoretical and experimental results. The maximum response is at 210 °C for all theoretical calculations in good agreement with the two NiO doping percentages 3 and 5 %, while the experimental 10 % NiO percentage deviates at 160 °C. Most available experimental data from other experiments agree with present theoretical results. As an example, the maximum response of C_2H_2 is at 206, 255, 200, 250, and 285 °C for the references [27–31], respectively that are all below the autoignition temperature at 300 °C in agreement with present results. The present calculations provide a unique method to distinguish gases. As an example, the H_2 autoignition temperature is at 536 °C that is far from that of acetylene and its maximum response can be distinguished easily.



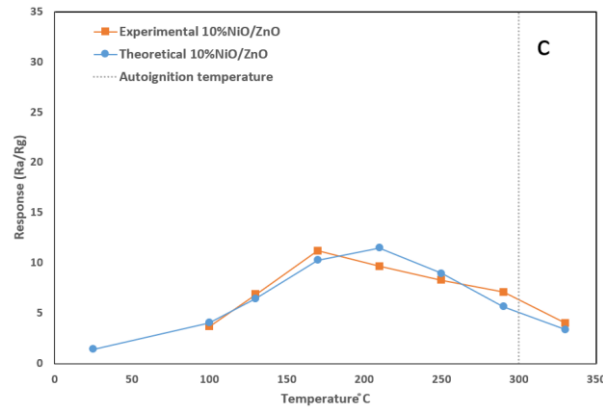


Figure 4. Change in theoretical response (R_a/R_g) for different NiO concentrations (3, 5, 10 % molar ratio) with temperature compared with experimental results [26] for 200 ppm C_2H_2 . The autoignition temperature of C_2H_2 is indicated

Fig. 5 shows the change in theoretical response (R_a/R_g) for different NiO concentrations (3, 5, 10 % molar ratio) with C_2H_2 concentration at 210 °C temperature compared with experimental results [26]. Good agreement can be seen between the experimental and theoretical results. The highest response is for 5 % NiO doping, as shown in Fig. 4.

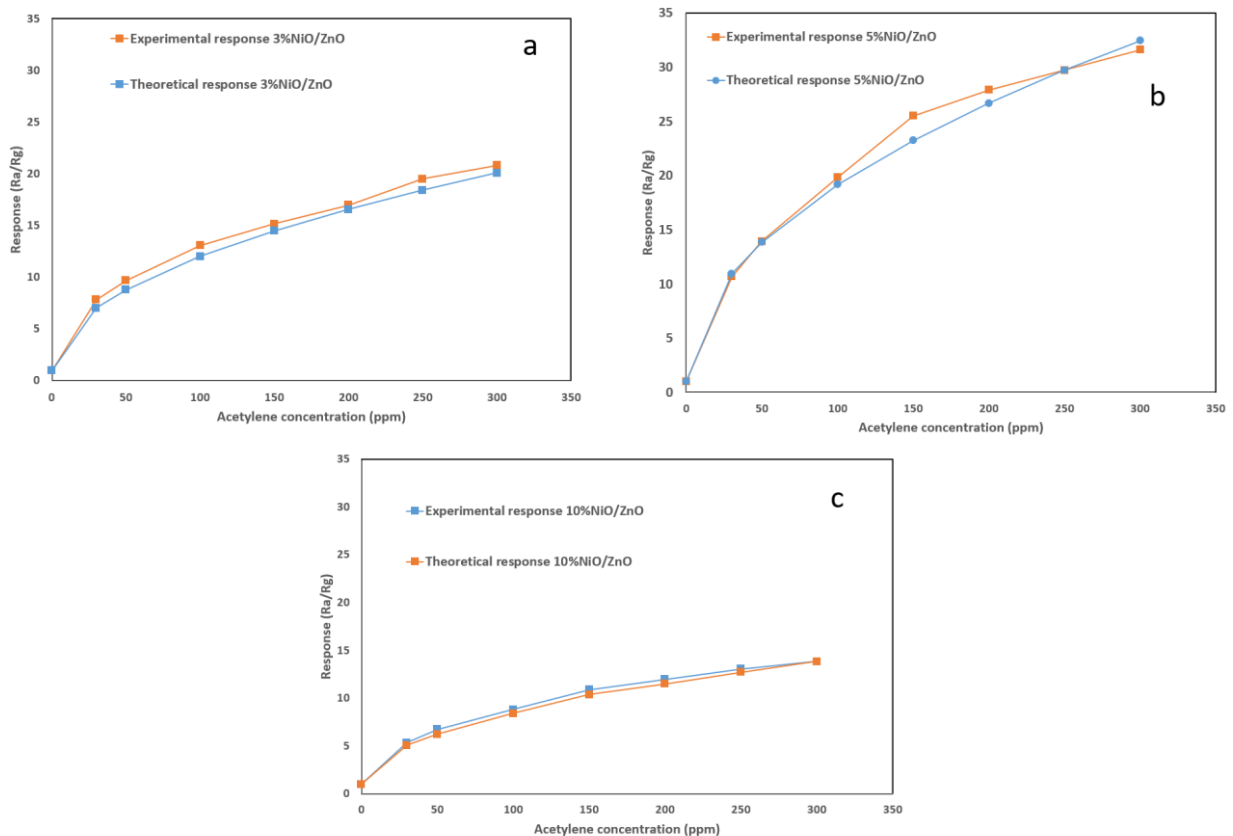


Figure 5. Change in theoretical response (R_a/R_g) for different NiO concentrations (3, 5, 10 % molar ratio) with C_2H_2 concentration at 210 °C compared to experimental results [26]

Table shows the parameters used in the simulation for the three different NiO doping percentages of ZnO.

Parameters used to simulate the C₂H₂ gas sensing reaction model for different NiO-doped ZnO
 ΔG^\ddagger values are at 25 °C and normal pressure

No.	Reaction	ΔG^\ddagger (eV)	A	m	v	k_s (K ⁻¹)	T ₀ (°C)	C (s)
1	[3 % NiO/ZnO – C ₂ H ₂] ^a ↓ [3 % NiO/ZnO – C ₂ H ₂] [‡]	0.142	$3.5 \cdot 10^{-11} \text{ s}^{-1} \cdot \text{K}^{-5}$	5	1/2	0.025	200	165
2	[5 % NiO/ZnO – C ₂ H ₂] ^a ↓ [5 % NiO/ZnO – C ₂ H ₂] [‡]	0.145	$5 \cdot 10^{-11} \text{ s}^{-1} \cdot \text{K}^{-5}$	5	1/2	0.025	200	190
3	[10 % NiO/ZnO – C ₂ H ₂] ^a ↓ [10 % NiO/ZnO – C ₂ H ₂] [‡]	0.152	$2.9 \cdot 10^{-11} \text{ s}^{-1} \cdot \text{K}^{-5}$	5	1/2	0.03	195	150

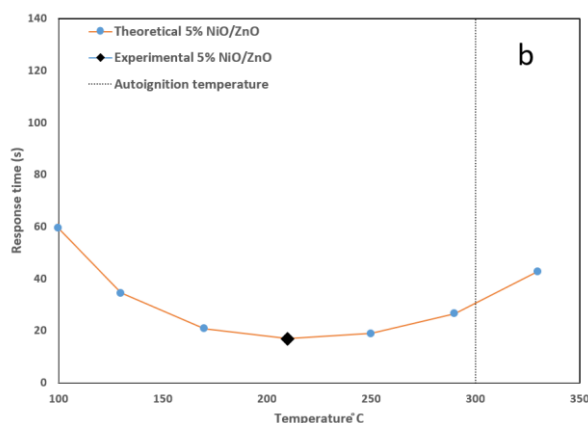
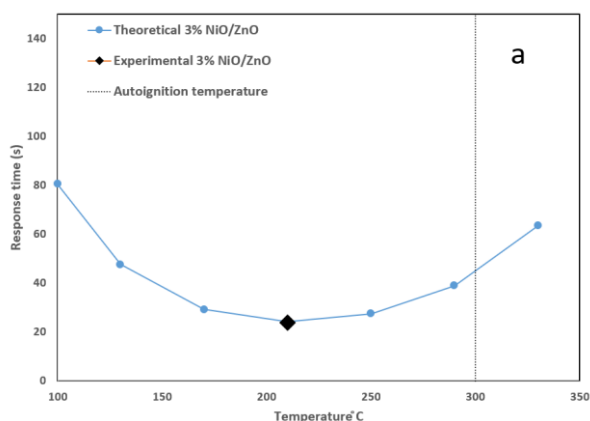
As can be seen in Table, the value of the Gibbs free energy of the transition rises as the doping percentage of NiO increases. However, at temperatures above 210 °C, the opposite trend was observed, as shown in Fig. 3. Parameter A has the highest value for the 5 % NiO doping percentage, which is also typical for the parameter C. This explains the highest sensitivity at 5 % NiO doping percentage. As the doping percentage rises, the reaction rate and sensitivity increase because of the destruction of the lattice periodicity. A further rise in the doping percentage (more than 5 %) will not lead to an increase in two parameters, A and C, since the lattice is already developing a new NiO cubic phase at the spots of higher concentration of NiO.

The value of the temperature exponent ($m = 5$) is the same for all doping percentages. This exponent reflects the reactivity and diffusivity of the C₂H₂ gas. In the original transition state theory, which did not take diffusivity into account, the value of m was equal to 1. The exponent v 's value is 1/2, which was also typical in many doping cases [32].

The remaining parameters, k_s and T_0 , have the same value for 3 % and 5 % NiO doping and slightly change for the 10 % NiO doping. These two parameters represent the decay in the concentration of C₂H₂ gas as it reaches its autoignition temperature. The almost equal values of k_s and T_0 show that the autoignition temperature depends only slightly on the type of sensitive material.

Fig. 6 shows the response time of the three different doping percentages of NiO as described by Eq. (7) compared to the experiment. Fig. 6 shows the reverse to Fig. 4 trend in response time. The response time is at its lowest value when the response is at its highest value. Good agreement is obtained between theory and experiment.

Fig. 7 explains the effect of doping ZnO by NiO. The energy gap is defined as the difference between the Lowest Unoccupied Molecular Orbital (LUMO) and the Highest Occupied Molecular Orbital (HOMO) energies. The experimental energy gap of ZnO is 3.3 eV [33]. This value is close to the present calculated value of 3.117 eV as in Fig. 7. As ZnO is doped with NiO (Fig. 1b), the energy gap decreases to 2.412 eV due to the entrance of NiO energy levels into the energy gap of ZnO and the destruction of the original hexagonal structure. The gap value for NiO is around 3 eV [34]. As the NiO doping increases, the energy gap increases to 3 eV when the cubic NiO structure becomes the dominant constituent.



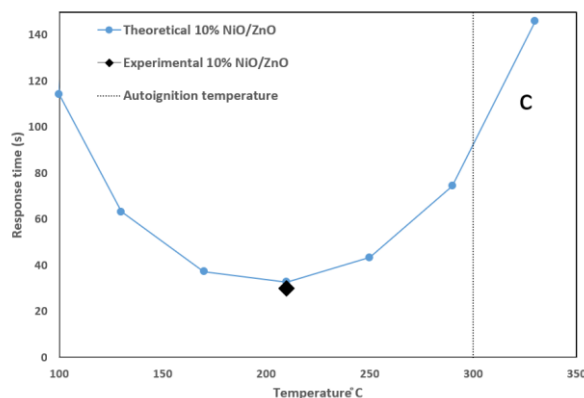


Figure 6. Experimental [26] and theoretical response time for the three cases of 3, 5, and 10 % NiO doped ZnO sensor as a function of temperature. The autoignition temperature of C_2H_2 is shown

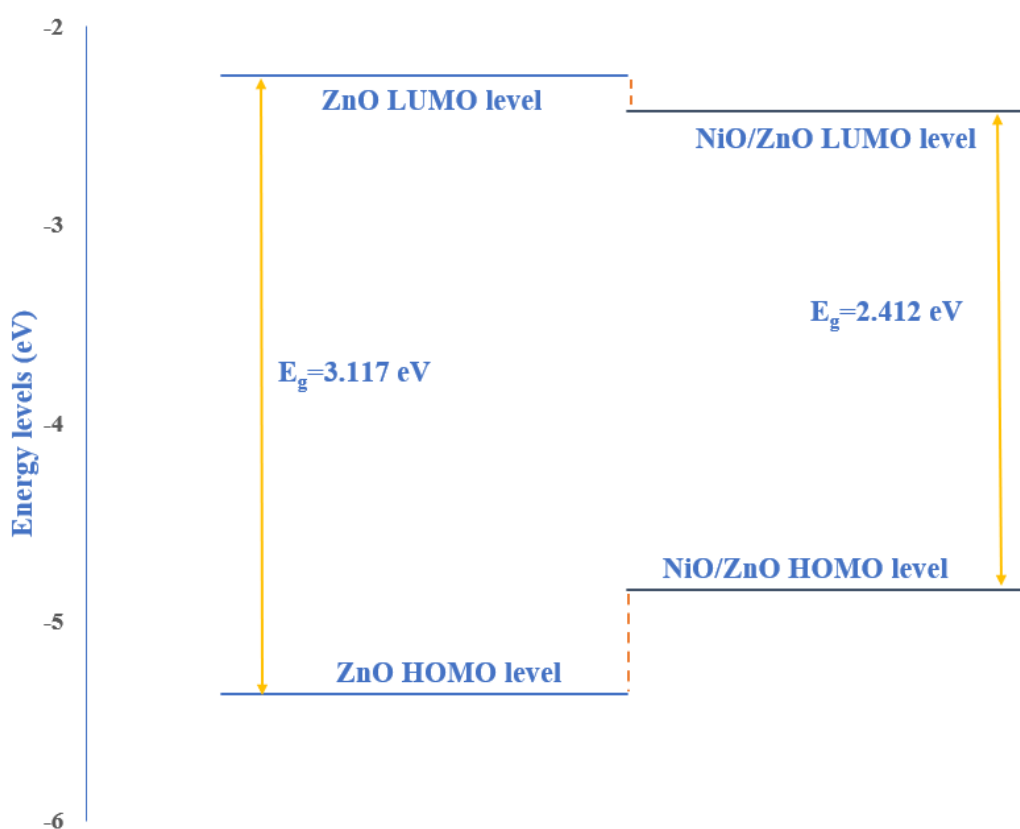


Figure 7. Calculated HOMO and LUMO energy levels for ZnO and NiO/ZnO. The NiO/ZnO corresponds to the optimized $NiZn_{12}O_{13}$ in Fig. 1b

Conclusions

NiO-doped ZnO gas sensor cluster was studied theoretically to detect C_2H_2 gas as a function of temperature and compared with available experimental data. The transition state theory with a modified Evans–Polanyi principle was used to estimate the Gibbs free transition energy for three different doping cases. The theoretical investigation was carried out using mainly two equations, namely Eq. (1) and Eq. (5). As the temperature increases, the C_2H_2 gas burns using the oxygen available in the air, and the concentration of the C_2H_2 gas decreases as described by Eq. (5). At the same time, C_2H_2 gas reacts with the sensing material NiO doped ZnO as described by Eq. (1). The result shows a maximum of sensing temperature, which is below the

autoignition temperature of acetylene of 300 °C. The above described model is in good agreement with the experiment presented in Figs (4–6) for the three different NiO doping concentrations. Figs (4–6) show the theoretical and experimental response results taking into account temperature, concentration, and response time. The motivation for the present study is that the autoignition of C₂H₂ has never been taken into account in gas sensor calculations, and gases can be easily distinguished by their autoignition temperature.

Author Information*

*The authors' names are presented in the following order: First Name, Middle Name and Last Name

Mudar Ahmed Abdulsattar — Chief Scientific Researcher, Head of Solid-State Department, Ministry of Science and Technology, Baghdad, Iraq, *e-mail*: mudarahmed3@yahoo.com; <https://orcid.org/0000-0001-8234-6686>

Conflicts of Interest

The authors declare no conflict of interest.

References

- 1 Karmakar, A., Chakraborty, T., Chakravarty, S., Nath, M., Chakraborty, S., Mitra, S., Sarkar, S., Mandal, G., Banerjee, A., Bhaumick, C., Sutradhar, S. and Bandyopadhyay, A. (2024). The Influence of Nd³⁺ Doping on the Structural, Optical, Magnetic, and Dielectric Characteristics of Nanoscale Hexagonal Wurtzite Type ZnO. *Journal of Magnetism and Magnetic Materials*, 591. <https://doi.org/10.1016/j.jmmm.2024.171728>.
- 2 Wang, J., Zhu, R., Gao, Y., Jia, Y. and Cai, G. (2023). Unveiling the Multistep Electrochemical Desorption Mechanism of Cubic NiO Films for Transmissive-to-Black Electrochromic Energy Storage Devices. *Journal of Physical Chemistry Letters*, 14, 2284–2291. <https://doi.org/10.1021/acs.jpcclett.3c00050>.
- 3 Das, A., Zajac, M., Huang, W.-H., Chen, C.-L., Kandasami, A., Delaunois, F., Noifalisse, X. and Bittencourt, C. (2024). Evolution of Structural Phase Transition from Hexagonal Wurtzite ZnO to Cubic Rocksalt NiO in Ni Doped ZnO Thin Films and Their Electronic Structures. *Physica Scripta*, 99. <https://doi.org/10.1088/1402-4896/ad16b1>.
- 4 Sun, X.W., Liu, Z.J., Chen, Q.F., Chu, Y.D. and Wang, C.W. (2006). Thermal Expansivity and Bulk Modulus of ZnO with NaCl-Type Cubic Structure at High Pressures and Temperatures. *Physics Letters, Section A: General, Atomic and Solid State Physics*, 360, 362–366. <https://doi.org/10.1016/j.physleta.2006.08.045>.
- 5 Lin, L., Liu, T., Miao, B. and Zeng, W. (2013). Hydrothermal Fabrication of Uniform Hexagonal NiO Nanosheets: Structure, Growth and Response. *Materials Letters*, 102–103, 43–46. <https://doi.org/10.1016/j.matlet.2013.03.103>.
- 6 Xu, C., Wei, P., Wei, Z. and Guo, X. (2024). Shear Horizontal Wave in a P-Type Si Substrate Covered with a Piezoelectric Semiconductor n-Type ZnO Layer with Consideration of PN Heterojunction Effects. *Acta Mechanica*, 235, 735–750. <https://doi.org/10.1007/s00707-023-03771-4>.
- 7 Tsay, C.Y., Chen, Y.C., Tsai, H.M. and Lu, F.H. (2023). Photoresponse of Solution-Processed Transparent Heterojunction Ultraviolet Photodetectors Composed of n-Type ZTO and p-Type NiO-Based Semiconductor Thin Films. *Materials Chemistry and Physics*, 295. <https://doi.org/10.1016/j.matchemphys.2022.127143>.
- 8 Chandak, V.S., Kumbhar, M.B. and Kulal, P.M. (2024). Highly Sensitive and Selective Acetone Gas Sensor-Based La-Doped ZnO Nanostructured Thin Film. *Materials Letters*, 357. <https://doi.org/10.1016/j.matlet.2023.135747>.
- 9 Thomas, A., Thirumalaisamy, L., Madanagurusamy, S. and Sivaperuman, K. (2024). Switching the Selectivity of ZnO Thin Films for Ultra-Sensitive Acetaldehyde Gas Sensors through Co Doping. *Sensors and Actuators B: Chemical*, 401. <https://doi.org/10.1016/j.snb.2023.135043>.
- 10 Nagarjuna, Y. and Hsiao, Y.J. (2024). TeO₂ Doped ZnO Nanostructure for the Enhanced NO₂ Gas Sensing on MEMS Sensor Device. *Sensors and Actuators B: Chemical*, 401. <https://doi.org/10.1016/j.snb.2023.134891>.
- 11 Cuong, N.D., Sinh, V.H., Quang, D.T., Hoa, L.T., Tan, V. Van, Mai, H.D., Jeon, K.J., Phuoc, P.H. and Hieu, N. Van. (2024). 3D Porous P-n α-Fe₂O₃/NiO Heteronanostructure for Ultrasensitive H₂S Gas Sensor. *Current Applied Physics*, 59, 153–164. <https://doi.org/10.1016/j.cap.2023.12.019>.
- 12 Shi, C., Yu, L., He, X., Zhang, Y., Liu, J., Li, S., Zhang, C., Cao, L., Nan, N., Du, H. and Yin, M. (2024). Vertically Aligned Mesoporous Ce Doped NiO Nanowalls with Multilevel Gas Channels for High-Performance Acetone Gas Sensors. *Sensors and Actuators B: Chemical*, 401. <https://doi.org/10.1016/j.snb.2023.134888>.
- 13 Pai, S.H.S., Mondal, A., Barathy T, R., Ajitha, B., Samuel E, J.J. and Reddy, Y.A.K. (2024). Effect of Calcination Temperature on NiO for Hydrogen Gas Sensor Performance. *International Journal of Hydrogen Energy*, 50, 928–941. <https://doi.org/10.1016/j.ijhydene.2023.07.345>.
- 14 Abdulsattar, M.A., Abduljalil, H.M. and Abed, H.H. (2023). Reaction Mechanisms of Pristine and Cu-Doped ZnO Clusters with Ethanol Using Evans-Polanyi Principle. *Emerging Materials Research*, 12, 60–67. <https://doi.org/10.1680/jemmr.22.00149>.

- 15 Sameer, A.K., Jasim, M.N. and Hussein, M.T. (2023). Concentration Effect on the Vibrational and Electronic Properties of $\text{MgXZn}_7\text{-XO}_7$ Wurtzoids Nanostructure via DFT. *Digest Journal of Nanomaterials and Biostructures*, 18, 1187–1195. <https://doi.org/10.15251/DJNB.2023.184.1187>.
- 16 Eliche-Quesada, D., Felipe-Sesé, M.A. and Fuentes-Sánchez, M.J. (2021). Biomass Bottom Ash Waste and By-Products of the Acetylene Industry as Raw Materials for Unfired Bricks. *Journal of Building Engineering*, 38. <https://doi.org/10.1016/j.jobbe.2021.102191>.
- 17 Abdulsattar, M.A. and Mahmood, T.H. (2023). Enhancement of SnO_2 Sensitivity to Acetone by Au Loading: An Application of Evans–Polanyi Principle in Gas Sensing. *Optik*, 275, 170604. <https://doi.org/10.1016/j.ijleo.2023.170604>.
- 18 Abdulsattar, M.A. (2023). GaIn_2XO_3 Surface Pyramids Interaction with Formaldehyde: Thermodynamic and Sensing Analysis. *Karbala International Journal of Modern Science*, 9, 8. <https://doi.org/10.33640/2405-609X.3324>.
- 19 Ashiq, M., Shehzad, R.A., Iqbal, J. and Ayub, K. (2024). Sensing Applications of Graphitic Carbon Nitride ($\text{g-C}_3\text{N}_4$) for Sensing SO_2 and SO_3 — A DFT Study. *Physica B: Condensed Matter*, 676. <https://doi.org/10.1016/j.physb.2024.415661>.
- 20 Frisch, M.J., Trucks, G.W., Schlegel, H.B., Scuseria, G.E., Robb, M.A., Cheeseman, J.R., Scalmani, G., Barone, V., Mennucci, B., Petersson, G.A., Nakatsuji, H., Caricato, M., Li, X., Hratchian, H.P., Izmaylov, A.F., Bloino, J., Zheng, G., Sonnenberg, J.L., Hada, M., Ehara, M., Toyota, K., Fukuda, R., Hasegawa, J., Ishida, M., Nakajima, T., Honda, Y., Kitao, O., Nakai, H., Vreven, T., Montgomery, J.A.J., Peralta, J.E., Ogliaro, F., Bearpark, M., Heyd, J.J., Brothers, E., Kudin, K.N., Staroverov, V.N., Kobayashi, R., Normand, J., Raghavachari, K., Rendell, A., Burant, J.C., Iyengar, S.S., Tomasi, J., Cossi, M., Rega, N., Millam, J.M., Klene, M., Knox, J.E., Cross, J.B., Bakken, V., Adamo, C., Jaramillo, J., Gomperts, R., Stratmann, R.E., Yazyev, O., Austin, A.J., Cammi, R., Pomelli, C., Ochterski, J.W., Martin, R.L., Morokuma, K., Zakrzewski, V.G., Voth, G.A., Salvador, P., Dannenberg, J.J., Dapprich, S., Daniels, A.D., Farkas, Ö., Foresman, J.B., Ortiz, J. V., Cioslowski, J. and Fox, D.J. (2013). Gaussian 09, Revision D.01. Gaussian, Inc., Wallingford CT.
- 21 Abdulsattar, M.A. (2024). Effect of Temperature on the Reaction of Pristine and Au-Doped SnO_2 Pyramid Clusters with H_2 : A Transition State Theory Study. *Passer Journal of Basic and Applied Sciences*, 6, 192–197. <https://doi.org/10.24271/PSR.2024.421994.1412>.
- 22 Hussein, M.T. and Abdullah, B.A. (2022). Study The Effect Of Size Variation And Stability On The Electronic And Spectroscopic Properties Of BN Wurtzoids-Diamantane Nanostructure Via Density Functional Theory. AIP Conference Proceedings. <https://doi.org/10.1063/5.0112191>.
- 23 Abdulsattar, M.A., Hussein, M.T. and Kahaly, M.U. (2023). Effect of Reduced Graphene Oxide Hybridization on ZnO Nanoparticles Sensitivity to NO_2 Gas: A DFT Study. *Journal of Ovonic Research*, 19, 153–163. <https://doi.org/10.15251/JOR.2023.192.153>.
- 24 Abdulsattar, M.A. and Al-Bayati, K.H.. (2007). Corrections and Parametrization of Semiempirical Large Unit Cell Method for Covalent Semiconductors. *Physical Review B — Condensed Matter and Materials Physics*, 75, 245201. <https://doi.org/10.1103/PhysRevB.75.245201>.
- 25 Abdulsattar, M.A. (2023). The Reaction of Pristine and Rh-Doped SnO_2 Clusters with Acetone: Application of Evans–Polanyi Principle to Transition State Theory. *Journal of Molecular Modeling*, 29. <https://doi.org/10.1007/s00894-023-05710-5>.
- 26 Zhang, H., Chen, W., Li, Y., Song, Z., Zeng, W., Tang, S., Wang, S. and Zhou, D. (2020). Hierarchical Heterostructures of Nanosheet-Assembled NiO-Modified ZnO Microflowers for High Performance Acetylene Detection. *Ceramics International*, 46, 3574–3581. <https://doi.org/10.1016/j.ceramint.2019.10.075>.
- 27 Lin, Y., Li, C., Wei, W., Li, Y., Wen, S., Sun, D., Chen, Y. and Ruan, S. (2015). A New Type of Acetylene Gas Sensor Based on a Hollow Heterostructure. *RSC Advances*, 5, 61521–61527. <https://doi.org/10.1039/c5ra10327d>.
- 28 Shen, Z., Zhang, X., Ma, X., Chen, Y., Liu, M., Chen, C. and Ruan, S. (2018). Synthesis of Hierarchical 3D Porous ZnO Microspheres Decorated by Ultra-Small Au Nanoparticles and Its Highly Enhanced Acetylene Gas Sensing Ability. *Journal of Alloys and Compounds*, 731, 1029–1036. <https://doi.org/10.1016/j.jallcom.2017.10.156>.
- 29 Iftexhar Uddin, A.S.M., Phan, D.T. and Chung, G.S. (2015). Low Temperature Acetylene Gas Sensor Based on Ag Nanoparticles-Loaded ZnO -Reduced Graphene Oxide Hybrid. *Sensors and Actuators, B: Chemical*, 207, 362–369. <https://doi.org/10.1016/j.snb.2014.10.091>.
- 30 Wang, X., Zhao, M., Liu, F., Jia, J., Li, X. and Cao, L. (2013). C_2H_2 Gas Sensor Based on Ni-Doped ZnO Electrospun Nanofibers. *Ceramics International*, 39, 2883–2887. <https://doi.org/10.1016/j.ceramint.2012.09.062>.
- 31 Qiao, P.Y., Zhang, L.X., Zhu, M.Y., Yin, Y.Y., Zhao, Z.W., Sun, H.N., Dong, J.Y. and Bie, L.J. (2017). Acetylene Sensing Enhancement of Mesoporous ZnO Nanosheets with Morphology and Defect Induced Structural Sensitization. *Sensors and Actuators, B: Chemical*, 250, 189–197. <https://doi.org/10.1016/j.snb.2017.04.158>.
- 32 He, K., Jin, Z., Chu, X., Bi, W., Wang, W., Wang, C. and Liu, S. (2019). Fast Response-Recovery Time toward Acetone by a Sensor Prepared with Pd Doped WO_3 Nanosheets. *RSC Advances*, 9, 28439–28450. <https://doi.org/10.1039/c9ra04429a>.
- 33 Goh, J.H., Tan, K.W., Liow, J.E., Khiew, P.S., Chiu, W.S. and Haw, C.Y. (2024). Modulating Oxygen Vacancy of ZnO for Visible-Light Driven Photocatalytic H_2 Evolution via Facile Gas Treatment Approach. *Materials Science in Semiconductor Processing*, 178. <https://doi.org/10.1016/j.mssp.2024.108445>.
- 34 Hosny, N.M. (2011) Synthesis, Characterization and Optical Band Gap of NiO Nanoparticles Derived from Anthranilic Acid Precursors via a Thermal Decomposition Route. *Polyhedron*, 30, 470–476. <https://doi.org/10.1016/j.poly.2010.11.020>.

Aida S. Rakhimzhanova¹ , Ruslan A. Muzaparov¹ , Irina A. Pustolaikina^{1*} ,
Alfiya F. Kurmanova¹ , Sergey N. Nikolskiy¹ , Darya D. Kapishnikova² ,
Alena L. Stalinskaya³ , Ivan V. Kulakov³ 

¹Department of Physical and Analytical Chemistry, Karaganda Buketov University, Karaganda, Kazakhstan;

²Institute of Chemistry, Saint Petersburg State University, Saint Petersburg, Russia;

³Higher School of Natural Science, University of Tyumen, Tyumen, Russia

(*Corresponding author's e-mail: ipustolaikina@gmail.com)

A Series of Novel Integrastatins Analogues: *In silico* Study of Physicochemical and Bioactivity Parameters

Integrastatins are naturally occurring heterotetracyclic compounds with a broad spectrum of biological activity. A number of new structural analogues of integrastatins **2a-u** have been synthesized using a novel one-step method [1], but a systematic theoretical study of their structural features and biological activity has not been realized. This study aimed to *in silico* investigate physicochemical and bioactivity properties for a series of 21 new synthetic analogues of natural integrastatins. Global chemical reactivity descriptors were assessed using DFT B3LYP 6-311++G(d, p) CPCM (solvent — water) calculations. High ionization potential IP in the range from 5.9 to 7.1 eV and electron affinity EA at the level of 2.1 to 3.2 eV were shown, which together with a sufficiently large energy gap ΔE_{gap} from 3.8 to 4.6 eV indicates the hard nature of the compounds **2a-u**. Antiviral activity and inhibitory potential as CYP2C19 inducers were identified using the PASSOnline resource. According to the results of molecular docking studies Human immunodeficiency virus HIV-1 reverse transcriptase protein (PDB ID: 3V81) and protein of the RNA-dependent RNA polymerase of the SARS-CoV-2 (PDB ID: 7AAP) can serve as a likely biological target for the compounds **2a-u**. Potentially high oral efficacy and a promising safety profile for the therapeutic use were showed using ADMETlab 3.0 online portal. Further experimental *in vitro* and *in vivo* studies of the pharmaceutical potential of compounds **2a-u** is need for more accurate evaluation the assumptions made on the basis of *in silico* approach.

Keywords: integrastatins, *in silico*, molecular docking, computational study, biological activity, ADMET, quantum chemical calculations, DFT, B3LYP, antiviral activity, global chemical reactivity descriptors, HIV-1, SARS-CoV-2.

1 Introduction

Integrastatins A, B are organic heterotetracyclic compounds containing a novel four-6'-ring system with an epoxybenzoxocine moiety (Fig. 1). They have a natural origin and are aromatic ethers, bridged compounds, cyclic ethers, a cyclic ketones, organic heterotetracyclic compounds, polyphenols and primary alcohols with a wide range of biological activity, including antiviral, antioxidant, antitumor, antifungal and antimicrobial properties [2].



Figure 1 Structural formulas of integrastatins

Integrastatin A and integrastatin B were first isolated in 2002 from the ATCC74478 and *Cytospora sp.* fungus, also their inhibitory activity at micromolar concentrations in the strand transfer reaction of recombinant HIV-1 integrase was shown [3]. These compounds immediately emerged as attractive targets for medicinal chemistry due to their antiviral potential, which integrase inhibitors have for the development of HIV

therapy. However, the use of integrastatins obtained by fungal fermentations was limited due to their low content in natural sources and the high cost of the resulting product. Therefore, chemical synthesis as a method that allows obtaining integrastatins in any quantities and with a high degree of purity has received its development. Several research groups have reported different methods of synthesis of the tetracyclic core of integrastatins in the subsequent decades [4–7]. Each of these methods has its own characteristics and advantages, and it should be noted that interest in this type of compounds encourages many chemists to further develop approaches to the synthesis of integrastatins [8–11].

Recent years, the research group of Professor I.V. Kulakov in University of Tyumen (Tyumen, Russia) has developed and repeatedly tested a new method for the one-stage synthesis of structural analogues of the integrastatin tetracyclic core [12–14] (Fig. 2).

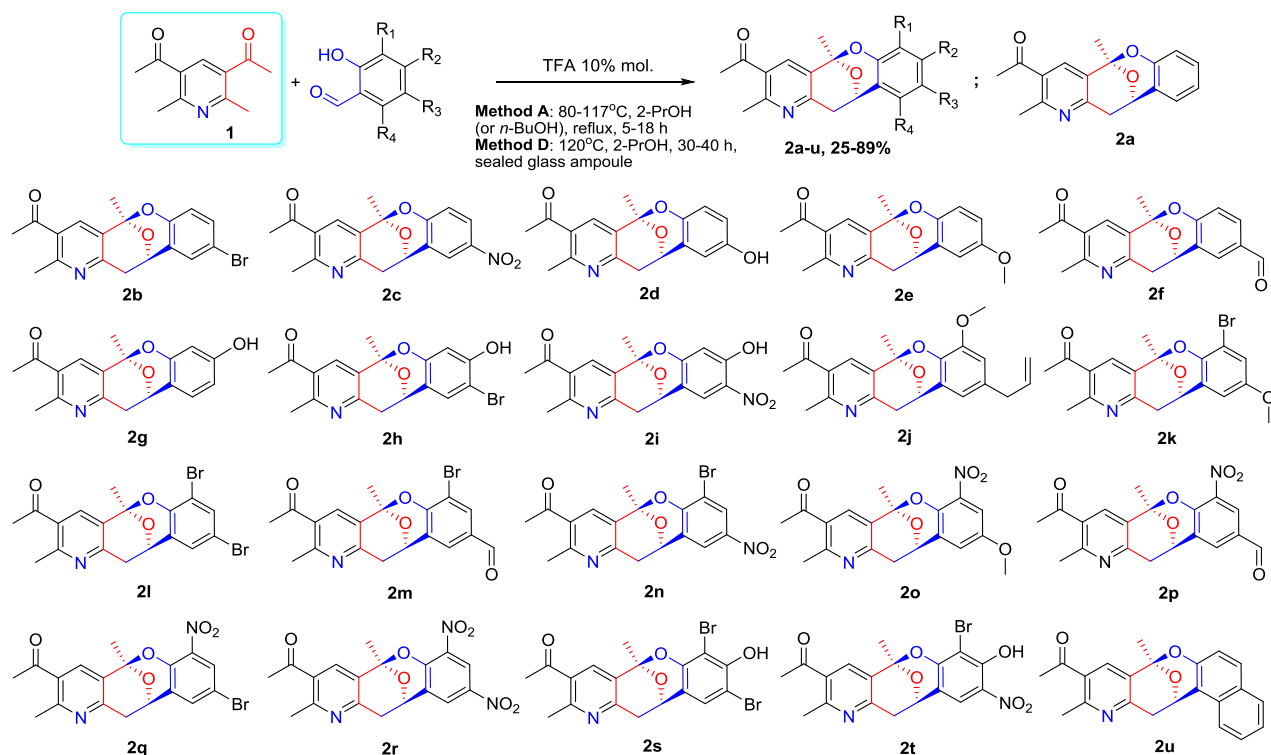


Figure 2. Scheme of synthesis of novel integrastatins analogues **2a-u** [1]

Thus, more than 20 new derivatives of oxocinopyridine **2a-u** with a basic oxocine pharmacophore ring were obtained on the base of 3,5-diacetyl-2,6-dimethylpyridine **1** as a precursor [1]. However, a systematic theoretical and practical study of the features of their structure, physicochemical properties and biological activity has not been implemented.

In silico studies are now widely used in modern chemistry, as they allow one to evaluate the physicochemical properties and pharmaceutical potential of a chemical compound based on knowledge of its structural formula [15]. The term “*in silico*” derives from the analogy with “*in vitro*” and “*in vivo*” experiments and today refers to simulations or analyses performed using computational models or digital tools, typically on a computer [16–18]. *In silico* computational tools cover a wide range of software and platforms designed to model, analyze, and predict biological, chemical, and physical processes, including techniques such as quantum chemical calculations, molecular docking and dynamics simulations, virtual screening, quantitative structure-activity relationship (QSAR) studies, machine learning, and artificial intelligence tools. *In silico* approaches are very valuable for saving time and resources by narrowing hypotheses before performing physical or biological experiments.

The aim of this study was to systematically *in silico* characterize the physicochemical and bioactive parameters of a series of 21 new synthetic analogues of natural integrastatins using quantum chemical calculations, PASS predictions, molecular docking and ADMETlab 3.0 computational tools. This will allow us to better understand the features of their structure and useful properties, as well as assess their pharmaceutical potential.

2 Experimental

2.1. Quantum-Chemical Calculations

Initially, the molecular structures of 21 studied compounds **2a-u** [1] were exported to the 2D ChemDraw editor [19], where they were assigned IUPAC names (Table S1). After that, each molecule was transformed into a 3D model using Chem3D program, its geometry was optimized according to the principle of energy minimization using the MM2 method [20] and saved in a *.mol format. Further calculations were performed using the Gaussian 16 program [21], visualization of input and output data was done using the GaussView 6.0.16 program [22].

To study the structural features and molecular properties of the studied compounds **2a-u**, DFT calculations with full geometry optimization were performed. To ensure a high level of accuracy in combination with optimal calculation time, the B3LYP exchange correlation functional and the 6-311++G(d, p) basis set [23–25] were used. A similar DFT basis set was tested by us earlier and it showed good agreement with the crystallographic data of compound **2a** [13]. Although the studied compounds are not very soluble in water, we used the macroscopic polarizable continuum model CPCM [26] to take into account the effect of the solvent (water) for better evaluation of their biologically active properties in aqueous solutions. In addition, the FREQ keyword was used to verify the truth of the obtained most stable conformation with the minimum energy and the absence of an imaginary frequency characteristic of an unstable transition state.

After optimization, analytical methods were used to construct the HOMO (Highest Occupied Molecular Orbital) and LUMO (Lowest Unoccupied Molecular Orbital) orbitals and estimate their values. Based on the calculated data, the reactivity of the studied compounds was assessed by calculating global chemical reactivity descriptors [27]. Parameters such as ionization potential (*IP*), electron affinity (*EA*), energy gap ΔE_{gap} , absolute electronegativity (χ), molecular hardness (η) and softness (σ), chemical potential (μ), index of electrophilicity (ω) and nucleophilicity (ε) were calculated using the following equations:

$$IP = -E_{\text{HOMO}}, \quad (1) \quad \chi = (IP + EA) / 2, \quad (4) \quad \omega = \mu^2 / 2\eta, \quad (7)$$

$$EA = -E_{\text{LUMO}}, \quad (2) \quad \mu = -(IP + EA) / 2 = -\chi, \quad (5) \quad \sigma = 1 / 2\eta, \quad (8)$$

$$\Delta E_{\text{gap}} = (E_{\text{LUMO}} - E_{\text{HOMO}}), \quad (3) \quad \eta = (IP - EA) / 2, \quad (6) \quad \varepsilon = 1 / \omega, \quad (9)$$

Also, based on the performed DFT calculations, a molecular electrostatic potential (MEP) map was constructed and analyzed to study the electrophilic and nucleophilic regions in molecules **2a-u**.

2.2. PASS Predictions

The predictive results of the PASS analysis were assessed for the test compounds **2a-u** via the PASS online platform available at <http://way2drug.com/PassOnline/predict.php>. This platform was developed by scientists from the Institute of Biomedical Chemistry (Moscow, Russia) and is based on a comprehensive analysis of a large data set covering chemical structures and their corresponding biological activity [28]. Predictive outputs from PASS were reported as Pa and Pi probability scores. The Pa or “activity probability” score takes values between 0 and 1 and estimates the probability that the compound under study belongs to the subclass of active compounds (resembling the molecular structures most typical of the “active” subclass of compounds in the PASS training set). The Pi score, or “inactive probability”, ranges from 0 to 1 and estimates the probability that the compound under study belongs to the inactive subclass of compounds (resembling the structures of molecules most typical of the “inactive” subclass in the PASS training set). In the context of drug discovery or virtual screening, researchers may set a threshold, such as 0.5 or higher, and consider compounds with a probability score equal to or greater than this threshold as potentially active [29–30]. However, it is important to emphasize that this threshold is not rigid and can be adapted according to the specific objectives of the study, reflecting the risk tolerance and scientific objectives of researchers.

2.3. Molecular Docking

Taking into account the PASS Predictions data, a molecular docking study was performed to evaluate the antiviral inhibitory potential of test compounds **2a-u** against HIV-1 and COVID-19 virus proteins, as well as the effect on the CYP2C19 enzyme. The docking procedure was carried out using AutoDock Vina and AutoDock MGL Tools 1.5.7 [31, 32]. Protein targets were downloaded from the Protein Data Bank (<https://www.rcsb.org>) [33]. The human immunodeficiency virus HIV-1 reverse transcriptase protein (PDB ID: **3V81**) [34], the RNA-dependent RNA polymerase protein of the severe acute respiratory syndrome virus

SARS-CoV-2 (PDB ID: **7AAP**) [35], and the Human Microsomal Cytochrome P450 protein (PDB ID: **4GQS**) [36] as a CYP2C19 inducer were taken as targets. The preparation of the molecular structures of the proteins included the steps of removing native ligands and water molecules, protonation, and creating a binding site. The position of the binding site was determined based on PDB data, and the following grid coordinates of the receptor active site were used: ($x = 40.622$, $y = 54.348$, $z = 48.272$) for the structure of HIV-1 reverse transcriptase (PDB ID: **3V81**), ($x = 98.598$, $y = 95.084$, $z = 104.491$) for the structure of SARS-CoV-2 RNA-dependent RNA polymerase (PDB ID: **7AAP**) and ($x = -76.892$, $y = 17.61$, $z = -45.518$) for the Human Microsomal Cytochrome P450 protein (PDB ID: **4GQS**).

MM2 optimized geometry of the compounds **2a-u** was used as the initial geometry of the ligands. Based on the docking results, a comparative analysis of the binding affinity and intermolecular interactions between the studied compounds **2a-u** and the proteins was performed. The study of non-covalent interactions between proteins and ligands was performed using the BIOVIA Discovery Studio Visualizer 2017 program [37].

2.4. ADMET Properties

ADMET (Absorption, Distribution, Metabolism, Excretion, and Toxicity) properties of chemical compounds are key pharmacokinetic and pharmacodynamic characteristics of drugs that influence their therapeutic potential. These properties play an important role in the drug development and safety evaluation process as they allow one to study how potential drug candidates will behave in the human body, assessing their absorption into the bloodstream, distribution to target tissues, metabolism by enzymes, elimination from the body and any potential toxicity issues [38, 39]. The ADMET criteria are based on the understanding that compounds that do not meet established thresholds may exhibit problems with membrane permeability, oral absorption, and pharmacokinetic characteristics. Thus, ADMET studies allow testing of the interaction of a compound with biological systems and guide decision-making in the drug development process.

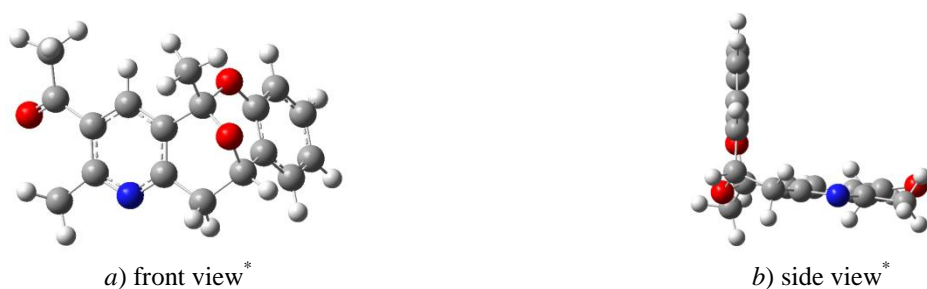
ADMET profiles of the compounds **2a**, **2r** and **2u** were assessed using the ADMETlab 3.0 comprehensive online tool (<https://admetlab3.scbdd.com/>) [40]. The drug-likeness of these compounds was assessed using Lipinski's rule of 5 [41], which predicts that molecules exceeding thresholds of five hydrogen bond donors, ten hydrogen bond acceptors, a molecular weight greater than 500 Da, and an estimated LogP greater than five are likely to exhibit poor absorption or penetration [42]. As a result, compounds that do not meet these requirements are generally considered unsuitable for oral bioavailability as pharmaceuticals [43].

3 Results and Discussion

3.1. Quantum — Chemical Calculations

The geometry optimization procedure of the studied compounds **2a-u** and evaluation of their calculated quantum-chemical parameters was carried out by the DFT B3LYP 6-311++G(d, p) CPCM (solvent — water) method using the Gaussian 16 program.

Quantum chemical geometry optimization procedure involves the automatic search for the most stable and energetically favorable conformation of a molecule by minimizing its potential energy. The resulting geometry of the molecule corresponds to its most energetically stable stationary state, which plays an important role in determining its physicochemical and biological properties, as well as its reactivity. Figure S2 shows the obtained optimized geometries of the studied molecules **2a-u**, which have a complex structure due to the presence of an oxocine ring in the center of the molecule, conjugated on one side with a benzene ring, and on the other side with a heterocyclic nitrogen-containing pyridine ring. The inclusion of various substituents ($-\text{OH}$, $-\text{Br}$, $-\text{NO}_2$, $-\text{OCH}_3$, $-\text{CHO}$, $-\text{CH}_2\text{CHCH}_2$, $-\text{C}_6\text{H}_4-$) into various positions of the side benzene ring allows modeling the physicochemical and biologically active properties of the molecules under study. The non-planar structure of the studied compounds is due, first of all, to the chair-shaped structure of the central epoxybenzo[7,8]oxocine fragment. The main “kink” of the molecules under study occurs in the oxocinic ring, which, due to its structural features, orients the two parts of the molecule almost perpendicular to each other (Fig. 3).



Note: *Gray spheres represent carbon atoms (C), white spheres represent hydrogen atoms (H), red spheres represent oxygen atoms (O), blue spheres represent nitrogen atoms (N).

Figure 3. Optimized geometry of **2a** molecule

The analysis of the frontier orbitals of the studied molecules was performed (Table S3, Figure 4) in order to assess global chemical reactivity descriptors of compounds **2a-u**.

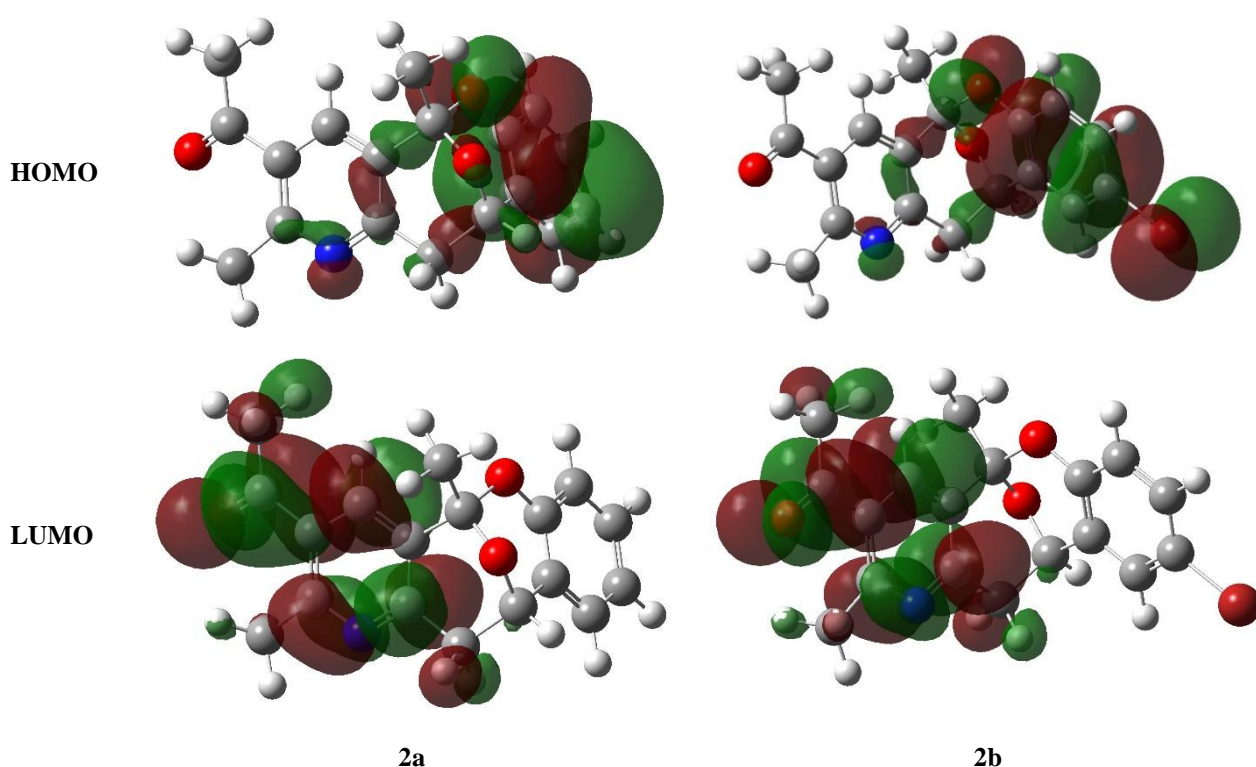


Figure 4. HOMO-LUMO diagrams for **2a** and **2b** molecules

As can be seen from the diagrams in Figure 4, the HOMO and LUMO orbitals are separated in space and localized in different parts of the molecules **2a-u**. The HOMO is mainly distributed over the epoxybenzo[7,8]oxocine fragment and the side substituent of the benzene ring, whereas the LUMO is delocalized over the acetylpyridine fragment. This separation in the space of HOMO and LUMO orbitals indicates the separation of nucleophilic and electrophilic centers of the studied molecules **2a-u**.

Based on the characteristics of HOMO and LUMO orbitals, global chemical reactivity descriptors were estimated, such as: ionization potential (IP), electron affinity (EA), energy gap ΔE_{gap} , molecular hardness (η) and softness (σ), absolute electronegativity (χ) and chemical potential (μ), electrophilicity (ω) and nucleophilicity (ϵ) indexes (Table 1).

Table 1

Global chemical reactivity descriptors of the studied compounds

Compound	Parameter								
	IP	EA	ΔE_{gap}	η	σ	χ	μ	ω	ε
2a	6.533185	2.138272	4.394913214	2.197457	0.227536	4.335728	-4.33573	4.277341	0.23379
2b	6.499987	2.180994	4.318993408	2.159497	0.231535	4.34049	-4.34049	4.362094	0.229248
2c	7.06925	3.003866	4.06538316	2.032692	0.245979	5.036558	-5.03656	6.239736	0.160263
2d	6.066782	2.158408	3.908373382	1.954187	0.255861	4.112595	-4.11259	4.327488	0.231081
2e	5.988957	2.138	3.850957328	1.925479	0.259676	4.063478	-4.06348	4.287728	0.233224
2f	6.835504	2.201402	4.63410142	2.317051	0.215792	4.518453	-4.51845	4.405691	0.226979
2g	6.328555	2.135279	4.19327674	2.096638	0.238477	4.231917	-4.23192	4.270913	0.234142
2h	6.362842	2.146163	4.216678544	2.108339	0.237153	4.254502	-4.2545	4.292666	0.232955
2i	6.956594	2.860734	4.095859928	2.04793	0.244149	4.908664	-4.90866	5.882766	0.169988
2j	6.041747	2.135006	3.906740698	1.95337	0.255968	4.088377	-4.08838	4.278458	0.233729
2k	6.142974	2.155959	3.987014328	1.993507	0.250814	4.149466	-4.14947	4.318538	0.23156
2l	6.612642	2.178	4.434641858	2.217321	0.225497	4.395321	-4.39532	4.35635	0.22955
2m	6.919859	2.272152	4.64770712	2.323854	0.21516	4.596005	-4.59601	4.544879	0.220028
2n	7.106257	3.108902	3.99735466	1.998677	0.250165	5.10758	-5.10758	6.526159	0.153229
2o	6.451823	2.971485	3.48033806	1.740169	0.287328	4.711654	-4.71165	6.378599	0.156774
2p	7.210205	3.067813	4.142391422	2.071196	0.241406	5.139009	-5.13901	6.375403	0.156853
2q	6.904076	3.077881	3.826194954	1.913097	0.261356	4.990979	-4.99098	6.510351	0.153602
2r	7.309254	3.244415	4.064838932	2.032419	0.246012	5.276835	-5.27683	6.850206	0.145981
2s	6.511416	2.169293	4.342123098	2.171062	0.230302	4.340354	-4.34035	4.338586	0.23049
2t	7.071699	2.944001	4.127697266	2.063849	0.242266	5.00785	-5.00785	6.075679	0.164591
2u	6.136987	2.144258	3.992728722	1.996364	0.250455	4.140623	-4.14062	4.293995	0.232883

Note: IP—ionization potential (eV); EA — electron affinity (eV); ΔE_{gap} — frontier molecular orbitals energy gap (eV); η — chemical hardness (eV); σ — chemical softness (eV^{-1}); χ — electronegativity (eV); μ — chemical potential (eV); ω — electrophilicity (eV); ε — nucleophilicity (eV^{-1}).

The global descriptors presented in Table 1 define the chemical reactivity of molecules **2a-u** as a whole. Thus, the ionization potential IP characterizes the ability of a molecule to give up an electron, and the lower it is, the easier the molecule gives up an electron, exhibiting reducing properties. All the studied molecules **2a-u** have a fairly high ionization potential, from 5.9 to 7.1 eV, which indicates their low reducing properties. Electron affinity characterizes the oxidative properties of molecules, and the higher it is, the higher the oxidation potential of the compound. The electron affinity EA varies from 2.1 to 3.2 eV for the studied compounds **2a-u**, which indicates their low oxidizing ability. Large energy gap ΔE_{gap} between HOMO and LUMO orbitals characterizes the high chemical stability of the compound. The energy gap ΔE_{gap} ranges from 3.8 to 4.6 eV for **2a-u** molecules, which indicates their chemical stability. The chemical hardness η of a molecule is determined by its resistance to deformation under the influence of an external electric field and the effect of chemical reactions. An increase in molecular hardness is associated with an increase in stability and a decrease in reactivity. A hardness compound has a large HOMO – LUMO gap, so the molecule with the smallest HOMO gap and LUMO has the highest reactivity. A high value of chemical softness σ indicates high polarizability of the molecule. A chemical compound is considered hard if the energy gap between HOMO and LUMO exceeds 1 eV. From the data presented in Table 3 it is evident that the hardness of the studied molecules **2a-u** varies from 1.7 to 2.3 eV, which, together with a fairly large energy gap from 3.8 to 4.6 eV indicates the hardness nature of the compounds. At the same time, the low softness value of about 0.2 eV indicates the average hardness of the compounds **2a-u**. Absolute electronegativity χ is defined by Mulliken as the half-sum of the first ionization potential and the electron affinity $\chi = 0.5(IP + EA)$. The electronegativity for molecules **2a-u** lies in the range of 4.0–5.1 eV. The electron chemical potential is electronegativity with the opposite sign, for the studied compounds **2a-u** the chemical potential μ has negative values in the range from -4.1 to -5.2 eV. The value of the electrophilicity index ω lies in the range of 4.1–6.8 eV, which indicates the tendency of the molecules **2a-u** to accept electrons. This is also confirmed by the low values of the nucleophilicity index ε in the range of 0.1–0.2 eV^{-1} .

Molecular electrostatic potential (MEP) analysis was applied to investigate the electrophilic and nucleophilic sites in the molecules **2a-u** (Figure S4). On the MEP surface, the most favorable nucleophilic

center, as expected, is located on the carbonyl oxygen atom, while other negative electrostatic potential sites are located on the remaining oxygen and nitrogen atoms. The hydrogen atom of pyridine is one of the most electrophilic regions of **2a-u** (Fig. 5).

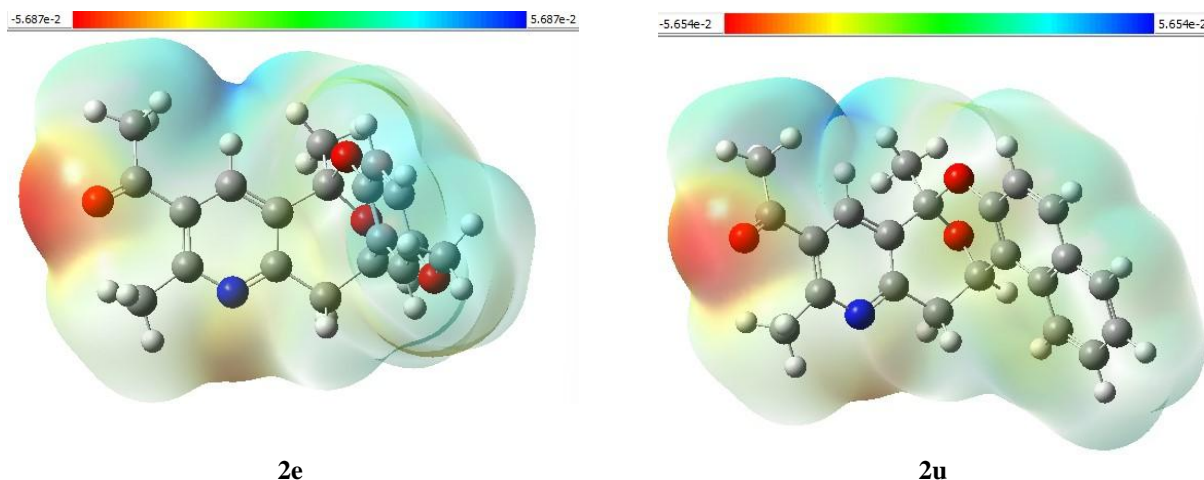


Figure 5 Map of electrostatic potentials for **7e** and **7u** molecules

Thus, the applied complex quantum-chemical approach contributed to a deeper understanding of the electronic structure and molecular properties of the studied compounds **2a-u**, as well as to the identification of their reaction centers and the assessment of the chemical potential for subsequent *in silico* studies of biological activity.

3.2. PASS (Prediction of Activity Spectra for Substances) Predictions

The PASS Online Internet resource (<https://www.way2drug.com/passonline/>) was used to assess the potential biological activity of the studied compounds **2a-u**. This online tool allows predicting more than 4000 types of biological activity in the form of Pa (the probability of being active) and Pi (the probability of being inactive) values based on the structural formula of a chemical compounds. Thus, a high probability of antiviral and antibacterial activity of the studied compounds **2a-u** was established, and it was also shown that all the studied molecules can be CYP2C19 inducers and proton pump inhibitors, and most are histidine kinase inhibitors. The corresponding Pa and Pi values for the studied compounds **2a-u** are presented in Table 2.

Table 2

PASS prediction data

Compound	Antiviral		CYP2C19 inducer		General pump inhibitor		Histidine kinase inhibitor		Antibacterial	
	Pa	Pi	Pa	Pi	Pa	Pi	Pa	Pi	Pa	Pi
2a	0.543	0,013	0,610	0,005	0.563	0.035	0.528	0.024	0.278	0.068
2b	0.492	0.027	0.555	0,008	0.410	0.127	0.425	0.045	0.293	0.063
2c	0.483	0.031	0.547	0,008	0.540	0.043	0.411	0.049	0.322	0.052
2d	0,520	0,018	0.564	0,007	0.616	0,021	0.658	0,011	0.328	0,050
2e	0.529	0,016	0,560	0,008	0.594	0.026	0.469	0.034	0.251	0.082
2f	0.499	0.025	0,570	0,007	0.435	0.103	0.489	0,030	0.376	0.036
2g	0.531	0,016	0.575	0,007	0.592	0.027	0.684	0,009	0.344	0.045
2h	0.491	0.028	0.540	0,009	0.441	0.099	0.559	0,020	0.378	0.036
2i	0.482	0.031	0.532	0,009	0.514	0.053	0.545	0.022	0.399	0,030
2j	0.492	0.027	0.528	0,009	0.477	0.073	0.260	0.139	0.337	0.047
2k	0.463	0,041	0.535	0,009	0.405	0.132	0.299	0.103	0.227	0.097
2l	0.457	0.044	0.555	0,008	–	–	0.312	0.094	0.347	0.044
2m	0.427	0.065	0.541	0,009	–	–	0.338	0.078	0.387	0.033
2n	0.417	0.074	0.521	0,010	0.344	0.207	0.270	0.127	0.307	0.057
2o	0.454	0.046	0.527	0,010	0.475	0.074	0.288	0,111	0.205	0.113
2p	0.417	0.074	0.533	0,009	–	–	0.327	0.085	0.339	0.046

Continuation of Table 2

Compound	Antiviral		CYP2C19 inducer		General pump inhibitor		Histidine kinase inhibitor		Antibacterial	
	Pa	Pi	Pa	Pi	Pa	Pi	Pa	Pi	Pa	Pi
2q	0.417	0.074	0.521	0,010	–	–	0.270	0.127	0.231	0.094
2r	0.447	0,050	0.547	0,008	0.410	0.127	0.301	0.102	0.242	0.087
2s	0.452	0.047	0,540	0,009	0.353	0.195	0.416	0.047	0.346	0.044
2t	0.416	0.075	0.508	0,011	0.372	0,170	0.368	0.064	0.278	0.068
2u	0.523	0,018	0.593	0.006	0.598	0.025	0.532	0.024	0.249	0.084

Note: Pa is the probability of being active; Pi is the probability of being inactive.

The data presented in Table 2 show that the highest Pa values of compound **2a-u** were in the region of antiviral activity (Pa~0.416–0.523). Antiviral activity refers to the ability of a substance or compound to inhibit the reproduction of viruses or destroy viral particles. Today there are many viruses that are dangerous to humans, including the human immunodeficiency virus (HIV-1), which destroys the immune system and makes a person vulnerable to various infections and diseases, and the coronavirus, which causes COVID-19 and can lead to serious complications and death, especially in people predisposed to this disease. These HIV-1 and COVID-19 viruses pose a significant threat to human health and require special attention and precautions to prevent their spread.

Also, compounds **2a-u** have demonstrated relatively high Pa values as CYP2C19 inducers (Pa~0.508–0.610). CYP2C19 inducers are substances that increase the activity of the CYP2C19 enzyme, which belongs to the cytochrome P450 family. This enzyme plays an important role in the metabolism of many drugs, including some proton pump inhibitors, antiepileptic drugs, and anticoagulants. Examples of drugs that induce CYP2C19 include: rifampin, an antibiotic used to treat tuberculosis; phenobarbital, an anticonvulsant used to treat various types of epilepsy; carbamazepine, an anticonvulsant used to treat various types of epilepsy and pain associated with trigeminal neuralgia; primidone, an anticonvulsant used to treat generalized, psychomotor, and focal epileptic seizures. Induction of CYP2C19 may affect drug metabolism, which may require dose adjustment or selection of alternative drugs.

Most compounds **2a-u** with a probability of Pa~0.344–0.598 can exhibit biological activity as Proton Pump Inhibitors (PPIs), a class of drugs that reduce the production of gastric acid. They act by irreversibly blocking the enzyme H⁺/K⁺-ATPase (Hydrogen/Potassium ATPase), which controls acid production in the parietal cells of the stomach wall. This enzyme is also known as the proton pump. PPIs are widely used to treat conditions such as: chronic gastroesophageal reflux disease (GERD), duodenal and gastric ulcers, erosive esophagitis, malignant necrotizing pancreatitis, Zollinger-Ellison syndrome. Examples of PPI drugs include omeprazole (Prilosec), lansoprazole (Prevacid), esomeprazole (Nexium) and pantoprazole (Protonix).

All studied compounds **2a-u** may also exhibit biological activity with Pa~0.270–0.684 as histidine kinase inhibitors (HKIs), a class of drugs that block the activity of histidine kinases. Histidine kinases are enzymes that play an important role in cell signaling, especially in bacteria. They are involved in so-called two-component signaling systems that help bacteria adapt to different environmental conditions. HKIs can be used to develop new antibacterial drugs, as they can block multiple regulatory networks associated with pathogenicity and antibiotic resistance. These inhibitors may be useful in the fight against microbial infections, especially in conditions where bacteria are becoming resistant to traditional antibiotics.

Compounds **2a-u** are predicted to also exhibit weak antibacterial activity with Pa~0.205–0.399, which refers to the ability of a substance to inhibit the growth of or kill bacteria. Substances with antibacterial activity are used to treat and prevent bacterial infections. Some of the most common and dangerous bacterial infections in humans are: tuberculosis — caused by the bacterium *Mycobacterium tuberculosis* (Koch's bacillus) and can affect the lungs and other organs; anthrax — caused by the gram-positive bacterium *Bacillus anthracis* and can lead to serious infections of the skin, lungs, and intestines; salmonellosis — caused by the bacterium *Salmonella* and is often associated with contaminated food; sepsis — a serious blood infection caused by various bacteria, such as *Staphylococcus aureus* and *Escherichia coli*; meningitis — an inflammation of the meninges caused by bacteria such as *Neisseria meningitidis* and *Streptococcus pneumoniae*; cholerae — caused by the bacterium *Vibrio cholerae* and results in severe dehydration and diarrhea; pneumonia — inflammation of the lungs caused by various bacteria such as *Streptococcus pneumoniae* and *Mycoplasma pneumoniae*; gonorrhoea — a sexually transmitted infection caused by the bacterium *Neisseria gonorrhoeae*; syphilis — a chronic disease caused by the bacterium *Treponema pallidum*. These infections

can be very serious and require treatment with antibacterial drugs. Antibacterial substances can work in a variety of ways, including inhibiting bacterial cell wall synthesis, suppressing protein synthesis, disrupting the cell membrane, or inhibiting DNA synthesis. Some plants and natural compounds, such as honey and garlic extracts, also have antibacterial activity. Antibacterial substances are widely used to treat infections caused by bacteria, such as pneumonia, urinary tract and skin infections. Antibacterial activity plays an important role in medicine and helps prevent and treat infectious diseases.

In summary, the evaluation of the potential biological activity of the studied compounds **2a-u** using the PASS Online resource revealed their antiviral and inhibitory potential as CYP2C19 inducers. These types of biological activities of compounds **2a-u** were further investigated using molecular docking method. Antiviral activity was assessed against such relevant diseases as human immunodeficiency virus (HIV-1) and COVID-19, caused by infection with severe acute respiratory syndrome coronavirus 2, also called SARS-CoV-2.

3.3. Molecular Docking

The molecular docking method using the AutoDock Vina program was applied for a more thorough assessment of the antiviral and inhibitory potential as CYP2C19 inducers of the studied molecules **2a-u**. The protein structure of human immunodeficiency virus HIV-1 reverse transcriptase protein (PDB ID: **3V81**), SARS-CoV-2 RNA-dependent RNA polymerase (PDB ID: **7AAP**) and the Human Microsomal Cytochrome P450 protein (PDB ID: **4GQS**) [36] as a CYP2C19 inducer were chosen as the target proteins. Well-known drugs were taken as reference drugs. Nevirapine was taken as an antiretroviral drug used to treat and prevent HIV-1 infection, Favipiravir was taken as an antiviral drug that inhibits RNA-dependent RNA polymerase of viruses (including COVID-19), preventing their replication, and Rifampin was taken as an antibacterial drug — CYP2C19 inducer used to treat tuberculosis and other bacterial infections. Table 3 presents the binding affinity of the studied compounds **2a-u** with target proteins obtained as a result of molecular docking procedure.

Table 3

Results of Molecular Docking of **2a-u** compounds with targets proteins

No.	Compound	Binding affinity, kcal/mol		
		HIV-1 protein (3V81)	SARS-CoV-2 protein (7AAP)	CYP2C19 inducer (4GQS)
<i>Reference drug</i>				
1	Nevirapine	-9.0		
2	Favipiravir		-7.0	
3	Rifampin			-7.8
<i>Ligand</i>				
1	2a	-9.7	-7.3	-8.9
2	2b	-9.0	-7.3	-7.1
3	2c	-9.8	-7.3	-7.9
4	2d	-9.3	-7.6	-9.3
5	2e	-8.9	-7.7	-6.9
6	2f	-9.3	-7.7	-8.5
7	2g	-9.1	-7.6	-7.4
8	2h	-9.0	-7.6	-7.1
9	2i	-9.6	-7.6	-7.7
10	2j	-8.9	-7.9	-6.9
11	2k	-8.8	-7.6	-7.1
12	2l	-9.0	-7.3	-7.3
13	2m	-9.0	-7.6	-7.6
14	2n	-9.0	-7.8	-7.4
15	2o	-9.0	-7.1	-6.8
16	2p	-9.1	-7.7	-7.0
17	2q	-9.1	-7.5	-6.8
18	2r	-9.2	-7.8	-9.4
19	2s	-9.2	-6.7	-7.2
20	2t	-9.2	-7.7	-7.3
21	2u	-10.2	-9.3	-8.0

As can be seen in Table 3, all tested compounds **2a-u** demonstrated high binding affinity, even compared to the reference drugs. Compound **2u** showed the highest antiviral potential against the HIV-1 virus (Binding Affinity = -10.2 kcal/mol) and against the SARS-CoV-2 virus (Binding Affinity = -9.3 kcal/mol). The binding affinity of **2u** compound to 3V81 and 7AAP receptors is higher than that of the reference drugs Nevirapine (Binding affinity = -9.0 kcal/mol) and Favipiravir (Binding Affinity = -7.0 kcal/mol), respectively. Ligand **2r** was found to be the best CYP2C19 inducer with a binding affinity of -9.4 kcal/mol compared to -7.8 kcal/mol for the reference drug Rifampicin.

Intermolecular interactions predominantly determine the binding efficiency of the top compounds **2u** and **2r** to the **3V81**, **7AAP** and **4GQS** receptors, so their analysis was performed (Figures 6–8, Table 4).

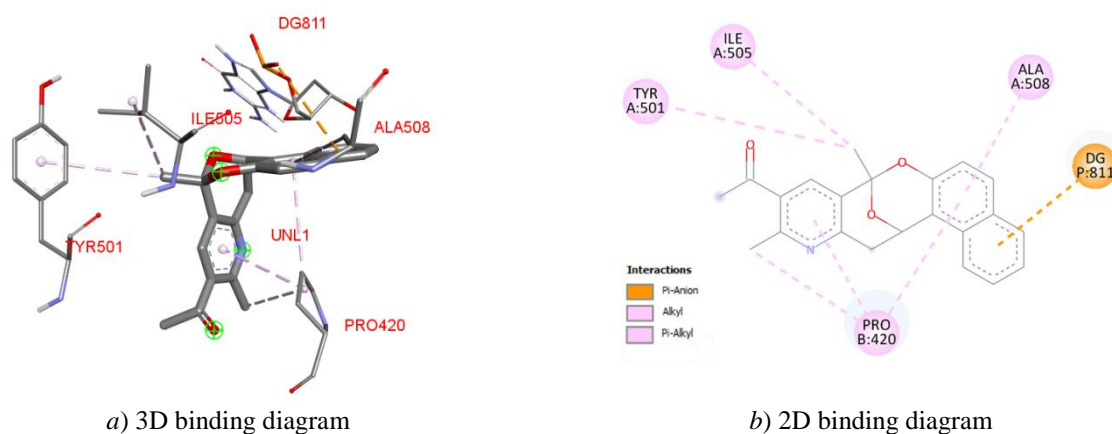


Figure 6. Visualization of **3V81** protein — **2u** ligand interactions



Figure 7. Visualization of **7AAP** protein — **2u** ligand interactions

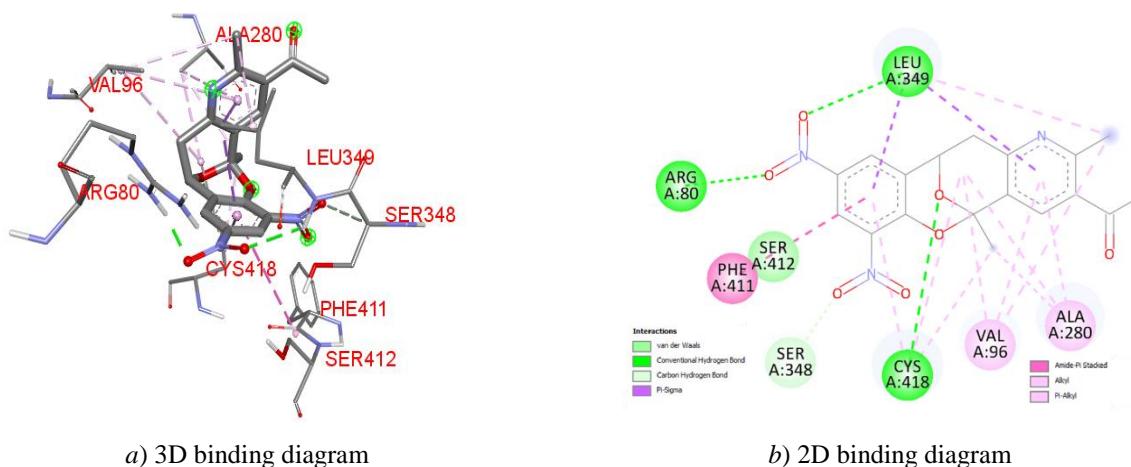


Figure 8. Visualization of **4GQS** protein– **2r** ligand interactions

Protein-Ligand Interactions

Ligand	Protein	Conventional Hydrogen Bond	Pi-Anion	Pi-Pi T-shaped	Alkyl	Pi-Alkyl
2u	3V81	–	DG811	–	TYR501	ILE505, PRO420, ALA508
2u	7AAP	ASN39	LYS50, ILE37	PHE35	–	ASP221
2r	4GQS	LEU359, CYS418, ARG80	SER348	SER412	VAL96, ALA280	PHE411

As can be seen in Figures 6–8 and Table 4, the most common types of intermolecular protein-ligand interactions are hydrogen and π -bonds. In particular, the ligand **2u** in complex with the protein **3V81** has demonstrated a distinct Pi-Anion interaction with DG811, which was facilitated by the conjugated benzene group on the ligand, indicating a unique binding orientation. Ligand **2u** also demonstrated Pi-Alkyl interactions with ILE505, PRO420, and ALA508 amino acids, but through different functional groups, suggesting alternative binding modes that may affect its potency and specificity (Table S5). Ligand **2u** in the complex with the second viral protein 7AAP showed hydrogen bonding with ASN39, as well as Pi-Anion binding with LYS50 and ILE37, Pi-Pi T-shaped binding with PHE35 and Pi-alkyl binding with ASP221 amino acids (Table S6).

Also ligand **2r** in the complex with the CYP2C19 inducer protein **4GQS** showed formation of three hydrogen bonds with LEU359, CYS418 and ARG80 amino acids, as well as Pi-Anion bonding with SER348, Pi-Pi T-shaped binding to SER412, Pi-Alkyl binding to PHE411, and Alkyl binding to VAL96 and ALA280 amino acids (Table S7). In general, hydrogen bonds and pi-bonds predominate in intermolecular interactions of the top **2r** and **2u** compounds with the target proteins, which directly affect the stability and specificity of the resulting ligand-protein complexes, influencing the overall docking score and potential biological activity of the compounds.

Thus, the molecular docking study showed the high antiviral potential of all 21 studied compounds against the HIV-1 and SARS-CoV-2 viruses. Ligand **2u** showed the best binding to both viral proteins. Human immunodeficiency virus HIV-1 reverse transcriptase protein (PDB ID: **3V81**) and protein of the RNA-dependent RNA polymerase of the SARS-CoV-2 (PDB ID: **7AAP**) can serve as a likely biological target for the compounds **2a-u**. The inhibitory potential of compounds **2a-u** as CYP2C19 inducers was also assessed using molecular docking procedure, and ligand **7r** showing the highest binding affinity with the **4GQS** protein.

3.4. ADMET Properties

At the final stage of the study, three representatives of the studied compounds — compounds **2a**, **2r** and **2u** — were subjected to *in silico* evaluation of ADMET properties using the ADMETlab 3.0 online portal. First of all, the physicochemical properties of the compounds were estimated, such as molecular weight (MW), number of hydrogen bond donors (nHA) and acceptors (nHD), number of freely rotating bonds (nRot), number of rings (nRing) and heteroatoms (nHet), topological polar surface area (TPSA), logarithm of water solubility (logS), logarithm of *n*-octanol/water partition coefficients at pH = 7.4 (logP), logarithm of *n*-octanol/water partition coefficient (logD), as well as their compliance with the Lipinski's Rule of Five (Table 5, Figure 9).

Table 5

Physicochemical properties of the studied compounds and Lipinski's Rule

Compound	MW, Da	nHA	nHD	nRot	nRing	MaxRing	nHet	nRig	TPSA, Å ²	logS	logP	logD	Lipinski's Rule
2a	295.12	4	0	1	4	16	4	21	48.42	-3.147	2.347	2.395	Yes
2r	385.09	10	0	3	4	16	10	23	134.7	-4.308	2.0	2.363	Yes
2u	345.14	4	0	1	5	20	4	26	48.42	-4.552	3.506	3.17	Yes

Note: MW — molecular weight of the molecule (Optimal: <500 Da), nHA — Number of hydrogen bond acceptors (Optimal: 0~12), nHD — Number of hydrogen bond donors (Optimal: 0~7), nRot — Number of rotatable bonds (Optimal: 0~11), nRing — Number of rings (Optimal: 0~6), MaxRing — Number of atoms in the biggest ring (Optimal: 0~18), nHet — Number of heteroatoms (Optimal: 1~15), nRig — Number of rigid bonds (Optimal: 0~30), TPSA — Topological Polar Surface Area (Optimal: 0~140 Å²), logS — logarithm of aqueous solubility value, logP — logarithm of the *n*-octanol/water distribution coefficients at pH = 7.4, logD — logarithm of the *n*-octanol/water distribution coefficient, Lipinski Rule — MW ≤ 500; logP ≤ 5; nHA ≤ 10; nHD ≤ 5. If two properties are out of range, a poor absorption or permeability is possible, one is acceptable.

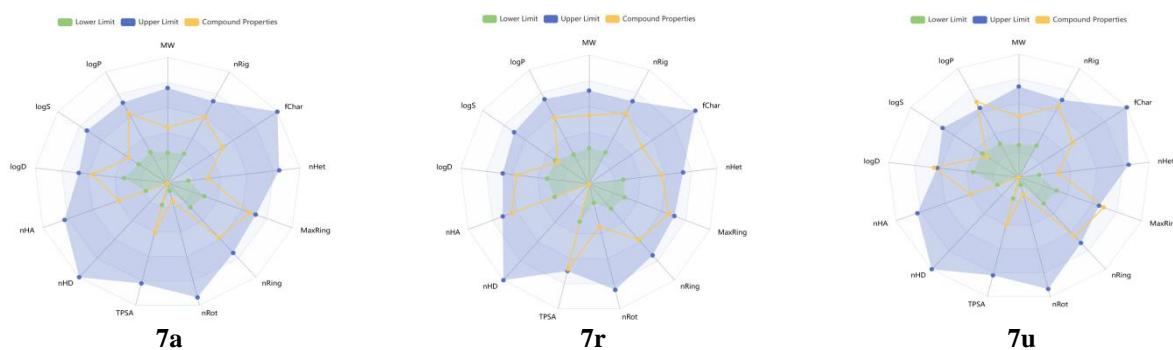


Figure 9. Radar view of the physicochemical properties of the studied compounds **7a**, **7r** and **7u**

As can be seen in Table 5, all the studied compounds with MM = 295.12–385.09 Da fall within the acceptable molecular weight range for drug-like molecules. Higher molecular weights can sometimes indicate complexity of synthesis and potential cell permeability problems, but all values here are within the acceptable range of <500 Da. The number of hydrogen bond acceptors nHA varies from 4 to 10, indicating the presence in **2a**, **2r** and **2u** molecules of oxygen and nitrogen atoms, which have unpaired electrons and can form hydrogen bonds with other molecules. At the same time, the **2a**, **2r** and **2u** molecules do not contain atoms that can donate hydrogen bonds (nHD = 0). These are usually hydrogen atoms bonded to oxygen or nitrogen atoms that can form hydrogen bonds with hydrogen bond acceptors. Both of these properties are important in chemistry and pharmaceuticals because they affect the interaction of molecules with biological targets and their solubility in water.

The number of rotatable bonds (nRot) for all compounds is moderate (from 1 to 3), indicating some flexibility without excessive molecular complexity that could hinder oral bioavailability. The number of ring structures (nRing) in the **2a**, **2r** and **2u** molecules varies from 4 to 5, which corresponds to the optimal range (from 0 to 6) ring structures for pharmaceutical compounds. These rings can be both aromatic and non-aromatic. The number of atoms in the largest ring MaxRing is 16 for **7a** and **7r** molecules, and 20 for **2u**. This property shows the size of the largest ring structure in the molecule, which is important for assessing its stability and interaction with biological targets.

Heteroatoms play an important role in the chemical and biological properties of molecules, as they can participate in hydrogen bonds, affect the polarity and reactivity of compounds. The optimal range for pharmaceutical compounds is usually from 1 to 15 heteroatoms. The number of heteroatoms (nHet) in the studied compounds **2a**, **2r** and **2u** varies from 4 to 10, which is within the recommended range.

The number of rigid bonds (nRig) in the studied molecules ranged from 21 to 26, which is within the optimal range of 0 to 30 rigid bonds for pharmaceutical compounds. Rigid bonds cannot rotate due to their structure, but their presence is important because they affect the three-dimensional structure of the molecule and its interaction with biological targets. The more rigid bonds reduce the flexibility of the molecule, which can be both an advantage and a disadvantage depending on the context.

The optimal range of TPSA (Topological Polar Surface Area) for pharmaceutical compounds is usually from 0 to 140 Å². The total area of all polar surfaces of a molecule is calculated based on its topological structure and for the studied compounds it was 48.42 Å² for molecules **2a** and **2u**, and 134.7 Å² for **2r** molecules. In this range, molecules have good absorption and penetration through biological membranes, which is important for their bioavailability.

The correct ratio of solubility coefficients in water and non-polar media is important for molecules that are potential medicinal substances, since it affects the behavior of the substance in various biological environments. Thus, within the framework of *in silico* evaluation of ADMET properties of the studied compounds **2a**, **2r** and **2u**, the following parameters were considered: logS — the logarithm of the solubility of a substance in water (compounds in the range up to 0.5 can be considered soluble), logP — the logarithm of the distribution coefficient of a substance between *n*-octanol and water at pH 7.4 (compounds in the range from 0 to 3 can be considered suitable), and logD — logarithm of the partition coefficient of a substance between *n*-octanol and water at a certain pH (compounds in the range from 1 to 3 can be considered suitable). As can be seen in Table 5 that substances **2a**, **2r** and **2u** have negative logS values, which indicates their poor solubility in water. At the same time, logP values in the range from 2.0 to 3.506 indicates their high lipophilicity, which is also confirmed by high positive logD values in the range from 2.363 to 3.17.

Overall, all three studied compounds comply with Lipinski's Rule of Five, which states that they have a molecular weight of less than 500 Da, a log *P* value less than 5, a number of hydrogen bond donors (nHD) no more than 5, a number of hydrogen bond acceptors (nHA) no more than 10, and a topological polar surface area (TPSA) less than 140 Å².

In conclusion ADMET properties of the compounds **2a**, **2r** and **2u** were *in silico* assessed (Table 6).

Table 6

In silico ADMET properties of the studied compounds

Compound	Absorption		Distribution		Metabolism				Excretion		Toxicity	
	Caco2 permeability	MDCK permeability	BBB Penetration	PPB (%)	CYP2C19 inhibitor	CYP2C19 substrate	CYP2C9 inhibitor	CYP2C9 substrate	CL _{plasma}	T _{1/2}	Hematotoxicity	RPMI-8226 Immunotoxicity
2a	-4.778	-4.62	1.0	96.383	0.847	0.039	0.674	0.009	7.302	0.862	0.534	0.223
2r	-4.809	-4.396	0.837	98.564	0.998	0.989	1.0	0.0	4.682	0.894	0.78	0.227
2u	-4.746	-4.61	0.999	97.458	0.999	0.486	0.545	0.0	5.388	0.588	0.409	0.21

Note: Caco2 Permeability (Optimal: higher than -5.15 Log unit); BBB Penetration — Blood-Brain Barrier Penetration (Category 1: BBB+; Category 0: BBB-); PPB — Plasma Protein Binding (Optimal: < 90 %); CYP2CX inhibitor — Category 1: Inhibitor; Category 0: Non-inhibitor, CYP2CX substrate — Category 1: Substrate; Category 0: Non-substrate, CL_{plasma} — unit of predicted CL_{plasma} penetration is ml/min/kg: >15 ml/min/kg: high clearance; 5–15 ml/min/kg: moderate clearance; < 5 ml/min/kg: low clearance, T_{1/2} — unit of predicted T_{1/2} is hours: ultra-short half-life drugs: 1/2 < 1 hour; short half-life drugs: T_{1/2} between 1–4 hours; intermediate short half-life drugs: T_{1/2} between 4–8 hours; long half-life drugs: T_{1/2} > 8 hours, Hematotoxicity — Category 0: non-hematotoxicity (-); Category 1: hematotoxicity (+), RPMI-8226 Immunotoxicity — Category 0: non-cytotoxicity (-); Category 1: cytotoxicity (+).

As can be seen in Table 6, the studied compounds **2a**, **2r** and **2u** are characterized by good Caco2 permeability (> -5.15 Log unit), which indicates a potentially high oral efficacy of the drug. The MDCK permeability assessment also predicts good absorption of the studied compounds in the human gastrointestinal tract. BBB (blood-brain barrier) penetration is the penetration of drugs acting on the central nervous system through the blood-brain barrier. These values were in the range of 0.837–1.0 for the studied compounds **2a**, **2r** and **2u**, which indicates their low potential for the blood-brain barrier penetrating.

The CYP2C19 inhibitor, CYP2C19 substrate, CYP2C9 inhibitor and CYP2C9 substrate values were analyzed to evaluate the metabolic potential of the compounds **2a**, **2r** and **2u**, which is important for understanding drug interactions and their side effects. The analysis showed that compounds **2a**, **2r** and **2u** have the potential to inhibit the CYP2C19 enzyme, slowing its ability to catalytically metabolize other compounds.

The CL_{plasma} and T_{1/2} parameters were analyzed to assess the excretion potential of the **2a**, **2r** and **2u** compounds. CL_{plasma} indicator characterizes the rate of removal of a substance from blood plasma and T_{1/2} parameter characterizes the time during which the concentration of a substance in the body decreases by half. As can be seen in Table 6, compounds **2a**, **2r** and **2u** have a moderate clearance of 4.682–7.302 in CL_{plasma}, i.e. they are excreted from the body with an average T_{1/2} rate of about 1 hour.

The toxicity of the studied compounds was assessed using hematotoxicity and immunotoxicity parameters. These parameters for the compounds **2a**, **2r** and **2u** fell within the ranges of 0.409–0.78 and 0.21–0.227, respectively, suggesting a promising safety profile for therapeutic use.

In summary, comprehensive assessment of ADMET properties of the compounds **2a**, **2r** and **2u** has provided insight into their safety and potential use in pharmaceutical research. However, further experimental studies are needed to better understand the underlying mechanisms of toxicity and to optimize the compound design to improve their efficacy and safety.

4 Conclusions

Structural analogs of natural integrastatins with an epoxydibenzoxocine fragment are of great interest to researchers and pharmacists worldwide due to their broad spectrum of biological activity, including antiviral, antioxidant, antimicrobial, antifungal and antitumor activity. At the same time, *in silico* studies can be successfully used to predict numerous physicochemical and pharmacological properties of natural and synthetic biologically active molecules. In the present study, an *in silico* approach was used to comparatively evaluate

the pharmaceutical potential of a series of 21 novel integrastatin derivatives, previously synthesized but not characterized in terms of physicochemical and bioactive parameters.

Initially, the molecular structures of 21 studied compounds **2a-u** were subjected to the procedure of quantum-chemical geometry optimization and evaluation of the calculated parameters using DFT RB3LYP 6-311++G(d, p) CPCM (solvent — water) method with the help of the Gaussian 16 program. It was shown that all the studied compounds have a non-planar structure due to the presence of a chair-shaped structure of the central epoxybenzo[7,8]oxocine fragment. The global chemical reactivity descriptors of the compounds **2a-u** were estimated based on the HOMO and LUMO frontier orbitals characteristics. It was shown that compounds **2a-u** are characterized by a sufficiently large energy gap ΔE_{gap} from 3.8 to 4.6 eV, have a high ionization potential IP from 5.9 to 7.1 eV and an electron affinity EA value at a level of 2.1 to 3.2 eV. The molecular hardness η of the studied molecules **2a-u** varies from 1.7 to 2.3 eV, which, together with a fairly large energy gap, indicates the hard nature of the compounds. Analysis of the molecular electrostatic potential (MEP) of compounds **2a-u** showed that the nucleophilic center is located on the oxygen atom of the carbonyl, while the hydrogen atom of the pyridine is one of the most electrophilic centers. The applied complex quantum-chemical approach contributed to a deeper understanding of the electronic structure and molecular properties of the studied compounds **2a-u**, as well as the identification of their reaction centers and an assessment of the chemical potential for subsequent *in silico* studies of biological activity.

PASS Online resource was used for the assessment of potential biological activity of the studied compounds **2a-u**, which allowed to identify their antiviral potential and inhibitory potential as CYP2C19 inducers. These types of biological activity of compounds **2a-u** were further investigated using the molecular docking method for the efficiency of binding with HIV-1 (PDB ID: **3V81**), SARS-CoV-2 (PDB ID: **7AAP**) and CYP2C19 inducer (PDB ID: **4GQS**) proteins using AutoDock Vina tool. All 21 tested compounds showed high antiviral potential against Human immunodeficiency virus HIV-1 reverse transcriptase protein (PDB ID: **3V81**) and protein of the RNA-dependent RNA polymerase of the SARS-CoV-2 (PDB ID: **7AAP**), and ligand **2u** demonstrated the best binding to both viral proteins. The inhibitory potential of compounds **2a-u** as CYP2C19 inducers was also assessed by docking, and ligand **2r** demonstrated the highest binding affinity with **4GQS** protein.

At the final stage of the study, three representatives of the studied series of compounds — compounds **2a**, **2r** and **2u** were subjected to *in silico* assessment of ADMET properties using ADMETlab 3.0 online portal. It was noted that all three studied compounds comply with Lipinski's Rule of Five, according to which they have a molecular weight less than 500 Da, a $\log P$ value less than 5, a number of hydrogen bond donors (nHD) no more than 5, a number of hydrogen bond acceptors (nHA) no more than 10, a topological polar surface area (TPSA) value less than 140 Å². The studied compounds **2a**, **2r** and **2u** showed potentially good Caco2 permeability and good absorption in the human gastrointestinal tract, which indicates a potentially high oral efficiency. At the same time, compounds **2a**, **2r** and **2u** demonstrated low potential for penetration through the blood-brain barrier and high potential for inhibition of the CYP2C19 enzyme. Evaluation of hematotoxicity and immunotoxicity of the studied compounds showed a promising safety profile for their therapeutic use.

In general, the complex *in silico* study of the properties of 21 new integrastatin derivatives showed their high potential as CYP2C19 inducers and high antiviral potential against HIV-1 and COVID-19 viruses, potentially high oral efficacy of pharmaceuticals based on them and a promising safety profile for their therapeutic use. However, further experimental *in vitro* and *in vivo* studies is need for more accurate evaluation the assumptions made on the basis of *in silico* approach, for better understanding of the underlying mechanisms of toxicity, pharmacokinetics, pharmacodynamics and side effects.

Supporting Information

The Supporting Information is available free at <https://ejc.buketov.edu.kz/index.php/ejc/article/view/207/155>

Funding

This research was funded by the Science Committee of the Ministry of Science and Higher Education of the Republic of Kazakhstan (Grant No. AP23488790 “De novo design, *in silico* study of the structure and properties of new synthetic analogues of natural integrastatins”).

*Author Information**

**The authors' names are presented in the following order: First Name, Middle Name and Last Name*

Aida Sabitovna Rakhimzhanova — Assistant Professor, Department of Physical and Analytical Chemistry, Karaganda Buketov University, Universitetskaya street, 28, 100024, Karaganda, Kazakhstan; e-mail: aida_ekb@mail.ru, <https://orcid.org/0000-0002-4984-623X>

Ruslan Arslanovich Muzaparov — 2nd Year Master Student, Department of Physical and Analytical Chemistry, Karaganda Buketov University, Universitetskaya street, 28, 100024, Karaganda, Kazakhstan; e-mail: mega.muzaparov@mail.ru, <https://orcid.org/0009-0005-4480-4355>

Irina Anatolevna Pustolaikina (*corresponding author*) — Candidate of Chemical Sciences, Associate Professor, Department of Physical and Analytical Chemistry, Karaganda Buketov University, Universitetskaya street, 28, 100024, Karaganda, Kazakhstan; e-mail: ipustolaikina@gmail.com, <https://orcid.org/0000-0001-6319-666>

Alfiya Faridovna Kurmanova — Candidate of Chemical Sciences, Professor, Department of Physical and Analytical Chemistry, Karaganda Buketov University, Universitetskaya street, 28, 100024, Karaganda, Kazakhstan; e-mail: alfiya_kurmanova@mail.ru, <https://orcid.org/0000-0003-4548-8145>

Sergey Nikolaevich Nikolskiy — Doctor of Chemical Sciences, Full Professor, Department of Physical and Analytical Chemistry, Karaganda Buketov University, Universitetskaya street, 28, 100024, Karaganda, Kazakhstan; e-mail: sergeynikolsky@mail.ru; <https://orcid.org/0000-0003-3175-6938>

Darya Dmitrievna Kapishnikova — Student, Institute of Chemistry, Saint Petersburg State University, Universitetskii prospect, 26, 198504, Saint Petersburg, Russia; e-mail: st130421@student.spbu.ru, <https://orcid.org/0009-0003-2129-9988>

Alena Leonidovna Stalinskaya — Assistant, School of Natural Sciences, University of Tyumen, Tyumen, 15a Perekopskaya St., 625003, Russia; e-mail: a.l.stalinskaya@utmn.ru; <https://orcid.org/0000-0002-2172-074X>

Ivan Vyacheslavovich Kulakov — Doctor of Chemical Sciences, Associate Professor, Higher School of Natural Science, University of Tyumen, Tyumen, 15a Perekopskaya St., 625003, Russia; e-mail: i.v.kulakov@utmn.ru; <https://orcid.org/0000-0001-5772-2096>

Author Contributions

The manuscript was written through contributions of all authors. All authors have given approval to the final version of the manuscript. **CRedit**: **Aida Sabitovna Rakhimzhanova** investigation, formal analysis, visualization; **Ruslan Arslanovich Muzaparov** investigation, formal analysis, visualization; **Irina Anatolevna Pustolaikina** funding acquisition, project administration, supervision, methodology, validation, writing-review & editing; **Alfiya Faridovna Kurmanova** resources, data curation, validation; **Sergey Nikolaevich Nikolskiy** resources, software, data curation; **Darya Dmitrievna Kapishnikova** formal analysis, visualization; **Alena Leonidovna Stalinskaya** investigation, data curation, visualization; **Ivan Vyacheslavovich Kulakov** conceptualization, data curation, methodology, writing-original draft.

Acknowledgments

Authors thank *University or Institution Name* for access to library facilities.

Conflicts of Interest

The authors declare no conflict of interest.

References

- 1 Kulakov, I. V., Stalinskaya, A. L., Chikunov, S. Y., & Gatilov, Y. V. (2021). Synthesis of new representatives of 11,12-dihydro-5H-5,11-epoxybenzo 7,8 oxocino 4,3-pyridines — structural analogues of integrastatins A, B. *New Journal of Chemistry*, 45(7), 3559–3569. <https://doi.org/10.1039/d0nj06117d>

- 2 Singh, S. B., Pelaez, F., Hazuda, D. J., & Lingham, R. B. (2005). Discovery of natural product inhibitors of HIV-1 integrase at Merck. *Drugs Fut*, 30(3), 277–299. <https://doi.org/10.1358/dof.2005.030.03.885746>
- 3 Singh, S. B., Zink, D. L., Quamina, D. S., Pelaez, F., Teran, A., Felock, P., & Hazuda, D. J. (2002). Integrastatins: structure and HIV-1 integrase inhibitory activities of two novel racemic tetracyclic aromatic heterocycles produced by two fungal species. *Tetrahedron Letters*, 43(13), 2351–2354. [https://doi.org/10.1016/s0040-4039\(02\)00265-4](https://doi.org/10.1016/s0040-4039(02)00265-4)
- 4 Johnson, A. A., Marchand, C., & Pommier, Y. (2004). HIV-1 integrase inhibitors: a decade of research and two drugs in clinical trial. *Current Topics in Medicinal Chemistry*, 4(10), 1059–1077. <https://doi.org/10.2174/1568026043388394>
- 5 Foot, J. S., Giblin, G. M., & Taylor, R. J. (2003). Synthesis of the Integrastatin Nucleus Using the Ramberg–Bäcklund Reaction. *Organic Letters*, 5(23), 4441–4444. <https://doi.org/10.1021/ol035786v>
- 6 Yamagiwa, Y., Haruna, N., Kawakami, H., & Matsumoto, K. (2020). Improved and Practical Synthesis of the Integrastatin Core. *Bulletin of the Chemical Society of Japan*, 93(8), 1036–1042. <https://doi.org/10.1246/bcsj.20200070>
- 7 Tadross, P. M., Bugga, P., & Stoltz, B. M. (2011). A rapid and convergent synthesis of the integrastatin core. *Organic & biomolecular chemistry*, 9(15), 5354–5357. <https://doi.org/10.1039/c1ob05725a>
- 8 More, A. A., & Ramana, C. V. (2016). o-Quinone methides via oxone-mediated benzofuran oxidative dearomatization and their intramolecular cycloaddition with carbonyl groups: an expeditious construction of the central tetracyclic core of integrastatins, Epicoccolide A, and Epicocconigrone A. *Organic letters*, 18(3), 612–615. <https://doi.org/10.1021/acs.orglett.5b03707>
- 9 Ramana, C. V., Reddy, C. N., & Gonnade, R. G. (2008). An expeditious one-step entry to the tetracyclic core of integrastatins. *Chemical communications*, (27), 3151–3153. <https://doi.org/10.1039/b801755g>
- 10 Jeong, J. Y., Sperry, J., & Brimble, M. A. (2019). Synthesis of the Tetracyclic Cores of the Integrastatins, Epicoccolide A and Epicocconigrone A. *The Journal of Organic Chemistry*, 84(18), 11935–11944. <https://doi.org/10.1021/acs.joc.9b01796>
- 11 More, A. A., & Ramana, C. V. (2016). Total synthesis of integrastatin B enabled by a benzofuran oxidative dearomatization cascade. *Organic letters*, 18(6), 1458–1461. <https://doi.org/10.1021/acs.orglett.6b00404>
- 12 Stalinskaya, A. L., Martynenko, N. V., Shulgau, Z. T., Shustov, A. V., Keyer, V. V., & Kulakov, I. V. (2022). Synthesis and Antiviral Properties against SARS-CoV-2 of Epoxybenzoxocino 4,3-Pyridine Derivatives. *Molecules*, 27(12), Article 3701. <https://doi.org/10.3390/molecules27123701>
- 13 Stalinskaya, A. L., Chikunov, S. Y., Pustolaikina, I. A., & Kulakov, I. V. (2022). Cyclization Reaction of 3,5-Diacetyl-2,6-dimethylpyridine with Salicylic Aldehyde and Its Derivatives: Quantum-Chemical Study and Molecular Docking. *Russian Journal of General Chemistry*, 92(5), 914–924. <https://doi.org/10.1134/s107036322205022x>
- 14 Stalinskaya, A. L., Chikunov, S. Y., Pustolaikina, I. A., Gatilov, Y. V., Kulakov, I. V. (2023). Synthesis of New Structural Analogues of Natural Integrastatins with a Basic Epoxybenzo[7,8]oxocine Skeleton: Combined Experimental and Computational Study. *Synthesis*. <https://doi.org/10.1055/s-0042-1751521>
- 15 Bortolato, A., Perruccio, F., & Moro, S. (2011). Successful Applications of In silico Approaches for Lead/Drug Discovery. In *In silico Lead Discovery*, 163–175. <https://doi.org/10.2174/978160805142711101010163>
- 16 Tian, S., Wang, J., Li, Y., Li, D., Xu, L., & Hou, T. (2015). The application of in silico drug-likeness predictions in pharmaceutical research. *Advanced drug delivery reviews*, 86, 2–10. <https://doi.org/10.1016/j.addr.2015.01.009>
- 17 Aldossary, A., Campos-Gonzalez-Angulo, J. A., Pablo-Garcia, S., Leong, S. X., Rajaonson, E. M., Thiede, L., ... & Aspuru-Guzik, A. (2024). In silico chemical experiments in the Age of AI: From quantum chemistry to machine learning and back. *Advanced Materials*, 2402369. <https://doi.org/10.1002/adma.202402369>
- 18 Paliwal, A., Jain, S., Kumar, S., Wal, P., Khandai, M., Khandige, P. S., ... & Srivastava, S. (2024). Predictive Modelling in pharmacokinetics: from in-silico simulations to personalized medicine. *Expert Opinion on Drug Metabolism & Toxicology*, 20(4), 181–195. <https://doi.org/10.1080/17425255.2024.2330666>
- 19 Evans, D. A. (2014). History of the Harvard ChemDraw Project. *Angewandte Chemie International Edition*, 53(42), 11140–11145. <https://doi.org/10.1002/anie.201405820>
- 20 van Gunsteren, W. F., & Oostenbrink, C. (2024). Methods for Classical-Mechanical Molecular Simulation in Chemistry: Achievements, Limitations, Perspectives. *Journal of Chemical Information and Modeling*, 64(16), 6281–6304. <https://doi.org/10.1021/acs.jcim.4c00823>
- 21 Gaussian 16, Revision A.03, M.J. Frisch, G.W. Trucks, H.B. Schlegel, G.E. Scuseria, M.A. Robb, J.R. Cheeseman, G. Scalmani, V. Barone, G.A. Petersson, H. Nakatsuji, X. Li, M. Caricato, A.V. Marenich, J. Bloino, B.G. Janesko, R. Gomperts, B. Mennucci, H.P. Hratchian, J.V. Ortiz, A.F. Izmaylov, J.L. Sonnenberg, D. Williams-Young, F. Ding, F. Lipparini, F. Egidi, J. Goings, B. Peng, A. Petrone, T. Henderson, D. Ranasinghe, V.G. Zakrzewski, J. Gao, N. Rega, G. Zheng, W. Liang, M. Hada, M. Ehara, K. Toyota, R. Fukuda, J. Hasegawa, M. Ishida, T. Nakajima, Y. Honda, O. Kitao, H. Nakai, T. Vreven, K. Throssell, J.A. Montgomery, Jr., J.E. Peralta, F. Ogliaro, M.J. Bearpark, J.J. Heyd, E.N. Brothers, K.N. Kudin, V.N. Staroverov, T.A. Keith, R. Kobayashi, J. Normand, K. Raghavachari, A.P. Rendell, J.C. Burant, S.S. Iyengar, J. Tomasi, M. Cossi, J.M. Millam, M. Klene, C. Adamo, R. Cammi, J.W. Ochterski, R.L. Martin, K. Morokuma, O. Farkas, J.B. Foresman, and D.J. Fox, Gaussian, Inc., Wallingford CT, 2016.
- 22 Dennington, R., Keith, T., Millam, J. GaussView, Version 6. Semichem Inc., Shawnee Mission, KS, 2016. <http://gaussian.com>
- 23 Ipek, C., Gümüş, H., Şimşek, M., & Tosun, M. (2022). DFT and Molecular Docking Study of 1-(2'-Thiophen)-2-propen-1-one-3-(2,3,5-trichlorophenyl) (TTCP) Molecule as Antiviral to Covid-19 Main Protease. *Arabian Journal for Science and Engineering*, 48(1), 1031–1040. <https://doi.org/10.1007/s13369-022-07293-4>

- 24 Rharmili, N., Sert, Y., Rödi, Y. K., Chahdi, F. O., Haoudi, A., Mague, J. T., ... & Sebbar, N. K. (2024). Synthesis of new N-alkylated 6-bromindoline-2,3-dione derivatives: crystal structures, spectroscopic characterizations, Hirschfeld surface analyses, molecular docking studies, DFT calculations, and antibacterial activity. *Results in Chemistry*, 7, 101338. <https://doi.org/10.1016/j.rechem.2024.101338>
- 25 Kulakov, I. V., Chikunov, S. Y., Pustolaikina, I. A., & Gatilov, Y. V. (2024). Synthesis of a New Heterocyclic System: Pyrimidine Structural Analogues of Natural Integrastatins A, B. *Synlett*, 35(15), 1799–1806. <https://doi.org/10.1055/a-2239-6657>
- 26 Tomasi, J., Mennucci, B., & Cammi, R. (2005). Quantum Mechanical Continuum Solvation Models. *Chemical Reviews*, 105(8), 2999–3094. <https://doi.org/10.1021/cr9904009>
- 27 Schueuermann, G. (2004). Quantum Chemical Descriptors in Structure-Activity Relationships—Calculation, Interpretation, and Comparison of Methods. *Predicting chemical toxicity and fate*, 85–149. <https://doi.org/10.1201/9780203642627-14>
- 28 Filimonov, D., & Poroikov, V. (2008). Probabilistic Approaches in Activity Prediction. *Chemoinformatics Approaches to Virtual Screening*, 182–216. <https://doi.org/10.1039/9781847558879-00182>
- 29 Makiyah, S. N. N., Usman, S., & Ahkam, A. H. (2024). Molecular Docking Investigation of Dioscorea alata Compounds Binding to CCKBR, CHRM3, CHRM5, and H2R for Gastric Ulcer Treatment. *Trends in Sciences*, 21(5), 7358–7358. <https://doi.org/10.48048/tis.2024.7358>
- 30 Sulimov, A. V., Ilin, I. S., Tashchilova, A. S., Kondakova, O. A., Kutov, D. C., & Sulimov, V. B. (2024). Docking and other computing tools in drug design against SARS-CoV-2. *SAR and QSAR in Environmental Research*, 35(2), 91–136. <https://doi.org/10.1080/1062936x.2024.2306336>
- 31 Eberhardt, J., Santos-Martins, D., Tillack, A. F., & Forli, S. (2021). AutoDock Vina 1.2.0: New Docking Methods, Expanded Force Field, and Python Bindings. *Journal of Chemical Information and Modeling*, 61(8), 3891–3898. <https://doi.org/10.1021/acs.jcim.1c00203>
- 32 Trott, O., & Olson, A. J. (2009). AutoDock Vina: Improving the speed and accuracy of docking with a new scoring function, efficient optimization, and multithreading. *Journal of Computational Chemistry*, 31(2), 455–461. <https://doi.org/10.1002/jcc.21334>
- 33 Berman, H.M., Westbrook, J., Feng, Z., Gilliland, G., Bhat, T.N., Weissig, H., Shindyalov, I.N., & Bourne, P.E. (2000). The Protein Data Bank Nucleic Acids Research 28: 235–242 <https://doi.org/10.1093/nar/28.1.235>
- 34 Das, K., Martinez, S.E., Arnold, E. (2011) Crystal structure of HIV-1 reverse transcriptase (RT) with DNA and the nonnucleoside inhibitor nevirapine. <https://doi.org/10.2210/pdb3V81/pdb>
- 35 Naydenova, K., Muir, K.W., Wu, L.F., Zhang, Z., Coscia, F., Peet, M., Castro-Hartman, P., Qian, P., Sader, K., Dent, K., Kimanius, D., Sutherland, J.D., Lowe, J., Barford, D., & Russo, C.J. (2020). Nsp7-Nsp8-Nsp12 SARS-CoV2 RNA-dependent RNA polymerase in complex with template:primer dsRNA and favipiravir-RTP. <https://doi.org/10.2210/pdb7AAP/pdb>
- 36 Reynald, R.L., Sansen, S., Stout, C.D., & Johnson, E.F. (2012). Structure of Human Microsomal Cytochrome P450 (CYP) 2C19. <https://doi.org/10.2210/pdb4GQS/pdb>
- 37 BIOVIA, Dassault Systèmes, BIOVIA Discovery Studio, Release 2021, Sand Diego: Dassault Systèmes, 2023.
- 38 Ekins, S., Lane, T. R., Urbina, F., & Puhl, A. C. (2024). In silico ADME/tox comes of age: twenty years later. *Xenobiotica*, 54(7), 352–358. <https://doi.org/10.1080/00498254.2023.2245049>
- 39 Chen, M., Yang, J., Tang, C., Lu, X., Wei, Z., Liu, Y., ... & Li, H. (2024). Improving ADMET prediction accuracy for candidate drugs: Factors to consider in QSPR modeling approaches. *Current Topics in Medicinal Chemistry*, 24(3), 222–242. <https://doi.org/10.2174/0115680266280005231207105900>
- 40 Wei, Y., Palazzolo, L., Mariem, O. B., Bianchi, D., Laurenzi, T., Guerrini, U., & Eberini, I. (2024). Investigation of in silico studies for cytochrome P450 isoforms specificity. *Computational and Structural Biotechnology Journal*. <https://doi.org/10.1016/j.csbj.2024.08.002>
- 41 Lohit, N., Singh, A. K., Kumar, A., Singh, H., Yadav, J. P., Singh, K., & Kumar, P. (2024). Description and In silico ADME Studies of US-FDA Approved Drugs or Drugs under Clinical Trial which Violate the Lipinski's Rule of 5. *Letters in Drug Design & Discovery*, 21(8), 1334–1358. <https://doi.org/10.2174/1570180820666230224112505>
- 42 Pereira, G. C. (2020). Computational Approaches in Drug Development and Phytocompound Analysis. *Plant-Derived Bioactives*, 529–548. https://doi.org/10.1007/978-981-15-2361-8_24
- 43 Sohail, A., & Li, Z. (2018). Computational Approaches in Biomedical Nanoengineering: An Overview. *Computational Approaches in Biomedical Nano-Engineering*, 1–22. <https://doi.org/10.1002/9783527344758.ch1>

INORGANIC CHEMISTRY

Article

Received: 3 September 2024 | Revised: 1 November 2024 |

Accepted: 7 November 2024 | Published online: 9 December 2024

UDC 543.4+519.242

<https://doi.org/10.31489/2959-0663/4-24-10>

Milana A. Turovets , Vitaliy N. Fomin , Nabira K. Kelesbek , Daulet Khan A. Kaykenov ,
Daniyar T. Sadyrbekov , Assanali A. Aynabayev , Saule K. Aldabergenova *

Karaganda Buketov University, Karaganda, Kazakhstan

(*Corresponding author's e-mail: aldsau@mail.ru)

Chemometric Approach for the Determination of Vanadium by the LIBS Method

Laser-Induced Breakdown Spectroscopy (LIBS) has proven to be a versatile analytical technique for the detection of trace elements in various sample matrices, including hydrocarbon materials. This study focuses on optimizing LIBS parameters to enhance the accuracy and sensitivity of vanadium (V) detection in coal and hydrocarbon-based samples. A probabilistic-deterministic design of experiments (PDDoE) was employed to fine-tune key factors such as lamp energy, delay, and the number of laser impulses. Optimal settings (lamp energy: 20 J, Q-SW1: 111 μ s, Δ Q-SW: 3 μ s, delay: 1 μ s, and 100 impulses) significantly improved the intensity of vanadium spectral lines, particularly in samples with low concentrations, achieving a limit of detection (LoD) of 0.03 % for vanadium. Calibration models were developed using Partial Least Squares Regression (PLS-R) and Multiple Linear Regression (MLR) methods. These models achieved an accuracy of 95–98 % for vanadium quantification in coal ash and hydrocarbon samples. Validation of the developed method was performed using Atomic Absorption Spectroscopy (AAS), demonstrating good correlation between predicted and experimental values. Although the method requires sample preparation and shows lower accuracy than traditional AAS, it offers a practical solution for cases where sample dissolution is difficult, such as the analysis of glasses, enamels, and geological materials. Furthermore, the method demonstrated satisfactory results in field applications, where rapid on-site analysis with portable LIBS devices was required.

Keywords: Laser-induced breakdown spectroscopy, PLS-R, MLR, Vanadium identification, Vanadium quantification, Coal, Coal ash, Design of Experiment, Chemometrics

Introduction

Laser-induced breakdown spectroscopy (LIBS) is a versatile analytical technique that has received considerable attention in recent studies. It is capable of analyzing a wide variety of sample types, including solids [1–3], gases [4], and liquids [5–7]. While LIBS offers reasonable sensitivity and selectivity, it faces limitations, particularly when dealing with complex samples. This challenge is especially evident in spectra containing elements at low concentrations, where noise and matrix interferences can reduce experimental accuracy [8]. Consequently, optimizing LIBS experiments to minimize the limit of detection (LoD) and enhance the reliability and repeatability of results has become a key focus in contemporary analytical chemistry research.

A critical aspect of ensuring the reliability and efficiency of experimental studies is the design of experiments (DoE). This systematic approach allows researchers to effectively plan, conduct, and analyze experiments, thereby optimizing the use of resource. The primary importance of DoE lies in its ability to control variables, minimize errors, and establish cause-and-effect relationships. By carefully designing experiments, researchers can reduce variability, identify significant factors, and improve the accuracy of their conclusions [9].

Building upon this framework, the probabilistic-deterministic design of experiment (PDDoE), developed by V.P. Malyshev [10-11], emerges as a novel approach for factorial analysis. PDDoE's capability to assess both individual and combined factor effects is particularly valuable for analyzing complex samples. Unlike traditional single-factor optimization, which considers the influence of one variable at a time, PDDoE enables a more comprehensive evaluation by accounting for interactions among variables. This multifaceted approach allows researchers to identify significant interactions that may not be evident with simpler methods, ultimately leading to more accurate models and interpretations of sample behavior. Such capabilities are crucial in fields such as cultural heritage [12] and material science [13–15]. The integration of probabilistic and deterministic components helps to balance randomness and predictability in analyses, thereby enhancing result precision and optimizing experimental resources.

To complement these techniques, chemometric methods apply mathematical and statistical approaches to extract meaningful information from complex chemical data. Techniques such as principal component analysis (PCA) [16], partial least squares regression (PLS-R) [17], and artificial neural networks [18, 19] aid in reducing dimensionality, recognizing patterns, and improving data interpretation. Chemometrics is widely employed across various fields, including spectroscopy, chromatography, and environmental science, to model relationships between variables, classify data, and predict outcomes [20, 21]. This field significantly improves the accuracy of both quantitative and qualitative chemical analyses, making it particularly applicable in spectral analysis and LIBS [22, 23].

In addition to its broader applications, LIBS has proven effective for the analysis of trace elements in hydrocarbon raw materials. It has been recognized as a promising technique for the analyses of hydrocarbons such as coal, oil, and tar [24, 25]. This method has been successfully applied to quantify carbon content in coal, demonstrating LIBS's applicability in evaluating coal quality and its energy properties [26]. Furthermore, the technique has been employed for compositional analysis of coal samples, facilitating the detection of heavy metals and both major and trace elements, thus providing a comprehensive understanding of hydrocarbon materials [27, 28].

Although there are numerous methods for analyzing petroleum materials, coal, and its ash, the application of LIBS for identification and quantification of vanadium has remained limited. This is primarily due to the low concentration of vanadium and the sensitivity challenges associated with the technique. Identifying vanadium in different samples is essential given its significant industrial and environmental relevance. Vanadium is widely utilized in steel production to increase the strength of alloys, in chemical catalysts, and in emerging energy storage technologies such as vanadium redox-flow batteries. Its presence in materials such as coal and crude oil can affect processing and quality. Additionally, vanadium pollution from industrial sources poses environmental risks, and its accumulation in ecosystems can be toxic to both wildlife and humans. Therefore, monitoring and analyzing vanadium content in various materials is crucial for resource management, pollution control, and advancing energy technologies.

LIBS has demonstrated its applicability for vanadium identification in general, such as in the analysis of medicinal plants [29]. The method employs a classification model with a high accuracy rate (up to 95 % using SNV preprocessing). A study conducted on vanadium and strontium in soils using LIBS reported the use of both univariate and multivariate data analysis methods, including Partial Least Squares Regression (PLS) and Least Squares Support Vector Regression (LS-SVR). Vanadium was successfully analyzed, achieving a correlation coefficient of 0.983 and an average relative prediction error below 2.88 %, demonstrating the high accuracy of LIBS in complex matrices for example soil [30]. However, few articles have focused on vanadium identification in hydrocarbon materials [31, 32]. Notably, research has demonstrated the use of a LIBS prototype analyzer for liquid petroleum sample analysis. This study showed detection limits for vanadium in oil and solvents as low as 0.01–0.04 ppm, indicating that LIBS can be more sensitive than other standard methods, such as ICP-OES. The method also exhibited good repeatability for vanadium, with a relative standard deviation of 1.5 % at a concentration of 100 ppm [33].

The aim of this study is to combine DoE and chemometric techniques to enhance instrument sensitivity and to develop a methodology for the identification and quantification of vanadium in coal, and coal ash samples. The integration of LIBS, PDDoE, and multiple linear regression calibration can help to improve sensitivity, spectral data quality, and greater accuracy of results.

Experimental

The sample selected for the quantitative analysis of vanadium was the “Kuznetsk” coal sample. Initially, the coal was completely ashed in a muffle furnace at 700 °C for two hours. The resulting ash was homog-

enized in a mechanical mortar and used to prepare sodium tetraborate-based glasses. A series of calibration glasses was made using mixtures of vanadium(V) oxide and anhydrous sodium tetraborate. In total, five mixtures were prepared with V(V) concentrations of 1 %, 0.75 %, 0.5 %, 0.25 %, and 0.1 %. A mixture for glass without any added vanadium was also prepared. Although this concentration significantly exceeds the levels of vanadium found in real samples, this range was deliberately chosen to gradually reduce the limit of detection and increase sensitivity. A preliminary determination of the acid-neutralizing capacity of the ash was carried out using acid-base titration to estimate the amount of tetraborate absorbed by the ash. Additionally, 2 % sodium nitrate was added to the mixture to ensure complete combustion of the coal particles. The melting of the glasses was carried out in a muffle furnace for one hour at a temperature of 1100 °C.

The concentration of vanadium in the glasses was determined by atomic absorption spectroscopy using the “Variant A140” instrument (Table 1). The analysis was repeated five times.

Table 1

V(V) concentration in the calibration glasses set

Sample	V(V) concentration, %
1	0.4607±0.012
2	0.3505±0.023
3	0.2406±0.018
4	0.131±0.009
5	0.0737±0.0042
6	0.0306±0.0026

The registration of the spectra of calibration samples was conducted using a two-pulse spectrometer “LAES Matrix Continuum” (SJSC Spectroscopic Systems, 2016, Russia) featuring a double Paschen-Runge optical scheme with optical path lengths of 250 mm and 125 mm, equipped with diffraction gratings of 2400 grooves/mm and 1200 grooves/mm, along with 7 CCD detectors from Toshiba, covering a wavelength range from 190 to 800 nm. Probabilistic-Deterministic Design of Experiments (PDDoE) using a matrix design was used to optimize the registration conditions. The matrix included six factors with five levels of variation (Table 2). The positions for the first factor – concentration – and the sixth factor – exposure time – were left vacant. These factors were chosen to simplify the construction of the overall dependence equation, as the concentration of vanadium in the sample remained constant throughout all 25 experiments, and the influence of exposure time on the analysis results is minimal.

Table 2

Factors and levels

Factor	Type	Level 1	Level 2	Level 3	Level 4	Level 5
C(V), %	V	1	2	3	4	5
Lamp Energy, J	N	15	16	17	18	19
QSW ₁ , μs	N	100	105	110	120	140
ΔQSW, μs	N	1	3	5	10	15
Delay, μs	N	1	2	3	4	5
Exposure, ms	V	1	2	3	4	5

Results and Discussion

The subject of optimization was the intensity of the vanadium V(II)310.224 line. The primary factor influencing the intensity of the line was the lamp energy value (Fig. 1). The other factors had no significant impact on the results of the experiment.

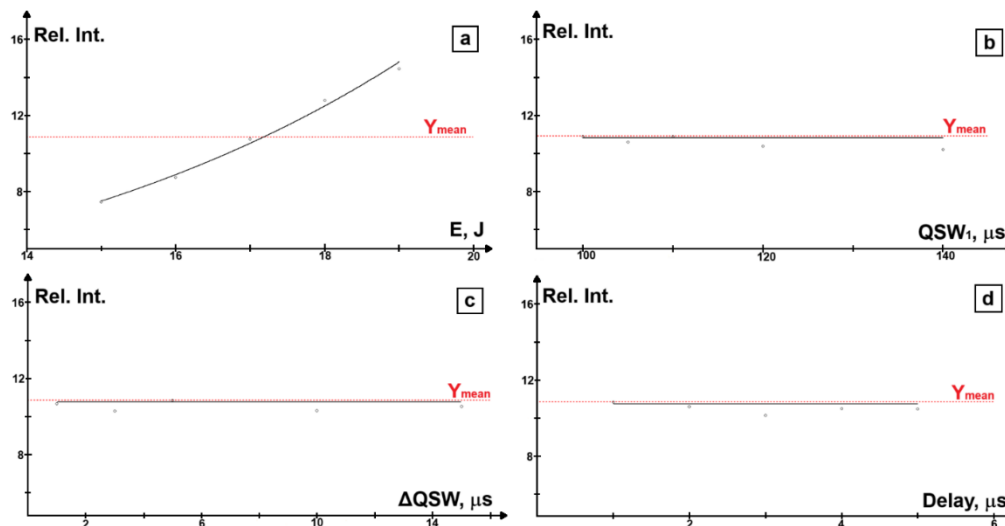


Figure 1. Partial dependencies of the V(II)_{310.224} line intensity on the device settings: Lamp Energy (a), QSW₁ (b), ΔQSW (c), Delay (d)

Overall, the optimal settings for the intensity of the V(II)_{310.224} line were as follows: Lamp energy — 19J, QSW₁ — 100 μs, ΔQSW — 1 μs, Delay — 1 μs, Vacant factor — exposure time — 3 ms. Spectra of 5 calibration glasses were recorded at the calculated optimal instrument settings.

The spectral data of the calibration glasses obtained after the optimization was analyzed in the *R* environment. A model based on PLS was chosen to predict the concentration of vanadium in coal ash samples. The model was applied to determine the concentration of vanadium in the glass without addition of V₂O₅. The concentration predicted by the model (0.06 %) differed significantly from that determined by AAS (0.03 %). Furthermore, the variation in predicted results was considerable, exceeding 20 %, which can be attributed to the wider range of vanadium concentrations in the calibration glasses. This is related to the wider range of vanadium addition in the calibration glasses, as the concentration of V(V) in the initial ash was, as expected, significantly lower than the range of the calibration curve.

A second set of calibration samples was prepared with the V₂O₅ addition corresponding to the approximate concentration of vanadium in the ash. The method remained identical and the initial composition of the glasses in the new calibration set is reflected in Table 3. The final concentrations of vanadium in the second set of calibration glasses were also checked using AAS, as shown in Table 4. The appearance of the new calibration set is depicted in Figure 2.

Table 3

Composition of the second calibration set

№	Ash, g	Sodium tetraborate with V ₂ O ₅ addition, g	Calculated concentration of the V(V) in the resulting glass, %	Lithium nitrate, %
1	1	0.64	0.05	2
2			0.04	
3			0.03	
4			0.02	
5			0.01	

Table 4

Final concentration of the vanadium in the glasses

№	V(V), %
1	0.0836±0.012
2	0.0727±0.0023
3	0.0615±0.0018
4	0.0507±0.009
5	0.0398±0.0042

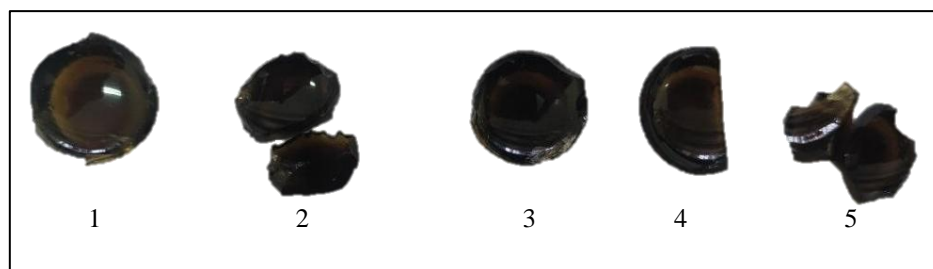
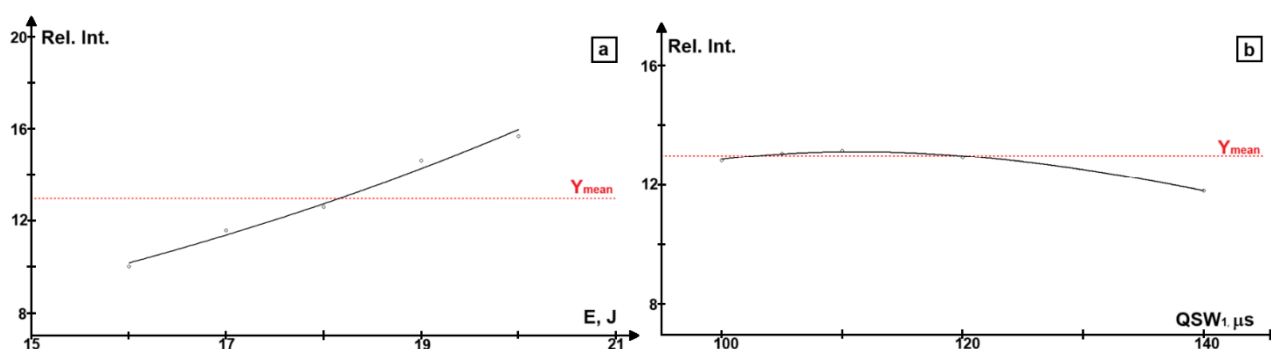


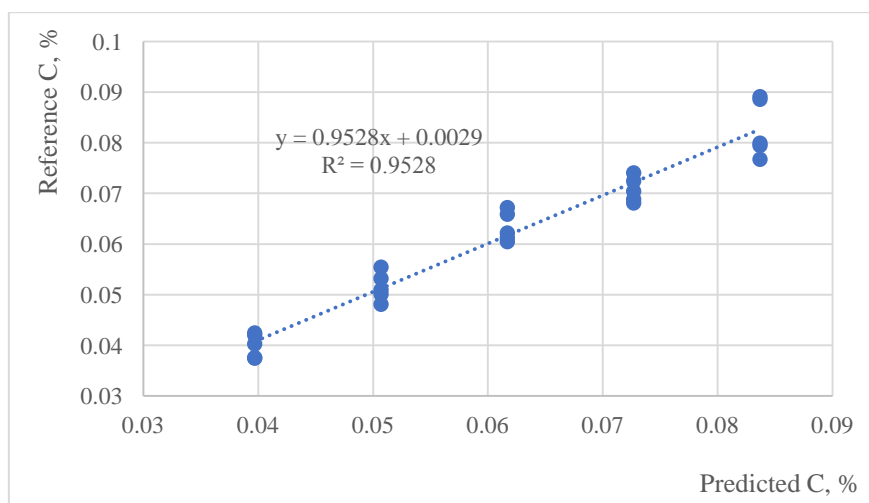
Figure 2. Second calibration set

The experimental design matrix was also modified by replacing the second vacant factor with the number of laser impulses (20–100). Additionally, the range of variation of the lamp energy value was increased to 20J. For the optimization experiment, glass with a concentration of $V(V) = 0.03\%$ was used.

The main influence on the intensity of the $V(II)_{310,224}$ line was also due to the lamp energy, as well as the value of QSW_1 (Fig. 3).

Figure 3. Partial dependence of the $V(II)_{310,224}$ line on Lamp Energy (a) and (b) value

Optimal values of factors for the analysis of the glasses with lower concentration were as follows: Lamp energy — 20 J, QSW_1 — 111 μs , ΔQSW — 3 μs , Delay — 1 μs , Number of impulses — 100. The spectra of the second set of glasses were recorded at the calculated optimal settings. The PLS-R model was retrained based on new data. The training of the model was conducted on 25 spectra (5 spectra for each calibration sample). The visualization of the resulting model characteristics is shown in Figures 4-5. The resulting model was used to determine the concentration of vanadium in the glass without V_2O_5 addition.

Figure 4. Predicted by PLS model and reference concentration of $V(V)$ in calibration set

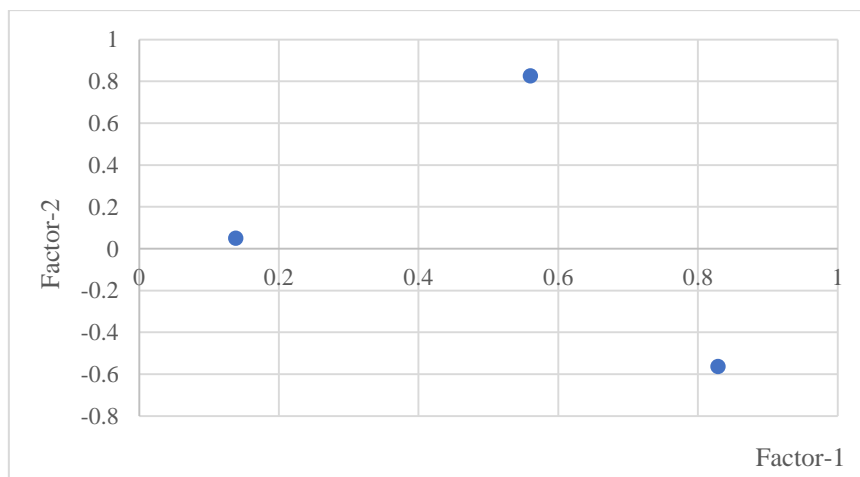


Figure 5. X and Y-loadings of the PLS model

The average V(V) concentration calculated by the model was 0.0299 ± 0.0022 %. New set of calibration samples with lower vanadium concentration increased model accuracy and yielded a refined concentration of vanadium in the glass without the V_2O_5 addition. Additionally, Multiple Linear Regression (MLR) model was trained on the same set of data. The visualization of the model training results is shown in Figure 6. This model was also applied to predict the concentration of vanadium in the glass without any addition.

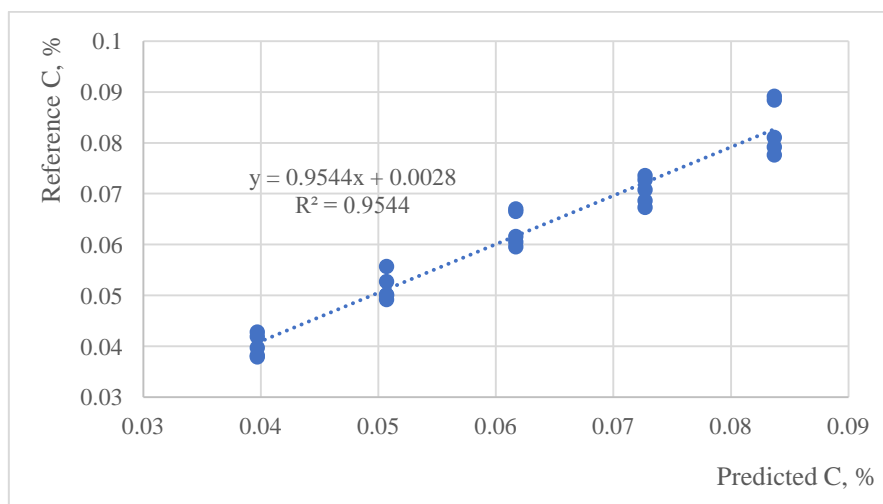


Figure 6. Predicted by MLR model and reference concentration of V(V) in calibration set

The concentration calculated by the model was 0.0297 ± 0.0027 %. The obtained models were additionally applied to samples with unknown vanadium content. Validation of the developed methodology was carried out using atomic emission spectroscopy to analyze samples with unknown vanadium content. The final values of vanadium concentration are reflected in Table 5.

Table 5

Validation of the method

Sample	% V(V) in glass, PLS-R	% V(V) in the ash, PLS-R, %	% V(V) in glass, MLR	% V(V) in the ash, MLR, %	% V(V) in glass, AAS	% V(V) in the ash, AAS, %
Coal ash #1	0.0299 ± 0.0022	0.0441 ± 0.003	0.0297 ± 0.0027	0.0436 ± 0.004	0.0299 ± 0.0016	0.0423 ± 0.0023
Coal ash #2	0.0523 ± 0.0094	0.0769 ± 0.014	0.0532 ± 0.0083	0.0758 ± 0.0118	0.0521 ± 0.0014	0.0774 ± 0.0021
Smelter slag	0.0341 ± 0.0026	0.0502 ± 0.0038	0.0338 ± 0.0032	0.0474 ± 0.0045	0.0352 ± 0.0011	0.0524 ± 0.0016

An attempt was also made to determine the vanadium (V) content in rock samples collected from the Soviet-era mines without additional sample preparation or glass production (Fig. 7). Collection point is indicated in Figure 8. The results of the model calculations and their comparison with the AAS results are presented in Table 6.



Figure 7. Burned-rock samples



Figure 8. Burned-rock sampling point (49°53'28.60"N, 73°5'15.10"E)

Table 6

Vanadium content in the samples analyzed without glass preparation

Sample	% V(V), PLS-R	% V(V), MLR	% V(V), AAS
1	0.0444±0.0078	0.0451±0.0071	0.0405±0.0012
2	0.0354±0.0028	0.0351±0.0032	0.0361±0.0014

An increase in experimental errors and a decrease in the reliability of the model results can be observed. This may be explained by the fact that samples such as rocks, minerals, and ores are heterogeneous; therefore, proper preparation and experimental setup are necessary for determining vanadium in objects of unknown composition. The model could be directly applied in cases where the accuracy of quantitative vanadium determination is not critical, such as in cases of rapid determination of vanadium in samples for quick quality control of raw materials and products in situ.

Conclusions

The developed method demonstrates strong performance in quantifying vanadium in coal ash-based samples. The settings were optimized using a probabilistic-deterministic design of experiment resulting in increase of accuracy in vanadium determination in hydrocarbon-based samples. To achieve the highest intensity of vanadium spectral lines in samples with low content, the optimal instrument settings are as follows: Lamp Energy — 20 J, Q-SW₁ — 111 μs, ΔQ-SW — 3 μs, Delay — 1 μs, number of laser impulses — 100.

Multidimensional calibrations for vanadium quantification were built using PLS-R and MLR methods. The accuracy of the models, calculated on the basis of spectral data from samples of known composition, was 95–98 %.

An analysis of samples with unknown vanadium content was conducted using a combination of the LIBS and chemometrics, followed by validation of the methodology by atomic absorption spectroscopy. Although the accuracy of this method is lower than of classical AAS analysis, and sample preparation is also time and resource consuming, this methodology can be effectively applied to samples where dissolution for subsequent analysis presents certain difficulties. The method can be directly applied to glass and enamel samples — whether from production or archaeological finds. Additionally, satisfactory accuracy was achieved on samples without preliminary preparation, which can be applied for rapid on-site analysis with portable LIBS devices.

Supporting Information

The Supporting Information is available free at <https://ejc.buketov.edu.kz/index.php/ejc/article/view/198/150>

Funding

This research was funded by the Science Committee of the Ministry of Science and Higher Education of the Republic of Kazakhstan (Grant No. AP19677716 “Development of methods for qualitative and quantitative analysis of lead and copper alloys using laser induced breakdown spectroscopy and chemometrics”).

Author Information*

*The authors' names are presented in the following order: First Name, Middle Name and Last Name

Milana Alexandrovna Turovets — Master of Technical Sciences, 1st year PhD Student, Engineer, LEP “Physical-chemical methods of investigation”, Universitetskaya street, 28, 100024, Karaganda, Kazakhstan; *e-mail*: turovec26.07@mail.ru; <https://orcid.org/0000-0002-0493-6426>

Vitaliy Nikolayevich Fomin — Candidate of Chemical Sciences, Head of LEP “Physical-chemical methods of investigation”, Universitetskaya street, 28, 100024, Karaganda, Kazakhstan; *e-mail*: vitfomin@mail.ru; <https://orcid.org/0000-0002-2182-2885>

Nabira Kydyrbekkyzy Kelesbek — Master of Physical Sciences, Junior Researcher, LEP “Physical-chemical methods of investigation”, Universitetskaya street, 28, 100024, Karaganda, Kazakhstan; *e-mail*: knk_93@bk.ru; <https://orcid.org/0000-0002-8578-8081>

Dauletkhan Asanovich Kaykenov — PhD, Lead Researcher, LEP “Physical-chemical methods of investigation”, Universitetskaya street, 28, 100024, Karaganda, Kazakhstan; *e-mail*: krq.daykai@mail.ru; <https://orcid.org/0000-0003-4621-7603>

Daniyar Tleuzhanovich Sadyrbekov — Candidate of Chemical Sciences, Lead Researcher, LEP “Physical-chemical methods of investigation”, Universitetskaya street, 28, 100024, Karaganda, Kazakhstan; *e-mail*: daniyar81@gmail.com; <https://orcid.org/0000-0002-3047-9142>

Assanali Anuarovich Aynabayev — Candidate of Chemical Sciences, Senior Researcher, LEP “Physical-chemical methods of investigation”, Universitetskaya street, 28, 100024, Karaganda, Kazakhstan; *e-mail*: aliopel_82t@mail.ru; <https://orcid.org/0000-0002-3443-446X>

Saule Kidirbayevna Aldabergenova (*corresponding author*) — Candidate of Chemical Sciences, Associated Professor, Department of Inorganic and Technical Chemistry, Karaganda Buketov University, Universitetskaya street, 28, 100024, Karaganda, Kazakhstan; *e-mail*: aldsau@mail.ru; <https://orcid.org/0000-0002-4262-911X>

Author Contributions

The manuscript was written through contributions of all authors. All authors have given approval to the final version of the manuscript. **CRedit**: **Milana Alexandrovna Turovets** conceptualization, data curation, investigation, methodology, validation, visualization, writing-review & editing; **Vitaliy Nikolayevich Fomin** data curation, formal analysis, methodology, visualization, supervision; **Nabira Kydyrbekkyzy Kelesbek** data curation, formal analysis; **Dauletkhan Asanovich Kaykenov** data curation, formal analysis, visualization; **Daniyar Tleuzhanovich Sadyrbekov** data curation, formal analysis; **Assanali Anuarovich Aynabayev** data curation, investigation, formal analysis; **Saule Kidirbayevna Aldabergenova** project administration, writing-review & editing.

Conflicts of Interest

The authors declare no conflict of interest.

References

- 1 Farooq, Z., Ali, R., Ahmed, N., Fahad, M., Ahmad, A. U., Yaseen, M., Mahmood, M. H. R., Hussain, S., Rehan, I., Khan, M. Z., Jan, T., Qayyum, M. A., Afzal, M., Mahr, M. S., & Shafique, M. (2023). Determination of the gold alloys composition by Laser-Induced plasma spectroscopy using an algorithm for matching experimental and calculated values of electron number density. *Journal of Applied Spectroscopy*, 90(1), 126–136. <https://doi.org/10.1007/s10812-023-01513-x>
- 2 Salloom, H., & Hamad, T. (2021). Investigation of compositional analysis and physical properties for Ni-Cr-Nb alloys using laser-induced breakdown spectroscopy. *Optica Applicata*, 51(3). <https://doi.org/10.37190/oa210310>
- 3 Fomin, V., Aldabergenova, S., Kelesbek, N., Kaykenov, D., & Turovets, M. (2024). Method of classification and quantitative analysis of vein quartz using LIBS and chemometric techniques. *Bulletin of the L.N. Gumilyov Eurasian National University Chemistry. Geography Ecology Series*, 147(2), 48–60. <https://doi.org/10.32523/2616-6771-2024-147-2-48-60>
- 4 He Y., Zhou W., Ke C., Xu T., Zhao Y. (2021). Review of Laser-Induced Breakdown Spectroscopy in Gas Detection. *Spectroscopy and spectral analysis*, 41(9), 2681–2687. [https://doi.org/10.3964/j.issn.1000-0593\(2021\)09-2681-07](https://doi.org/10.3964/j.issn.1000-0593(2021)09-2681-07)
- 5 Chen, Y., Si, J., Wan, X., Wang, Y., Chen, A., & Jin, M. (2024). Sub-ppb detection limit of Cr, Pb, and Cu in water by surface-enhanced LIBS with femtosecond laser. *Spectrochimica Acta Part B Atomic Spectroscopy*, 213, 106880. <https://doi.org/10.1016/j.sab.2024.106880>
- 6 Ma, S., Guo, L., & Dong, D. (2022). A molecular laser-induced breakdown spectroscopy technique for the detection of nitrogen in water. *Journal of Analytical Atomic Spectrometry*, 37(3), 663–667. <https://doi.org/10.1039/d1ja00419k>
- 7 Goncharova, I., Guichaoua, D., Taboukhat, S., Tarbi, A., Chtouki, T., Erguig, H., & Sahraoui, B. (2024). Laser-induced breakdown spectroscopy application for heavy metals detection in water: A review. *Spectrochimica Acta Part B Atomic Spectroscopy*, 217, 106943. <https://doi.org/10.1016/j.sab.2024.106943>
- 8 Al-Najjar, O. A., Wudil, Y. S., Ahmad, U. F., Al-Amoudi, O. S. B., Al-Osta, M. A., & Gondal, M. A. (2022). Applications of laser induced breakdown spectroscopy in geotechnical engineering: a critical review of recent developments, perspectives and challenges. *Applied Spectroscopy Reviews*, 58(10), 687–723. <https://doi.org/10.1080/05704928.2022.2136192>
- 9 De Morais, C. P., Nicolodelli, G., Mitsuyuki, M. C., Mounier, S., & Milori, D. M. B. P. (2021). Optimization of laser-induced breakdown spectroscopy parameters from the design of experiments for multi-element qualitative analysis in river sediment. *Spectrochimica Acta Part B Atomic Spectroscopy*, 177, 106066. <https://doi.org/10.1016/j.sab.2021.106066>
- 10 Malyshev V. P. (1981). Veroyatnostno-determinirovanoe planirovanie eksperimenta [Probabilistic and deterministic experiment planning]. Almaty: Nauka, 115 p.
- 11 Belyaev S. V., Malyshev V. P. (2008). Puti razvitiia veroyatnostno-determinirovannogo planirovaniia eksperimenta. Kompleksnaia pererabotka mineralnogo syria Kazakhstana [Ways of developing probabilistic and deterministic experiment planning. Complex processing of mineral raw materials of Kazakhstan]. *Sostoianie, problemy, resheniia — Status, problems, solutions*, 9, 8, 599–633.
- 12 Fomin V. N., Usmanova E. R., Gyul E. F., Kelesbek N. K., Turovets M. A., Zemskiy O. I., Saulebekov D. M., Aldabergenova S. K. Method for qualitative and quantitative analysis of ancient lead enamel using laser induced breakdown spectroscopy. (2022). *Bulletin of the University of Karaganda-Chemistry*, 108, 107–117. <https://doi.org/10.31489/2022Ch4/4-22-16>
- 13 Fomin V. N., Aynabaev A. A., Kaykenov D. A., Sadyrbekov D. T., Aldabergenova S. K., Turovets M. A., Kelesbek N. K. Optimization of coal tar gas chromatography conditions using probabilistic-deterministic design of experiment. (2021). *Bulletin of the University of Karaganda-Chemistry*, 104, 39–46. <https://doi.org/10.31489/2021Ch4/39-46>
- 14 Fomin, V. N., Aldabergenova, S. K., Rustembekov, K. T., Omarov, K. B., Rozhkovoy, I. E., Dik, A. V., & Saulebekov, D. M. (2021). Optimization of the parameters of a laser induced breakdown spectrometer (LIBS) using probabilistic-deterministic design of experiment. *Industrial Laboratory Diagnostics of Materials*, 87(5), 14–19. <https://doi.org/10.26896/1028-6861-2021-87-5-14-19>

- 15 Gogol, D. B., Rozhkovoy, I. E., Sadyrbekov, D. T., & Makasheva, A. M. (2023). Deposition of Transition Metal onto Carbonate Materials Surface: Theoretical Evaluation of Optimal Parameters. *Eurasian Journal of Chemistry*, 28(4)(112). <https://doi.org/10.31489/2959-0663/4-23-13>
- 16 Gupta, V., Rai, A. K., Kumar, T., Junjuri, R., Kumar, G. M., & Rai, A. K. (2023). Chemical and physical studies of metallic alloy-based old Indian coins with LIBS coupled with multivariate analysis. *Plasma Science and Technology*, 25(9), 095501. <https://doi.org/10.1088/2058-6272/accd9>
- 17 Gupta, V., Rai, A. K., Kumar, T., Tarai, A., Gundawar, G. M. K., & Rai, A. K. (2023). Compositional analysis of copper and iron-based alloys using LIBS coupled with chemometric method. *Analytical Sciences*, 40(1), 53–65. <https://doi.org/10.1007/s44211-023-00429-y>
- 18 Farhadian, A. H., & Fard, S. S. M. (2021). Quantitative analysis and identification improvement in Laser-Induced breakdown spectroscopy by Self-Absorption correction and artificial neural network. *IEEE Transactions on Plasma Science*, 49(12), 3853–3859. <https://doi.org/10.1109/tps.2021.3123434>
- 19 Cioccia, G., De Morais, C. P., Babos, D. V., Milori, D. M. B. P., Alves, C. Z., Cena, C., Nicolodelli, G., & Marangoni, B. S. (2022). Laser-Induced Breakdown Spectroscopy Associated with the Design of Experiments and Machine Learning for Discrimination of *Brachiaria brizantha* Seed Vigor. *Sensors*, 22(14), 5067. <https://doi.org/10.3390/s22145067>
- 20 Adarsh, U., Bankapur, A., Pai, A. K., Kartha, V., & Unnikrishnan, V. (2024). Advanced chemometric methodologies on single shot hyphenated LIBS data for rapid and reliable characterization of plastic classes. *Talanta*, 277, 126393. <https://doi.org/10.1016/j.talanta.2024.126393>
- 21 Dou, Y., Wang, Q., Wang, S., Shu, X., Ni, M., & Li, Y. (2023). Quantitative analysis of coal quality by a portable laser induced breakdown spectroscopy and three chemometrics methods. *Applied Sciences*, 13(18), 10049. <https://doi.org/10.3390/app131810049>
- 22 Liu, Z., Li, L., Xu, W., Xu, X., Cui, Z., Jia, L., Lv, W., Shen, Z., & Shu, R. (2023). Investigation into the Affect of Chemometrics and Spectral Data Preprocessing Approaches upon Laser-Induced Breakdown Spectroscopy Quantification Accuracy Based on MarSCoDe Laboratory Model and MarSDEEP Equipment. *Remote Sensing*, 15(13), 3311. <https://doi.org/10.3390/rs15133311>
- 23 Brunnbauer, L., Gajarska, Z., Lohninger, H., & Limbeck, A. (2022). A critical review of recent trends in sample classification using Laser-Induced Breakdown Spectroscopy (LIBS). *TrAC Trends in Analytical Chemistry*, 159, 116859. <https://doi.org/10.1016/j.trac.2022.116859>
- 24 Liu, C., Luo, Y., & Zhang, Q. (2021). Laser-Induced Breakdown Spectroscopy-Based Coal-Rock Recognition: An in situ sampling and recognition method. *IEEE Access*, 9, 164732–164741. <https://doi.org/10.1109/access.2021.3133886>
- 25 Liu, K., He, C., Zhu, C., Chen, J., Zhan, K., & Li, X. (2021). A review of laser-induced breakdown spectroscopy for coal analysis. *TrAC Trends in Analytical Chemistry*, 143, 116357. <https://doi.org/10.1016/j.trac.2021.116357>
- 26 Israr, M. A., Abbas, Q., Haq, S. U., & Nadeem, A. (2022). Analysis of carbon contents and heavy metals in coal samples using calibration-free LIBS technique. *Journal of Spectroscopy*, 2022, 1–11. <https://doi.org/10.1155/2022/3328477>
- 27 Liu, C., Luo, Y., & Zhang, Q. (2021). Laser-Induced Breakdown Spectroscopy-Based Coal-Rock Recognition: An in situ sampling and recognition method. *IEEE Access*, 9, 164732–164741. <https://doi.org/10.1109/access.2021.3133886>
- 28 Zhang, W., Zhuo, Z., Lu, P., Sun, T., Sun, W., & Lu, J. (2021). Determination of vanadium, iron, and nickel in petroleum coke by laser-induced breakdown spectroscopy. *Spectrochimica Acta Part B Atomic Spectroscopy*, 177, 106076. <https://doi.org/10.1016/j.sab.2021.106076>
- 29 Khan, M. N., Wang, Q., Idrees, B. S., Waheed, R., Haq, A. U., Abrar, M., & Jamil, Y. (2023). Evaluation of medicinal plants using laser-induced breakdown spectroscopy (LIBS) combined with chemometric techniques. *Lasers in Medical Science*, 38(1). <https://doi.org/10.1007/s10103-023-03805-2>
- 30 Lu, C., Wang, M., Wang, L., Hu, H., & Wang, R. (2019). Univariate and multivariate analyses of strontium and vanadium in soil by laser-induced breakdown spectroscopy. *Applied Optics*, 58(27), 7510. <https://doi.org/10.1364/ao.58.007510>
- 31 Lu, P., Zhuo, Z., Zhang, W., Sun, T., Sun, W., & Lu, J. (2022). Quantitative analysis of trace elements (vanadium, sodium, and calcium) in petroleum coke using laser-induced breakdown spectroscopy with binder. *Spectrochimica Acta Part B Atomic Spectroscopy*, 190, 106388. <https://doi.org/10.1016/j.sab.2022.106388>
- 32 Du, H., Sun, T., Ke, S., Qi, D., Zhang, W., Wei, J., Yang, B., & Zheng, H. (2024). An ensemble model for rapid quantitative determination of vanadium (V) in petroleum coke by laser-induced breakdown spectroscopy. *Journal of Analytical Atomic Spectrometry*. <https://doi.org/10.1039/d4ja00300d>
- 33 Bol'shakov, A. A., Pandey, S. J., Mao, X., & Liu, C. (2021). Analysis of liquid petroleum using a laser-induced breakdown spectroscopy instrument. *Spectrochimica Acta Part B Atomic Spectroscopy*, 179, 106094. <https://doi.org/10.1016/j.sab.2021.106094>

Saida Soualmi^{1*} , Meriem Henni¹ , Leila Djahnit^{2,3} , Hanane Hamdani¹

¹Laboratory of Synthesis and Catalysis, University of Ibn Khaldoun Tiaret, Tiaret, Algeria;

²Chemistry Department, Faculty of Exact Sciences and Informatics, University Hassiba Benbouali Chlef (UHBC), Chlef, Algeria;

³Renewable Energy and Materials Laboratory, University of Medea, Medea, Algeria

(*Corresponding author's e-mail: saida.soualmi@univ-tiaret.dz)

Sol-gel Synthesized ZnO–SrMn₂O₄ Nanocomposite and Its Antibacterial Properties

This paper presents the synthesis of new binary oxide nanoparticles (NPs), ZnO–SrMn₂O₄, with a spinel structure. The sol-gel technique was used to synthesize ZnO–SrMn₂O₄ spinel-type oxides, which were subsequently investigated for their antibacterial properties. The NPs were characterized by a range of methods, namely Fourier transform infrared spectroscopy (FTIR), X-ray diffraction (XRD), scanning electron microscopy (SEM), and energy dispersive X-ray analysis (EDX). The FTIR analysis revealed the presence of peaks characteristic of SrMn₂O₄ and ZnO/SrMn₂O₄. These peaks confirm the presence of metal-oxygen bonds, namely Zn–O, Mn–O, and Sr–O. SEM was used to analyze the morphology, chemical composition, and size of the nanocrystals. The morphology of the particles is observed to be more irregular in shape, with a wide range of nanoparticle sizes, from 54 to 250 nm. The synthesized nanoparticles, ZnO–SrMn₂O₄, were used to assess their antibacterial properties against *Bacillus cereus*, *Bacillus subtilis*, *Staphylococcus aureus*, as well as *Escherichia coli* and demonstrated pronounced antibacterial efficacy. The highest antibacterial activity was recorded against *Escherichia Coli*, with a diameter range of 16–23 mm, followed by the strain *Staphylococcus aureus* with a diameter range of 13.5–27.5 mm. The next most active strain was *Bacillus subtilis*, with a diameter range of 12.5–22 mm, and *Bacillus cerus*, with a diameter range of 13.5–19 mm. Further use of the obtained ZnO–SrMn₂O₄ powder is recommended for application in photocatalysis of dye degradation.

Keywords: Nanocomposite, antibacterial activity, spinel, zinc oxide, Sol-gel, SEM, XRD, binary oxide.

Introduction

This paper presents the synthesis of binary oxide nanoparticles ZnO (30 %) SrMn₂O₄ with a spinel structure. In recent years, there has been a considerable increase in interest in nanocomposites, driven by their prospective applications in a range of fields, including public health and environmental remediation. In particular, the combination of photocatalytic and antibacterial properties offers a powerful strategy for eliminating contaminants and infections from water, air, and a range of other environments. These nanocomposites have shown promising antibacterial efficacy against both Gram-positive and Gram-negative bacterial strains, as well as strains with multidrug resistance. Thus, ZnO-based nanomaterials have been reported to be synthesized with improved antibacterial properties, especially when Au NPs are incorporated [1–5]. Moreover, researchers attributed the various trends observed for the interactions between the diverse components of the nanocomposite and the bacterial cells to the enhanced antimicrobial performance of ZnO NPs in the presence of GO or RGO [6]. The synthesis and design of MnO and ZnO nanoparticles have resulted in the preparation of new MnO/ZnO nanocomposites with marked antibacterial efficacy. These nanocomposites have demonstrated high inhibition rates against *E. coli* and other pathogenic bacteria, indicating that they play a vital role in overcoming bacterial resistance [7]. Further research is required to synthesize the ZnMn₂O₄/ZnO nanocomposite for antibacterial purposes, as the existing research base for new materials claiming improved antimicrobial efficiency is insufficient. Previous research indicates that the synthesis of nanocomposites comprising zinc oxide nanoparticles and manganese (II) oxide enhances the antibacterial properties of the nanoparticles [8]. Moreover, numerous other nanocomposites, including Fe₃O₄/ZnO-based materials, have demonstrated noteworthy antibacterial properties, suggesting potential applications in the management of bacterial infections [9]. Previous research established candidature-level reactions in ZnO and MnWO₄, and both of these nanoparticles show potent antibacterial results. The synthesis of ZnO nanoparticles has been optimized for antibacterial properties, considering synthesis parameters [10]. The nanostructures of ZnO surfaces possess great antibacterial activity, which causes bacterial cell lysis in microfluidic devices [11]. In contrast, MnO₂ nanoparticles have been demonstrated to exhibit antibacterial and anti-

biofilm properties against quinolone-resistant gram-positive and negative pathogenic bacteria, including *S. aureus* and *E. coli* [12]. It is conceivable that a synergistic effect may be observed between ZnO and MnWO_4 , which could result in an enhanced antibacterial activity of the composite material. Further research into the antibacterial efficacy of a composite material comprising ZnO doped with SrMn_2O_4 could facilitate the modification and enhancement of the efficiency of the antibacterial agents employed in the medical field, as well as other professional contexts. ZnO nanoparticles have demonstrated high antibacterial efficacy due to a number of mechanisms, including the liberation of Zn^{+2} , the generation of reactive oxygen species (ROS), and the intercalation of microbial cell membranes [13]. Furthermore, the antibacterial efficacy of ZnO nanomaterials can be enhanced through the formation of composites with other materials, such as SrMn_2O_4 , which has the potential to markedly inhibit the recombination of electrons and holes [14]. The literature indicates that ZnO and Mn-doped ZnO nanoparticles, when immobilized on titanium implants, are effective against the majority of bacterial profiles. Furthermore, the $\text{Zn}_x\text{Mn}_{(1-x)}\text{O}@\text{Ti}$ hybrids have been shown to outperform $\text{ZnO}@\text{Ti}$ [15]. The results of this research study allow us to hypothesise that the addition of ZnO with other materials, such as SrMn_2O_4 , and the introduction of metal ions, including Mn, will enhance the creation of more effective antibiotics with the potential to combat microbial antibiotic resistance.

Experimental

Materials used

Strontium nitrate ($\text{Sr}(\text{NO}_3)_2$), manganese (II) nitrate hydrate ($\text{Mn}(\text{NO}_3)_2 \cdot 4\text{H}_2\text{O}$), zinc acetate ($\text{Zn}(\text{O}_2\text{CCH}_3)_2 \cdot 2\text{H}_2\text{O}$), sodium hydroxide (NaOH), ethanol and Acid citric were purchased from Sigma Aldrich. Fourier transform infrared (FT-IR) spectra were recorded using an FTIR-8400 type SHIMADZU spectrometer. The measurement of X-ray diffraction patterns was carried out using a Rigaku MINIFLEX 600 diffractometer. The products morphology was determined using scanning electron microscopy (SEM) techniques on the SEM-QUANTA 650 FEI.

Synthesis of ZnO nanoparticles

In order to synthesize ZnO nanoparticles, a solution of $\text{Zn}(\text{NO}_3)_2 \cdot 6\text{H}_2\text{O}$ (250 mL, 0.2 M) and a solution of NaOH (250 mL, 0.5 M) were prepared with deionized water. The sodium hydroxide solution was added dropwise using a burette to the zinc acetate solution at room temperature. This was achieved by stirring vigorously until a pH of 12 was reached. This resulted in the formation of a white precipitate of zinc hydroxide ($\text{Zn}(\text{OH})_2$), which was separated by centrifugation for 30 min and washed three times with distilled water and then ethanol. The resulting product was dried at 60 °C in an air atmosphere for 24 hours to convert $\text{Zn}(\text{OH})_2$ into ZnO NPs.

Synthesis of SrMn_2O_4 nanoparticles

The synthesis of SrMn_2O_4 NPs involved the dissolution of 1.571 g of $\text{Sr}(\text{NO}_3)_2$ in 40 ml of ethanol. Conversely, 4.713 g of manganese nitrate (II) hydrate ($\text{Mn}(\text{NO}_3)_2 \cdot 4\text{H}_2\text{O}$) was dissolved in 110 ml of ethanol. The two solutions previously obtained were added, in a dropwise manner, to a solution of citric acid, which was prepared by dissolving 5.106 g of $\text{C}_6\text{H}_8\text{O}_7$ in 100 ml of demineralized water. Subsequently, the solution was heated to 80 °C for a period of three hours, with stirring using a magnetic stirrer.

The solution underwent evaporation, forming a gel that was subsequently subjected to drying at 60 °C and calcination at 700 °C for four hours. This process resulted in the formation of SrMn_2O_4 nanocomposites, as illustrated in Figure 1.



Figure 1. Preparation of ZnO (30 %) SrMn_2O_4 using the sol gel method.

Synthesis of ZnO (30 %) SrMn₂O₄ nanocomposites

In order to develop ZnO (30 %) SrMn₂O₄ nanocomposite powders, the same synthesis protocol for SrMn₂O₄ must be followed, with the exception that the previous solutions are mixed with the incorporation of ZnO 30 % (molar percentage).

Results and Discussion

To explain the phase structure and the degree of crystallinity of the synthesized products X-ray diffraction was used. The XRD pattern of the prepared samples is presented in Figure 2. The reflection peaks observed at values of 25°, 60.63°, 33.39°, 36.73°, 45.06°, 50.48°, 59.61°, and 61.45° correspond to the data of JCPDS n°96-400-1312 and card n° JCPDS 96-9007521. The prepared sample of ZnO NPs corresponds to the JCPDS card n°96.101-1259. XRD data confirm formation of ZnO.

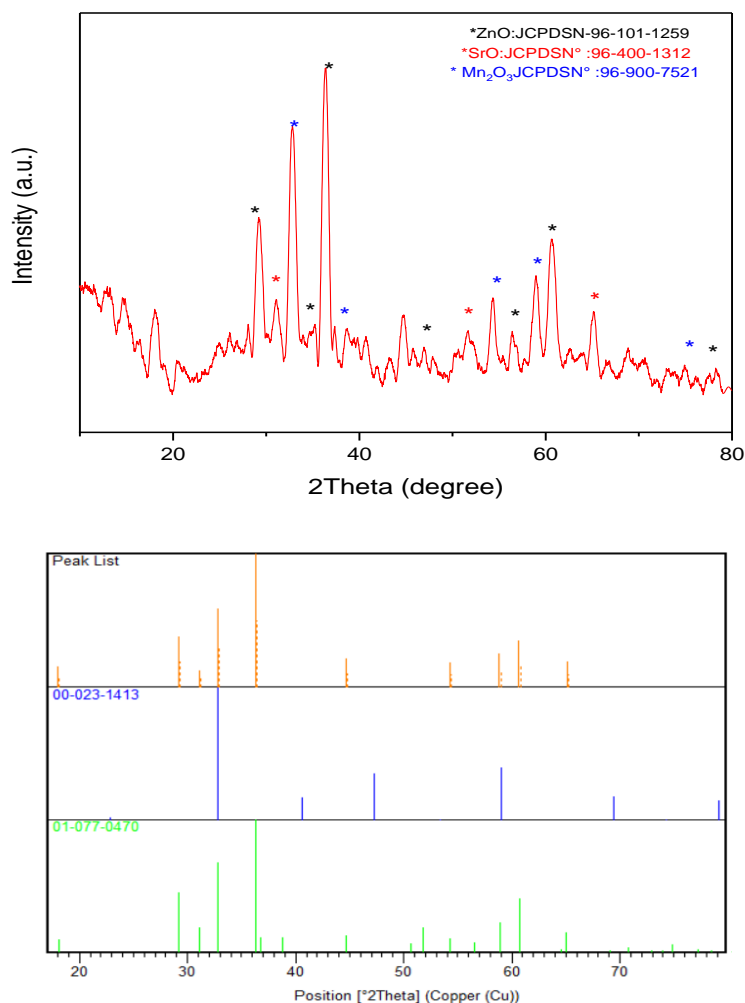


Figure 2. XRD pattern of SrMn₂O₄ with Reference number

In the case of ZnO (30 %) SrMn₂O₄, the reflected peaks were observed at 25°, 60.63°, 33.39°, 36.73°, 45.06°, 50.48°, 59.61°, and 61.45°, corresponding to plans (101), (112), (103), (202), (220), (204), (321), and (224) (Fig. 3).

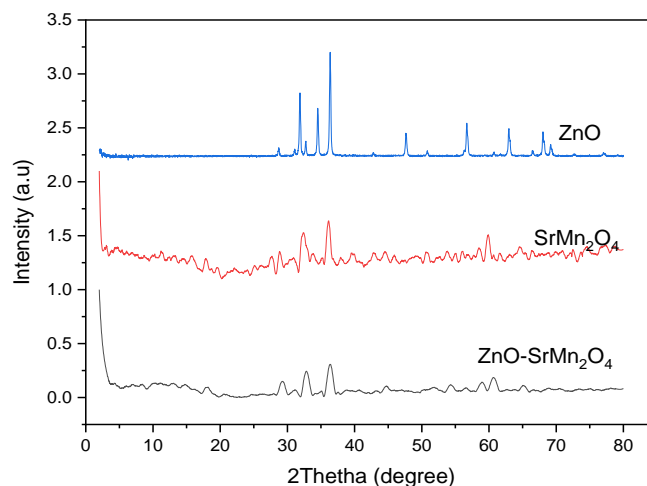


Figure 3. XRD pattern of ZnO, SrMn₂O₄ and ZnO (30 %) SrMn₂O₄

The Scherrer equation [16], which is $D_c = K\lambda/\beta \cos\theta$, was used for the calculation of crystallites. In this formula, β represents the width of the observed diffraction peak at half of its maximum height, also known as FWHM, which stands for full width at half maximum. K is the shape factor, its value varies and it is approximately equal to 0.9 and λ is the X-ray wavelength (CuK α radiation, which is equal to 0.154 nm). From the Scherrer equation, the average crystalline sizes were found to be 42 nm for ZnO, 13 nm for SrMn₂O₄, and 20 nm for the ZnO (30 %) SrMn₂O₄ composite, respectively.

The FTIR spectra for ZnO, SrMn₂O₄, and ZnO (30 %) SrMn₂O₄ are presented in (Fig. 4) below. In the case of ZnO, the stretching vibration of the Zn–O bond is related to the peak at 498.75 cm⁻¹. In the case of SrMn₂O₄, the large peak observed at approximately 512.85 cm⁻¹ is due to the vibration of the Mn–O functional group, which is associated with the tetrahedral coordination of MnO₂ ions. Bands at approximately 611.52 cm⁻¹ correspond to stretching vibrations of Sr–O [17]. The presence of peaks for SrMn₂O₄ and ZnO/SrMn₂O₄ confirm the existence of metal-oxygen bonds (Zn–O, Mn–O, and Sr–O). A less intense band appears approximately at 3500 cm⁻¹, which can be attributed to the stretching vibration of the O–H group originating from H₂O molecules adsorbed on the surface of the material. Another peak was identified at 1600 cm⁻¹, which is attributed to O–H bending vibrations.

In the case of ZnO (30 %) SrMn₂O₄ (Fig. 4), a shift in the FTIR peaks was observed, which is frequently associated with alterations in the bond lengths and bond angles within the crystal structure. ZnO can cause a change in the vibrational frequencies of Sr–O bonds, a phenomenon that is frequently observed by FTIR. This shift is a consequence of the substitution of Zn²⁺ ions within the structure, which results in alterations to the intermediate distances and bond strengths.

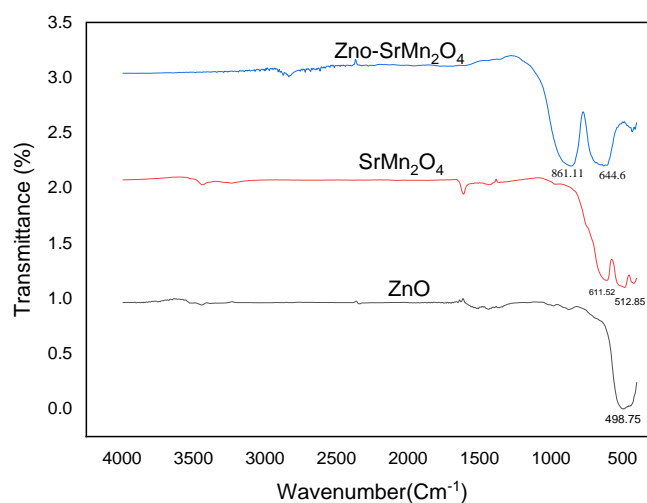


Figure 4. FTIR spectra of ZnO nanoparticles, SrMn₂O₄ and ZnO (30 %) SrMn₂O₄.

Figure 5 illustrates the morphology of the particles, which exhibit a more irregular shape and a wide range of nanoparticle sizes, spanning from 54 to 250 nm.

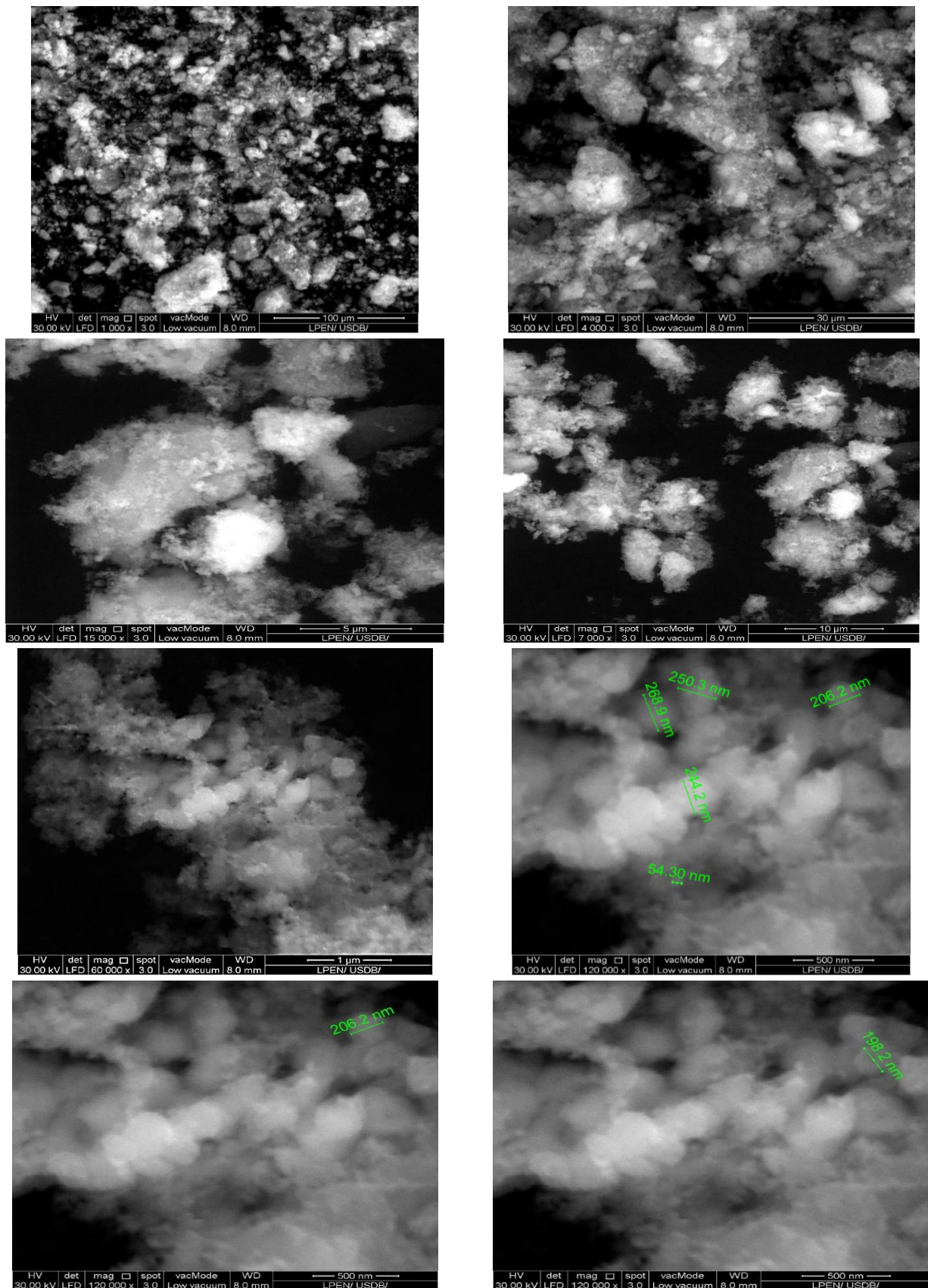


Figure 5. SEM micrograph of ZnO (30 %) SrMn₂O₄ NPs

Energy dispersive X-ray (EDX) analysis was used to examine the chemical components of the produced nanoparticles, which revealed the presence of zinc, oxygen, Sr and Mn atoms (Fig. 6). Table 1 presents the atomic percentages of each element. These results demonstrate that the ZnO sample (30 %) SrMn₂O₄ contains amounts of Sr, Zn, Mn, and O. Additionally, carbon was detected, originating from the support where the material used during the EDX manipulation was deposited.

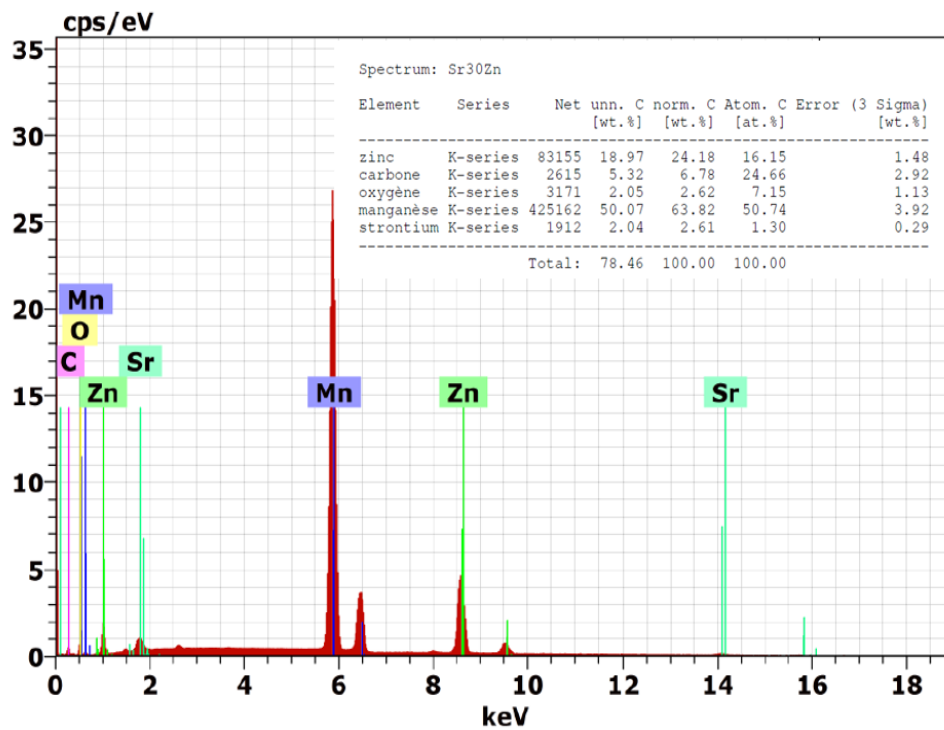


Figure 6. EDX images of synthesized ZnO (30 %) SrMn₂O₄ NPs

Antibacterial activity

The antibacterial activity of ZnO (30 %) SrMn₂O₄ nanoparticles was determined using the well diffusion method [18, 19]. An 18-hour culture of Gram-positive (*Bacillus cereus* (ATCC10876), *Bacillus subtilis* (ATCC 6633), and *Staphylococcus aureus* (ATCC 25925)) and Gram-negative (*Escherichia coli* (ATCC 25922)) strains was adjusted to 0.5 McFarland. Freshly prepared Mueller-Hinton agar plates were inoculated with 100 µl of bacterial suspension. Four wells of 8 mm in diameter were created on the agar plates. Subsequently, 100 µl of ZnO (30 %) SrMn₂O₄ nanoparticles of different concentration were added to each well. Then, the Petri dishes were left at 4 °C for 30 min for good diffusion of the nanoparticles. The plates were incubated at 37 °C for 24 hours. Inhibition zones were measured in millimetres.

The antibacterial activity of the ZnO (30 %) SrMn₂O₄ nanoparticles was confirmed by the appearance of clear zones around the wells (Fig. 7).

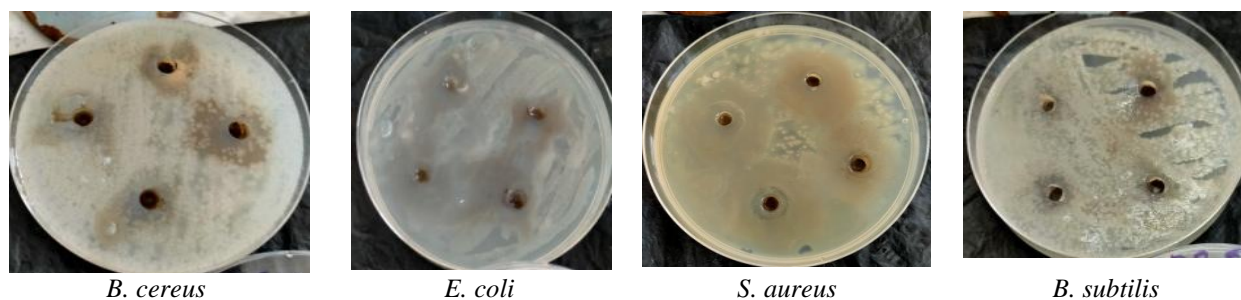


Figure 7. Results of the antibacterial activity of ZnO (30 %) SrMn₂O₄

The diameters of the inhibition zones of the nanoparticles against Gram-positive and Gram-negative bacteria are presented in Figure 8 and Table 1. These results demonstrate the effective inhibitory effect of the synthesized nanoparticles. Furthermore, the highest antibacterial activity was observed against *Escherichia Coli*, with a diameter ranging between 16 and 23 mm, followed by the strain *Staphylococcus aureus*, with a diameter ranging from 13.5 to 27.5 mm, *Bacillus subtilis* with a diameter ranging from 12.5 to 22 mm and *Bacillus cereus* with a diameter ranging from 13.5 to 19 mm. These data affirm that the increase in the concentration of SrMn₂O₄ 30 %ZnO nanoparticles is accompanied by the increase in inhibition of the growth of these bacteria. Furthermore, this variation in activity can be attributed to the structural variations in the cell walls of the pathogenic strains selected and also to the size, morphology and composition of the nanoparticles under consideration.

Additionally, the mechanism of antimicrobial action of nanoparticles is generally described as adhering to one of three models: induction of oxidative stress [20], the release of metal ions [21] or non-oxidative mechanisms [22]. It is possible for all three types of mechanisms to occur simultaneously.

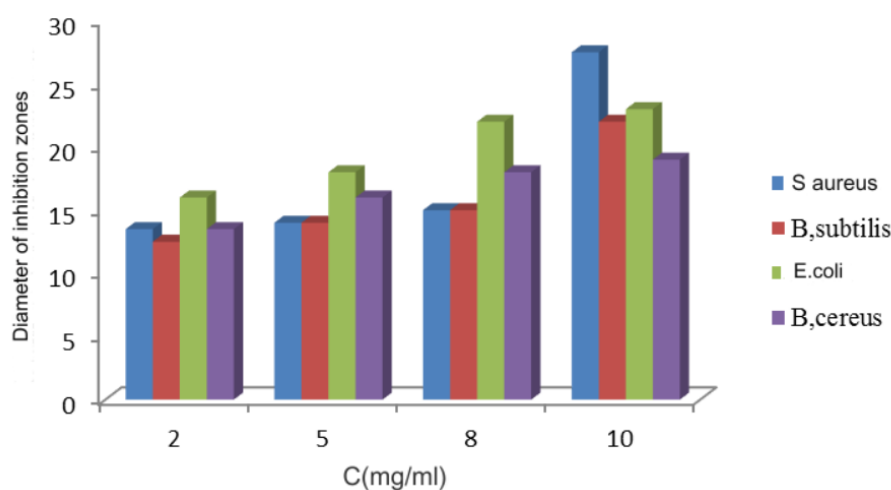
The findings of our research indicate that SrMn₂O₄ 30 %ZnO nanoparticles exhibit considerable efficacy in combating pathogens. The nanoparticles function in a manner analogous to other compounds, including ZnO/SrZnO₂ and ZnMn₂O₄-chitosan. The synthesis of these nanoparticles was carried out using sol-gel methods. [23–26]. These compounds have been demonstrated to be highly effective in the killing of bacteria, including *E. coli*, *S. aureus*, and *P. aeruginosa*. The *E. coli* demonstrated greater susceptibility to the ZnO/SrZnO₂ composite than either oxide individually, as it relies on pure ZnO or SrZnO₂ oxide for normal cellular activity.

ZnO–SnO₂ nanoparticles demonstrated pronounced antibacterial activity against *Staphylococcus aureus*, *Streptococcus mutans*, and *Escherichia coli*. The efficacy of the nanoparticles was demonstrated at both high and low concentrations. The ZnO–CuO composite particles were also observed to exhibit antibacterial activity against both gram-positive and gram-negative bacteria. The nanoparticles were tested against a range of bacteria, including *Staphylococcus aureus*, *E. coli*, and *Pseudomonas aeruginosa*.

Table 1

Zone of inhibition of SrMn₂O₄-ZnO against bacterial strains

Microorganisms	ZnO (30 %) SrMn ₂ O ₄ NPs			
	2(mg/ml)	5(mg/ml)	8(mg/ml)	10(mg/ml)
<i>Staphylococcus aureus</i>	13.5	14	15	27.5
<i>Bacillus subtilis</i>	12.5	14	15	22
<i>Escherichia coli</i>	16	18	22	23
<i>Bacillus cerus</i>	13.5	16	18	19

Figure 8. Antimicrobial activity of ZnO (30 %) SrMn₂O₄ nanoparticles

Comparison of results with published data nanoparticles

Nanocomposite	Antimicrobial Activity	Effective Bacteria/Fungi	Mechanism	Average particle sizes	Stability	Ref.
ZnO	99.99 % 99.63 %	<i>E. coli</i> <i>S. aureus</i> <i>B. cinerea</i>	ROS, Disruption of Cell Membrane Integrity	20–40 nm	Size and Surface Area Effects and Role of Plant Extracts	27
ZnO	significant	<i>E.coli</i> and <i>S. aureus</i> <i>A. nige</i>	Physical and chemical interactions like Electrostatic Effects: Membrane Abrasion and ROS	nanoporous	Surface Area Effects	28
ZnO–Ag	higher	against <i>E. coli</i> compared to <i>S. aureus</i>	Membrane Disruption and ROS, Inhibition of Cellular Functions and Multitarget Mechanism	14.8 nm	pH range of 7-8 increasing Ag concentrations ameliorate stability in various environments	29
Zn–CuO	superior	<i>S. aureus</i> and <i>E. coli</i>	ROS and Cell Membrane Disruption	8 nm to 25.58 nm	Stabilization by Vaccinium arctostaphylos L. fruit extract Zingiber officinale Rhizome Extract	30, 31
ZnO/TiO ₂	significant	<i>Staphylococcus aureus</i> and Gram-negative bacteria (<i>Escherichia coli</i> , <i>Pseudomonas aeruginosa</i> , <i>Klebsiella pneumoniae</i> , <i>Salmonella Paratyphi A</i>) as well as fungi (<i>Candida albicans</i> , <i>Aspergillus flavus</i>)	The antimicrobial mechanism is primarily attributed to the production of reactive oxygen species (ROS), which induce oxidative stress and apoptosis in microbial cells	30 to 100 nm	/	32
MnO/ZnO	High Inhibition Rate: The MnO/ZnO-2.5 % nanocomposite 92.3 %	Achieving an inhibition rate against <i>E. coli</i>	ROS Damage to Bacterial Cells Photocatalytic Activity	/	Synergistic Effects of Doping:	33
Our research	Significant	<i>S. aureus</i> <i>B. subtilis</i> <i>E. coli</i> <i>B. cerus</i>	ROS, release of metal ions, non-oxidative mechanisms	Particles in a more irregular shape with a wide (54-250)	Stabilization by citric acid	

Conclusions

In conclusion, the sol-gel process for the synthesis of ZnO, SrMn₂O₄, and ZnO (30 %) SrMn₂O₄ nanostructures has been described in detail above. The characterization of the developed samples was carried out using FTIR, SEM, EDX, and XRD. The synthesised nanostructures were employed to assess their antibacterial characteristics, and the results demonstrated that the SrMn₂O₄/30 %ZnO NPs exhibited a pronounced pathogen-suppressing capacity. It is recommended that the ZnO-SrMn₂O₄ powder be employed further for the photocatalytic degradation of dyes. The ZnO/SrZnO₂ material demonstrated a notable photocatalytic effect for the degradation of Congo red dye after 80 minutes of UV/vis irradiation [23], and as an electrode material in supercapacitors, as evidenced by the NiO/ZnMn₂O₄ materials, which exhibited a specific capacity [34].

 Author Information*

*The authors' names are presented in the following order: First Name, Middle Name and Last Name

Saida Soualmi (*corresponding author*) — Doctor and Researcher, Laboratory of Synthesis and Catalysis, University of Ibn Khaldoun Tiaret, 14000, Tiaret, Algeria; *e-mail*: saida.soualmi@univ-tiaret.dz; <https://orcid.org/0009-0009-4858-8695>

Meriem Henni — Doctor and Researcher, Laboratory of Synthesis and Catalysis, University of Ibn Khaldoun Tiaret, 14000, Tiaret, Algeria; *e-mail*: hanan1112@yahoo.fr, <https://orcid.org/0009-0005-5378-0674>

Leila Djahnit — Doctor and Researcher, Chemistry Department, Faculty of Exact Sciences and Informatics, University Hassiba Benbouali Chlef (UHBC), 02000, Chlef, Algeria; Renewable Energy and Materials Laboratory, University of Medea, 26000, Medea, Algeria; *e-mail*: Leila_djahnit@yahoo.fr, <https://orcid.org/0000-0001-5834-8024>

Hanane Hamdani — Master Student. Chemistry Department, Laboratory of Synthesis and Catalysis, University of Ibn Khaldoun Tiaret, 14000, Algeria; *e-mail*: hananehamdani25@gmail.com

 Author Contributions

The manuscript was written through contributions of all authors. All authors have given approval to the final version of the manuscript: **Saida Soualmi** conceptualization, data curation, investigation, methodology, validation, visualization, writing-review & editing; **Meriem Henni** application of the antibacterial activity of the synthesized materials; **Leila Djahnit** conservation of antibacterial activity data, **Hanane Hamdani** synthesis of material.

 Conflicts of Interest

The authors declare no conflict of interest.

 References

- 1 Behera, S. K., Huwaikem, M., Jena, B., Shah, M. P., Chakraborty, S., Tripathy, S. K., & Mishra, A. (2023). Fabrication of ZnO/Gypsum/Gelatine nanocomposites films and their antibacterial mechanism against Staphylococcus aureus. *Biotechnology and Genetic Engineering Reviews*, 1–24. <https://doi.org/10.1080/02648725.2023.2216419>
- 2 Krishnan, M., Subramanian, H., Ramachandran, S. K., Muthukumarasamy, A., Ramadoss, D., Mahalingam, A., ... & Hwang, J. S. (2023). Synthesis of bimetallic BiPO₄/ZnO nanocomposite: enhanced photocatalytic dye degradation and antibacterial applications. *International Journal of Molecular Sciences*, 24(3), 1947. <https://doi.org/10.3390/ijms24031947>
- 3 Dediu, V., Busila, M., Tucureanu, V., Bucur, F. I., Iliescu, F. S., Brincoveanu, O., & Iliescu, C. (2022). Synthesis of ZnO/Au Nanocomposite for Antibacterial Applications. *Nanomaterials*, 12(21), 3832. <https://doi.org/10.3390/nano12213832>
- 4 Sreekanth, R., Kumar, S. N., Reddy, M., Pattar, J., & BV, D. R. (2024). Investigating the effect of acidic and basic precipitation on the antibacterial activity of ZnO nanoparticles against Gram-negative and Gram-positive bacteria. *Journal of Materials Chemistry B*, 12(8), 2180–2196. <https://doi.org/10.1039/d3tb02119j>
- 5 Alshammari, E. M., Sherwani, S., Alqahtani, F. O., Khan, M., Khan, W. A., Khan, M. W. A., Alsukaibi, A. K. D., Al-Motair, K., Alenezi, K. M., & Umar, A. (2023). Green Synthesis of Novel Antimicrobial ZnO Nanorods. *Science of Advanced Materials*, 15(8), 1000–1005. <https://doi.org/10.1166/sam.2023.4517>
- 6 Ahmadi, R., Fattahi Nafchi, R., Sangpour, P., Bagheri, M., & Badiei, E. (2023). A comparative study: Green synthesis and evaluation of ZnO-GO and ZnO-RGO nanocomposites for antibacterial applications. *Materials Science and Engineering: B*, 294, 116555. <https://doi.org/10.1016/j.mseb.2023.116555>
- 7 Kong, J., Zhang, J., Shen, M., Zhang, S., Shen, P., & Ren, C. (2022). Preparation of manganese(II) oxide doped zinc oxide nanocomposites with improved antibacterial activity via ROS. *Chemical Physics Letters*, 806, 140053. <https://doi.org/10.1016/j.cplett.2022.140053>
- 8 Hussain Shah, M. B., Mansoor, Q., Jan, T., Farooq, Z., & Ilyas, S. Z. (2023). Synthesis of SnO₂ nanoparticles coated ZnO-g-C₃N₄ composite nanostructures with novel antibacterial activity. *Zeitschrift Für Naturforschung A*, 78(6), 557–562. <https://doi.org/10.1515/zna-2023-0032>
- 9 Alasmari, A., Alshehri, K., Azab, A. A., & Solyman, S. (2024). Detailed investigation of the structural and electrical properties of ZnO/Fe₃O₄ nanocomposites. *Physica Scripta*, 99(3), 035921. <https://doi.org/10.1088/1402-4896/ad21c9>

- 10 Narang, K., Kumar, J., Saxena, S., Chaudhary, M., Narender, & Chandwani, G. (2024). Smart Computing Optimization of the Bactericidal Potential of ZnO Nanoparticles: A Support Vector Machine Approach. *2024 IEEE International Conference on Computing, Power and Communication Technologies (IC2PCT)*, 1635–1639. <https://doi.org/10.1109/ic2pct60090.2024.10486492>
- 11 Xesfyngi, Y., Georgoutsou-Spyridonos, M., Tripathy, A., Milionis, A., Poulidakos, D., Mastellos, D. C., & Tserapi, A. (2023). A High-Performance Antibacterial Nanostructured ZnO Microfluidic Device for Controlled Bacterial Lysis and DNA Release. *Antibiotics*, *12*(8), 1276. <https://doi.org/10.3390/antibiotics12081276>
- 12 AboKsour, M. F., Al-Marjani, M. F., & Rheima, A. M. (2024). Preparation and Effects of Manganese Oxide Nanoparticles Against Quinolone-Resistant Bacteria Isolated from Hospital Wastewater. *Al-Rafidain Journal of Medical Sciences* (ISSN 2789-3219), *6*(2), 94–100. <https://doi.org/10.54133/ajms.v6i2.728>
- 13 Gudkov, S. V., Burmistrov, D. E., Serov, D. A., Rebezov, M. B., Semenova, A. A., & Lisitsyn, A. B. (2021). A Mini Review of Antibacterial Properties of ZnO Nanoparticles. *Frontiers in Physics*, *9*. <https://doi.org/10.3389/fphy.2021.641481>
- 14 Abebe, B., Zereffa, E. A., Tadesse, A., & Murthy, H. C. A. (2020). A Review on Enhancing the Antibacterial Activity of ZnO: Mechanisms and Microscopic Investigation. *Nanoscale Research Letters*, *15*(1). <https://doi.org/10.1186/s11671-020-03418-6>
- 15 Calabrese, G., De Luca, G., Franco, D., Morganti, D., Rizzo, M. G., Bonavita, A., ... & Conoci, S. (2023). Structural and antibacterial studies of novel ZnO and Zn_xMn_(1-x)O nanostructured titanium scaffolds for biomedical applications. *Biomaterials Advances*, *145*, 213193. <https://doi.org/10.1016/j.bioadv.2022.213193>
- 16 Syah, R., Hussein Altajer, A., F Abdul-Rasheed, O., Amri Tanjung, F., M Aljeboree, A., Abd Alrazzak, N., & F Alkaim, A. (2021). CuMoO₄/ZnO nanocomposites: novel synthesis, characterization, and photocatalytic performance. *Journal of Nanostructures*, *11*(1), 73–80.
- 17 Vázquez-Olmos, A., Redón, R., Rodríguez-Gattorno, G., Esther Mata-Zamora, M., Morales-Leal, F., Fernández-Osorio, A. L., & Saniger, J. M. (2005). One-step synthesis of Mn₃O₄ nanoparticles: Structural and magnetic study. *Journal of Colloid and Interface Science*, *291*(1), 175–180. <https://doi.org/10.1016/j.jcis.2005.05.005>
- 18 Vahidi, H., Kobarfard, F., Kosar, Z., Mahjoub, M. A., Saravanan, M., & Barabadi, H. (2020). Mycosynthesis and characterization of selenium nanoparticles using standard penicillium chrysogenum PTCC 5031 and their antibacterial activity: A novel approach in microbial nanotechnology. *Nanomed. J*, *7*(4), 315–323. <https://doi.org/10.22038/nmj.2020.07.00008>
- 19 Bhat, K. G., & Nalawade, T. M. (2016). Antimicrobial Activity of Endodontic Medicaments and Vehicles using Agar Well Diffusion Method on Facultative and Obligate Anaerobes. *International Journal of Clinical Pediatric Dentistry*, *9*(4), 335–341. <https://doi.org/10.5005/jp-journals-10005-1388>
- 20 Gurunathan, S., Han, J. W., Dayem, A. A., Eppakayala, V., & Kim, J. H. (2012). Oxidative stress-mediated antibacterial activity of graphene oxide and reduced graphene oxide in *Pseudomonas aeruginosa*. *International journal of nanomedicine*, 5901–5914. <https://doi.org/10.2147/IJN.S37397>
- 21 Nagy, A., Harrison, A., Sabbani, S., Munson Jr, R. S., Dutta, P. K., & Waldman, W. J. (2011). Silver nanoparticles embedded in zeolite membranes: release of silver ions and mechanism of antibacterial action. *International journal of nanomedicine*, 1833–1852. <https://doi.org/10.2147/IJN.S24019>
- 22 Leung, Y. H., Ng, A. M. C., Xu, X., Shen, Z., Gethings, L. A., Wong, M. T., Chan, C. M. N., Guo, M. Y., Ng, Y. H., Djurišić, A. B., Lee, P. K. H., Chan, W. K., Yu, L. H., Phillips, D. L., Ma, A. P. Y., & Leung, F. C. C. (2013). Mechanisms of Antibacterial Activity of MgO: Non-ROS Mediated Toxicity of MgO Nanoparticles Towards *Escherichia coli*. *Small*, *10*(6), 1171–1183. Portico. <https://doi.org/10.1002/sml.201302434>
- 23 Ahmad, M. Aadil, S.R. Ejaz, M. Akhtar, H. Noor, S. Haider, Ibrahim A. Alsafari, Ghazalah Yasmin (2022.). Sol-gel synthesis of nanostructured ZnO/SrZnO₂ with boosted antibacterial and photocatalytic activity. *Ceramics International*, *48*, 2, 2394–2405. <https://doi.org/10.1016/j.ceramint.2021.10.020>
- 24 Packirisamy, R. G., Govindasamy, C., Sanmugam, A., Karuppasamy, K., Kim, H.-S., & Vikraman, D. (2019). Synthesis and Antibacterial Properties of Novel ZnMn₂O₄-Chitosan Nanocomposites. *Nanomaterials*, *9*(11), 1589. <https://doi.org/10.3390/nano9111589>
- 25 Bandekar, S. S., Hosamane, S. N., Patil, C., Yaragatti, A., Hukerikar, A., Patil, S., & Chachadi, P. (2020). ZnO-CuO nanocomposites: synthesis, characterization and antibacterial activity. *Journal of Physics: Conference Series*, *1706*(1), 012018. <https://doi.org/10.1088/1742-6596/1706/1/012018>
- 26 Kumar, A. A., & Jain, R. K. (2024). Synthesis and Characterization of the Zinc-Oxide: Tin-Oxide Nanoparticle Composite and Assessment of Its Antibacterial Activity: An In Vitro Study. *Cureus*. <https://doi.org/10.7759/cureus.53016>
- 27 Ma, W., Zhu, G., Zhang, Y., & Guo, J. (2024). Green synthesis of ZnO NPs with long-lasting and ultra-high antimicrobial activity. *Surfaces and Interfaces*, *50*, 104506. <https://doi.org/10.1016/j.surfin.2024.104506>
- 28 de Lucas-Gil, E., Leret, P., Monte-Serrano, M., Reinoso, J. J., Enríquez, E., Del Campo, A., Cañete, M., Menéndez, J., Fernández, J. F., & Rubio-Marcos, F. (2018). ZnO Nanoporous Spheres with Broad-Spectrum Antimicrobial Activity by Physicochemical Interactions. *ACS Applied Nano Materials*, *1*(7), 3214–3225. <https://doi.org/10.1021/acsanm.8b00402>
- 29 Mtavangu, S. G., Machunda, R. L., van der Bruggen, B., & Njau, K. N. (2022). In situ facile green synthesis of Ag-ZnO nanocomposites using *Tetradenia riparia* leaf extract and its antimicrobial efficacy on water disinfection. *Scientific Reports*, *12*(1). <https://doi.org/10.1038/s41598-022-19403-1>
- 30 Mohammadi-Aloucheh, R., Habibi-Yangjeh, A., Bayrami, A., Latifi-Navid, S., & Asadi, A. (2018). Enhanced anti-bacterial activities of ZnO nanoparticles and ZnO/CuO nanocomposites synthesized using *Vaccinium arctostaphylos* L. fruit extract. *Artificial Cells, Nanomedicine, and Biotechnology*, *46*(sup1), 1200–1209. <https://doi.org/10.1080/21691401.2018.1448988>

- 31 Takele, E., Feyisa Bogale, R., Shumi, G., & Kenasa, G. (2023). Green Synthesis, Characterization, and Antibacterial Activity of CuO/ZnO Nanocomposite Using Zingiber officinale Rhizome Extract. *Journal of Chemistry*, 2023, 1–15. <https://doi.org/10.1155/2023/3481389>
- 32 Pang, S., He, Y., Zhong, R., Guo, Z., He, P., Zhou, C., Xue, B., Wen, X., & Li, H. (2019). Multifunctional ZnO/TiO₂ nanoarray composite coating with antibacterial activity, cytocompatibility and piezoelectricity. *Ceramics International*, 45(10), 12663–12671. <https://doi.org/10.1016/j.ceramint.2019.03.076>
- 33 Kong, J., Zhang, J., Shen, M., Zhang, S., Shen, P., & Ren, C. (2022). Preparation of manganese(II) oxide doped zinc oxide nanocomposites with improved antibacterial activity via ROS. *Chemical Physics Letters*, 806, 140053. <https://doi.org/10.1016/j.cplett.2022.140053>
- 34 Pearlina, C. L., Abel, M. J., Pramothkumar, A., Senthilkumar, N., Anbalagan, P., & Prince, J. J. (2020). Investigation on structural, optical and electrochemical behavior of NiO/ZnMn₂O₄ ternary nanocomposites via two-step synthesis approach for supercapacitor application. *Chemical Papers*, 75(2), 641–651. <https://doi.org/10.1007/s11696-020-01258-3>

CHEMICAL TECHNOLOGY

Article

Received: 9 June 2024 | Revised: 30 November 2024 |

Accepted: 4 December 2024 | Published online: 18 December 2024

UDC 661.634.225

<https://doi.org/10.31489/2959-0663/4-24-4>

Ilkhom E. Khoshimov¹, Shakhzoda I. Turdialieva^{1*}, Atanazar R. Seytnazarov¹,
Shafaat S. Namazov¹, Mohamed Rifky²

¹*Institute of General and Inorganic Chemistry of the Academy of Sciences of the Republic of Uzbekistan, Tashkent, Uzbekistan;*

²*Faculty of Technology, Eastern University, Sri Lanka, Chenkalady, Sri Lanka*

(*Corresponding author's e-mail: turdialiyeva81@mail.ru)

Investigation of Vapor Pressure and Infrared Spectroscopic Analysis of Phosphoric Acid Extract Evaporation after Desulfation with SrCO₃

Ammophos-Maxam JSC is renowned for the production highly concentrated phosphorus fertilizers such as ammophos, ammonium sulfate phosphate, and suprephos, using thermally concentrated phosphorites sourced from the Central Kyzylkums. The production process heavily relies on wet-process phosphoric acid (WPA), which typically contains 16–18 % phosphorus pentoxide (P₂O₅). However, converting low P₂O₅ WPA into these high-phosphorus fertilizers during the stages of evaporation, drying, and granulation stages significantly increases the heat and energy consumption per unit of the final product. To address these challenges, extensive initiatives are currently underway in the republic. These efforts are aimed at improving the production of various phosphorus fertilizers, including ammophos, suprephos-NS, ammonium sulfate phosphate, PS-Agro, enriched superphosphate, and feed ammonium phosphates. These products are derived from the processing of washed burnt phosphoconcentrate (WBP-26) obtained from Kyzylkum phosphorites. This paper describes the results of recent studies on the evaporation process of WPA at Ammophos-Maxam JSC. The research focuses on examining the boiling point of WPA solutions, vapor pressure, and the composition of the resulting precipitates. Additionally, infrared (IR) spectroscopy was conducted to provide deeper insights into the material properties. These investigations are crucial for optimizing production processes and reduce energy costs.

Keywords: phosphorus, wet process phosphoric acid (WPA), Central Kyzylkums, ammophos, superphosphate, fertilizers, feed phosphates, IR spectroscopy.

Introduction

Simultaneously, the field of animal husbandry has long sought innovative solutions, particularly in the realm of feed additives for farm animals. This pursuit reflects the adaptability of the agricultural sector to the changing demands and challenges of modern practices. One notable example is the exploration and incorporation of advanced nutritional supplements for farm animals to optimize their health, productivity, and overall welfare. This concerted effort underscores the commitment of farmers to embrace new technologies and practices, contributing to the resilience and sustainability of global agriculture amid the complexities of contemporary agro-industrial dynamics.

The global demand for Mono and Diammonium Phosphates (MAP and DAP) [1, 2], as well as Nitrogen-Phosphorus (NP) and Nitrogen-Phosphorus-Potassium (NPK) fertilizers, underscores their pivotal role in modern agriculture. The production of these fertilizers relies exclusively on concentrated phosphoric acid. Consequently, the imperative task at hand is the advancement of technology for the concentration of WPA, aiming to achieve the production of high-quality phosphorus-containing fertilizers. At the same time, the Re-

public is actively engaged in the development of functional feed additives for animal husbandry, where domestic products are progressively competing with their foreign counterparts. In order to meet these challenges, it becomes essential to substantiate pertinent scientific solutions in several key areas. Firstly, the identification optimal conditions for desulfurizing weak WPA is a foundational step. Subsequently, the concentration of desulfurized WPA through evaporation must be refined to ensure efficiency. Concurrently, efforts are directed towards enhancing the rheological characteristics of evaporated WPA, a critical aspect of the production process. Lastly, the development of technology for various grades of ammonium phosphates, complex fertilizers, and feed additives derived from concentrated WPA requires meticulous attention. This multifaceted approach not only meets the urgency of the task at hand but also positions the domestic industry on a competitive front against foreign counterparts in the dynamic landscape of fertilizer and feed additive production.

In the production processes of double superphosphate, ammophos, nitroammophos, and liquid fertilizers at chemical plants, a concentrated phosphoric acid solution, referred to as WPA, plays a crucial role. The concentration of this solution is carefully adjusted according to the specific fertilizer being produced. For double superphosphate and ammophos, the WPA concentration falls within the range of 45–55 % P_2O_5 , while a higher concentration of 72–83 % P_2O_5 is utilized for ammonium polyphosphates and liquid fertilizers [3–5]. To achieve higher concentrations, the WPA is evaporated, reducing its water content and thereby increasing the concentration of phosphorus pentoxide (P_2O_5). The evaporation process theoretically allows for the production of solutions with exceptionally high P_2O_5 concentrations, as the steam produced from pure H_3PO_4 consists entirely of water. This highlights the advanced technological processes involved in crafting various phosphorus-based fertilizers, enabling the synthesis of products with diverse P_2O_5 concentrations to meet the specific needs of agricultural practices [6].

The scientific and technical literature provides valuable insights [7–11] into the prospect of producing evaporated WPA from the thermal concentrate derived from Kyzylkum phosphorite, and the subsequent formulation of liquid complex fertilizers. However, it must be recognized that the composition of WPA originating from thermal concentrate diverges from that produced at JSC Ammophos-Maxam, where washed burnt phosphoconcentrate (WBP–26) serves as the primary source. The distinctive chemical composition of WPA, particularly in terms of impurities such as MgO , Fe_2O_3 , Al_2O_3 , CaO and SO_3 , is of considerable significance. These impurities possess the potential to exert a notable influence on both the evaporation process and the rheological characteristics of the resulting evaporated phosphoric acids. Consequently, a nuanced understanding of these variations becomes pivotal in optimizing the production processes and ensuring the desired rheological attributes of the evaporated phosphoric acids in the context of diverse phosphorite sources and processing techniques.

As sulfate ions constitute the primary impurity in WPA, the pivotal purification step should focus on desulfurization.

In a previous study by the authors [12], desulfurization of WPA with a composition as described above was conducted using $Ca(OH)_2$ and $CaCO_3$, employing WBP–26, containing up to 20 % CaO_{dig} . Subsequently, for further purification of the desulfurized WPA, a treatment with acetone (99.5 % C_3H_6O) was employed with a three-fold excess. However, despite the utilization of calcium-based substances and WBP–26, complete removal of sulfate ions was not achieved, with the removal rate not exceeding 85 %.

To overcome this limitation, the authors propose a more effective method involving the use of strontium salts [13] for the deepest desulfurization. The main technological advantage associated with strontium salts is their ability to significantly reduce the residual SO_4^{2-} content in the WPA solution, achieving a remarkable reduction by 30–40 times. This approach represents a promising avenue for enhanced desulfurization, addressing the challenges encountered with conventional calcium-based substances and offering a more comprehensive solution for sulfate ion removal in the processing of WPA.

The article describes the key applications of infrared (IR) spectroscopy in the examination of sediments derived from the initial desulfurized and the precipitation of evaporated WPA. Recognized as one of the most efficient spectroscopic techniques for chemical analysis, IR spectroscopy boasts exceptional capabilities in providing valuable qualitative insights into the composition of substances. However, it is acknowledged that its precision in quantitatively determining compounds is comparatively modest. In chemistry, IR spectroscopy is mainly used for the qualitative determination of compounds. Regardless of molecular structure, functional groups within molecules exhibit absorption lines at specific wavenumber values, known as characteristic wave frequencies. These characteristic frequencies serve as informative markers, providing valuable insights into the nature of the analyzed substance. The vibrational spectrum, with its high-quality

information, is considered a unique physical property of a substance. Consequently, infrared (IR) spectra are widely used to identify chemical compounds and mixtures within individual compounds. Additionally, the technique proves invaluable in studying the mechanisms of chemical reactions, further cementing its significance in the comprehensive understanding of chemical phenomena [14].

Experimental

The evaporation process of WPA from the current production at Ammophos-Maxam was systematically investigated in the laboratory. The WPA under examination exhibited the following composition by weight: P₂O₅ 18.95; CaO 0.27; MgO 0.26; Fe₂O₃ 0.41; Al₂O₃ 0.56; F 0.45; SO₃_{tot.} 2.96 and SO₃_{dig.} 0.15. A notable deviation from conventional practices was introduced in the desulfurization step, where strontium salt replaced calcium minerals. The desulfurization process involved the utilization of strontium carbonate, specifically the “chemically pure” grade (minimum 98 % SrCO₃). This substitution was made owing to the strontium salt's proven efficacy in purifying phosphoric acid from sulfate ions. Furthermore, during the subsequent evaporation process of desulfurized phosphoric acid, achieving concentrations of 45–60 % phosphorus oxide (V), an additional purification step was observed, effectively eliminating other impurities from the acid. These distinctive features, namely the utilization of strontium salt during desulfurization and the consequential evaporation process, highlight the experiment's unique qualities. The incorporation of these innovative steps in the laboratory study showcases a deliberate approach to enhance the purity and quality of phosphoric acid, thereby contributing to the advancement of the production processes at Ammophos-Maxam. Experiments on the purification of WPA using SrCO₃ were conducted three times, and the average mean was calculated. A long with this standard deviation (SD), confidential interval (CI) and p-level of significance was noted to be 0.05. Based on them corresponding Student coefficient was used. The calculation was performed using MS Excel (Windows 10) with a 95 % confidence level (P = 95 %) and preliminary standard deviation (S) estimation based on a sample size of $n = 3-4$ [15].

Concentrated solutions were obtained through the evaporation of desulfated acid, and their chemical composition was meticulously assessed using various analytical techniques. The determination of P₂O₅ content was conducted through photolorimetric methods, while SO₃ levels were quantified gravimetrically, and F-content was assessed potentiometrically. Calcium and magnesium content were ascertained via the complexometric method, where the change in color of the indicator (fluorexone for calcium and dark blue acid chromium for magnesium) induced by Trilon B played a crucial role. Sulfate content was determined gravimetrically by inducing sulfate precipitation through the addition of barium chloride in an acidic environment, followed by measuring the weight of the resulting sediment. The complexometric method was applied to determine iron and aluminum oxide levels. Specifically, 0.0125 M iron was titrated with Trilon B solution in the presence of sulfosalicylic acid, followed by the back titration of excess Trilon B using a 0.0125 M zinc sulfate solution. This complex procedure allowed the determination of aluminum content in the presence of a xylene orange indicator. Furthermore, the density of solutions was also determined using pycnometric methods, and the kinematic viscosity was ascertained using viscometric techniques. These analytical methods collectively contribute to a comprehensive understanding of the chemical composition and properties of the concentrated solutions obtained from the evaporation of desulfated acid.

The relationship between temperature and saturated vapor pressure is expressed by the equation:

$$\lg P = A - B / T .$$

In Table 1, there are data with Vapor pressure (kPa) at temperature (K), approximation equation and coefficients of determination (R^2).

As shown that vapor pressure increases as temperature rising but vapor pressure decreases with increasing WPA concentration. Approximation equation and Coefficients of determination (R^2) were calculated according to calculation Excel 2019. The confidence interval was 95 %.

According to their respective concentrations, the relationships between temperature (T) and saturated vapor pressure (P) for WPA are expressed by the following equations given in Table 1.

The reported values of the coefficient of determination R^2 are in the range of 0.9746–0.9995 meaning that the approximation equations fit the actual data quite well. Significantly higher R^2 values nearer to 1 as WPA (50.01 %, 55.25 %, and 60.34 %) show better fitness of the model that is able to predict almost all the fluctuations in vapor pressure data.

These equations provide a mathematical description of the temperature-dependent behavior of saturated vapor pressure for varying concentrations of phosphoric acid solutions. They play a crucial role in understanding the thermodynamic characteristics of the evaporation process for different WPA compositions.

Table 1

Vapor pressure of desulfated evaporated phosphoric acid

WPA concentration, P ₂ O ₅ , %	lg P = A - B/T	Vapor pressure (kPa) at temperature (K)					Approximation equation	Coefficients of determination (R ²)	MSE (kPa ²)	RMSE (kPa)
		293	303	313	323	333				
45.62	lgP = 5.1838 - 979.5/T	7.56	11.98	15.09	18.98	23.37	y = 8E-21x ^{8.5179}	0.9746	11483.45	107.16
50.01	lgP = 5.5457 - 1150.6/T	5.63	7.59	9.78	12.9	16.24	y = 2E-20x ^{8.2849}	0.9993	5230.13	72.32
55.25	lgP = 5.6590 - 1210.5/T	4.5	6.22	8.39	10.81	13.93	y = 9E-22x ^{8.7995}	0.9985	3744.12	61.19
60.34	lgP = 5.6399 - 1263.5/T	2.85	3.93	5.43	7.16	9.44	y = 2E-23x ^{9.3674}	0.9995	1603.53	40.04

IR spectroscopic analysis was conducted using a Perkin-Elmer FT-IR Spectrum 3 spectrophotometer [16], covering a frequency range of 4000–400 cm⁻¹. The acquired spectral data were validated by careful comparison with specific and authenticated reference sources. This rigorous authentication process ensures the reliability and accuracy of the obtained IR spectroscopic results, underscoring the integrity of the analytical methodology employed in this study

Results and Discussion

The optimum dosage of strontium carbonate for the formation of strontium sulfate was determined to be 100 % of the stoichiometry. In the procedure, the initial WPA was introduced into a reactor equipped with a screw stirrer and gradually heated up to 75 °C within a water thermostat. Subsequently, a calculated quantity of strontium carbonate powder was gradually added to the WPA over a 30-minute period, with continuous stirring. Following this dosing phase, the reactor contents were allowed to settle for 60 minutes at 60–65 °C. After settling, the desulfurized WPA was separated from the sediment through filtration, dried, and then weighed. The clarified portion, comprising the desulfurized WPA and its sediment, underwent analysis for the total content of SO₃ and P₂O₅ using established methods [17]. Based on the acquired data, the degree of desulfurization of WPA was calculated, and the results are presented in Table 2. This methodical approach ensures a systematic and comprehensive evaluation of the desulfurization efficiency in the context of varying strontium carbonate dosages.

Table 2

The degree of desulfurization of extraction phosphoric acid depending on the rate of strontium carbonate*

The SrCO ₃ norm, %	WPA _{desulfated} , % (± Confidence interval with Student's distribution in α = 0.05)		P ₂ O ₅ content in dry sediment, %	Desulphurization degree, %
	P ₂ O ₅	SO ₃		
95	20.86±0.41	0.15±0.16	0.71±0.80	96.17±0.20
97.5	20.86±0.41	0.13±0.06	0.73±0.75	96.48±0.21
100	20.53±0.30	0.10±0.03	0.79±0.72	97.34±0.23
102.5	21.04±0.19	0.10±0.03	0.82±0.74	97.36±0.30
105	21.39±0.20	0.10±0.03	0.91±0.77	97.37±0.41
SD	0.3136	0.0230	0.0795	0.5757
Conf/inter with p < 0.05	0.3894	0.0286	0.0987	0.7148

*Note: Each value is expressed as the mean ± SD (n = 3). Means with different letters within a column are significantly different (p < 0.05).

The desulfurized WPA, characterized by a composition of 20.53 % P₂O₅, 0.28 % CaO, 0.27 % MgO, 0.45 % Fe₂O₃, 0.62 % Al₂O₃ and 0.10 % SO₃, underwent controlled evaporation to achieve a predetermined P₂O₅ content. This evaporation process was conducted under atmospheric pressure within a tubular quartz reactor, featuring a bladed quartz stirrer and heated externally by a specialized electric furnace. The resulting evaporated phosphoric acids exhibited concentrations ranging from 45.62 % to 60.34 % P₂O₅. Notably, visual observation indicated that as the concentration of P₂O₅ increased during the evaporation of WPA, the fluid state of the solution was maintained without thickening. However, an increase in P₂O₅ concentration corresponded to a noticeable increase in sediment volume. This phenomenon suggests that, as the initial WPA undergoes concentration, phosphates of cationic impurities, including strontium, calcium, sodium, and potas-

sium sulfate, crystallize due to a reduction in their solubility. The composition of the resulting evaporated phosphoric acids is depicted in Figure 1, providing a visual representation of the evolving chemical composition during the controlled evaporation process.

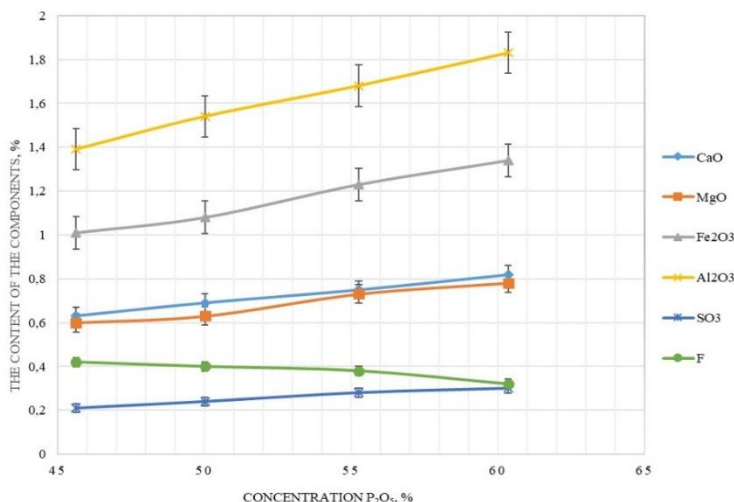


Figure 1. The content of impurity components in the evaporated acid depends on the concentration of phosphorus pentoxide

In order to regulate the evaporation process of WPA and, consequently, produce concentrated fertilizers and feed phosphates with acceptable transport and storage conditions, a thorough examination of the physical and chemical properties was conducted. This included a study of the boiling point at varying concentrations of WPA (ranging from 45.62 % to 60.34 %) without the clarification stage. The investigation considered the P₂O₅ content and residual pressure values in the system, which ranged from 743 to 443 mm Hg. Additionally, the elasticity of vapors above these acids was explored, contingent on the concentration of WPA (45.62–60.34 % P₂O₅) and temperatures ranging from 293 to 333 K. The constants *A* and *B* were determined by applying of the Clausius-Clapeyron equation, utilizing the least squares method. Subsequently, empirical equations were derived to predict the pressure of saturated vapors over solutions at different temperatures. The relationship between saturated vapor pressure and temperature follows a specific equation, as depicted in Figure 2. These findings contribute crucial insights into the thermodynamic characteristics of WPA solutions during the evaporation process, facilitating the optimization of conditions for the production of concentrated fertilizers and feed phosphates with desirable transport and storage attributes.

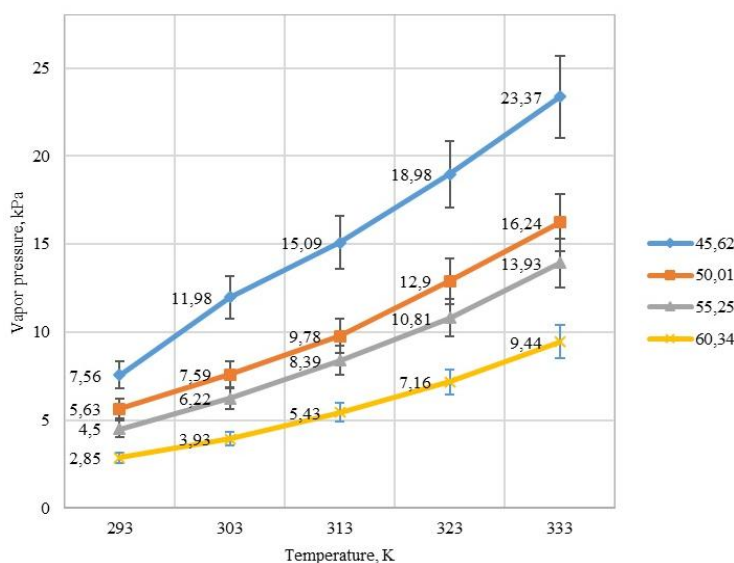


Figure 2. Elasticity of saturated vapors over desulfurized evaporated phosphoric acid

Figure 2 illustrates the concentration-dependent characteristics of WPA with P_2O_5 concentrations ranging from 45.62 % to 60.34 %. The constants A and B , within this range, span 5.1838–979.5 and 5.6399–1263.5, respectively. Across the temperature range of 293–333 K, an inverse relationship is observed between vapor pressure and WPA concentration. Higher temperatures correspond to increased saturated vapor pressure above the acid. Specifically, at 293–313 K, the measured pressure of saturated vapors over evaporated WPA samples ranges from 2.85–23.37 kPa, indicating low volatility in the arid climate of Central Asia. This low volatility suggests prolonged storage stability without significant changes in physico-chemical properties.

The boiling points of the evaporated WPA samples are depicted in Figure 3.

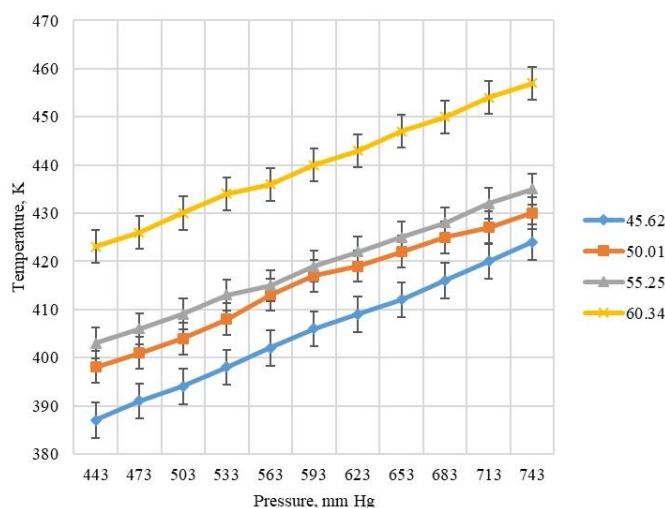


Figure 3. Boiling point of desulfurized evaporated phosphoric acid

The data in Figure 3 establish a direct relationship between the concentration of WPA and the boiling point of its solutions. An increase in the concentration of WPA corresponds to a higher boiling point. For instance, at a concentration of 45.62 % P_2O_5 and a pressure of 743 mm Hg, the boiling point is recorded at 424 K or 131 °C. Similarly, at a concentration of 50.01 %, the boiling point elevates to 137 °C, further rising to 165 °C for a concentration of 55.25 % P_2O_5 and reaching 184 °C at a concentration of 60.34 % P_2O_5 . Notably, a reduction in pressure significantly decreases the boiling point of WPA solutions.

As P_2O_5 concentration in WPA exceeds 45.62 %, visible precipitation of insoluble particles and salts becomes evident, intensifying with higher P_2O_5 concentrations, particularly reaching prominence at 60.34 %. This escalating P_2O_5 concentration leads to reduced solubility of elements such as Fe, Al, Ca, Mg, resulting in heightened crystallization. Analytical methods were employed to quantify P_2O_5 and associated impurities. The observed precipitate, rich in iron and aluminum phosphates, serves as a phosphorus component in phosphorus fertilizers. Those with P_2O_5 content between 17.94 % and 21.42 % are returned to ammonium phosphate production for amalgamation with ammonium phosphate pulp (Table 3).

Table 3

The composition of precipitation formed during the evaporation of desulfurized WPA washed with acetone

	Concentration P_2O_5 , %	The content of the components, % (\pm Confidence interval with Student's distribution in $\alpha = 0.05$)				
		CaO	MgO	Fe ₂ O ₃	Al ₂ O ₃	SO ₃
	21.42 \pm 0.50	9.25 \pm 0.60	2.77 \pm 0.4	4.68 \pm 0.15	2.35 \pm 0.30	5.74 \pm 0.50
	28.54 \pm 0.52	6.49 \pm 0.70	1.39 \pm 0.35	6.51 \pm 0.90	3.17 \pm 0.25	4.88 \pm 0.40
	17.25 \pm 0.40	7.43 \pm 0.65	0.39 \pm 0.30	7.51 \pm 0.80	3.03 \pm 0.15	5.02 \pm 0.030
	17.94 \pm 0.43	18.38 \pm 0.55	0.39 \pm 0.20	1.39 \pm 0.70	4.21 \pm 0.20	18.3 \pm 0.90
SD	5.7089	1.4032	1.1950	1.4351	0.4386	0.4614
Conf/inter with p<0,05	9.0841	2.2328	1.9016	2.2836	0.6980	0.7343

In this investigation, the precipitated SrSO_4 resulting from the desulfurization process of the initial WPA, along with precipitates obtained during the evaporation of the clarified portion of desulfurized WPA to distinct concentrations (45.62 %, 50.01 %, 55.25 % and 60.34 % P_2O_5), underwent a thorough washing with acetone to attain a neutral state. Following the drying of these samples, infrared (IR) spectroscopic analyses were conducted. The analyses were carried out using a Perkin-Elmer FT-IR Spectrum 3 spectrophotometer [18], operating within a frequency range of 4000–400 cm^{-1} . The accuracy of the results obtained was ensured through verification against specific references [19, 20]. Figures 4–8 depict the outcomes of the IR spectroscopic analysis. Two important concepts are discussed here: transmittance (% T) and wave-number (cm^{-1}).

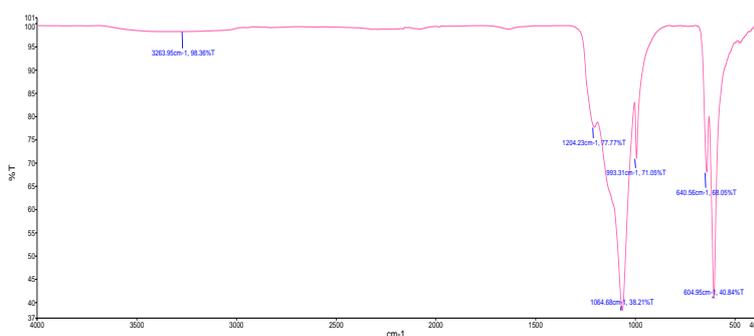


Figure 4. IR spectroscopic analysis of the precipitate of desulfurized evaporated WPA_(initial)

Figure 4 reveals the results of the IR spectroscopic analysis of the precipitate obtained through the desulfurization process with SrCO_3 of the initial extracted phosphoric acid. Wavelengths of 604.95 and 640.56 cm^{-1} are identified, corresponding to the SO_4^{2-} ion, while the wavelength of 993.31 cm^{-1} corresponds to the PO_4^{3-} ion. Additional features are noted at 1064.68 cm^{-1} for the (S=O) bond, 1204.23 cm^{-1} for (C–O), and 3263.95 cm^{-1} for (O–H), as suggested by certain sources.

Figure 5 shows the IR spectroscopic analysis of the precipitate obtained after the evaporation of desulfurized WPA with SrCO_3 to a concentration of 45.62 % P_2O_5 is presented. Wavelengths of 474.86, 492.00, 580.02, 919.30, 967.80 and 1061.53 cm^{-1} are indicative of the PO_4^{2-} ion, while the wavelength of 712.23 cm^{-1} suggests the presence of the (POH) bond. Moreover, sources propose the existence of the (C=C) bond at a wavelength of 1631.08 cm^{-1} and the (O–H) bond at 3039.38 cm^{-1} . Confidence interval was maintained at 95 %.

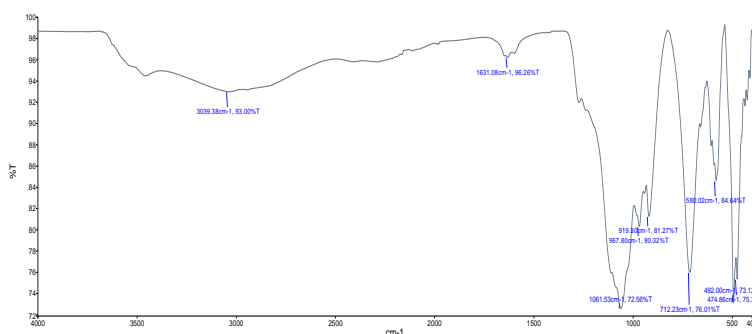


Figure 5. IR spectroscopic analysis of the precipitate of desulfurized evaporated WPA with a content of 45.62 % P_2O_5

In Figure 6, the IR spectroscopic analysis of the precipitate obtained after the evaporation of desulfurized WPA with SrCO_3 to 50.01 % P_2O_5 reveals wavelengths of 493.23, 578.67, 920.61, 966.96 and 1051.04 cm^{-1} corresponding to the PO_4^{2-} ion. Additionally, the wavelength of 720.15 cm^{-1} indicates the presence of the (POH) bond. Some sources suggest the existence of the (C–O) bond at 1273.57 cm^{-1} , the (C=O) bond at 1634.84 cm^{-1} , and the (O–H) bond at 3039.86 cm^{-1} .

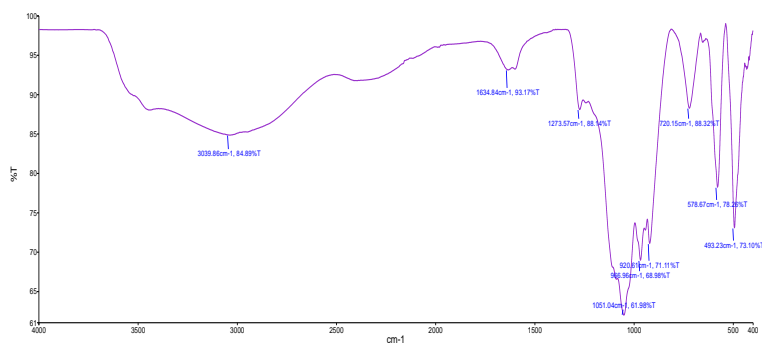


Figure 6. IR spectroscopic analysis of the precipitate of desulfurized evaporated WPA containing 50.01 % P₂O₅

Moving to Figure 7, the IR spectroscopic analysis of the precipitate obtained after the evaporation of desulfurized WPA with SrCO₃ to 55.25 % P₂O₅ indicates wavelengths of 430.93, 493.74, 579.48, 919.83, 967.37 and 1053.36 cm⁻¹ corresponding to the PO₄²⁻ ion, with a wavelength of 715.05 cm⁻¹ indicating the presence of the (POH) bond. Sources also indicate the presence of the (C=O) bond at 1598.97 cm⁻¹ and the (O–H) bond at 2977.29 cm⁻¹.

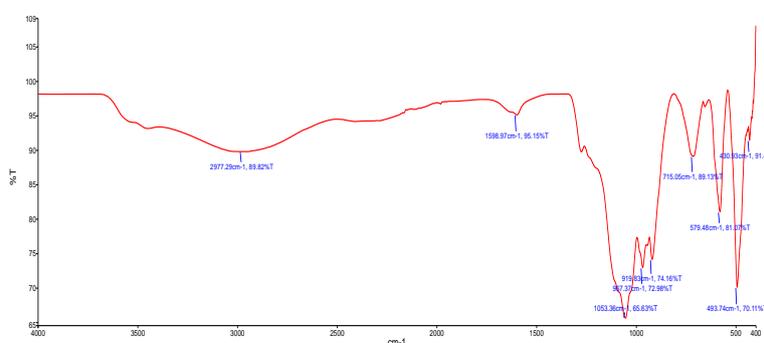


Figure 7. IR spectroscopic analysis of the precipitate of desulfurized evaporated WPA containing 55.25 % P₂O₅

Figure 8 illustrates the IR spectroscopic analysis of the precipitate obtained after the evaporation of WPA desulfurized with SrCO₃ to 60.34 % P₂O₅. Wavelengths of 494.85, 606.22, 651.84, 992.78, 1066.08 and 1111.16 cm⁻¹ correspond to the PO₄²⁻ ion, while the wavelength of 724.55 cm⁻¹ indicates the presence of the (POH) bond. Additionally, sources [18, 19] suggest the existence of the (C=O) bond at 1635.67 cm⁻¹ and the (O–H) bond at 3117.42 cm⁻¹.

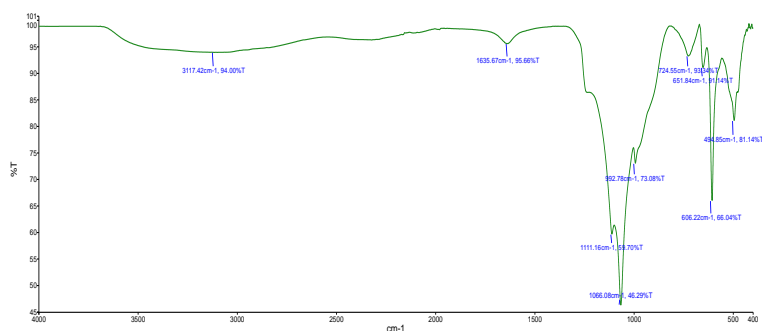


Figure 8. IR spectroscopic analysis of the precipitate of desulfurized evaporated WPA containing 60.34 % P₂O₅

Conclusion

In conclusion, this investigation elucidates the proficient desulfurization of weak WPA sourced from Washed Burnt Phosphoconcentrate-26 (WBP–26) via strategic application of strontium carbonate, culminating in the attainment of a substantial concentration, specifically 60 % P₂O₅, through a meticulously executed

process of evaporation. The empirical analysis substantiates the salient attribute of low volatility exhibited by the resultant concentrated WPA, a characteristic particularly germane in regions characterized by heightened thermal conditions, as underscored by the delineated range of saturated vapor pressures.

Furthermore, the concentrated phosphoric acid exhibits notable versatility, affirming its aptitude for the synthesis of premium-grade fertilizers, including Monoammonium Phosphate (MAP) and Diammonium Phosphate (DAP), alongside its applicability in the production of feed phosphates. Significantly, this research augments scholarly discourse by shedding light on the compound's nuanced involvement in the formulation of liquid complex fertilizers, featuring ammonium polyphosphates characterized by specific N:P₂O₅ ratios. As a scholarly endeavor, this inquiry advances our comprehension of phosphorus-rich fertilizer production paradigms, contributing to the refinement of agro-industrial methodologies with tangible implications for optimized agricultural practices.

*Author Information**

*The authors' names are presented in the following order: First Name, Middle Name and Last Name

Ilkhom Erkin ugli Khoshimov — 2nd year PhD Student, Institute of General and Inorganic Chemistry of the Academy of Sciences of the Republic of Uzbekistan, Mirzo Ulugbek Avenue (former Khabib Abdullaev), 77A, 100071, Tashkent, Uzbekistan; e-mail: Emmim1991@mail.ru; <https://orcid.org/0000-0003-4442-772X>

Shakhzoda Ismatullaevna Turdialieva (*corresponding author*) — Doctoral Student, Institute of General and Inorganic Chemistry of the Academy of Sciences of the Republic of Uzbekistan, Mirzo Ulugbek Avenue (former Khabib Abdullaev), 77A, 100071, Tashkent, Uzbekistan; e-mail: turdialiyeva81@mail.ru; <https://orcid.org/0009-0009-6541-3897>

Atanazar Reypnazarovich Seytnazarov — Doctor of Technical Sciences, Professor, Chief Researcher, Institute of General and Inorganic Chemistry of the Academy of Sciences of the Republic of Uzbekistan, Mirzo Ulugbek Avenue (former Khabib Abdullaev), 77A, 100071, Tashkent, Uzbekistan; e-mail: atanazar77@mail.ru; <https://orcid.org/0000-0002-0629-8878>

Shafaat Sattarovich Namazov — Professor, Doctor of Technical Sciences, Academician, Head of laboratory, Institute of General and Inorganic Chemistry of the Academy of Sciences of the Republic of Uzbekistan, Mirzo Ulugbek Avenue (former Khabib Abdullaev), 77A, 100071, Tashkent, Uzbekistan; e-mail: diana-ye@yandex.com; <https://orcid.org/0009-0009-2396-3161>

Mohamed Rifky — Lecturer, Doctor of Technical Sciences, Faculty of Technology, Eastern University, Sri Lanka, 30350, Chenkalady, Sri Lanka; e-mail: rifyalm@esn.ac.lk; <https://orcid.org/0000-0001-5470-4589>

Author Contributions

The manuscript was written through contributions of all authors. All authors have given approval to the final version of the manuscript. CRediT: **Ilkhom Erkin ugli Khoshimov** conducts a thorough purification of extraction phosphoric acid of phosphorites of the Central Kyzylkum; **Shakhzoda Ismatullaevna Turdialieva** took part in research and analysis of scientific and technical literature; **Atanazar Reypnazarovich Seytnazarov** substantiated the idea of conducting research on the development of technology for purifying WPA and its practical application, and also took part in writing the article; **Shafaat Sattarovich Namazov** created the conditions for conducting all laboratory experiments, the formulation of the goals and objectives of the research; **Mohamed Rifky** contributed to the calculations involving standard deviations, confidence intervals, approximation errors, and coefficients of determination, as well as addressing the reviewer's comments.

Acknowledgments

The authors express their gratitude to the managing committee, the laboratory of phosphorus Fertilizers at the Institute of General and Inorganic Chemistry of the Academy of Sciences of the Republic of Uzbekistan, and the Institute of Plant Substance Chemistry. The collaborative efforts and invaluable support provided by these institutions, particularly in facilitating the conduct of IR spectroscopy analyses, are duly

acknowledged. Such collaborative endeavors significantly contributed to the robustness and comprehensiveness of the research findings.

Conflicts of Interest

The authors declare no conflict of interest.

References

- Buchanan, G. H., & Winner, G. B. (1920). The Solubility of Mono- and Diammonium Phosphate. *Journal of Industrial and Engineering Chemistry*, 12(5), 448–451. <https://doi.org/10.1021/ie50125a012>
- Zhang, F., Wang, Q., Hong, J., Chen, W., Qi, C., & Ye, L. (2017). Life cycle assessment of diammonium- and monoammonium-phosphate fertilizer production in China. *Journal of Cleaner Production*, 141, 1087–1094. <https://doi.org/10.1016/j.jclepro.2016.09.107>
- Pozin, M.E. (1970). Technology mineralnyx soley [Technology of mineral salts], Part II. *Publishing house Chemistry Leningrad branch*, 1274 [in Russian].
- Sokolovsky, A.A., & Yashke, E.V. (1971). Technology mineralnyx udobreniy i kislot [Technology of mineral fertilizers and acids]. *Chemistry*, 307. Moscow [in Russian].
- Kopilev, V.A. (1972). Tekhnologiya ekstraksii fosfornoy kisloty [Extraction Phosphoric Acid Technology]. *Chemistry*, 289. Moscow [in Russian].
- Hannachi, A., Habaili, D., Chtara, C., & Ratel, A. (2007). Purification of wet process phosphoric acid by solvent extraction with TBP and MIBK mixtures. *Separation and Purification Technology*, 55(2), 212–216. <https://doi.org/10.1016/j.seppur.2006.12.014>
- Bakhriddinov, N.S. (1991). Liquid and complex fertilizers based on extraction phosphoric acid from phosphorites of the Central Kyzylkum, Candidate of Technical Sciences, *Dissertation, General and Inorganic Chemistry Institute of Academy Sciences of the Republic of Uzbekistan*. Tashkent.
- Turdialiyeva, Sh.I., Alimov, U.K., Namazov, Sh.S., & Seytnazarov, A.R. (2018). Concentration of weak extraction phosphoric acid and its physico-chemical properties, *Chemical industry*, 95.4, 171–178.
- Bakhriddinov, N.S., Abdullaev, B.D., Erkaev, A.U., & Namazov, Sh.S. (1991). Concentrated extraction phosphoric acid from phosphorites of the Central Kyzylkum and its physicochemical properties, *Uzbek Chemical Journal*, 1, 21–25.
- Namazov, Sh.S., Bakhriddinov, N.S., Erkaev, A.U., & Abdullaev, B.D. (1991). Physico-chemical properties of evaporated extraction phosphoric acid from phosphorites of the Central Kyzylkum, *Uzbek Chemical Journal*, 1, 25–28.
- Kakharov, E.M., Alimov, U.K., Mirsalimova, S.R., Seytnazarov, A.R., & Namazov, Sh.S. (2021). Obtaining thermophosphates by firing products of phosphoric acid decomposition of high calcareous phosphorite powder, *Universum: technical sciences*, (8–2 (89)), 43–48. <https://doi.org/10.32743/unitech.2021.89.8.12208>
- Karshiev, B.N., Kakharov, E.M., Seytnazarov, A.R., & Namazov, Sh.S. (2020). Desulphurization and purification of extraction phosphoric acid using calcium minerals and acetone. *Chemical Industry*, 97(3), 136–144.
- Zlobina, E.P., Bushuev, N.N., Petropavlovsky, I.A., Rakcheeva, L.B., & Kochetkov, S.P. (2002). Study of the process of purification of extraction phosphoric acid from sulfate ion with strontium carbonate. *Chemical Technology*, 12, 24–26.
- Rozmetov, A.Kh. (2023). Synthesis, structure and biological properties of new metal complexes based on isomers of hydroxybenzoic acid and monoethanolamine, *PhD, Dissertation, National University of Uzbekistan named after Mirzo Ulugbek, Uzbekistan*. Tashkent.
- Hasanguliyeva, N. M., Shakunova, N. V., & Litvishkov, Y. N. (2024). Microwave Solid-Phase Synthesis of Ni-Co Ferrites and their Activities in Liquid-Phase Oxidation of m-Xylene. *Eurasian Journal of Chemistry*, 29(3(115)), 82–91. <https://doi.org/10.31489/2959-0663/3-24-1>
- Finch, A., & Redklif, K. (1973). Primeneniye dlinnovolnovoy IK-spektroskopii v khimii [Application of long-wave IR spectroscopy in chemistry]. *Mir*. 139–146. Moscow [in Russian].
- Vinnik, M.M., Erbanova, L.N., & Zaytsev, P.M. (1975). Metody analiza fosfatnogo syr'ya, fosfornykh kompleksnykh udobreniy, kormovykh fosfatov [Methods for analyzing phosphate raw materials, phosphorus complex fertilizers, feed phosphates]. *Chemistry*, 218. Moscow [in Russian].
- Gorbacheva, S. B. (1963). Praktikum po fizicheskoy khimii [Workshop on physical chemistry]. *Graduate School*, 554 [in Russian].
- Sigma Aldrich. (Accessed 2024). IR Spectrum Table. Retrieved from <https://www.sigmaaldrich.com/UZ/en/technical-documents/technical-article/analytical-chemistry/photometry-and-reflectometry/ir-spectrum-table>
- LibreTexts. (Accessed 2024). Infrared Spectroscopy Absorption Table. Retrieved from https://chem.libretexts.org/Ancillary_Materials/Reference/Reference_Tables/Spectroscopic_Reference_Tables/Infrared_Spectroscopy_Absorption_Table

Oleg V. Surov* , Marina I. Voronova 

G.A. Krestov Institute of Solution Chemistry of the Russian Academy of Sciences, Ivanovo, Russia
(*Corresponding author's e-mail: ovs@isc-ras.ru)

Obtaining Cellulose Nanocrystals in a Medium of Primary Monohydric Alcohols

The lack of a universal method for isolating cellulose nanocrystals (CNCs) has encouraged researchers to look for new methods and approaches as alternatives to traditional sulfuric acid hydrolysis. Acid alcoholysis has long been actively used in cellulose depolymerization processes to obtain a variety of alkyl glycosides and further alcoholysis products. In the present article, the authors continue their earlier research on the synthesis of CNCs in the presence of a sulfuric acid catalyst in an alcoholic environment. In this work, CNCs were obtained from sulfate-bleached pulp in a medium of primary monohydric alcohols ($C_nH_{2n+1}OH$, $n = 5-8$). A maximum CNC yield of 60 % was achieved with pentanol-1 at a sulfuric acid concentration of 50 %. The work revealed that the alcohols studied can be ranked in descending order based on both the acid concentration corresponding to the maximum CNC yield and the yield itself, as follows: pentanol-1, hexanol-1, heptanol-1, and octanol-1. For octanol-1 the maximum CNC yield was 20 % at an acid concentration of 40 %. The physicochemical properties of the isolated CNCs were studied. No surface alkylation of the synthesized CNCs was found to occur during cellulose treatment in the media of the alcohols studied, as the properties of the CNCs, in general, were similar to those of CNCs obtained by standard sulfuric acid hydrolysis. This study broadens the scope of alternative methods to traditional sulfuric acid hydrolysis, and is likely to appeal to researchers engaged in developing novel approaches for CNC extraction.

Keywords: cellulose, alcohols, cellulose nanocrystals, synthesis, hydrolysis, alcoholysis, yield, properties.

Introduction

Cellulose is the most accessible renewable natural resource. As a low-cost biopolymer, cellulose plays an important role in the production of environmentally friendly biocompatible and biodegradable functional materials [1]. Almost defect-free crystalline rod-shaped particles of nanocrystalline cellulose, i.e., cellulose nanocrystals (CNCs), can be isolated from cellulose fibres by acid or enzymatic hydrolysis [2]. Currently, CNCs are of great interest to materials scientists due to their unique combination of physical and chemical properties, including biocompatibility, biodegradability, large specific surface area and high elastic modulus [3]. The scope of CNC application is extensive. CNCs can be used to produce thermal insulation materials, create selective membranes, and deliver systems for medicinal and biologically active compounds. These new materials offer vast opportunities for scientific research and practical applications [4–6].

One of the obstacles to the commercialization of promising materials based on CNCs is that CNC isolation is a rather costly process (associated with the high consumption of energy and reagents, problems with equipment corrosion, environmental risks, and low final product yield). The lack of a universal method for obtaining CNCs has encouraged researchers to search for new methods and approaches (using metal salts, heteropolyacids, ionic liquids, and deep eutectic solvents), as well as to exploit a variety of physical and combined effects (ultrasound, steam explosion, electron beam, supercritical conditions, plasma chemistry, etc.) [7, 8].

The classical method of CNC production is sulfuric acid hydrolysis of cellulose under controlled conditions [9]. Treatment with an acid causes selective hydrolysis of the amorphous regions of cellulose, whereas the presence of glycosidic bonds between the elementary units of cellulose macromolecule is responsible for the relatively low resistance of cellulose to aqueous acid solutions. The generally recognized mechanism of acid hydrolysis of cellulose involves protonation of glycosidic oxygen, followed by cleavage of the glycosidic bond and addition of water molecules [10, 11]. The glycosidic bond cleavage of a cellulose macromolecule in the presence of mineral acids can also be carried out in nonaqueous media. The best studied process from this point of view is alcoholysis, which is the action of solutions of mineral acids in alcohols on the process of cellulose depolymerization [12–14]. Cellulose alcoholysis is similar to hydrolysis, however, the cleavage of glycosidic bonds is accompanied by the acetalization of the resulting free hydroxyl group

[15]. In contrast to complete cellulose hydrolysis, complete alcoholysis produces an alkyl glycoside rather than glucose. It is considered proven that alcoholysis is more effective than hydrolysis and proceeds at a much higher rate, although researchers explain this fact in different ways, and there is no single point of view on this issue [16–19]. However, an analysis of the literature data allows us to conclude that the activation energy for glycosidic bond cleavage during cellulose depolymerization in alcoholic media is lower than that in an aqueous medium, which is responsible for the higher efficiency of cellulose alcoholysis compared to hydrolysis [20]. Currently, cellulose alcoholysis in the presence of an acid catalyst is being actively studied to obtain alkyl glycosides as well as products of further alcoholysis [21–27].

Consequently, it is reasonable to assume that an alcohol medium can be used to obtain CNCs. In one of the recent works [28], we confirmed this hypothesis and showed that cellulose treatment with sulfuric acid in a medium of primary monohydric alcohols makes it possible to obtain CNCs in a higher yield and under milder conditions (at a reduced acid concentration) than hydrolysis in water. We obtained CNCs through sulfuric acid treatment of sulfate-bleached pulp in methanol, ethanol, propanol, and butanol-1 and studied their physicochemical properties. The alcohol media were shown to increase the yield of CNCs and reduce the optimal acid concentration. The properties of the CNCs obtained in the alcohols studied were similar to those of the CNCs obtained by hydrolysis in water, i.e., no functionalization of the surface of the CNC particles with the alkyl groups of the respective alcohols was observed. However, there was an increase in the content of surface sulfate groups and in the surface charge. Under certain synthesis conditions (0.025 g mL⁻¹ concentration of the pulp suspension, 55 % H₂SO₄ concentration, 50 °C temperature, 2-hour duration), the use of butanol-1 medium enables us to obtain a maximum possible CNC yield of 60 %.

In this work, we continued to investigate acid cellulose treatment for obtaining CNCs, expanding the range of alcohols used. Namely, in this work, we studied the optimal conditions for CNC synthesis in the media of pentanol-1, hexanol-1, heptanol-1, and octanol-1 and explored the properties of the synthesized CNCs.

Experimental

To obtain CNCs, dried sulfate-bleached pulp of coniferous wood (State Standard 9571-89, Arkhangelsk Pulp and Paper Mill, Russia) (Table 1), sulfuric acid (98 %, chemically pure, State Standard 4204-77, Chimmed, Russia), pentanol-1 (Chimmed, Russia), hexanol-1, heptanol-1, and octanol-1 (Sigma–Aldrich, USA) were used. All the alcohols used were chemically pure or extra pure and were used without further purification.

Table 1

Chemical composition of the sulfate-bleached pulp of coniferous wood (State Standard 9571-89)

Component	Content, %
Cellulose	93–96
Hemicellulose	3–6
Lignin	0.1–0.4
Oils, resins, waxes	0.1–0.2
Ash	0.1–0.15

The process of preparing CNCs was similar to the procedure described earlier [28]. In brief, the pulp ground in a blender was subjected to treatment in sulfuric acid solutions of various concentrations (20–55 wt%) in an appropriate alcohol at 50 °C for 2 hours with vigorous stirring. The concentration of the pulp suspension was 0.025 g mL⁻¹. The reaction was carried out in a water bath using a flask equipped with a reflux condenser. After completing the treatment, the heating was stopped, and the reaction mixture was diluted 10-fold with ice-cold deionized water. The CNC suspension was left to settle overnight, followed by decantation of the supernatant. The suspension was then washed in successive cycles of centrifugation (3–5 times for 10 minutes at 8000 rpm) and removal of the supernatant, first with distilled water and then with the appropriate alcohol. The final washing step involved treatment with water. Subsequently, the CNC aqueous suspension was treated with ultrasound (Sonorex DT100, Bandelin, Germany) for 15–30 min, followed by purification with ion exchange resin (TOKEM MB-50(R)) and a dialysis membrane (cut-off of 14 kDa, Roth, Germany) until a constant pH was reached.

The CNC yield was determined by the gravimetric method described elsewhere [29]. The CNC aqueous suspension was left to stand at a temperature of 4 °C for one month, during which large particle aggregates

with a small surface charge precipitated. The CNC suspension was separated from the sediment, and its volume was determined. Three parallel samples of a precisely measured volume were taken, poured into pre-weighed Petri dishes and air-dried until the weight was constant. Having thus determined the concentration of the suspension and knowing its volume, the total yield of the CNCs was calculated taking into account the initial pulp mass (under the assumption that all the water-soluble products had been removed at the stage of washing and dialysis). The relative error in determining the CNC yield in the three parallel samples did not exceed 3 %.

For some further recordings, CNC film samples were obtained by free evaporation of water at room temperature from aqueous CNC suspensions at a concentration of 10 gL⁻¹.

A JEOL JEM-1011 transmission electron microscope (TEM) (Japan) with an 8.5 megapixel ORIUS SC1000 W digital camera, an acceleration voltage up to 100 kV, and an image resolution up to 0.3 nm was used to examine the shape and size of the CNC particles. A diluted CNC suspension (approximately 0.01 gL⁻¹) was sonicated and then coated onto a copper TEM grid with a 200-mesh size. After complete drying, the samples were treated by shadowing with tungsten oxide WO₃ on a JEOL JEE-4C vacuum evaporator.

The elemental composition of the CNC films was determined by X-ray energy dispersive analysis using an X-Max 6 spectrometer (Oxford Instruments NanoAnalysis) with an x-ACT detector included in a VEGA 3 TESCAN scanning electron microscope (SEM). Range of the analyzed elements: ₄Be–₉₄Pu. The equipment was synchronized with the SEM electron gun, allowing detailed surface elemental mapping and providing a highly accurate analysis.

The FTIR spectra were obtained on a VERTEX 80v spectrophotometer (Bruker, Germany) in the frequency range of 4000–400 cm⁻¹. The samples were pressed into tablets containing 1 mg of the analyte and 100 mg of potassium bromide.

The Raman spectra of the CNC samples were recorded on a Confotec NR 500 instrument (Sol Instruments, Belarus). The spectral range for recording the Raman signals ranged from 30 cm⁻¹ to approximately 6000 cm⁻¹ and a spectral resolution of 0.25 cm⁻¹ was achieved by simultaneous use of 3 lasers (785 nm, 633 nm, 488 nm) through automatic switching of the necessary components within the system.

The sizes of the CNC particles in the aqueous suspensions were measured by the dynamic light scattering method (DLS) (emission wavelength of 633 nm) on a Zetasizer Nano ZS device (Malvern Instruments Ltd., UK) operating in the range of 0.3 nm – 6 μm. The measurements were carried out in disposable polystyrene cuvettes at a 0.1 gL⁻¹ suspension concentration. During the measurements, the cuvette with the test sample was thermostated at a temperature of 20 °C. The obtained particle size values are the results of averaging over five successive measurement cycles. The value obtained in each cycle is, in turn, the result of automatic processing of 10–15 measurements. The sizes of the CNC particles obtained by the DLS method are averaged values for the hydrodynamic diameters of equivalent spheres and do not reflect the real physical sizes of anisotropic rod-shaped CNC particles; rather, they are used for comparative analysis [30].

The surface charge of the CNC particles in an aqueous suspension was evaluated by the ζ-potential (Zetasizer Nano ZS). The obtained ζ-potential values were the results of averaging over five successive measurement cycles.

X-ray diffraction (XRD) analysis was carried out on a Bruker D8 Advance diffractometer according to the Bragg-Brentano scheme using Cu-K_α radiation (λ = 0.1542 nm). The angular scanning range was 2–45° with a 0.01° step. A Vantec-1 high-speed meter was used. The pulse acquisition time at each scanning point was 0.5 s. The CNC crystallinity index according to Segal [31] was determined as

$$IC = (I_{200} - I_a)/I_{200},$$

where I_{200} is the intensity of the reflection corresponding to the crystallographic plane (200) and I_a is the intensity of the amorphous halo (the minimum between the peaks corresponding to crystallographic planes (200) and (110)).

The sizes of the CNC crystallites (L) were calculated using the Scherrer formula [32]:

$$L = 0.9\lambda/\beta\cos\theta,$$

where λ is the X-ray wavelength, nm; β is the full width of the diffraction peak, measured at its half-maximum, rad.; θ is the diffraction angle of the peak, degrees.

Thermogravimetric analysis was performed on a TG 209 F1 Iris thermomicrobalance (Netzsch, Germany) using platinum crucibles in an atmosphere of dry argon at a flow rate of 30 ml min⁻¹ and a heating rate of 10 K min⁻¹.

The degree of polymerization of the CNC samples was determined by the viscosity of the solutions in cadoxene, as described earlier [33].

Results and Discussion

Pulp treatment was carried out at a temperature of 50 °C for two hours with intense stirring, changing sulfuric acid concentration (from 20 to 55 wt%). Figure 1 shows the CNC yield in the media of alcohols studied: pentanol-1, hexanol-1, heptanol-1, and octanol-1. Each of the alcohols is characterized by its own sulfuric acid concentration range in which CNCs can be isolated. This range is limited by the minimum sulfuric acid concentration, at which virtually no depolymerization of cellulose occurs (the CNC yield is low), or the maximum concentration, at which cellulose is depolymerized to low-molecular-weight oligomers, glucose and other soluble products (the CNC yield is also low). The maximum CNC yield and the proper optimal acid concentration depend on the alcohol used. Both the acid concentration corresponding to the maximum CNC yield and the yield itself decreased in the pentanol-1, hexanol-1, heptanol-1, and octanol-1 series (Table 2).

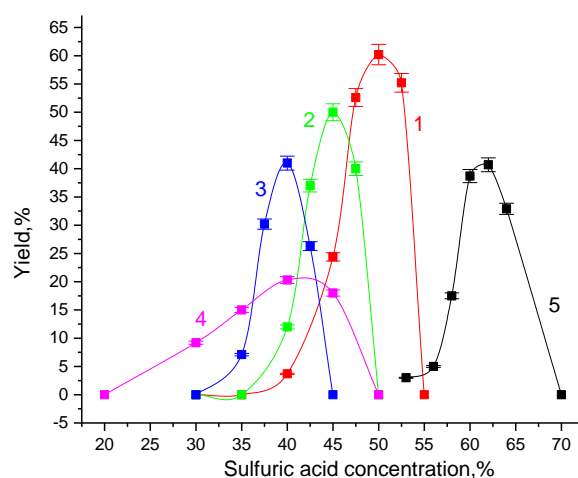


Figure 1. CNC yield during pulp treatment in pentanol-1 (1), hexanol-1 (2), heptanol-1 (3), and octanol-1 (4). For comparison, the curve for hydrolysis in water is shown (5) [28]

Table 2

The concentration of sulfuric acid corresponding to the maximum CNC yield in the alcohols studied. For comparison, data for hydrolysis in water is shown [28]

Medium	H ₂ SO ₄ concentration range for CNC isolation, wt%	H ₂ SO ₄ concentration corresponding to the maximum CNC yield, wt%	Maximum CNC yield, %
Pentanol-1	35–55	50	60±2
Hexanol-1	35–50	45	45±1
Heptanol-1	30–45	40	23±1
Octanol-1	20–50	40	20±1
Water	53–70	62	41±1

It should be taken into account that a certain amount of acid is spent on interactions with alcohols to form the respective alkyl sulfates and dialkyl ethers [10, 20]. As a result of interactions with sulfuric acid, alcohols become darker, from light yellow for pentanol-1 to dark brown for octanol-1. Titration of the reaction medium with sodium hydroxide after alcoholysis was completed showed that the sulfuric acid consumption in esterification reactions was approximately 30 % of the initial acid amount (determined for the sulfuric acid–alcohol systems, in which the maximum CNC yield was registered). For this reason, the acid concentrations in Table 2 and Figure 1 are somewhat overestimated because the initial concentrations are given without considering acid consumption for interactions with alcohols.

The transmission electron microscopy (TEM) images show that the CNC particles have an anisotropic rod-like shape (Fig. 2). The length of the particles ranges from approximately 200 to 400 nm, and the diame-

ter is approximately 10–20 nm, although aggregates of the particles formed due to their lateral interaction are observed.

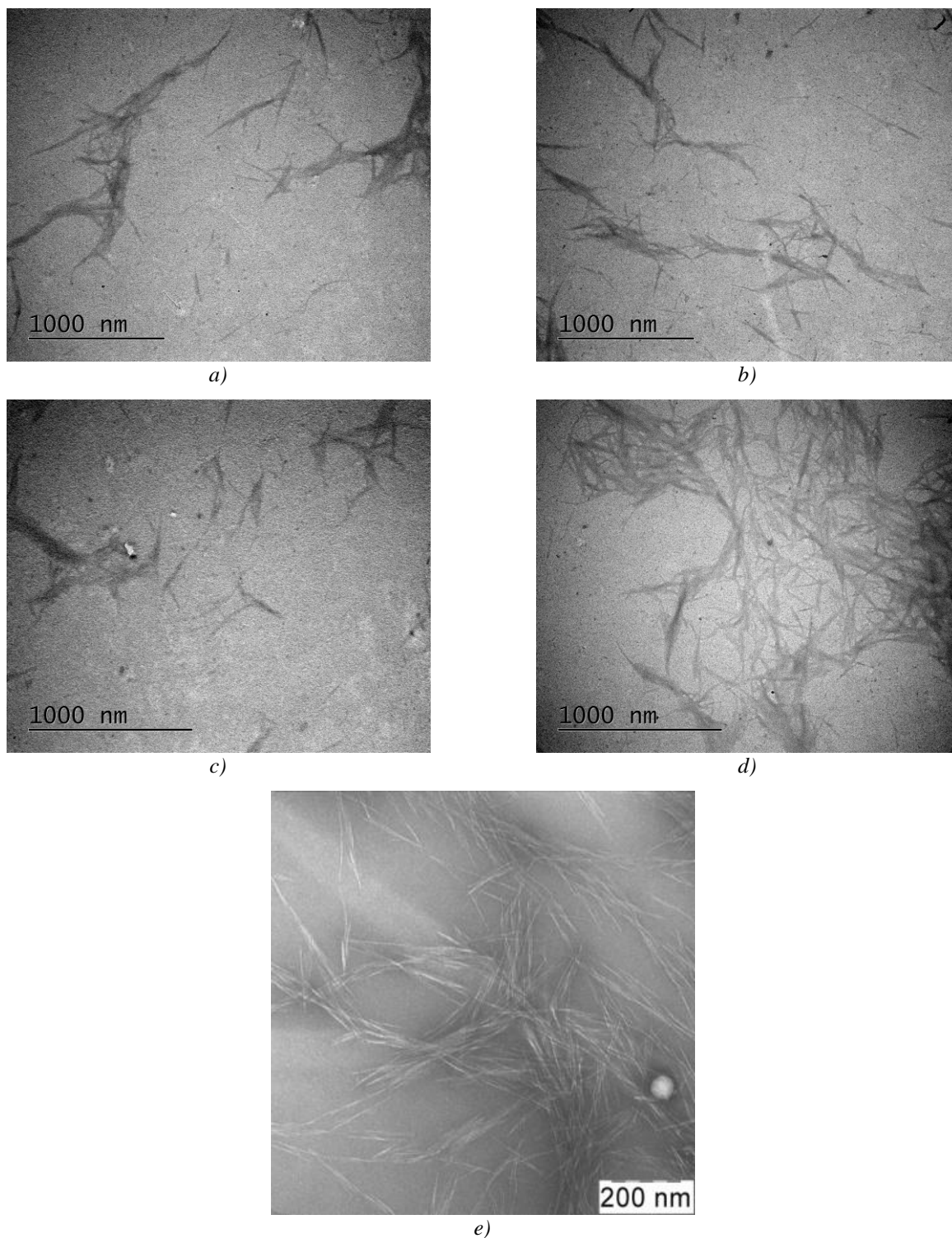


Figure 2. TEM images of CNC particles obtained in pentanol-1 (*a*), hexanol-1 (*b*), heptanol-1 (*c*), and octanol-1 (*d*). For comparison, an image of CNC particles obtained through hydrolysis in water is shown (*e*) [28]. The scales are 1 μm (*a–d*), and 200 nm (*e*)

The data obtained by DLS were in good agreement with the TEM images of the CNC particles. The DLS experimental data (Fig. 3) for aqueous suspensions show polydispersity of the size distribution of the CNC particles. Two groups of particles can be distinguished at approximately 100–300 and 10–40 nm in size.

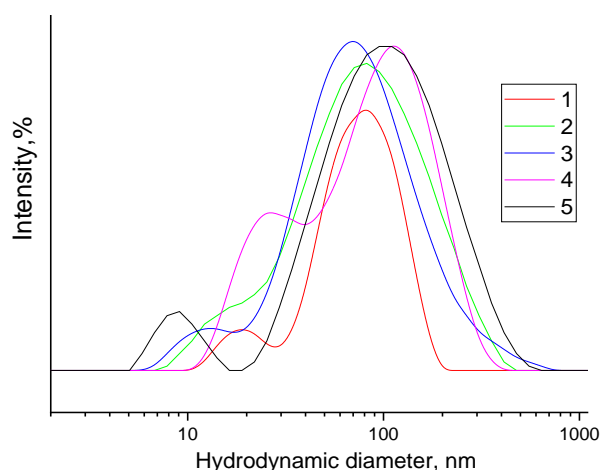


Figure 3. Hydrodynamic diameters of the CNC particles obtained in pentanol-1 (1), hexanol-1 (2), heptanol-1 (3), and octanol-1 (4). For comparison, data for CNC particles obtained through hydrolysis in water are shown (5) [28]

Notably, the results shown in Figures 2 and 3 and further discussed in the article refer to the CNCs obtained with the maximum yield.

Aqueous suspensions of CNCs exhibit high colloidal stability for a long time (a month or longer), which is due to the significant charge of sulfate groups grafted onto the surface of the CNC particles during sulfuric acid treatment. The ζ -potential values of the aqueous CNC suspensions and the sulfur content (as part of the surface sulfate groups) of the samples are given in Table 3.

Table 3

Particle charge and elemental composition of the CNC samples obtained in the alcohols studied. For comparison, the data for hydrolysis in water are shown [28]

Medium	ζ -potential, mV	*Elemental composition, %			O/C ratio
		S	C	O	
Pentanol-1	-47±3	1.2±0.1	54.5±0.1	45.9±0.1	0.84
Hexanol-1	-46±3	1.0±0.1	54.1±0.1	44.9±0.1	0.83
Heptanol-1	-45±2	0.9±0.1	52.9±0.1	45.5±0.1	0.86
Octanol-1	-41±2	0.8±0.1	53.5±0.1	46.6±0.1	0.87
Water	-38±2	0.7±0.1	47.6±0.1	39.6±0.1	0.83

* Determined by X-ray energy dispersive analysis

The oxygen-to-carbon ratios for all the CNC samples are close to the theoretical value of 0.83 for a pure cellulose surface [34, 35].

The thermal stability of CNCs largely depends on the content of surface sulfate groups. The sulfate groups catalyze the thermal decomposition of CNC samples, decreasing their thermal stability [36]. The high sulfur content in the samples is confirmed by the lower decomposition temperatures than those of CNCs with surface carboxyl groups or microcrystalline cellulose (MCC) [37]. The TG curves of the CNC samples under study are characterized by three main mass loss regions (Fig. 4). The first region (approximately 100 °C) is associated with water evaporation, the second region (from approximately 200 to 400 °C) is associated with CNC pyrolysis and the formation of gaseous products, and the third region (above 400 °C) is associated with the thermal decomposition of carbonaceous matter [38].

The X-ray diffraction patterns of the CNC films shown in Figure 5 indicate that the resulting CNCs are cellulose I. Despite the relatively low intensity of the diffraction patterns, there is a clearly visible peak at a Bragg angle of $2\theta = 22.9^\circ$, an implicit double peak in the region $2\theta = 15-17^\circ$, and a diffraction peak of low intensity at approximately $2\theta = 34.5^\circ$, which corresponds to the crystallographic planes (200), (1-10), (110), and (004) of cellulose I β , respectively [39]. The CNC films are characterized by a high crystallinity index (approximately 90 %) and a crystallite size of approximately 4 nm (perpendicular to the (200) crystallographic plane) (Table 4).

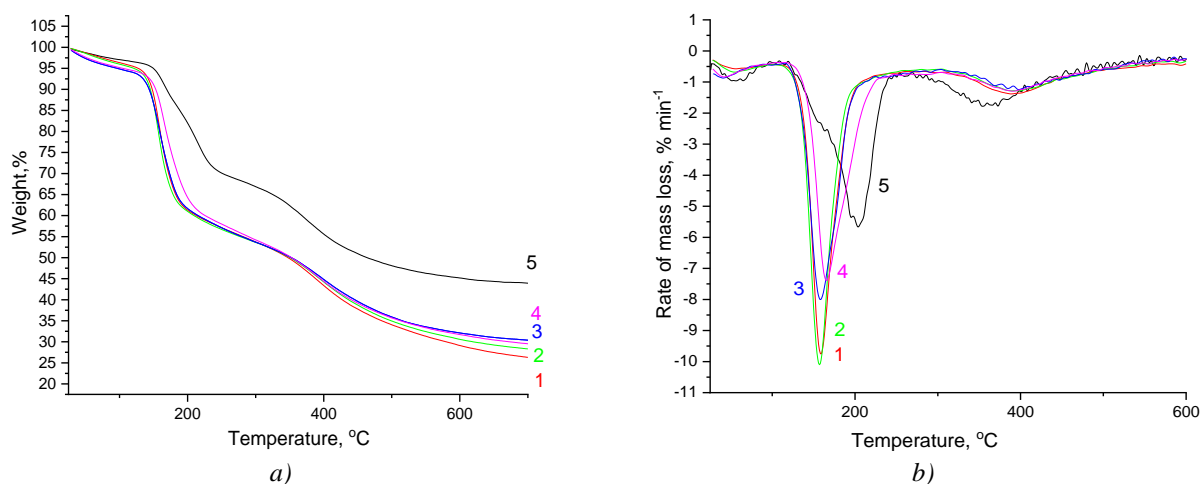


Figure 4. TG (a) and DTG (b) curves of the CNC samples obtained in pentanol-1 (1), hexanol-1 (2), heptanol-1 (3), and octanol-1 (4). For comparison, curves for the CNC sample obtained by hydrolysis in water (5) [28] are shown

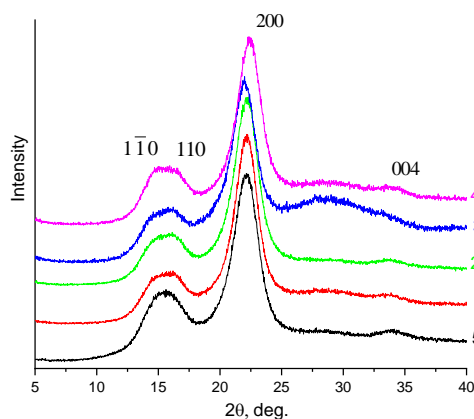


Figure 5. X-ray diffraction patterns for CNC films obtained in pentanol-1 (1), hexanol-1 (2), heptanol-1 (3), and octanol-1 (4). For comparison, diffraction patterns for the CNC sample obtained by hydrolysis in water (5) [28] are shown

Table 4

Properties of the CNC samples obtained in the alcohols studied and in water [28]

Medium	Crystallinity index, %	Crystallite size perpendicular to the (200) plane, nm
Pentanol-1	87±4	3.9±0.2
Hexanol-1	86±4	4.1±0.2
Heptanol-1	84±4	3.6±0.1
Octanol-1	86±4	4.0±0.2
Water	80±4	3.3±0.1

The degree of polymerization of the CNC samples ranges from approximately 90 to 110, which is characteristic of the leveling off degree of polymerization of nanocrystalline cellulose; i.e., CNCs were formed, and the crystallites were left intact [40, 41].

Figure 6 shows the FTIR spectra of the CNC samples obtained in pentanol-1, hexanol-1, heptanol-1, and octanol-1. The spectra are typical of cellulose and are characterized by intense absorption bands in the wavenumber regions of 3500–3300 cm^{-1} and 3000–2750 cm^{-1} , which correspond to the stretching vibrations of the OH and C–H bonds of the cellulose macromolecule. In the range of 1500–1200 cm^{-1} , bending vibra-

tions of the OH, CH and CH₂ groups appear. The absorption region at 1200–950 cm⁻¹ refers to the stretching vibrations of the C–O and C–C bonds of the pyranose ring. The bands in the frequency range of 950–400 cm⁻¹ are caused by the vibrations of large fragments of the cellulose macromolecule, as well as out-of-plane vibrations of the hydroxyl groups. The fairly intense band at approximately 1640 cm⁻¹ is due to the stretching vibrations of the adsorbed water. In general, the FTIR spectra of the CNC samples obtained in the alcohols studied are identical to those obtained by standard sulfuric acid hydrolysis [28].

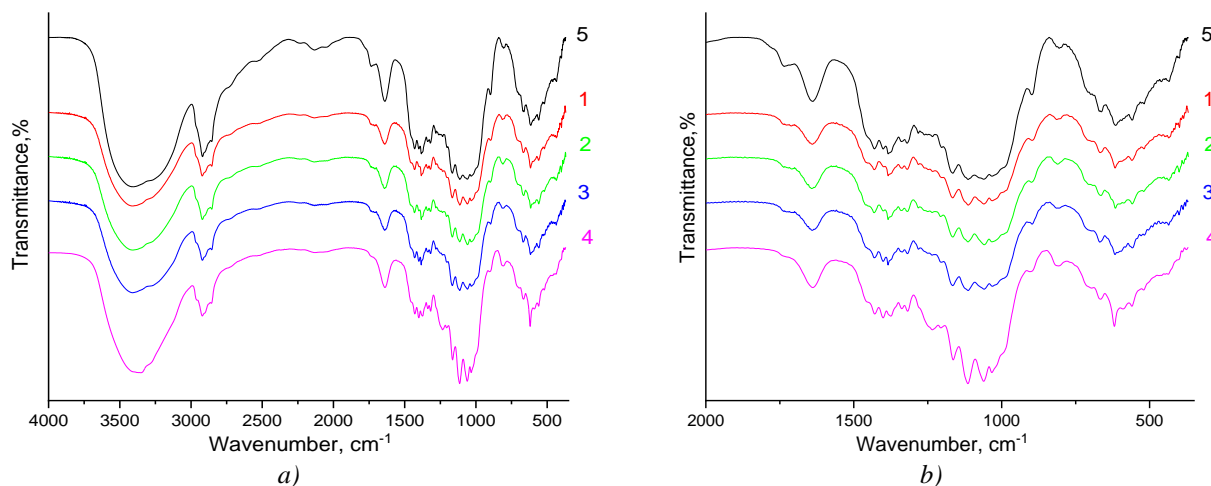


Figure 6. FTIR spectra of the CNC samples obtained in pentanol-1 (1), hexanol-1 (2), heptanol-1 (3), and octanol-1 (4) in the wavenumber ranges of 4000–400 cm⁻¹ (a) and 2000–400 cm⁻¹ (b). For comparison, the FTIR spectrum of the CNC sample obtained by hydrolysis in water (5) [28] is shown

The Raman spectra of the studied CNC samples generally correspond to MCC spectra [42]. The intense peak at a frequency of 1096 cm⁻¹ is attributed to the stretching vibrations of the C–O and C–C bonds of the pyranose ring (Fig. 7). The intense peak at 1380 cm⁻¹ in the “fingerprint” region characterizes the ring bending vibrations. The intense bands in the spectral regions of 2800–3000 cm⁻¹ and 1430–1480 cm⁻¹ describe the stretching and bending vibrations of the CH groups, respectively. The less intense band in the range of 3100–3600 cm⁻¹ is ascribed to the stretching vibrations of the OH groups [43, 44].

The CNCs samples obtained in the alcohols studied were cellulose I, as evidenced by the presence of the characteristic peak at 1480 cm⁻¹ (CH₂ bending vibrations of the hydroxymethyl group in the *tg* conformation) and 380 cm⁻¹ (out-of-plane vibrations of the pyranose ring). In addition, the high intensity of the peak at 380 cm⁻¹ proves the high crystallinity of the samples [43]. Another peak at 93 cm⁻¹ (twisting deformations along the polymer chain), also used to characterize the crystallinity of cellulose samples [45, 46], has a lower intensity and is much less pronounced.

In the spectra of the CNC samples under study, the bands at 1060 and 1274 cm⁻¹ are attributed to the symmetric and asymmetric O=S=O stretching vibrations of sulfate esters, respectively [47]. For the CNCs under study, there are surface sulfate groups on the surface of the nanoparticles as a result of esterification of the hydroxyl groups (mainly the primary hydroxyl groups at the carbon atom C6). The intensity and width of the bands at 1060 and 1274 cm⁻¹ increase as the substitution degree increases, i.e., as the content of the surface sulfate groups increases. The sulfate groups grafted onto the surface of the CNC particles also affect the vibrational modes of the entire pyranose. Therefore, for the CNC samples under study, the ratio of the intensities of the bands at 2896 and 2969 cm⁻¹ changes (these bands reflect the CH and CH₂ stretching vibrations, respectively). The intensity of the CH₂ stretching vibrations increases when going from octanol-1 to pentanol-1, and that of the CH vibrations decreases. In comparison, for the CNC sample obtained by hydrolysis in water, the peak at 2896 cm⁻¹ (CH vibrations) is much greater than that of the other materials, and the band at 2969 cm⁻¹ (CH₂ vibrations) appears only as a shoulder. However, the replacement of protons with sulfate groups as a result of esterification does not reduce the intensity of the bands in the range of 3100–3600 cm⁻¹ (stretching vibrations of the OH groups) compared to that of MCC [42] since the substitution degree is low.

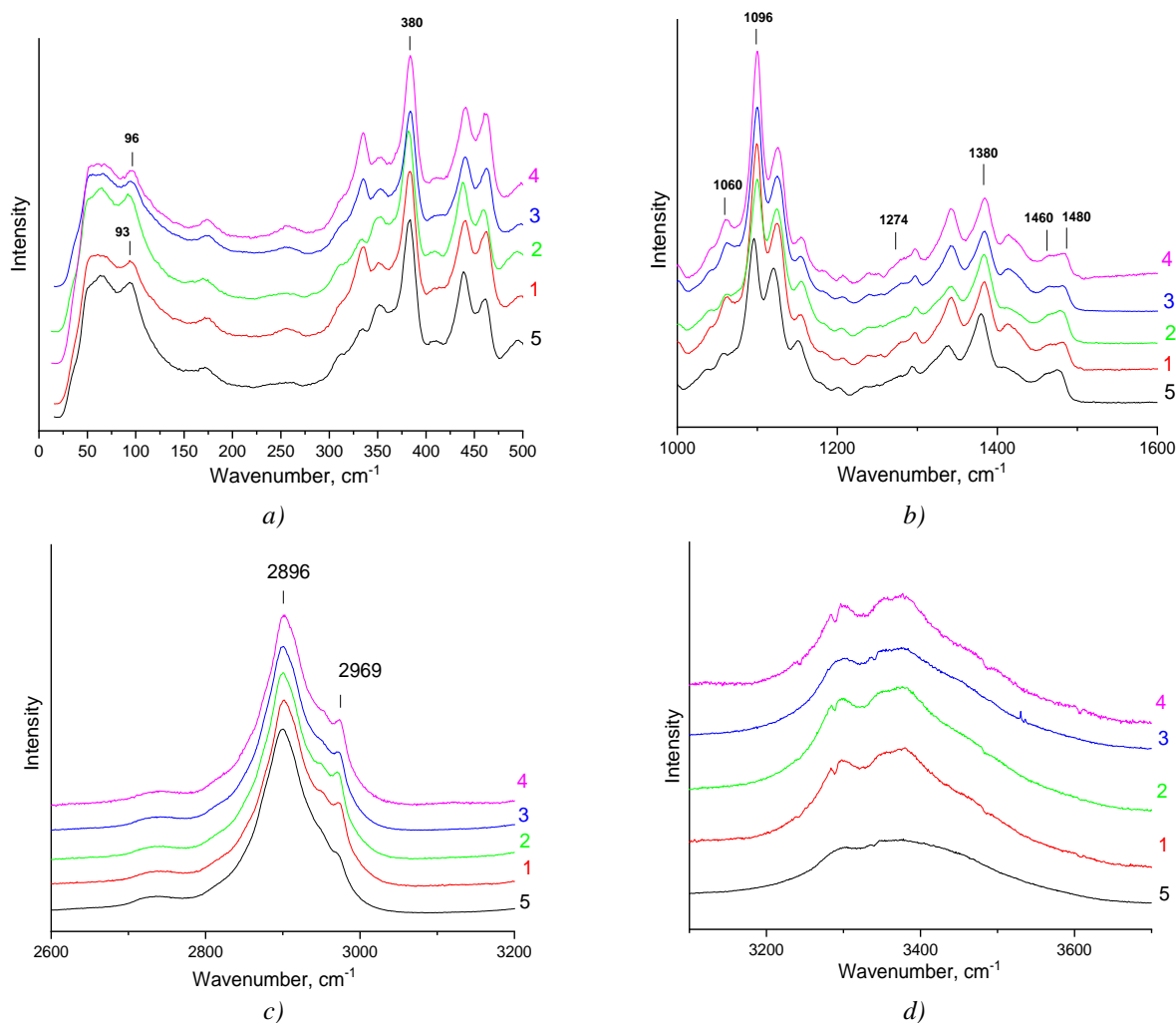


Figure 7. Raman spectra of the CNC samples obtained in pentanol-1 (4), hexanol-1 (3), heptanol-1 (2), octanol-1 (1), and by hydrolysis in water (5) [28] in the wavenumber ranges of 0–500 cm^{-1} (a), 1000–1600 cm^{-1} (b), 2600–3200 cm^{-1} (c), and 3100–3700 cm^{-1} (d), respectively. The spectra are normalized to the band at 1096 cm^{-1}

The formation of ester bonds at C6 may be responsible for the appearance of rotamers of the unsubstituted surface CH_2OH groups, while in the crystalline phase, they are in the *tg* conformation (for cellulose I α and I β) [43, 48, 49]. The intensity ratio of the bands at 1460 and 1480 cm^{-1} is used to estimate the *gt/tg* rotamer ratio of the CH_2OH group of cellulose I [50]. The higher intensity of the band at 1460 cm^{-1} for the CNC samples obtained in the alcohols studied indicates an increase in the proportion of rotamers of the CH_2OH groups with the *gt* conformation.

As we have previously shown [28], an acid treatment of cellulose in methanol, ethanol, propanol, and butanol-1 is not accompanied by CNC surface alkylation. We observed the same phenomenon during CNC isolation in pentanol-1, hexanol-1, heptanol-1, and octanol-1. The elemental analysis, FTIR and Raman spectra did not reveal any differences between the CNC samples obtained in the alcohols studied and the CNC sample obtained by hydrolysis in water (Table 3, Figures 6, 7) [28].

When the surface of CNC particles are alkylated during alcoholysis, one expects an increase in the intensity of the absorption bands of the methylene groups and the appearance of new bands corresponding to the methyl groups. In this case, symmetric and asymmetric stretching vibrations, as well as bending vibrations of the C–H bond, are expected to appear in the FTIR spectra in the wavenumber ranges of 2800–3000 cm^{-1} , 1365–1395 cm^{-1} , and 1430–1470 cm^{-1} , respectively. We did not observe any changes in the Raman spectra associated with possible alkylation of the surface of the CNC particles during alcoholysis either. In the case of CNC alkylation, one expects an increase in the intensity of the bands in the Raman spectra associated with the stretching and bending vibrations of the methyl and methylene groups (spectral regions of 2800–3000 cm^{-1} and 1430–1480 cm^{-1} , respectively).

Apparently, in contrast to the homogeneous process of alkylation of glucose during complete alcoholysis, the heterogeneous process of acid cellulose treatment in alcohol media during CNC production does not involve CNC surface alkylation. One possible cause of this difference may be that, despite the use of an alcohol medium, hydrolysis ultimately occurs due to the presence of water in the alcohol, the acid catalyst, and/or cellulose. Alternatively, water can result from side reactions of alcohol esterification (part of the sulfuric acid will be irretrievably consumed by the reactions) [51].

We have previously shown [28] that in the series water–methanol–ethanol–propanol–butanol-1, the acid concentration corresponding to the maximum yield of CNCs decreases, and the yield itself increases. Since protonation of the glycosidic oxygen in an aqueous environment with subsequent cleavage of the glycosidic bond in the elementary units of the cellulose macromolecule requires rather harsh conditions (strong acid, high proton concentration), we hypothesized that the process of cellulose depolymerization can proceed more efficiently in an environment in which the solvated proton has much greater acidity than that of the hydronium ion H_3O^+ (pKa -1.7). Protic solvents, particularly alcohols, can create such an environment. According to the literature, the pKa values for protonated alcohols decrease in the series CH_3OH_2^+ , $\text{C}_2\text{H}_5\text{OH}_2^+$, $(\text{CH}_3)_2\text{CHOH}_2^+$, and $(\text{CH}_3)_3\text{COH}_2^+$ and are, respectively, -2.2 , -2.4 , -3.2 , and -3.8 [52, 53].

We found [28] that the dependence of the maximum yield of CNCs on the pKa value of the protonated solvent (water and alcohols, methanol, ethanol, propanol, and butanol-1) is well described by the following quadratic function: $\text{Max.yield} = a \cdot \text{pKa}^2 + b \cdot \text{pKa} + c$, where Max.yield is the maximum yield of the CNCs; pKa are the pKa values of the protonated solvents (water, methanol, ethanol, propanol, and butanol-1); and a , b , and c are constants. Notably, we used published data on the pKa values for protonated isopropanol $(\text{CH}_3)_2\text{CHOH}_2^+$ and tert-butanol $(\text{CH}_3)_3\text{COH}_2^+$, although the experiment was carried out with propanol and butanol-1.

The coordinates of the parabola vertex, according to the parameters of this quadratic equation are $\text{pKa} = -3.65$ and $\text{Max.yield} = 60.08$. This means that under the given conditions for CNC synthesis (the pulp suspension concentration of 0.025 g ml^{-1} , a temperature of $50 \text{ }^\circ\text{C}$, and a duration of 2 hours), the butanol-1 medium enables us to obtain a maximum possible CNC yield of approximately 60 %. In this regard, it would be interesting to check whether the values of the maximum CNC yield obtained in the media of pentanol-1, hexanol-1, heptanol-1, or octanol-1 lie on the descending branch of the parabola. It is difficult to answer this question because the pKa values for the protonated alcohols, pentanol-1, hexanol-1, heptanol-1, and octanol-1, are, to our knowledge, unavailable in the literature.

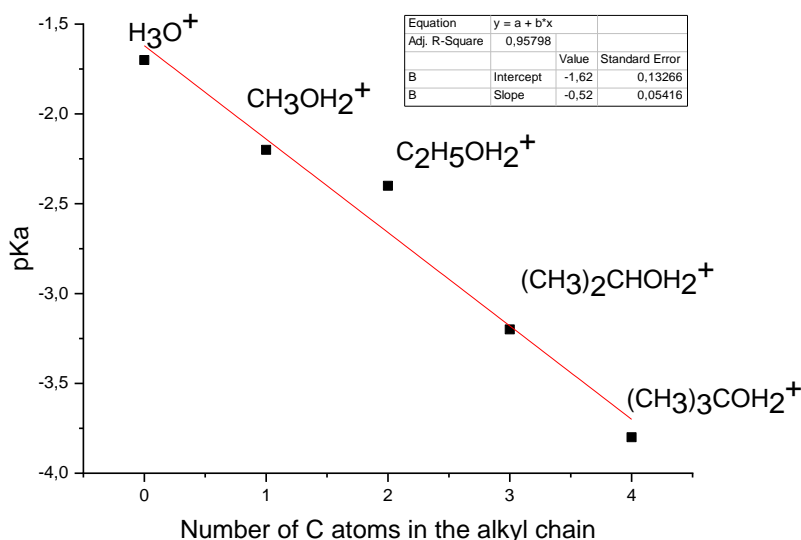


Figure 8. Dependence of the pKa of a protonated solvent (water, methanol, ethanol, isopropanol, or tert-butanol) on the number of carbon atoms in the alkyl chain

However, since, in the series $\text{H}_3\text{O}^+ - \text{CH}_3\text{OH}_2^+ - \text{C}_2\text{H}_5\text{OH}_2^+ - (\text{CH}_3)_2\text{CHOH}_2^+ - (\text{CH}_3)_3\text{COH}_2^+$, the dependence of the pKa values on the alkyl chain length is well approximated by a linear function (Figure 8 and the inset in it), it is possible to estimate the probable pKa values for protonated pentanol-1, hexanol-1, heptanol-1, and octanol-1. According to the parameters of the linear equation given in the inset in Figure 8, these val-

ues are -4.2 ± 0.4 , -4.7 ± 0.5 , -5.3 ± 0.6 and -5.8 ± 0.6 for protonated pentanol-1, hexanol-1, heptanol-1, and octanol-1, respectively.

Thus, based on the estimated pKa values for protonated pentanol-1, hexanol-1, heptanol-1, and octanol-1, plotting the dependence of the maximum yield of the synthesized CNCs on the pKa of the protonated alcohols from methanol to octanol-1 is possible (Fig. 9).

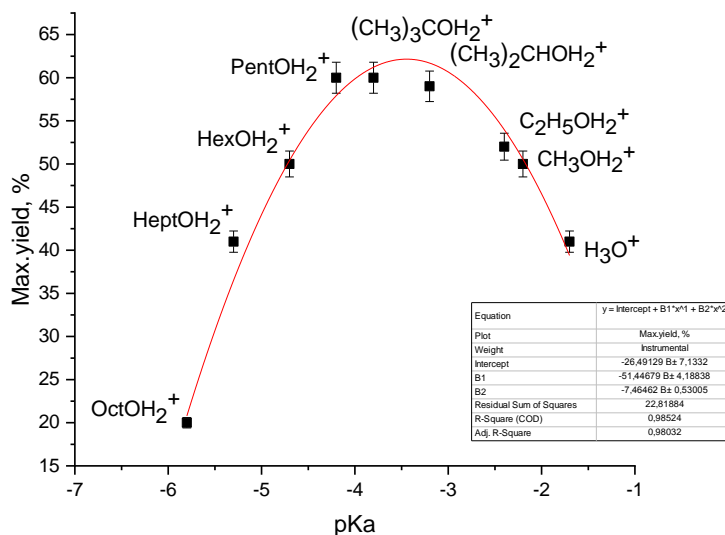


Figure 9. Dependence of the maximum CNC yield on the pKa values of protonated solvents (water and alcohols)

Figure 9 indeed shows that the values of the maximum CNC yield obtained in the media of pentanol-1, hexanol-1, heptanol-1, and octanol-1 lie on the descending branch of the parabola. In addition, in pentanol-1, a maximum yield of 60 % is achieved at an even lower acid concentration (50 wt%) than that in butanol-1 (55 wt%).

Thus, the dependence of the maximum CNC yield on the pKa of protonated alcohols is extreme and is quite well described by a parabola with a vertex corresponding to the pKa values of protonated butanol-1 and pentanol-1 (approximately -4) and a yield of approximately 60 %. The extreme nature of the dependence is apparently determined by the competition of at least two factors. On the one hand, the increase in the acidity of the protonated alcohols with increasing length of the alkyl radical (the increase in the negative pKa values) promoted cellulose depolymerization and, accordingly, an increase in the CNC yield. On the other hand, due to process heterogeneity, the hydrolysis and alcoholysis rates (and, accordingly, cellulose depolymerization) depend on phenomena such as cellulose wetting and swelling, adsorption and diffusion of reagents. The process of cellulose swelling is reduced to the penetration of solvent molecules into the intermolecular space of cellulose and solvation of the respective sections of the polymer chain, which changes the intermolecular interactions between the macromolecules, increases their mobility and makes it easier for the reagents to enter the intermolecular space. However, the swelling degree of cellulose is known to be lower for aliphatic alcohols than for water and decreases with increasing length of the hydrocarbon radical [54]. Therefore, this factor does not increase the hydrolysis rate in an alcohol environment.

In a recently published paper, Zhao et al. [55] studied the mechanism of catalytic conversion of cellulose into 5-ethoxymethylfurfural and ethyl levulinate in ethanol and water-ethanol mixtures. A mixture of Brønsted and Lewis acids (H_2SO_4 and AlCl_3) was used to catalyze the reaction. Based on the experimental data and results of computer simulations, the authors showed that the presence of water lowers the energy barrier of the depolymerization of cellobiose (as a model of cellulose) compared to that for pure ethanol. Thus, the presence of water in the system contributes to the maximum conversion of cellulose into products of alcoholysis.

Apparently, when CNCs are produced in an alcohol medium, water plays a key role, and the alcohol medium promotes hydrolysis, increasing the yield of the synthesized CNCs and lowering the optimal acid concentration. Obviously, further research, including computer simulation methods, is required for a detailed elucidation of the mechanism of acid hydrolysis of cellulose in an alcohol environment during CNC synthesis, which is the goal of our further work.

Conclusions

For the first time, CNCs were obtained by sulfuric acid treatment of sulfate-bleached pulp in pentanol-1, hexanol-1, heptanol-1, and octanol-1, and their physicochemical properties were studied. In pentanol-1, the maximum CNC yield was 60 % at a sulfuric acid concentration of 50 wt%. During cellulose treatment in the alcohol media, no alkylation of the CNC surface occurs, and the properties of the CNCs are similar to those of the CNCs obtained by standard sulfuric acid hydrolysis. In CNC synthesis, water plays a key role, and alcohol media promote hydrolysis, increasing the CNC yield and reducing the optimal acid concentration. Additional studies in organic solvents and mixed aqueous-organic media are necessary to fully elucidate the mechanism of cellulose solvolysis during the production of CNCs.

Author Information*

*The authors' names are presented in the following order: First Name, Middle Name and Last Name

Oleg Valentinovich Surov (*corresponding author*) — Candidate of Chemical Sciences, Senior Researcher, G.A. Krestov Institute of Solution Chemistry of the Russian Academy of Sciences, Akademicheskaya St., 1, 153045, Ivanovo, Russia; *e-mail*: ovs@isc-ras.ru, <https://www.scopus.com/redirect.uri?url=https://orcid.org/0000-0002-7164-364X&authorId=8338558100&origin=AuthorProfile&orcid=0000-0002-7164-364X&category=orcidLinkhttps://orcid.org/0000-0002-7164-364X>

Marina Igorevna Voronova — Candidate of Chemical Sciences, Senior Researcher, G.A. Krestov Institute of Solution Chemistry of the Russian Academy of Sciences, Akademicheskaya St., 1, 153045, Ivanovo, Russia; *e-mail*: miv@isc-ras.ru, <https://www.scopus.com/redirect.uri?url=https://orcid.org/0000-0002-7164-364X&authorId=8338558100&origin=AuthorProfile&orcid=0000-0002-7164-364X&category=orcidLinkhttps://www.scopus.com/redirect.uri?url=https://orcid.org/0000-0002-8535-6940&authorId=6701319869&origin=AuthorProfile&orcid=0000-0002-8535-6940&category=orcidLinkhttps://orcid.org/0000-0002-8535-6940>

Author Contributions

The manuscript was written through contributions of all authors. All authors have given approval to the final version of the manuscript. **CRedit**: **Oleg Valentinovich Surov** conceptualization, data curation, investigation, methodology, validation, visualization, writing-original draft, writing-review & editing; **Marina Igorevna Voronova** data curation, formal analysis, validation, visualization, writing-review & editing.

Acknowledgments

Authors thank the *Upper Volga Region Centre of Physicochemical Research* (Ivanovo, Russia) for some measurements taken with the use of its equipment.

Conflicts of Interest

The authors declare no conflict of interest.

References

- 1 Habibi, Y., Lucia, L. A., & Rojas, O. J. (2010). Cellulose nanocrystals: Chemistry, self-assembly, and applications. *Chem. Rev.*, *110*(6), 3479–3500. <https://doi.org/10.1021/cr900339w>
- 2 Klemm, D., Kramer, F., Moritz, S., Lindstrom, T., Ankerfors, M., Gray, D., & Dorris, A. (2011). Nanocelluloses: a new family of nature-based materials. *Angew. Chem. Int. Ed.*, *50*(24), 5438–5466. <https://doi.org/10.1002/anie.201001273>
- 3 Moon, R. J., Martini, A., Nairn, J., Simonsen, J., & Youngblood, J. (2011). Cellulose nanomaterials review: Structure, properties and nanocomposites. *Chem. Soc. Rev.*, *40*, 3941–3994. <https://doi.org/10.1039/C0CS00108B>
- 4 Thomas, B., Raj, M. C., Athira, K. B., Rubiyah, M. H., Joy, J., Moores, A., Drisko, G. L., & Sanchez, C. (2018). Nanocellulose, a versatile green platform: From biosources to materials and their applications. *Chem. Rev.*, *118*(24), 11575–11625. <https://doi.org/10.1021/acs.chemrev.7b00627>
- 5 Dhali, K., Ghasemlou, M., Daver, F., Cass, P., & Adhikari, B. (2021). A review of nanocellulose as a new material towards environmental sustainability. *Sci. Total Environ.*, *775*, 145871. <https://doi.org/10.1016/j.scitotenv.2021.145871>

- 6 Zhu, H., Luo, W., Ciesielski, P. N., Fang, Z., Zhu, J. Y., Henriksson, G., Himmel, M. E., & Hu, L. (2016). Wood-derived materials for green electronics, biological devices, and energy applications. *Chem. Rev.*, *116*(16), 9305–9374. <https://doi.org/10.1021/acs.chemrev.6b00225>
- 7 Kargarzadeh, H., Ahmad, I., Thomas, S., & Dufresne, A. (2017). *Handbook of nanocellulose and cellulose nanocomposites* (1st ed.). Wiley.
- 8 Hu, L., Jiang, F., & Chen, C. (2023). *Emerging nanotechnologies in nanocellulose*. Springer International Publishing.
- 9 Rana, A. K., Frollini, E., & Thakur, V. K. (2021). Cellulose nanocrystals: Pretreatments, preparation strategies, and surface functionalization. *Int. J. Biol. Macromol.*, *182*, 1554–1581. <https://doi.org/10.1016/j.ijbiomac.2021.05.119>
- 10 Deng, W., Zhang, H., Xue, L., Zhang, Q., & Wang, Y. (2015). Selective activation of the C–O bonds in lignocellulosic biomass for the efficient production of chemicals. *Chin. J. Catal.*, *36*(9), 1440–1460. [https://doi.org/10.1016/S1872-2067\(15\)60923-8](https://doi.org/10.1016/S1872-2067(15)60923-8)
- 11 Bikales, N. M., & Segal, L. (1971). *Cellulose and cellulose derivatives* (2nd ed., part IV). Wiley.
- 12 Reeves, R. E., Schwartz, W. M., & Giddens, J. E. (1946). The alcoholysis of cellulose. *J. Am. Chem. Soc.*, *68*(7), 1383–1385. <https://doi.org/10.1021/ja01211a505>
- 13 Reeves, R. E., Mazzeno Jr, L. W., & Hoffpauir, C. L. (1950). The heterogeneous methanolysis of native and mercerized cotton cellulose. *J. Am. Chem. Soc.*, *72*(10), 4773–4777. <https://doi.org/10.1021/ja01166a121>
- 14 Yamada, T., Yamaguchi, M., Kubo, S., & Hishikawa, Y. (2015). Direct Production of Alkyl Levulinates from Cellulosic Biomass by a Single-Step Acidic Solvolysis System at Ambient Atmospheric Pressure. *BioResources*, *10*(3). <https://doi.org/10.15376/biores.10.3.4961-4969>
- 15 Rogovin, Z. A. (1972). *Khimiya tsellyulozy [Chemistry of cellulose]*. Khimia [in Russian].
- 16 Valley, R.B. (1955). A study of the alcoholysis of cellulose. *Text. Res. J.*, *25*(11), 930–939. <https://journals.sagepub.com/toc/trjc/25/11> <https://doi.org/10.1177/004051755502501104>
- 17 Heath, J. E., & Jeffries, R. (1968). The alcoholysis of cellulose. *J. Appl. Polym. Sci.*, *12*(3), 455–465. <https://doi.org/10.1002/app.1968.070120306>
- 18 Bouchard, J., Lacelle, S., Chornet, E., Vidal, P. P., & Overend, R. R. (1993). Mechanism of depolymerization of cellulose by ethylene glycol solvolysis. *Holzforschung*, *47*(4), 291–296. <https://doi.org/10.1515/hfsg.1993.47.4.291>
- 19 Zhu, S., Guo, J., Wang, X., Wang, J., & Fan, W. (2017). Alcoholysis: A Promising Technology for Conversion of Lignocellulose and Platform Chemicals. *ChemSusChem*, *10*(12), 2547–2559. Portico. <https://doi.org/10.1002/cssc.201700597>
- 20 Deng, W., Liu, M., Zhang, Q., & Wang, Y. (2011). Direct transformation of cellulose into methyl and ethyl glucosides in methanol and ethanol media catalyzed by heteropolyacids. *Catalysis Today*, *164*(1), 461–466. <https://doi.org/10.1016/j.cattod.2010.10.055>
- 21 Zou, X., Qin, T., Wang, Y., & Huang, L. (2011). Mechanisms and product specialties of the alcoholysis processes of poplar components. *Energy Fuels*, *25*(8), 3786–3792. <https://doi.org/10.1021/ef200726w>
- 22 Hishikawa, Y., Yamaguchi, M., Kubo, S., & Yamada, T. (2013). Direct preparation of butyl levulinate by a single solvolysis process of cellulose. *J. Wood Sci.*, *59*, 179–182. <https://doi.org/10.1007/s10086-013-1324-8>
- 23 Wang, Y., Yao, S., Jin, G., Qian, L., & Song, H. (2017). Catalytic alcoholysis of bagasse cellulose for the total reducing sugars with temperature-sensitive phase-variable ionic liquid. *Separation Science and Technology*, *52*(15), 2456–2462. <https://doi.org/10.1080/01496395.2017.1307225>
- 24 Chen, X., Zhang, Y., Mei, J., Zhao, G., Lyu, Q., Lyu, X., Lyu, H., Han, L., & Xiao, W. (2019). Ball milling for cellulose depolymerization and alcoholysis to produce methyl levulinate at mild temperature. *Fuel Process. Technol.*, *188*, 129–136. <https://doi.org/10.1016/j.fuproc.2019.02.002>
- 25 Chen, W., Zhang, Q., Lin, X., Jiang, K., & Han, D. (2020). The degradation and repolymerization analysis on solvolysis liquefaction of corn stalk. *Polymers*, *12*(10), 2337. <https://doi.org/10.3390/polym12102337>
- 26 Zhou, L., Gao, D., Yang, J., Yang, X., Su, Y., & Lu, T. (2020). Conversion of recalcitrant cellulose to alkyl levulinates and levulinic acid via oxidation pretreatment combined with alcoholysis over Al₂(SO₄)₃. *Cellulose*, *2*(3), 1451–1463. <https://doi.org/10.1007/s10570-019-02903-1>
- 27 Badgujar, K. C., Badgujar, V. C., & Bhanage, B. M. (2023). Synthesis of alkyl levulinate as fuel blending agent by catalytic valorization of carbohydrates via alcoholysis: Recent advances and challenges. *Catal. Today*, *408*, 9–21. <https://doi.org/10.1016/j.cattod.2022.10.008>
- 28 Surov, O. V., Afineevskii, A. V., & Voronova, M. I. (2023). Sulfuric acid alcoholysis as a way to obtain cellulose nanocrystals. *Cellulose*, *30*, 9391–9404. <https://doi.org/10.1007/s10570-023-05470-8>
- 29 Lee, M., Heo, M., Lee, H., & Shin, J. (2021). Facile and quantitative method for estimating the isolation degree of cellulose nanocrystals (CNCs) suspensions. *Materials*, *14*(21), 6463. <https://doi.org/10.3390/ma14216463>
- 30 Beck, S., Bouchard, J., & Berry, R. (2012). Dispersibility in water of dried nanocrystalline cellulose. *Biomacromolecules*, *13*(5), 1486–1494. <https://doi.org/10.1021/bm300191k>
- 31 Segal, L., Creely, J. J., Martin, A. E., & Conrad, C. M. (1959). An empirical method for estimating the degree of crystallinity of native cellulose using the X-ray diffractometer. *Text. Res. J.*, *29*(10), 786–794. <https://doi.org/10.1177/004051755902901003>
- 32 Scherrer, P. (1918). Bestimmung der Gröse und der inneren Struktur von Kolloidteilchen mittels Rontgenstrahlen. *Nachrichten von der Gesellschaft der Wissenschaften zu Göttingen, Mathematisch-physikalische Klasse*, *1918*, 98–100.

- 33 Rubleva, N. V., Lebedeva, E. O., Afineevskii, A. V., Voronova, M. I., Surov, O. V., & Zakharov, A. G. (2019). Production of cellulose nanocrystals by hydrolysis in mixture of hydrochloric and nitric acids. *ChemChemTech*, 62(12), 85–93. <https://doi.org/10.6060/ivkkt.20196212.5984>
- 34 Gaiolas, C., Belgacem, M. N., Silva, L., Thielemans, W., Costa, A. P., Nunes, M., & Silva, M. J. S. (2009). Green chemicals and process to graft cellulose fibers. *J. Colloid. Interface Sci.*, 330(2), 298–302. <https://doi.org/10.1016/j.jcis.2008.10.059>
- 35 Surov, O. V., Voronova, M. I., Rubleva, N. V., Kuzmicheva, L. A., Nikitin, D., Choukourov, A. Titov, V. A., & Zakharov, A. G. (2018). A novel effective approach of nanocrystalline cellulose production: Oxidation–hydrolysis strategy. *Cellulose*, 25, 5035–5048. <https://doi.org/10.1007/s10570-018-1910-4>
- 36 Voronova, M. I., Surov, O. V., & Zakharov, A. G. (2013). Nanocrystalline cellulose with various contents of sulfate groups. *Carbohydr. Polym.*, 98(1), 465–469. <https://doi.org/10.1016/j.carbpol.2013.06.004>
- 37 Voronova, M. I., Surov, O. V., Kuziyeva, M. K., & Atakhanov, A. A. (2022). Thermal and mechanical properties of polymer composites reinforced by sulfuric acid-hydrolyzed and TEMPO-oxidized nanocellulose: a comparative study. *ChemChemTech*, 65(10), 95–105. <https://doi.org/10.6060/ivkkt.20226510.6596>
- 38 Lin, N., & Dufresne, A. (2014). Surface chemistry, morphological analysis and properties of cellulose nanocrystals with gradiented sulfation degrees. *Nanoscale*, 6, 5384–5393. <https://doi.org/10.1039/C3NR06761K>
- 39 French, A. D. (2013). Idealized powder diffraction patterns for cellulose polymorphs. *Cellulose*, 21(2), 885–896. <https://doi.org/10.1007/s10570-013-0030-4>
- 40 Kontturi, E., Meriluoto, A., Penttila, P. A., Baccile, N., Malho, J. -M., Potthast, A., Rosenau, T., Ruokolainen, J., Serimaa, R., Laine, J., & Sixta, H. (2016). Degradation and crystallization of cellulose in hydrogen chloride vapor for high-yield isolation of cellulose nanocrystals. *Angew. Chem. Int. Ed.*, 55(46), 14455–14458. <https://doi.org/10.1002/anie.201606626>
- 41 Lorenz, M., Sattler, S., Reza, M., Bismarck, A., & Kontturi, E. (2017). Cellulose nanocrystals by acid vapour: towards more effortless isolation of cellulose nanocrystals. *Faraday Discuss.*, 202, 315–330. <https://doi.org/10.1039/C7FD00053G>
- 42 Adar, F. (2016). Characterizing modified celluloses using Raman spectroscopy. *Spectroscopy*, 31(11), 29–32. www.spectroscopyonline.com
- 43 Makarem, M., Lee, C. M., Kafle, K., Huang, S., Chae, I., Yang, H., Kubicki, J. D., & Kim, S. H. (2019). Probing cellulose structures with vibrational spectroscopy. *Cellulose*, 26, 35–79. <https://doi.org/10.1007/s10570-018-2199-z>
- 44 Agarwal, U. P., Ralph, S. A., Baez, C., & Reiner, R. S. (2021). Detection and quantitation of cellulose II by Raman spectroscopy. *Cellulose*, 28, 9069–9079. <https://doi.org/10.1007/s10570-021-04124-x>
- 45 Agarwal, U. P. (2017). Raman spectroscopy in the analysis of cellulose nanomaterials. In U.P. Agarwal, R.H. Atalla, & A. Isogai (Eds.), *Nanocelluloses: Their preparation, properties, and applications* (ACS Symposium Series, 1251, 4, 75–90). <https://doi.org/10.1021/bk-2017-1251.ch004>
- 46 Agarwal, U. P., Ralph, S. A., Reiner, R. S., & Baez, C. (2018). New cellulose crystallinity estimation method that differentiates between organized and crystalline phases. *Carbohydr. Polym.*, 190, 262–270. <https://doi.org/10.1016/j.carbpol.2018.03.003>
- 47 Zhang, K., Brendler, E., & Fischer, S. (2010). FT Raman investigation of sodium cellulose sulfate. *Cellulose*, 17, 427–435. <https://doi.org/10.1007/s10570-009-9375-0>
- 48 Agarwal, U. P., Reiner, R. S., Ralph, S. A., Catchmark, J., Chi, K., Foster, E. J., Hunt, C. G., Baez, C., Ibach, R. E., & Hirth, K. C. (2021). Characterization of the supramolecular structures of cellulose nanocrystals of different origins. *Cellulose*, 28, 1369–1385. <https://doi.org/10.1007/s10570-020-03590-z>
- 49 Li, Q., & Renneckar, S. (2011). Supramolecular structure characterization of molecularly thin cellulose I nanoparticles. *Biomacromolecules*, 12, 650–659. <https://doi.org/10.1021/bm101315y>
- 50 Agarwal, U. P., Ralph, S. A., Reiner, R. S., & Baez, C. (2016). Probing crystallinity of never-dried wood cellulose with Raman spectroscopy. *Cellulose*, 23, 125–144. <https://doi.org/10.1007/s10570-015-0788-7>
- 51 Reutov, O. A., Kurts, A. L., & Butin, K. P. (2021). *Organicheskaya khimiya [Organic chemistry]*. Laboratoriia znaniia [in Russian].
- 52 Bruice, P. Y. (2009). *Essential organic chemistry* (2nd ed.). Prentice Hall.
- 53 Ripin, D. H. B. (2011). pKa. In S. Caron (Ed.), *Practical synthetic organic chemistry: Reactions, principles, and techniques* (1st ed., chapter 18, pp. 771–803). Wiley. <https://doi.org/10.1002/9781118093559.ch18>
- 54 El Seoud, O. A., Fidale, L. C., Ruiz, N., D’Almeida, M. L. O., & Frollini, E. (2008). Cellulose swelling by protic solvents: which properties of the biopolymer and the solvent matter? *Cellulose*, 15, 371–392. <https://doi.org/10.1007/s10570-007-9189-x>
- 55 Zhao, H., Jia, Y., Liang, X., Hao, J., Xu, G., Chen, B., He, C., Jiao, Y., & Chang, C. (2024). Theoretical and experimental study of 5-ethoxymethylfurfural and ethyl levulinate production from cellulose. *Chem. Eng. J.*, 480, 148093. <https://doi.org/10.1016/j.cej.2023.148093>

**Index of articles published in
“Eurasian Journal of Chemistry”
in 2024**

№ p.

CHEMICAL TECHNOLOGY

<i>Aitbekova, D.E., Baikenov, M.I., Muratbekova, A.A., Bolatbay, A.N., Balpanova, N.Zh., Tyanakh, S., Fengyun Ma, Khamitova, T.O.</i> The Use of the Catalysts Based on Coal Ash Microsphere and Chrysotile in the Thermal Destruction of Primary Coal Tar.....	1	73
<i>Dzhumadullaeva, S.A., Baeshov, A.B.</i> An Efficient Ion-Exchange Resin Catalysts for the Liquid-Phase Selective Hydrazinolysis of Succinic Acid.....	1	66
<i>Khoshimov, I.E., Turdialieva, Sh.I., Seytnazarov, A.R., Namazov, Sh.S., & Rifky, M.</i> Investigation of Vapor Pressure and Infrared Spectroscopic Analysis of Phosphoric Acid Extract Evaporation after Desulfation with SrCO ₃	4	82
<i>Megbenu, H.K., Azhikhanova, Zh., Inkar, G., Rakhimgaliyev, N., Mels, A., Kenzheshov, A., Askarov, A., Shaimardan, M. & Nuraje, N.</i> Catalytic Dehydration of Biomass-Derived Feedstocks to Obtain 5-Hydroxymethylfurfural and Furfural.....	2	96
<i>Muravlev, D.A., Doroganov, A.P., Philippova, O.E., & Shibaev, A.V.</i> Natural Polyelectrolyte Hydrogels With Two Types of Cross-Links with Different Energy.....	2	89
<i>Shakayeva, A.Kh., Yeszhanov, A.B., Zhumazhanova, A.T., Korolkov, I.V., Zdorovets, M.V.</i> Fabrication of Hydrophobic PET Track-Etched Membranes using 2,2,3,3,4,4,4-Heptafluorobutyl Methacrylate for Water Desalination by Membrane Distillation.....	2	81
<i>Surov, O.V., & Voronova, M.I.</i> Obtaining Cellulose Nanocrystals in a Medium of Primary Monohydric Alcohols.....	4	92

INORGANIC CHEMISTRY

<i>Soualmi, S., Henni, M., Djahnit, L., & Hamdani, H.</i> Sol-gel Synthesized ZnO-SrMn ₂ O ₄ Nanocomposite and Its Antibacterial Properties.....	4	71
<i>Turovets, M.A., Fomin, V.N., Kelesbek, N.K., Kaykenov, D.A., Sadyrbekov, D.T., Aynabayev, A.A., Aldabergenova, S.K.</i> Chemometric Approach for the Determination of Vanadium by the LIBS Method.....	4	61

**NANO- AND PHOTO- CATALYSIS IN CURRENT CHEMISTRY:
POSSIBILITIES AND CHALLENGES**

<i>Andreeva, A.V., Baimuratova, R.K., Dorokhov, V.G., Akkuratov, A.V., Shilov, G.V., Kugabaeva, G.D., Golubeva, N.D., & Dzhardimalieva, G.I.</i> Rational Synthesis of UiO-66 and its Application in the Hydrogenation Reaction of p-Chloronitrobenzene.....	3	92
<i>Baikenov, M.I., Izbastanova, D.S., Su, X., Tusiphan, A., Akanova, Z.B., Balpanova, N.Zh., Baikenova, G.G., Zhao, Zh., & Li, W.</i> Optimal Conditions for Demetallization of the Heavy Fraction of Low-Temperature Coal Tar of Shubarkol Komir JSC in the Presence of “Coal Shale” Catalytic Additive.....	3	30
<i>Bayeshov, A., Bayeshova, A.K. & Turlybekova, M.N.</i> Catalytic Effect of Titanium Ions on the Cathodic Reduction of Selenium (VI), Copper (II), Uranium (VI) Ions and Other Metals in an Aqueous Solutions.....	3	55
<i>Burkeyeva, G.K., Kovaleva, A.K., Ibadullaeva, M.N., Ubaydullauly, M., Plocek, J. & Sergaziyeva, K.E.</i> Synthesis and Investigation of Catalytic Properties of Metal-Polymer Nanocomposites Based on Unsaturated Polyester Resins.....	3	148
<i>Hasanguliyeva, N.M., Shakunova, N.V., & Litvishkov, Y.N.</i> Microwave Solid-Phase Synthesis of Ni-Co Ferrites and their Activities in Liquid-Phase Oxidation of m-Xylene.....	3	82
<i>Ivanova, N.M., Vissurkhanova, Ya.A., Soboleva, Ye.A., & Kenzhetaeva, S.O.</i> Copper Nanoparticles Supported on Nickel Ferrite: Synthesis and Electrocatalytic Activity.....	3	109
<i>Kolesnik, O.V., Grabovoy, A.S., Badun, G.A., Churilov, G.N., & Kudryasheva, N.S.</i> Radioprotective Properties of Fullerenol: Cellular, Biochemical and Physicochemical Approaches.....	3	72

<i>Kudaibergenov, S.E.</i> Catalytic Properties of Polyampholytes, Polyampholyte-Metal Complexes, Polyampholyte-metal Nanoparticles and Polyampholyte-Enzyme Conjugates: A Mini-Review.....	3	42
<i>Li, Q., Li, J., Zhao, Y., Zhu, Y., Baikenov, M.I., Liu, X., & Su, X.</i> Thermal Catalytic Production of Potassium Humate Fertilizer from Tobacco Straw and its Performance in Wheat Hydroponics.....	3	7
<i>Liu, X., Bekchanov, D., Baikenov, M.I., & Su, X.</i> Construction of Ag/AgCl@MIL-53(Fe): Achieving Efficient Photocatalytic Water Oxidation via the Plasma-Phase Silver and Heterojunction Synergistic Effect	3	160
<i>Maksotova, K.S., Akbayeva, D.N., Bakirova, B.S., Serikkyzy, A., Lesbek, B.M., Tatykhanova, G.S. & Kudaibergenov, S.E.</i> Preparation and Characterization of Copper Nanoparticles Stabilized by Poly(vinyl alcohol) for Catalytic Oxidation of 1-Propanol.....	3	119
<i>Saman, D., Bondarenko, L.S., Baimuratova, R.K., Dzeranov, A.A., Dzhardimalieva, G.I., Tropkaya, N.S., & Kydralieva, K.A.</i> A Statistical Design Approach for an Effective Catalyst in the Fenton Reaction in Case of Fe ₃ O ₄ -MOF MIL-88b (Fe) in Methylene Blue Degradation Kinetics	3	16
<i>Sidorov, V.L., Baimuratova, R.K., Korchagin, D.V., Ivanov, A.V., Kydralieva, K.A., & Dzhardimalieva, G.I.</i> Magnetically Separable Fe ₃ O ₄ /γ-Fe ₂ O ₃ @MIL-88b(Fe) and Fe ₃ O ₄ /γ-Fe ₂ O ₃ @NH ₂ -MIL-88b(Fe) Composites for the Photocatalytic Degradation of Congo Red Dye	3	130
<i>Sushko, E.S., Zenkov, A.V., & Kudryasheva, N.S.</i> Effects of Selenite-Ions on a Luminescence Enzymatic System	3	65

ORGANIC CHEMISTRY

<i>Gorokhov, V.Yu., Zabolotnykh, S.A., Chekanova, L.G., & Vaulina, V.N.</i> A New Method for the Synthesis of Ald(ket)azines and their Antioxidant Activity	4	4
<i>Kaldybekov, D.B., Shatabayeva, E.O., Polatkhani, A.A., Tuleyeva, R.N., Irmukhametova, G.S., & Khutoryanskiy, V.V.</i> Development and Investigation of Mucoadhesive Polymers Based on Chitosan for Intravesical Therapy.....	4	13
<i>Kulakov, I.I., Chikunov, S.Y., Elyshev, A.V., Kulakov, I.V.</i> Multicomponent Synthesis of Novel Unsymmetric 6-Aryl Substituted 5-Nitropyridines.....	2	13
<i>Palamarchuk, I.V., & Kulakov, I.V.</i> A New Method for Obtaining Carboxylic Derivatives of Oxazolo[5,4-b]pyridine Based on 3-Aminopyridine-2(1 <i>H</i>)-ones	2	32
<i>Salkeyeva, L.K., Pevzner, L.M., Vojtišek, P., Minayeva, Ye.V.</i> On the Bromination of Diethyl 3,5-dimethyl-1 <i>H</i> -pyrrole-2,4-dicarboxylate: the True Structure of the Halbig's Product.....	1	14
<i>Shakhabutdinov, S.Sh., Yugay, S.M., Ashurov, N.Sh., Ergashev, D.J., Atakhanov, A.A., & Rashidova, S.Sh.</i> Characterization Electrospun Nanofibers Based on Cellulose Triacetate Synthesized from Licorice Root Cellulose	2	21
<i>Tazhbayev, Y.M., Kazhmuratova, A.T., Zhaparova, L.Zh., Tuleuov, U.B., Nassikhatuly, Y., Mitricheva, E.S., Kwiatkowski, A.L., & Shibaev, A.V.</i> Synthesis of Water-Soluble Polyethylene Glycol Fumarates for Biomedical Applications	2	4
<i>Turgunaliyeva, D.M., Kulakov, I.V.</i> New Synthesis of 2-Aminopyrimidines by Amination of Biginelli Reaction Products — Oxadiazocines.....	1	5
<i>Yessentayeva, N.A., Galiyeva, A.R., Daribay, A.T., Sadyrbekov, D.T., Zhumagalieva, T.S., Marsel, D.T.</i> Synthesis and Optimization of Bovine Serum Albumin Nanoparticles Immobilized with Antituberculosis Drugs	1	33
<i>Zhakina, A.Kh., Arnt, O.V., Vassilets, Ye.P., Alzhankyzy, A., & Zhakin, A.M.</i> Synthesis, Characterization and Application of New Polymers Imprinted with Zinc (II) Ions.....	2	45
<i>Zhengis, A., Amrenova, Ye., Yergesheva, A., Kanzhigitova, D., Imekova, G., Toktarbay, Zh., Toktarbaiuly, O., Abutalip, M., Nuraje, N.</i> Structural Studies and Applications of Sulfobetaine-Based Polybetaines at Interfaces.....	1	24

PHYSICAL AND ANALYTICAL CHEMISTRY

<i>Abdulsattar, M.A.</i> Effect of Acetylene Properties on its Gas Sensing by NiO Doped ZnO Clusters: A Transition State Theory Model.....	4	35
<i>Gandhi, S.P., Mate, G.D., Nagore, D.H., Chitlange, S.S.</i> Quantifying Curcumin, Gallic Acid, and Resveratrol in a Polyherbal Mixture: a Robust HPTLC Method	1	56
<i>Karaush-Karmazin, N.M., Minaev, B.F., Minaeva, V.A., Panchenko, O.O., Ågren, H.</i> Hirshfeld Surfaces Analysis of Intermolecular Interaction in the Series of Steroid Hormone Molecular Crystals.....	1	43

<i>Kwiatkowski, A.L., Kalinin, P.V., & Philippova, O.E.</i> Effect of Salt Content on Solubilization of Hydrophobic Polymer by Wormlike Micelles of Ionic Surfactant	2	74
<i>Kwiatkowski, A.L., Molchanov, V.S., Orekhov, A.S., Kuklin, A.I., & Philippova, O.E.</i> Detecting Shape of Hybrid Polymer/Surfactant Micelles: Cryo-Transmission Electron Microscopy, Small-Angle Neutron Scattering and Dynamic Light Scattering Study	2	54
<i>Lahmar, N., Djehiche, M., & Bachiri, M.</i> Removal of E110 from Aqueous Solution Using Heat-Activated Persulfate	4	22
<i>Rakhimzhanova, A.S., Muzaparov, R.A., Pustolaikina, I.A., Kurmanova, A.F., Nikolskiy, S.N., Kapishnikova, D.D., Stalinskaya, A.L., & Kulakov, I.V.</i> A Series of Novel Integrastatins Analogues: <i>In Silico</i> Study of Physicochemical and Bioactivity Parameters	4	44
<i>Sarsenbekova, A.Zh., Bolatbay, A.N., Havlicek, D., Issina, Zh.A., Sarsenbek, A.Zh., Kabdenova, N.A., & Kilybay, M.A.</i> Effect of Heat Treatment on the Supramolecular Structure of Copolymers Based on Poly(propylene glycol fumarate phthalate) with Acrylic Acid	2	61

PREFACE

About new journal website	1	4
<i>Su, X., Dzhardimalieva, G.I., & Baikenov, M.I.</i> Special Issue Foreword from Guest Editors	3	4

RETRACTION NOTE

<i>Tulasi, S.L., Sumalatha, P., Rani, N.U., Peddi, P.</i> Retraction Note to: Green Synthesis, Characterization and Environmental Application of Copper Oxide Nanoparticle obtained Using Aqueous Extract of <i>Schrebera Swietenoides Roxb.</i>	1	82
--	---	----